THE FORMATION OF GASEOUS NITROUS ACID (HONO): A KEY DETERMINANT OF TROPOSPHERIC OZONE AND FINE PARTICLES

Final Report
Contract No. 97-311

Prepared for:

California Air Resources Board and the
California Environmental Protection Agency
Research Division
P.O. Box 2815
Sacramento, CA 95812

Prepared by:

Principal Investigator: Barbara J. Finlayson-Pitts
Researchers: Najat A. Saliba
Lisa M. Wingen

William S. Barney
Michihiro Mochida
Husheng Yang

Department of Chemistry
University of California, Irvine
Irvine, CA 92697-2025

Collaborator: Donald Dabdub
Researcher: Eladio Knipping

Department of Mechanical and Aerospace Engineering, UCI

July 11, 2001

Disclaimer

The statements and conclusions in this report are those of the contractor and not necessarily those of the California Air Resources Board. The mention of commercial products, their source, or their use in connection with material reported herein is not to be construed as actual or implied endorsement of such products.

ACKNOWLEDGEMENTS

The authors are grateful to the California Air Resources Board (Contract No. 97-311) for support of this work. The salary of Dr. Michihiro Mochida was provided by a Research Fellowship of the Japan Society for the Promotion of Science for Young Scientists. The authors would like to thank M. J. Ezell and T. Nordmeyer for initial work on the single reflectance apparatus, M.T. Kleinman for assistance with the ion chromatography, K. Shea, D. Batra and K. R. Muroya for assistance with the BET surface area measurements, and M. Gebel for providing mass spectrometry data. The authors would also like to thank R. A. Dluhy, P. R. Griffiths, J. P. Devlin, G. E. Ewing, D. J. Donaldson, J. C. Hemminger, and J. N. Pitts, Jr. for helpful discussions. We especially appreciate R. A. Dluhy for providing his programs for the calculation of infrared reflectance spectrum on an N-phase system of parallel, optically isotropic layers, and the calculation of the penetration depth in the last phase, as well as G. Nathanson for providing a preprint prior to publication, J. P. Devlin for providing an unpublished spectrum of anhydrous nitric acid, and B. E. Koel for providing preprints prior to publication.

This Report was submitted in fulfillment of ARB Contract No. 97-311 under the sponsorship of the California Air Resources Board. Work was completed as of December 31, 2000.

TABLE OF CONTENTS

Page

LIST OF FIGURES …….. i

LIST OF TABLES …… vi

ABSTRACT ……. vii

EXECUTIVE SUMMARY ……. viii

1. INTRODUCTION …..……... 1

2. METHODS AND MATERIALS …….. 5
   - I. ANALYTICAL METHODS AND EQUIPMENT ……. 5
     - I.A. Environmental Chamber …….. 5
       - I.A.1. Infrared Spectrometer ……. 5
       - I.A.2. UV/Visible (DOAS) Spectrometer ……. 7
     - I.B. Long Path Infrared Cell …… 7
     - I.C. Porous Glass Cell …… 8
     - I.D. Single-Reflectance FTIR ……. 11
     - I.E. Cell for Measurement of Water on Glass ……. 12
     - I.F. Description of Airshed Model ……. 14
       - I.F.1. 100% Land Reaction. …… 15
       - I.F.2. 10% Land Reaction. ……. 15
       - I.F.3. Svensson. …….. 15
   - II. MATERIALS …….. 16
     - II.A. HONO Generator ……. 16
     - II.B. Gas Synthesis and Solution Preparation ……... 18

3. RESULTS ……. 19
   - I. MEASUREMENT OF HONO …….… 19
     - I.A. HONO Titration by the Reaction HONO + HCl → ClNO + H_2O … 19
       - I.A.1. Current Measurement Techniques for HONO …… 19
       - I.A.2. New Technique for Quantification of HONO ……... 19
       - I.A.3. Analysis of UV/Visible and FTIR Data ……. 20
       - I.A.4. Stoichiometry of Reaction of HONO With HCl ……... 21
       - I.A.5. Kinetics of Reaction of HONO With HCl ……. 25
       - I.A.6. HONO Quantification …… 27
     - I.B. Infrared Absorption Cross-Sections of Nitrous Acid (HONO) …… 31
       - I.B.1. Reference Spectra …….. 31
       - I.B.2. Data Analysis ……. 33
       - I.B.3. Water Subtraction …….. 39
       - I.B.4. High-Resolution Studies …… 39
       - I.B.5. Model References …….. 42

I.B.6. Uncertainty, Detection Limit, and Linearity ……. 45
II. KINETICS OF HONO FORMATION …… 47
II.A. NO_2 Hydrolysis - The Effect of Aerosol ……. 47
II.B. Experiments in the Long Path Cell …….. 49
II.B.1. Reaction Order and Kinetics ……. 52
II.B.2. Dependence of Kinetics on Surface Area-to-Volume Ratio 58
II.B.3. Product Yields – Nitrous Acid and Nitrous Oxide …… 59
III. MECHANISM OF HONO FORMATION …….. 64
III.A. N_2O_4 Enhancement on Porous Glass at Room Temperature: A Key Intermediate in Heterogeneous Hydrolysis of NO_2? ……. 64
III.A.1. Dependence on Surface Water Content ……. 69
III.B. FTIR Study of N_2O_3 on Porous Glass at Room Temperature …….. 72
III.B.1. Evidence for N_2O_3 Adsorbed on Porous Glass ……. 72
III.B.2. Dependence of Gas and Surface-Adsorbed N_2O_3 on Gas Phase NO and NO_2 ……..…….. 77
III.B.3. Effects of Added Water Vapor …….. 78
III.C. FTIR Study of the Reaction of Gaseous NO with HNO_3 on Silica Surfaces: Implications for Conversion of HNO_3 to Photochemically Active NO_x in the Atmosphere ….…… 82
III.C.1. Formation of NO_2 by Exposure of HNO_3 Adsorbed on Porous Glass to Gas Phase NO ..…….……. 82
III.C.2. Possible Reaction Mechanisms ……. 85
III.C.3. Kinetics of Reaction of HNO_3(ads) + NO(g) on Porous Glass ……. 89
III.D. Reaction of Adsorbed Nitric Acid With Gaseous Nitric Oxide in Long Path Cell …….. 92
III.D.1. Effect of Relative Humidity ..…… 92
III.D.2. Thermodynamic Considerations …… 97
III.D.3. Water Coverage on the Cover Glass Surface …… 99
III.D.4. Estimate of HNO_3 Concentration on the Borosilicate Glass Walls of the Long Path Cell …… 101
IV. INFRARED SPECTROSCOPIC STUDIES OF BINARY SOLUTIONS OF NITRIC ACID AND WATER AND TERNARY SOLUTIONS OF NITRIC ACID, SULFURIC ACID AND WATER AT ROOM TEMPERATURE: EVIDENCE FOR MOLECULAR NITRIC ACID AT THE SURFACE … 102
IV.A. Spectra of Binary Solutions of HNO_3 and H_2O …… 102
IV.B. Spectra of Ternary Solutions of HNO_3, H_2SO_4 and H_2O …….. 107
V. INITIAL AIRSHED MODELING RESULTS ……. 111

4. DISCUSSION …… 118

5. SUMMARY AND CONCLUSIONS ……... 128

6. RECOMMENDATIONS …….. 130

REFERENCES ……. 131

LIST OF PUBLICATIONS ……. 142

GLOSSARY OF TERMS, ABBREVIATIONS, AND SYMBOLS …….. 143

APPENDIX - ANALYSIS OF SPECTROSCOPIC DATA …… 146

LIST OF FIGURES

2. METHODS AND MATERIALS

Figure 2.1. The environmental chamber used for the HONO titration and HONO cross section measurements. Also shown are the instruments interfaced to it including DOAS, FTIR, API-MS and the aerosol generator. …….. 6

Figure 2.2. The long path cell used for the NO_2 hydrolysis and NO + HNO_3(ads) reaction studies. …….. 8

Figure 2.3. The porous glass cell used to study the NO+HNO_3(ads) and NO + N_2O_3 reactions. …… 9

Figure 2.4. Single Reflectance FTIR set up used to measure species present at the interface. i.e. HNO_3 on the HNO_3-H_2O interface. ……. 12

Figure 2.5. Borosilicate cover glass cell used to measure water coverage on the cover glass. …… 13

Figure 2.6. Set up used to generate N_2(g) at different relative humidities. …. 14

Figure 2.7. The HONO generator setup. ……. 17

3. RESULTS

I. MEASUREMENT OF HONO

Figure 3.I.1. Infrared spectra showing the loss of HONO and increase in ClNO with time during a typical experiment (#2). ……. 22

Figure 3.I.2. UV/visible spectra of gaseous HONO corresponding to approximately the same times as the IR spectra shown in Figure 3.I.1. …… 23

Figure 3.I.3. Kinetics modeling plots to show the difference in time profiles for HONO and ClNO with and without additional (wall) losses taken into account. ……. 23

Figure 3.I.4. Typical stoichiometry plot showing the net production of ClNO versus the net decrease in HONO for equal time intervals. ……. 24

Figure 3.I.5. Typical plots of ln(a_{HONO}) versus time. …… 27

Figure 3.I.6. Kinetics modeling results using ACUCHEM showing the effect of adding HCl wall loss to the system. …… 28

Figure 3.I.7. Time profiles for HONO measured by DOAS and ClNO by FTIR during a typical experiment (#1). …… 29

Figure 3.I.8. DOAS (UV) spectra of HONO and NO_2. …….. 34

Figure 3.I.9. Linear regression fits of uncalibrated concentrations (from IR spectra) to absolute concentrations (from DOAS spectra). …… 35

Figure 3.I.10. Water subtraction. …… 40

Figure 3.I.11. (a) Actual *trans*-ν_3 reference spectrum compared to 5-Gaussian model spectrum. Inset shows the five Gaussian functions used. … 44

Figure 3.I.12. Comparison of HONO concentrations for experiment no. 5 determined from actual reference spectra (a) for 1263 cm^{-1} peak, (b) for 852 cm^{-1} peak, to simulated reference spectra. …… 46

II. KINETICS OF HONO FORMATION
Figure 3.II.1. Hydrolysis of NO_2 and formation of HONO in the environmental chamber in the presence and absence of aerosol. …… 48
Figure 3.II.2. FTIR spectra of (a) decrease of NO_2, and (b) formation of HONO during a typical NO_2 hydrolysis experiment (experiment 12). …… 51
Figure 3.II.3. FTIR spectra showing the formation of small amounts of N_2O (experiment 12). …….. 51
Figure 3.II.4. Time profiles of NO_2, HONO, and N_2O during hydrolysis of NO_2 (experiment 12). ……. 52
Figure 3.II.5a. Plots to determine reaction order with respect to NO_2 for a typical low relative humidity experiment (#6). …….. 53
Figure 3.II.5b. Plots to determine reaction order with respect to NO_2 for a typical medium relative humidity experiment (#11). …….. 54
Figure 3.II.5c. Plots to determine reaction order with respect to NO_2 for a typical high relative humidity experiment (#19). …… 54
Figure 3.II.6. Plots of ln[NO_2] and $[NO_2]^{-1}$ versus time for the hydrolysis experiment performed in the 561 L chamber. ……. 56
Figure 3.II.7. Plot of the decay constant of NO_2 versus initial [H_2O]. ……. 56
Figure 3.II.8. Plots of HONO time traces for three experiments at high water vapor concentrations (experiments 15 (Δ), 19 (O), and 22 (◊)). …. 60
Figure 3.II.9. Plots of ln[HONO] versus time to obtain the HONO formation rate constants, k_a, from reaction (II.1). …… 60
Figure 3.II.10. Plot of the HONO formation rate constant, k_a (s^{-1}), versus initial NO_2 concentration for experiments 15, 19, and 22 showing a linear dependence. …… 61
Figure 3.II.11. Nitrous oxide formation versus time showing the dependence of N_2O formation upon water concentration. …….. 62
Figure 3.II.12. Plots of the time profiles of N_2O showing the increase in the rate of N_2O formation with $[NO_2]_0$. …… 63

III. MECHANISM OF HONO FORMATION
Figure 3.III.1. FTIR spectra of 2.9 Torr NO_2 in N_2 (total pressure 508 Torr) in the "dry" porous glass cell. …….. 65
Figure 3.III.2. FTIR spectra of 3.3 Torr NO_2 in N_2 (total pressure 573 Torr) in the "wet" porous glass cell. ……. 67
Figure 3.III.3. Gas phase spectrum taken under same experimental conditions as Fig. III.1d showing the presence of gaseous N_2O. ……. 68
Figure 3.III.4. Gas phase spectrum taken under the same experimental conditions as in Fig. III.2 showing the presence of gaseous HONO. …… 69
Figure 3.III.5. Uptake of NO_2 on porous glass cell under dry and wet conditions. 70
Figure 3.III.6. Gas phase species from wet (upper) and dry (lower) porous glass experiments. …… 71

Figure 3.III.7. Infrared spectra of combined gas and adsorbed species after the introduction of (a) NO_2/N_2O_4 (1.7×10^{17} molecule cm^{-3}) into the reaction cell containing the porous glass followed by NO at concentrations of (b) 3.0×10^{17}, (c) 6.4×10^{17}, and (d) 9.5×10^{17} molecule cm^{-3}, respectively. …… 73
Figure 3.III.8. Infrared spectra of gas and surface species after the introduction of 3.3×10^{17} molecule cm^{-3} of NO_2/N_2O_4 and 9.5×10^{17} molecule cm^{-3} of NO into the cell containing the porous glass. ……. 75
Figure 3.III.9. Infrared bands of surface-adsorbed N_2O_3 with two isotopes, ^{14}N and ^{15}N. …… 76
Figure 3.III.10. Measured (a) gas phase concentrations of N_2O_3 measured using the 1830 cm^{-1} band and (b) integrated intensities of the band at 1870 cm^{-1} due to surface-adsorbed N_2O_3 when increasing amounts of NO are added to an initial NO_2/N_2O_4 mixture at the initial concentrations of NO_2 shown. …… 77
Figure 3.III.11. Measured (a) gas phase concentrations of N_2O_3 using the 1830 cm^{-1} band, and (b) integrated intensities of the band at 1870 cm^{-1} due to surface-adsorbed N_2O_3 when increasing concentrations of NO_2/N_2O_4 are added to either 2.9 or 6.1×10^{17} molecule cm^{-3} NO in the cell. …….. 78
Figure 3.III.12. The difference (ΔI_{N2O3}) shown in Figure 3.III.11 as a function of square of the NO_2(g) concentration. …… 79
Figure 3.III.13. Infrared spectra of (a) the gas phase plus surface-adsorbed species before adding water (dotted line) and after adding water vapor, and (b) spectrum of surface-adsorbed N_2O_3 before and after the addition of water vapor. The cell with the porous glass had been heated to 520 K for several hours prior to introducing the gases. …….. 80
Figure 3.III.14. Time-concentration profiles of HONO with 1.1×10^{18} molecules cm^{-3} of NO and 1.6×10^{17} molecules cm^{-3} of NO_2 in the cell before and after the addition of 6.6×10^{17} molecules cm^{-3} of water vapor in 650 Torr of He. …….. 81
Figure 3.III.15. FTIR spectra of (a) surface species after the introduction of HNO_3; the porous glass has 9.4×10^{18} adsorbed molecules of HNO_3 (determined by ion chromatography); (b) spectrum of gas plus surface species 60 min after introduction of NO (6.7×10^{16} molecules cm^{-3}) along with 460 Torr of He to the reaction cell; (c) the gas phase spectrum under the same conditions as (b); (d) the difference spectrum between (b) and (c) due to surface adsorbed species. …….. 83
Figure 3.III.16. Gas phase infrared spectra (a) after 120 min during the reaction of adsorbed HNO_3 (initially 9×10^{18} molecules) with 6.5×10^{16} molecules cm^{-3} NO; (b) after subtraction of the ν_{11} band of N_2O_4 from (a), showing the ν_3 band of gas phase *trans*-HONO whose intensity corresponds to a concentration of $\sim 2 \times 10^{14}$ molecules cm^{-3}; (c) of NO alone. …….. 84
Figure 3.III.17. Infrared spectra of surface-adsorbed HNO_3 with some gaseous nitrogen oxides. …….. 85

Figure 3.III.18. Infrared spectra of the combination of gas and adsorbed species after the reaction of surface adsorbed HNO_3 with gas phase NO at various reaction times. ……. 89
Figure 3.III.19. The time evolution of surface-adsorbed HNO_3 (1.1×10^{19} molecules) and gaseous NO_2 product measured using infrared bands at 1677 cm^{-1} and 1620 cm^{-1}, respectively, when NO (6.1×10^{16} molecules cm^{-3}) was added to the cell in the presence of 450 Torr He. …….. 90
Figure 3.III.20. (a) The observed pseudo-first order rate constants for HNO_3 decay on porous glass as a function of the initial NO concentration in the gas phase at two different initial amounts of adsorbed HNO_3. (b) Same as (a) but plotted in terms of the rate, $-dN_{HNO3}/dt$ (molecules s^{-1}). …….. 91
Figure 3.III.21. (a) Measured pseudo-first order rate constants for HNO_3 decay as a function of initial adsorbed HNO_3 on the porous glass at a constant NO concentration of 6×10^{16} molecules cm^{-3} (total of 5×10^{18} molecules available for reaction in the cell). (b) Same as (a) but plotted in terms of the rate, $-dN_{HNO3}/dt$. ……... 91
Figure 3.III.22. Decay of gas phase NO and formation of NO_2 in the long path cell whose walls had first been exposed to HNO_3 at 0% relative humidity. …….. 92
Figure 3.III.23. Decay of gas phase NO and formation of NO_2 in the long path cell whose walls had first been exposed to HNO_3 for (a) 20% relative humidity and (b) 30% relative humidity. ……. 94
Figure 3.III.24. Decay of gas phase NO and formation of NO_2 in the long path cell whose walls had first been exposed to HNO_3 for (a) 40% relative humidity and (b) 50% relative humidity. …….. 94
Figure 3.III.25. Decay of gas phase NO and formation of NO_2 in the long path cell whose walls had first been exposed to HNO_3. …….. 96
Figure 3.III.26. Rate of NO_2 formation as a function of initial NO concentration in the long path cell at 1 atm pressure and 50% RH. ……. 96
Figure 3.III.27. Absorption bands between 3800 to 2800 $cm^{-1}$of H_2O adsorbed on cover glass at different relative humidities. …… 100
Figure 3.III.28. Number of layers of adsorbed H_2O on cover glass shown as a function of different relative humidities. …… 100

IV. INFRARED SPECTROSCOPIC STUDIES OF BINARY SOLUTIONS OF NITRIC ACID AND WATER AND TERNARY SOLUTIONS OF NITRIC ACID, SULFURIC ACID AND WATER AT ROOM TEMPERATURE: EVIDENCE FOR MOLECULAR NITRIC ACID AT THE SURFACE
Figure 3.IV.1. SR spectra of $HNO_3 – H_2O$ solutions. The concentrations of HNO_3 for spectra (a)-(f) are 40, 16, 7.4, 3.7, 1.8 and 0.9 mol %, respectively. Spectrum (g) is for pure water. …….… 103
Figure 3.IV.2. ATR spectra of the HNO_3 solutions shown in Figure 3.IV.1. …….. 105
Figure 3.IV.3. Comparison of the (a) ATR and (b) SR spectra of the 40 mol % HNO_3 solution. Spectrum (a) is the same as Figure 3.IV.2a, and spectrum (b) is the same as Figure 3.IV.1a. ……. 106

Figure 3.IV.4. Comparison of the ATR spectra for the 3.7 mol % $HNO_3 – H_2O$ solution as recorded; (b) corrected for the wavelength dependence; (c) the SR spectrum. The agreement of the relative band intensities between (b) and (c) substantiates the wavenumber correction of the ATR spectrum. …… 107
Figure 3.IV.5. SR spectra of ternary solutions of $H_2SO_4 – HNO_3 – H_2O$. The mol % H_2SO_4 is 25 % in all 5 solutions. The mol % HNO_3 is (a) 25, (b)15, (c) 10, (d) 5, and (e) 0. …… 108
Figure 3.IV.6. Comparison of SR spectra of (a) 28.5 mol % $HNO_3 – H_2O$ solution with (b) H_2SO_4 (25 mol %) – HNO_3 (25 mol %) – H_2O (50 mol %) as in Figure 3.IV.5a. The concentration of undissociated HNO_3 is the same in these two mixtures; (c) is the difference spectrum between H_2SO_4 (25 mol %) – HNO_3 (25 mol %) – H_2O (50 mol %) and H_2SO_4 (25 mol %) – H_2O (75 mol %), i.e. Figure 3.IV.5a – Figure 3.IV.5e; (d) difference spectrum in (c) with one third of water peak at 3400 cm^{-1} observed in Figure 3.IV.5e added back to adjust for the different amounts of water in the subtracted spectrum. …….. 110

V. INITIAL AIRSHED MODELING RUNS
Figure 3.V.1. Model of ozone: Base Case, observations, 100% land reaction, and 10% land reaction for Central L.A. ……. 113
Figure 3.V.2. Model of ozone: Base Case, observations, 100% land reaction, and 10% land reaction for Riverside. ……. 113
Figure 3.V.3. Model of PM 2.5 nitrate: Base Case, observations, 100% land reaction, and 10% land reaction for Central L.A. …… 114
Figure 3.V.4. Model of PM 2.5 nitrate: Base Case, observations, 100% land reaction, and 10% land reaction for Riverside. …… 114
Figure 3.V.5. Model of ozone: Base Case, observations, and Svensson kinetics for Central L.A. …… 115
Figure 3.V.6. Model of ozone: Base Case, observations, and Svensson kinetics for Riverside. …… 115
Figure 3.V.7. Model of PM2.5 nitrate: Base Case, observations, and Svensson kinetics for Central L.A. …….. 116
Figure 3.V.8. Model of PM2.5 nitrate: Base Case, observations, and Svensson kinetics for Riverside. …… 116
Figure 3.V.9. Model of HONO: Base Case and Svensson et al. (1987) parameterization for Central L.A. ……. 117
Figure 3.V.10. Model of HONO: Base Case and Svensson et al. (1987) parameterization for Riverside. …….. 117

APPENDIX
Figure A.1. Comparison of SR and transmission spectra for a saturated $NaHSO_3$ solution. (a) reflectance spectrum ($R_{\bar{\nu}}$) using a reflecting gold mirror for the background; (b) KK transform of the reflectance spectrum; (c) transmission spectrum with solution sandwiched between CaF_2 windows; (d) ATR spectrum. …….. 150

LIST OF TABLES

3. RESULTS

I. MEASUREMENT OF HONO

Table 3.I.1. Summary of Stoichiometry and Kinetics Data for HONO Titration Experiments. ……. 24
Table 3.I.2. Summary of Kinetic Data for HONO Titration Experiments. ……. 26
Table 3.I.3. Summary of $[HONO]_0$ Data for HONO + HCl Titration Experiments. ……. 30
Table 3.I.4. Experimental Conditions for Infrared Cross-Section Measurements. 32
Table 3.I.5. Infrared Absorption Cross-Sections: Q-Branch Intensity at Given Wavenumber. ……. 37
Table 3.I.6. Infrared Absorption Cross-Sections: Integrated Band. …….. 37
Table 3.I.7. Absorbance Ratios of HONO to Water for Q-Branches of Typical Spectra. …….. 41
Table 3.I.8. Sensitivity of Q-Branch Total Absorbance and Least-Squares Fit Methods to Water Subtraction Errors. …….. 43
Table 3.I.9. Parameters Used to Generate Model Reference Spectra. ……. 43

II. KINETICS OF HONO FORMATION …… 47

Table 3.II.1. Experimental Conditions for NO_2 Hydrolysis in Chamber With and Without Aerosol. ……. 47
Table 3.II.2. Summary of NO_2 Hydrolysis Experiments Performed in the Long Path Cell. …….. 50
Table 3.II.3. Summary of Rate Constants for NO_2 Hydrolysis Experiments. ….. 57

III. MECHANISM OF HONO FORMATION

Table 3.III.1. Initial Reactant HNO_3 and NO and Measured Stoichiometry for Reactants and Product NO_2. …… 87
Table 3.III.2. Summary of Long Path Cell FTIR Measurements of the Decay of NO and Formation of NO_2 in the Reaction of NO with HNO_3 Adsorbed on the Cell Walls. …… 95
Table 3.III.3. Summary of Long Path Cell FTIR Measurements of the Decay of NO and Formation of NO_2 in the Reaction of NO with HNO_3 Adsorbed on the Cell Walls. …… 95
Table 3.III.4. Thermodynamic Values Retrieved from NBS Tables (1982). ……. 97
Table 3.III.5 Reaction Thermodynamics for Reactions of HNO_3 in Various Forms with NO. …….. 98
Table 3.III.6. Experimental Results for the Number of Layers at Different RH. .. 101

ABSTRACT

Oxides of nitrogen ($NO_x = NO + NO_2$)are the only known anthropogenic source of ozone in polluted urban areas in California and are also a major contributor to the formation of particles. While the gas phase chemistry of oxides of nitrogen is reasonably well understood and represented in current airshed models, it is known that NO_x also undergoes "heterogeneous" reactions on surfaces, *e.g*. of particles, buildings, roads etc. These surface reactions can have a significant impact on the overall chemistry, but because they are not understood, they are not explicitly included in airshed models used for control strategy development. In this project, some of the heterogeneous reactions of oxides of nitrogen were studied using a variety of experimental systems where both the gas and surfaces could be probed spectroscopically. One of these heterogeneous reactions is the hydrolysis of nitrogen dioxide (NO_2) on surfaces which generates nitrous acid (HONO). Nitrous acid is the major source of the hydroxyl radical in the morning in coastal urban areas in California, setting off the chain chemistry that leads to the formation of ozone, particles and associated pollutants. We have shown that the mechanism of the surface reaction of nitrogen dioxide (NO_2) with water is different than proposed in earlier studies and as represented in current models. Nitric acid (HNO_3) is also produced in the NO_2 hydrolysis reaction, but rather than being released to the gas phase, it remains adsorbed on the surface. We established that, in contrast to current understanding where nitric acid is deposited out or forms particulate nitrate, this nitric acid on the surface can undergo further reactions with nitric oxide to regenerate nitrogen dioxide. This makes at least some of the nitric acid available for further regeneration of ozone. Initial airshed modelling incorporating this chemistry shows that it may have significant implications for the chemistry used in current models and hence potentially on the predicted impacts of various degrees of control of VOC and NO_x.

EXECUTIVE SUMMARY

Background: Oxides of nitrogen ($NO_x = NO + NO_2$) are the sole known anthropogenic source of ozone in polluted urban atmospheres. They are also a source of particulate nitrate, a major component of PM2.5 and PM10 in California. The gas phase chemistry of oxides of nitrogen leading to the formation of ozone and particulate nitrate is reasonably well understood. However, it has been known for more than five decades that oxides of nitrogen also undergo unique reactions on surfaces (so-called "heterogeneous" reactions); such reactions affect the interpretation of the gas phase chemistry of oxides of nitrogen in both laboratory systems and ambient air. Even though there have been many attempts to study the kinetics and mechanisms of these heterogeneous reactions, they are still not understood. As a result, current models used for control strategy development generally exclude such chemistry, despite the fact that it may significantly impact the predicted effects of VOC (volatile organic compounds) and NO_x controls on the formation of ozone, particles and associated air pollutants. The goals of our laboratory studies were to elucidate the kinetics and mechanisms of some of the heterogeneous reactions of oxides of nitrogen that are relevant to the formation of ozone, particles and associated air pollutants. In addition, a preliminary assessment of the implications of this chemistry for the development of ozone and particles in the South Coast Air Basin of California was carried out.

Methods: Several approaches were applied as experimental models of the heterogeneous chemistry which may occur in air: (1) two chambers, one 561 L in volume with a surface-to-volume (S/V) ratio of 8 m^{-1} and a smaller 8 L chamber with a S/V of 42 m^{-1}, were used to study the formation of nitrous acid from the surface reaction of nitrogen dioxide with water. Both were equipped with long path Fourier transform infrared spectrometry (FTIR) for gas analysis, and the larger chamber also had an ultraviolet/visible long path spectrometer; (2) the chemistry occurring on thin water films in the atmosphere was simulated by the use of porous silica surfaces. Both the gas and surface species present in the cell and on the porous glass surfaces were followed simultaneously as a function of reaction time; (3) single reflectance FTIR of nitric acid-water solutions was used to probe the nature of the surface film of these solutions in order to elucidate the role of nitric acid on the surfaces in secondary heterogeneous chemistry; (4) initial airshed model runs were carried out which incorporated this chemistry into a model of the South Coast Air Basin of California.

Results. Studies of the kinetics and mechanisms of the heterogeneous hydrolysis of nitrogen dioxide (NO_2) on surfaces showed that this reaction likely proceeds via the initial formation of its dimer (N_2O_4), followed by the reaction of the dimer with water. This is in contrast to previous studies of this reaction that ruled out the dimer as an important intermediate, and is inconsistent with the parameterization of this reaction in current airshed models. This reaction generates gas phase nitrous acid (HONO) whose generation in our experimental system was in agreement with a parameterization of HONO formation proposed by earlier researchers. However, this parameterization was shown to be inappropriate for inclusion in airshed models because of the very different surface-to-volume ratios for particles in air compared to the experimental system. A parameterization appropriate for airshed models remains to be developed.

The reaction of gas phase NO_2 with water on surfaces not only generates gas phase nitrous acid but also nitric acid, the latter remaining on the chamber surfaces. This results in a thin film of nitric acid and water on the surface that then plays a key role in secondary reactions in this system. For the first time, we accounted for this reactivity of the thin nitric acid-water film, and showed that gaseous nitric oxide (NO) can react with nitric acid in this surface film to regenerate NO_2. The form of nitric acid in the thin films, *e.g.,* dissociated vs undissociated, may control the chemistry of such films. We have also determined that a number of factors, including the relative humidity and amount of nitric acid on the surface, control the chemistry of this film and the form of the nitric acid. Accepted understanding has been that once nitric acid is formed, it is not reduced in air back to photochemically active NO_2 and hence is not involved in the further formation of ozone. However, our results suggest that this may not be the case and further reactions of nitric acid on the surface may lead to its reduction back to NO_2, *i.e.*, a catalytic cycle may be contributing to the overall NO_x chemistry.

Preliminary airshed modelling predicts that this reaction of gaseous NO with surface nitric acid may be important with respect to the formation of both ozone and particulate nitrate in polluted urban airsheds in California; changes in both the concentrations and profiles of ozone and particulate nitrate were predicted when the reaction of gaseous NO with deposited nitric acid was included.

Conclusions. Heterogenous reactions of oxides of nitrogen on surfaces are very complex but potentially quite important in polluted urban air. For example, the heterogeneous hydrolysis of nitrogen dioxide forms gas phase nitrous acid as well as nitric acid which stays on the surface, forming highly acidic films. The key intermediate in the reaction appears to be the dimer of NO_2 (N_2O_4). The build-up of a nitric acid film on the surface catalyzes a number of secondary reactions. One potentially important reaction of the nitric acid film is its reaction with gaseous NO to generate NO_2. This appears to be the first reaction identified in such systems which can regenerate NO_2 from nitric acid and has potential important control strategy implications.

A great deal of experimental work is needed to elucidate this heterogeneous chemistry in order to include it in airshed models and to assess the impacts on various control strategies. For example,

- What is the most appropriate parameterization for HONO formation from the surface hydrolysis of NO_2 to use in airshed models?

- What is the mechanism of the photoenhancement of HONO formation that has been observed in studies by other researchers?

- What is the reaction probability for the reaction of gaseous NO with the surface film of nitric acid, and how is it affected by relative humidity, the nature of the surface etc?

- Are there other reactions of the nitric acid film, *e.g.* with CO, SO_2 or CH_4, that have been proposed by other researchers that may also generate NO_2 from HNO_3?

- Do forms of nitrate other than nitric acid such as ammonium nitrate undergo the same chemistry?

- Does the simultaneous presence of sulfuric acid in the thin films alter the molecular nature of nitric acid and hence its reactions?

- Does gas phase nitrous acid also react with nitric acid on the surface, and if so, does this affect how much nitrous acid is released into air by the surface hydrolysis of NO_2?

- Can this chemistry be integrated into a comprehensive model that will explain the experimental observations made by many research groups over the years on the behaviour of oxides of nitrogen in laboratory systems? How does this extrapolate to the urban air situation?

1. INTRODUCTION

Nitrous acid is an important tropospheric trace gas because it is a source of hydroxyl radicals (OH). While OH/HO_2 production also occurs by ozone and formaldehyde photolysis, HONO photodissociation has been found to be the predominant source of OH in the early morning in some urban areas (*Chan et al.,* 1976a; *Winer and Biermann,* 1994; *Harrison et al.,* 1996). This large production of OH at dawn initiates oxidation of organics which, in the presence of NO, leads to ozone production through the set of reactions shown below, in which RCH_2R' is a hydrocarbon (*Finlayson-Pitts and Pitts*, 2000).

$$HONO + h\upsilon\ (\lambda<400\ nm) \rightarrow OH + NO \quad (1)$$
$$OH\cdot + RCH_2R' \rightarrow RCHR'\cdot + H_2O \quad (2)$$
$$RCHR'\cdot + O_2 + M \rightarrow RCH(OO)R'\cdot + M \quad (3)$$
$$RCH(OO)R'\cdot + NO \rightarrow RCH(O)R'\cdot + NO_2 \quad (4)$$
$$NO_2 + h\upsilon\ (\lambda<420\ nm) \rightarrow NO + O(^3P) \quad (5)$$
$$O(^3P) + O_2 + M \rightarrow O_3 + M \quad (6)$$

Any source of OH is therefore a potential source of O_3, a toxic component in photochemical smog. The major source of OH in the atmosphere at dawn is HONO, which consequently controls the timing and magnitude of photochemical smog formation. In addition, particles are formed in the chemical process of ozone production, and so generation of HONO is intimately tied to particle formation in air. HONO is also linked to particles in that its major sources are believed to be heterogeneous reactions on surfaces including particles (*Finlayson-Pitts and Pitts*, 2000).

HONO has also direct and indirect negative health effects. It has been shown to irritate the mucous membranes and the respiratory and pulmonary systems of asthmatics (*Rasmussen et al.,* 1995; *Beckett et al.,* 1995), and to react with secondary and tertiary amines to form carcinogenic nitrosamines (*Pitts et al.,* 1978). This is especially of concern indoors where elevated HONO levels have been found during the use of unvented combustion processes, e.g. gas space heaters and stoves (*Pitts et al.,* 1985; *Brauer et al.,* 1990; *Spicer et al.,* 1993; *Spengler et al.,* 1993; *Vecera and Dasgupta,* 1994).

The highest HONO concentrations have been detected at dawn in a number of polluted urban environments (*Winer and Biermann*, 1994; *Finlayson-Pitts and Pitts*, 2000, and references therein). The night-time concentration of HONO has been measured to reach up to 10–15 ppb in heavily polluted areas (*Perner and Platt,* 1979; *Vecera and Dasgupta,* 1991; *Winer and Biermann,* 1994; *Lammel and Cape,* 1996; *Febo et al.,* 1996). Past atmospheric HONO measurements suggested that the known sources of HONO did not account for accumulated night-time levels (e.g. *Heikes and Thompson,* 1983*; Lammel and Cape,* 1996). For example, the three-body reaction of OH with NO, reaction (7), produces HONO too slowly to account for the measured night-time HONO levels,

$$OH + NO \xrightarrow{M} HONO \quad (7)$$

and the heterogeneous reaction (8) of NO, NO_2 and water,

$$NO + NO_2 + H_2O \xleftrightarrow{Surface} 2\ HONO \qquad (8, -8)$$

is thought to be of little or no importance in HONO generation (*Wayne and Yost*, 1951; *Graham and Tyler*, 1972; *Cox and Derwent*, 1976/77; *Chan et al.*, 1976a; b; *Kaiser and Wu*, 1977b; *Sakamaki et al.*, 1983; *Pitts et al.*, 1984a; *Atkinson*, 1986).

Although, the hydrolysis of NO_2 on various surfaces (*Wayne and Yost*, 1951; *Graham and Tyler*, 1972; *Chan et al.*, 1976a, b; *Sakamaki et al.*, 1983; *Pitts et al.*, 1984a; *Akimoto et al.*, 1987; *Svensson et al.*, 1987; *Jenkin et al.*, 1988; *Lammel and Perner*, 1988; *Febo and Perrino*, 1991; *Bambauer et al.*, 1994; *Mertes and Wahner*, 1995; *Kleffmann et al.*, 1998a, b) is considered to be a major source of HONO in air, it has not been included directly in airshed models.

$$2\ NO_2 + H_2O \xrightarrow{Surface} HONO + HNO_3 \qquad (9)$$

Only a surrogate reaction representing the conversion of NO_2 to HONO is included in such models.

NO_2 has also been shown to react with soot, generating HONO and NO (*Smith et al.*, 1988, *Chughtai et al.* 1990a, b, *Tabor et al.*, 1993, *Tabor et al.*, 1994; *Ammann et al*. 1995, *Kalberer et al.*, 1996, *Rogaski et al.*, 1997; *Lur'e and Mikhno*, 1997, *Chughtai et al.* 1998, *Ammann et al.*, 1998; *Gerecke et al.*, 1998; *Aumont et al.*, 1999; *Kalberer et al.*, 1999a, b; *Longfellow et al.*, 1999, *Kleffmann et al.* 1999, *Ravishankara and Longfellow*,1999, *Kirchner et al.* 2000, *Al-Abadheh and Grassian*, 2000, *Stadler and Rossi*, 2000, *Alcala-Jornod et al.*, 2000). However, it is not clear whether or not the surface is deactivated during the reactions; if it is, this will not represent a major source of HONO in air. The reaction of HO_2 with NO_2 (*Tyndall et al.,* 1995), peroxyacetyl nitrate decomposition, NO_2 abstraction of allylic hydrogen atoms, and direct emission from combustion processes also contribute to a small extent to HONO formation (*Pitts et al.,* 1984a; *Spicer et al.,* 1993; *Vecera and Dasgupta,* 1994; *Kirchstetter et al.,* 1996; *Finlayson-Pitts and Pitts,* 2000).

The result of this large amount of research devoted to understanding mechanisms of HONO formation is that the heterogeneous reaction of NO_2 and H_2O remains as the likely major source of HONO in the atmosphere. Some evidence suggests that this reaction occurs at the air-water interface (*Pitts et al.,* 1984a, *Svensson et al.,* 1987; *Notholt et al.,* 1992; *Mertes and Wahner*, 1995; *Wiesen et al.,* 1995; *Wang et al.,* 1998). This area of chemistry at water interfaces is new, and is only now receiving increased attention. If indeed HONO formation is determined by reactions at the air-water interface, models need to be modified to incorporate this new "dimension". In order to provide the data for accurate model representation of such processes, the detailed kinetics and mechanisms of HONO formation and fate in the troposphere must be understood. Thus, a complete 'chemical picture', which translates into the development of cost-effective control strategies, needs to be established.

Our goals, then, are to:

1. Prepare pure samples of HONO and develop accurate methods for HONO quantification, such as HONO titration and HONO IR cross section measurements. Quantification of HONO in laboratory systems utilizes the reaction of HONO with excess HCl to produce ClNO:

   $$HONO + HCl \rightarrow ClNO + H_2O \qquad (10)$$

   The product nitrosyl chloride can be synthesized in high purity for calibrations and is easily measured using FTIR. We also report FTIR absorption cross-sections for HONO determined for the first time by simultaneous FTIR and differential optical absorption spectroscopy (DOAS) measurements, using the revised UV/visible cross-sections of Bongartz et al. (1991,1994). This approach avoids the problem of indirectly determining the HONO concentrations.

2. Reinvestigate the kinetics and mechanism of the reaction of NO_2 in the presence of water under the heterogeneous influence of the reaction chamber surfaces. This is a critical step in elucidating the reaction mechanism for HONO formation. The reaction orders with respect to NO_2 and H_2O are addressed, and product formation under these conditions is discussed.

3. Evaluate other sources of HONO in the atmosphere such as N_2O_3, which has been suggested as an intermediate in the formation of nitrous acid:

   $$NO + NO_2 + M \leftrightarrow N_2O_3 + M \qquad (11, -11)$$

4. Investigate secondary reactions of nitric acid adsorbed on surfaces on reactions such as (12) and determine their importance in air.

   $$NO + HNO_3 \xrightarrow{Surface} HONO + NO_2 \qquad (12)$$

   This specific reaction is between adsorbed nitric acid on wet silica surfaces and/or the borosilicate glass walls of the long path cell, and gaseous nitric oxide. A comparison of the kinetics of this reaction to all other known sources of HONO suggests that this reaction may be an important source of HONO in polluted urban areas. Also, this reaction is consistent with the observed correlation of atmospheric levels of HONO with NO concentrations (*Sjodin and Ferm*, 1985; *Notholt et al.*, 1992; *Calvert et al.*, 1994; *Winer and Biermann*, 1994). More importantly, it provides a mechanism of converting HNO_3 back into photochemically active forms. This not only helps to reconcile the discrepancy between measured and modeling ratios of HNO_3 to NO_x in the troposphere (*Chatfield*, 1994; *Hauglustaine et al.*, 1996), but may impact the predicted benefits of VOC versus NO_x controls.

5. Apply single reflectance FTIR studies to probe the chemical and physical state of nitric acid at the air-water interface and in thin water films, in order to understand at

the molecular level the mechanisms of heterogeneous NO_x reactions such as the reaction of surface HNO_3 with gaseous NO.

6. Incorporate these results into an airshed model to probe their impacts on the chemistry leading to ozone and particle formation.

2. MATERIALS AND METHODS

I. ANALYTICAL METHODS AND EQUIPMENT

I.A. Environmental Chamber

The environmental chamber used to perform the HONO titration and IR cross section experiments is a 561 L stainless steel and aluminum chamber with two sets of White cell optics (*White*, 1942) for long path UV/visible and FTIR spectroscopy. A description of the chamber and White cell optics is detailed below.

The environmental chamber used in these studies is a rectangular, 48 × 48 × 220 cm, 561 L chamber consisting of an aluminum baseplate and stainless steel frame with 17 removable panels (41 × 41 cm) made of aluminum. With the exception of windows and mirrors, the inner surfaces are coated with an inert halocarbon wax (Halocarbon Products Corp., Series 1500) to minimize surface reactivity. There are two sets of White cell optics, for long path FTIR and DOAS (UV/visible) experiments, with a base path length of 2 m and maximum path length of up to 200 m each, giving correspondingly lower detection limits for the gases of interest. It is also interfaced to an atmospheric pressure ionization mass spectrometer (API-MS) for detecting a variety of gases in real time. It has heating and cooling capabilities as well as interchangeable windows for photolysis experiments. A particle generator is interfaced to the metal chamber for performing experiments in the presence of particles of various sizes and compositions. Pressure measurements are made with a Leybold CMH1000 capacitance manometer accurate to ± 0.25% (at atmospheric pressure). Temperature measurements are made with a Vaisala HMP234 temperature/humidity gauge accurate to ± 0.1 °C and ± 2% relative humidity, and volume measurements are accurate to ± 3%. The chamber has a surface area to volume ratio of S/V = 8 m^{-1} and is evacuable to $<1\times10^{-3}$ Torr using a mechanical pump and two sorption pumps. A schematic diagram of the chamber is shown in Figure 2.1.

The detection limits of HONO and NO_2 in the chamber are ~ 30 ppb and 1 ppb, respectively. Measured NO_2 pressures were corrected for N_2O_4 using the equilibrium constant (*DeMore et al.*, 1997) $[N_2O_4]/[NO_2]^2 = 2.5\times10^{-19}$ cm^3 $molecule^{-1}$.

I.A.1. Infrared Spectrometer

The IR system (Mattson Infinity AR) interfaced to the environmental chamber, including its entire external optical path and HgCdTe detector, is enclosed in a Plexiglas box that is purged with dry nitrogen during the experiments. IR spectra consisted of 32 coadded scans at 0.5 cm^{-1} resolution. The IR beam enters and exits the chamber through 1°-wedge ZnSe windows, which are resistant to water and somewhat resistant to nitrogen oxides. A set of gold-coated White optics (*White*, 1942) (base path length 2 m) allow multiple passes through the chamber. In this work, 26 passes were used, increasing the path length to 52.5 ± 0.07 m.

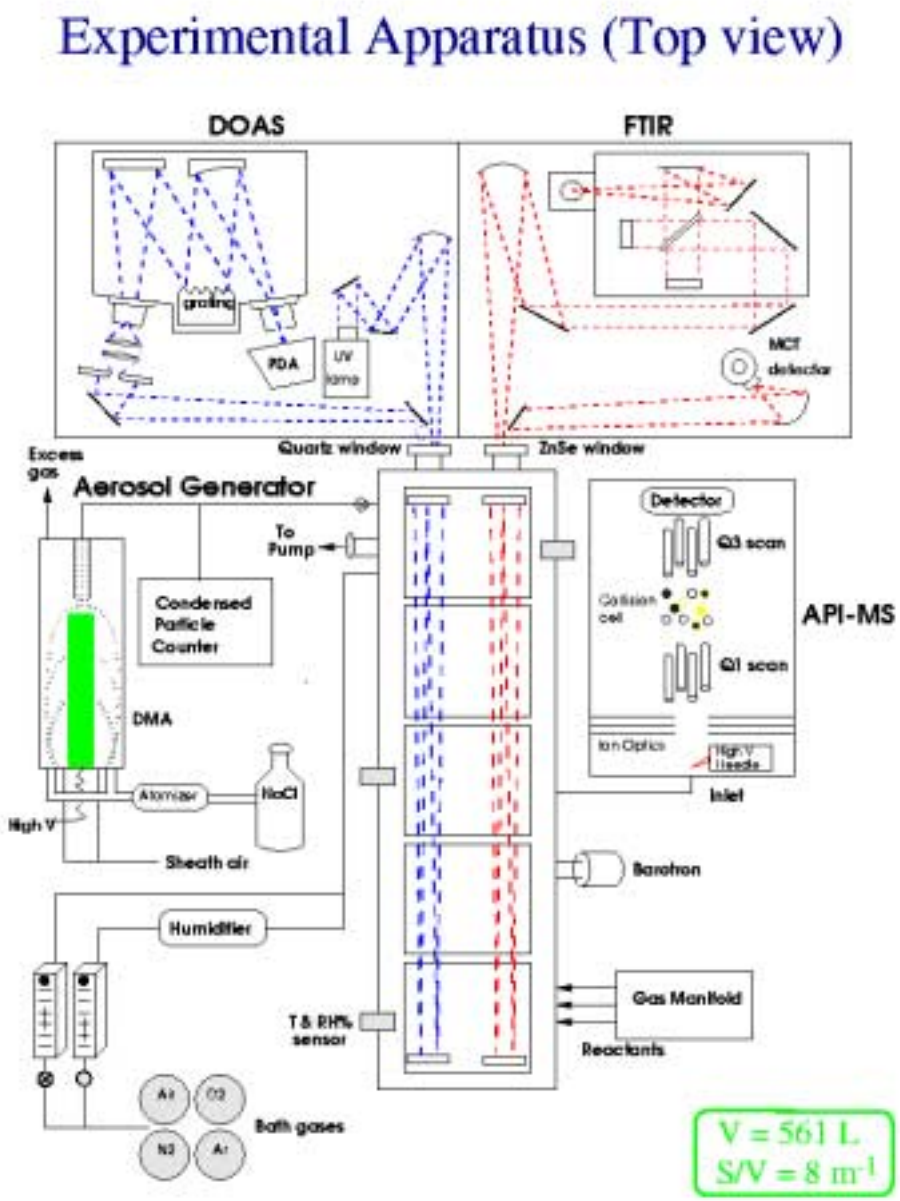

Figure 2.1. The environmental chamber used for the HONO titration and HONO cross section measurements. Also shown are the instruments interfaced to it including DOAS, FTIR, API-MS and the aerosol generator.

I.A.2. UV/Visible (DOAS) Spectrometer

UV/visible measurements are made by differential optical absorption spectroscopy (DOAS). The light source is a high-pressure Xenon arc lamp (Oriel), which enters and exits the chamber through quartz windows. A second set of White cell optics is used inside the chamber for the UV/visible beam. These are installed parallel to the IR optics and have a protected aluminum coating, but are otherwise identical to the IR optics. The light exiting from the chamber is focused on the entrance slit of a Jobin Yvon-Spex (Model 460MST24) monochromator equipped with a holographic grating (1200 grooves/mm blazed at 330 nm) and a 1024-channel diode array detector. The dispersion of 0.0433 ± 0.0002 nm/pixel gives a spectral range of approximately 44 nm. HONO and NO_2 bands were monitored in the 340–380 nm region with a resolution of 0.27 nm. Absolute wavelength calibration is maintained by recording a mercury lamp spectrum at the beginning of each experiment.

I.B. Long Path Infrared Cell

This long path infrared cell is used to study the NO_2 hydrolysis and the NO + HNO_3 experiments described in Chapter 3, sections II and III. As shown in Figure 2.2, it is mounted vertically in the sample compartment of an FTIR (Mattson, Cygnus) with an MCT detector. The mirrors are held on two stainless steel end mirror mounts separated by 0.8 m using two stainless steel rods, giving a base path length of 0.8 m. The internal stainless steel parts of the cell are coated with halocarbon wax (Halocarbon Products Corp., Series 1500). The optics are located inside a glass cylinder, which is sealed by end plates. The cell is evacuable through a port in the top plate, which is connected with Teflon tubing to a vacuum, manifold. The bottom plate has ZnSe windows for entrance and exit of the infrared beam. The beam enters the sample compartment horizontally and is directed into the cell using three transfer optics, the last of which focuses the IR beam onto the ZnSe entrance window. The beam undergoes multiple reflections off the internal cell mirrors before exiting the cell, giving a 40 m maximum total path length (different in each project). All optics have a protected aluminum coating which has a reflectance of 98.9 to 99.2% in the 400 to 4000 cm^{-1} range. The cell has a volume of 7.6 L and a surface to volume ratio of S/V = 40 m^{-1}. The long path cell was wrapped in a dark cloth to prevent photolysis of reactants and products from occurring.

NO_2 hydrolysis experiments were carried out at 1 cm^{-1} resolution with 128 co-added scans. The combination band of NO_2 ($\nu_1+\nu_3$) at 2910 cm^{-1} was used to follow NO_2 due to strong water absorptions interfering with the larger symmetric stretch absorption at 1617 cm^{-1}. Two absorptions for nitrous acid were followed: the ν_3 fundamental of *trans*-HONO (H-O-N bend) centered at 1263 cm^{-1} and the ν_4 fundamental of *cis*-HONO (O-N stretch) centered at 852 cm^{-1}. The strongest absorption for N_2O is ν_3 (N-N stretch), centered at 2223 cm^{-1}.

Studies of the reaction of adsorbed HNO_3 with NO (g) were carried out at 1 cm^{-1} resolution with 150 co-added scans. The IR bands at 1875, 2910, and 1263 cm^{-1} were used to follow NO, NO_2, and HONO, respectively.

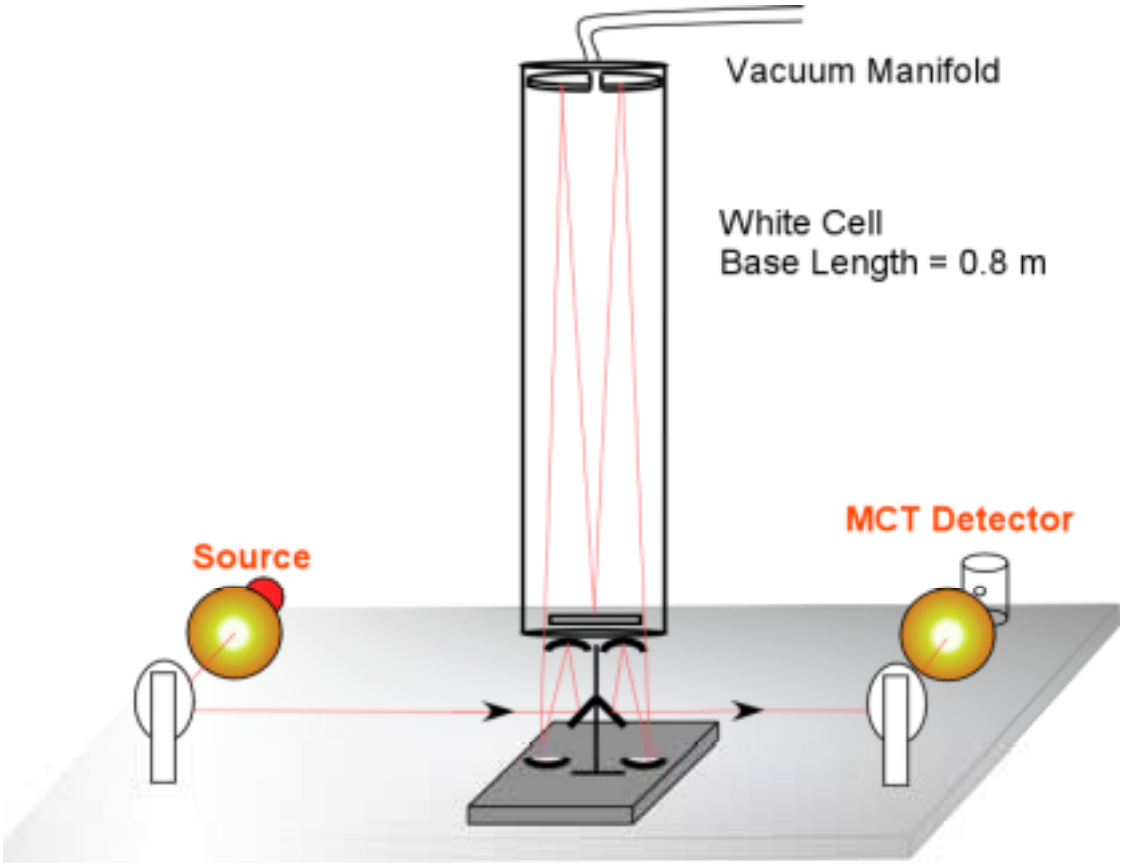

Figure 2.2. The long path cell used for the NO_2 hydrolysis and NO + HNO_3(ads) reaction studies.

In most cases, unless otherwise stated, spectra were quantitatively analyzed for these species using a least squares fitting procedure described in detail in Gomer et al. (1995) and in Appendix A. The least squares fitting procedure determines the concentration of species relative to a reference spectrum of known concentration. Absolute concentrations for the nitric oxide, nitrogen dioxide, and nitrous oxide reference spectra were determined using calibrations of the pure gases. Nitrous acid was quantified using infrared cross sections for the HONO peak at 1263 cm^{-1} determined by Barney et al. (2000a) in this laboratory.

I.C. Porous Glass Cell

Both the reaction mechanism of the NO_2 hydrolysis on the surface and the reaction between NO and HNO_3(ads) were studied in the porous glass cell. The volume of this cell is 79 cm^3. Figure 2.3 is a schematic diagram of the reaction cell. It is made of borosilicate glass and has ZnSe windows at each end, providing a 6.7 cm path length for the infrared beam. The porous glass is held at the end of a positioning rod and can be withdrawn into the side arm for heating and for obtaining the infrared spectrum of the gases alone. With the

porous glass sample in the infrared beam, the spectrum of both the surface species and the gases is recorded. By subtraction of the gas phase spectrum, that of the porous glass and surface-adsorbed species can be extracted. Spectra were recorded as 64 co-added scans at 0.5 cm^{-1} resolution.

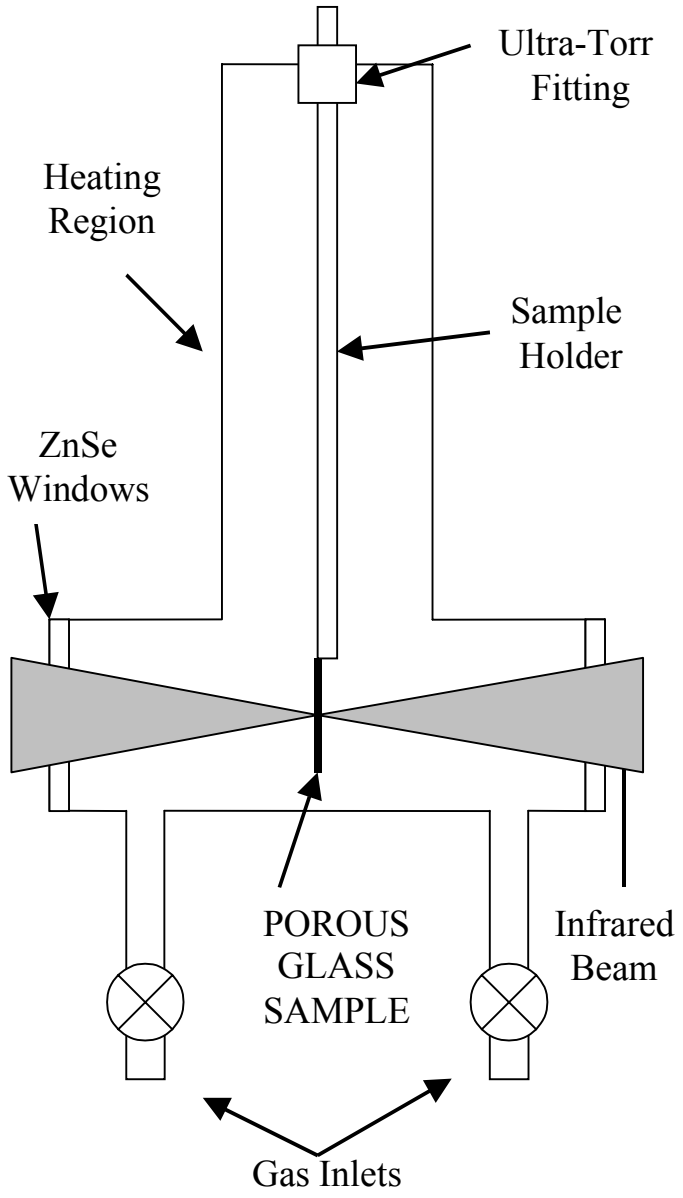

Figure 2.3. The porous glass cell used to study the $NO+HNO_3(ads)$ and $NO+N_2O_3$ reactions.

Porous glass transmits infrared radiation well above ~ 2000 cm^{-1}; however, it drops off rapidly at lower wavenumbers (*Kiselev and Lygin*, 1975). Because the bands of interest

for adsorbed species are below 2000 cm^{-1}, it was necessary to have a porous glass plate thinner than is commercially available. A plate of porous glass (Corning) approximately 1 mm thick was further etched by immersion in a 7.7 % (v:v) HF solution for 21 minutes. It was then rinsed in Nanopure water and dried in an oven for 1 hour at 120°C. Before use, the plate was mounted on the holder and inserted into the cell, which was evacuated and heated from the outside for 35 minutes at 280°C and then cooled to room temperature before gases were added. The porous glass plate has a surface area of 28.5 ± 0.3 m^2 as determined by the Brunauer-Emmett-Teller (BET) method using nitrogen as an adsorbate (ASAP2000, Micromeritics). This large surface area, relative to the geometric area of the plate of 12 cm^2, is due to the numerous small pores in the glass. However, the experimental evidence suggests that not all of this surface area is available for uptake of gases, perhaps because of water in the pores under our experimental conditions, and/or the larger size molecules such as N_2O_3 compared to N_2 used for the BET measurements. This issue will be discussed in more detail in Chapter 3, Section III.

Silica surfaces are terminated by hydroxyl groups (Si-OH) which hold water molecules *via* hydrogen bonding. There are three types of surface species (*Kiselev and Lygin*, 1975): i) free vibrating hydroxyl groups, ii) hydrogen bonded hydroxyl groups, and iii) strained siloxane bridges. Their relative abundances depend on the heat treatment of the silica surface and the H_2O partial pressure. Under most of our experimental conditions where the porous glass was not heated, hydroxyl groups terminate the silica surface and act to hold water on the surface.

During NO_2 hydrolysis experiments, the porous glass was cleaned, in between two experiments, by soaking it in water (Barnstead, Nanopure, 18 MΩ cm) to remove adsorbed species such as nitrate and nitrite. It was then returned to the cell, which was evacuated for ~ 2 hours prior to exposure to the gases. This procedure does not remove water strongly bound to the surface as indicated by a broad infrared absorption in the 3400 cm^{-1} region. In most experiments, there was no heating of the surface before reaction because the intent was to study the reactions on a hydrated surface. In order to elucidate the effects of water vapor on the surface species in one set of experiments, the porous glass was heated at 520 K for several hours under vacuum and then cooled to room temperature prior to addition of the gases and water vapor.

Before experiments of NO on adsorbed HNO_3 were initiated, the porous glass was placed in the cell and evacuated for 3-10 hours in order to remove excess adsorbed water prior to introducing gases. The porous glass was exposed to $10^{16} – 10^{17}$ molecule cm^{-3} of gaseous HNO_3 for half an hour and then pumped out to remove gaseous and some adsorbed HNO_3. On rough pumping, a slow decrease in the peak intensity at 1677 cm^{-1} was observed due to desorption of surface HNO_3. To start the reaction with NO, the valve to the pump was closed and gaseous NO at concentrations from 2×10^{16} to 6×10^{17} molecule cm^{-3} was introduced. All reactions were carried out at room temperature either without added carrier gas or with ~ 500 Torr He added to the cell.

Concentrations of the gas phase species, NO, NO_2, HNO_3 and N_2O were obtained by measuring the intensities of the infrared bands centered at 1876, 1617, 1711 and 2224 cm^{-1},

respectively, and then compared to calibration spectra recorded for these gases under conditions of pressure and temperature used in these experiments. HONO was measured using its absorption at 1263 cm^{-1} and the integrated band intensity determined in previous studies in this laboratory (*Barney et al.*, 2000a).

In order to quantify the amount of surface adsorbed HNO_3, and to calibrate its 1677 cm^{-1} infrared band, a certain amount of HNO_3 was adsorbed on the surface and the peak intensity at 1677 cm^{-1} was recorded. The porous glass plate was then removed from the cell and soaked in Nanopure water. The concentration of nitrate ion in solution was measured using ion chromatography (column: Vydac, mobile phase: potassium hydrogen phthalate 2×10^{-3} M, conductivity detector: Wescan). Since the inner walls of the reaction cell also adsorb HNO_3, these walls were rinsed with water and the solution was collected and analyzed. A comparison of these results show that > 90 % of the HNO_3 was adsorbed on the porous glass plate rather than on the inner cell walls, consistent with the high surface area of the porous glass relative to that of the reaction cell. The number of adsorbed HNO_3 molecules was varied from 4.2×10^{17} to 1.1×10^{19} molecules.

I.D. Single-Reflectance FTIR

Single reflectance spectra of $HNO_3 - H_2O$ and $HNO_3 - H_2SO_4 - H_2O$ solutions were measured using the apparatus shown in Figure 2.4. The external infrared beam from the FTIR spectrometer (Mattson GL-5020) was focused on the aqueous surface with an incident angle of 35° to the normal by an off-axis parabolic aluminum mirror (PM1). The beam reflected from the aqueous surface was captured by two off-axis parabolic mirrors (PM2) and (PM3) and then directed to a liquid nitrogen cooled MCT detector via an ellipsoidal mirror. The IR beam focused on the aqueous surface passed through two ZnSe windows to a custom-built Teflon cell. This cell can be sealed, for both safety reasons (NO_2 is a toxic gas), and to maintain similar experimental conditions over a long period of time for signal averaging. It is equipped with a temperature-control bath for temperature dependent measurements. The whole system was enclosed in Plexiglas box, which was purged with dry N_2 to reduce the contributions from gas phase H_2O and CO_2 to the spectra. The aqueous surface was open to the N_2 purge during the measurements.

The intensity and shape of absorption bands in an SR spectrum depend on the angle of incidence and on the polarization (*Dluhy et al.*, 1995). We calculated the reflectance spectra of water using classical electromagnetic theory for both parallel and perpendicular polarization as described elsewhere (*Dluhy et al.*, 1995, *Dluhy*, 1986), and the optical constants of H_2O reported by Bertie and Lan (1996). Both spectra have the same shape at angles of incidence from 0 to 45°, encompassing the 35° used in these studies. As a result, a polarizer was not used in order to optimize the signal-to-noise ratio.

Transmission spectra were obtained by sandwiching the solutions between AgBr, NaCl or ZnSe windows; the latter two were protected from the liquid by a thin Teflon® film. While this was successful for a saturated $NaHSO_3$ solution used to test the comparison of different types of spectra, reproducibility problems were encountered for the strongly acidic

solutions. Hence for the acid solutions, we report here wavelength-corrected ATR spectra for comparison to the single reflectance spectra.

ATR spectra were measured using a Tunnel® cell (Axiom Analytical Incorporated, Irvine, CA) with an AMTIR crystal, which was placed between the third parabolic mirror and the ellipsoidal mirror in Figure 2.4. Absorbance spectra were calculated by taking the ratio of a sample single-beam spectrum to the background single-beam spectrum of the empty ATR cell.

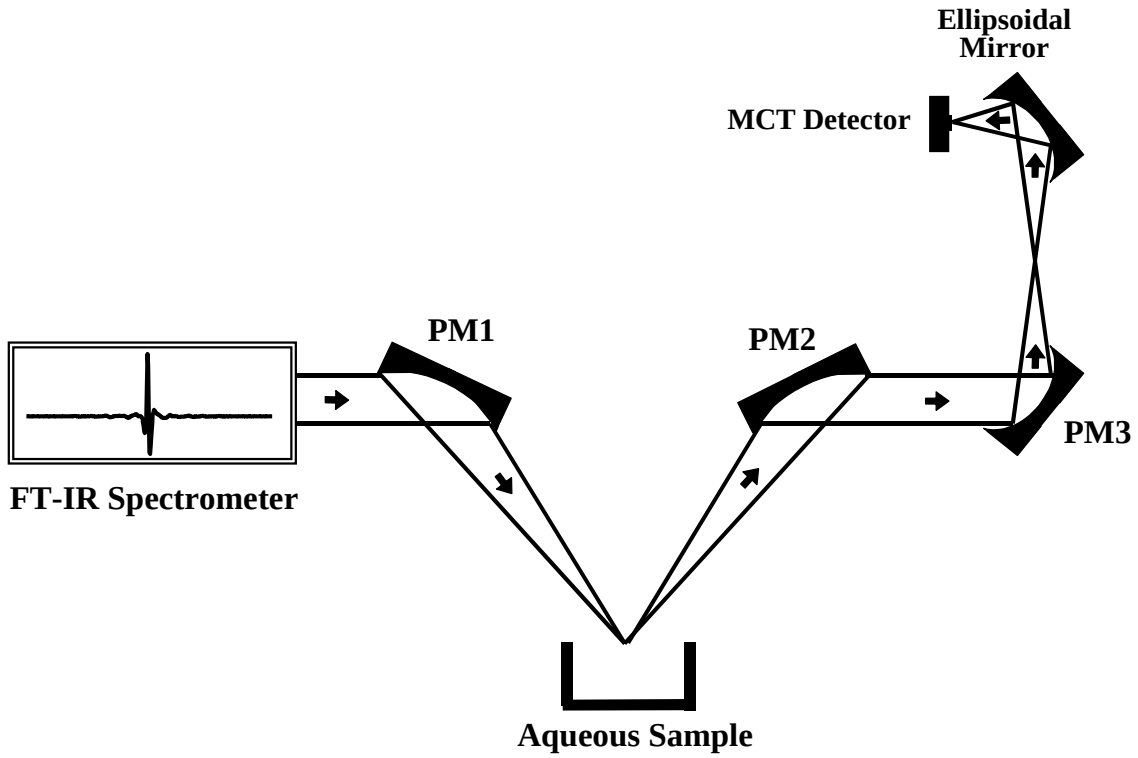

Figure 2.4. Single Reflectance FTIR set up used to measure species present at the interface. i.e. HNO_3 on the HNO_3-H_2O interface.

I.E. Cell for Measurements of Water on Glass

The amount of H_2O adsorbed on the borosilicate glass at different relative humidities (RH) was determined by transmission infrared spectroscopy. The borosilicate glass samples were thin Micro Cover Glasses (VWR Scientific, Inc.) with 0.13 to 0.17 mm thickness and 25 mm diameter. The cover glasses and water vapor were enclosed in an infrared gas cell as shown in Figure 2.5. The cell was made from Pyrex glass with an 11 cm pathlength and 3.2 cm diameter. Two ZnSe windows were mounted on each side of the cell, and the gas inlet and outlet allowed water vapor to flow through the cell. In order to increase the signal intensity, a U-shaped glass rod with thin slots to hold 5 pieces of cover glass standing in such a way that their surfaces are parallel to each other and to the ZnSe surfaces was used.

Nitrogen gas at different RH was generated using the setup shown in Figure 2.6. N_2(g) with 100% RH was obtained by bubbling it through nanopure water. The 100% RH N_2(g) was mixed with dry N_2(g) to obtain lower RH. The flow rate of the 100% RH N_2(g) and dry N_2(g) were controlled by Matheson TF 1050 flowmeters, which were calibrated by a Hewlett-Packard soap film flowmeter.

IR transmission spectra were taken when N_2(g) at a given RH was flowing through the gas cell. The background spectrum that was used to calculate the absorbance spectrum of adsorbed H_2O was measured after the cell and cover glasses were purged with dry N_2(g) for 24 hours. Integration of the water absorption band from 3200 to 2800 cm^{-1} was performed in GRAMS/32 (Galactic Industries Corp., Salem, NH). The absorption bands of gas phase H_2O were subtracted before integration. Reference spectra of gas phase H_2O at different RH were measured in the same cell before introducing the cover glasses inside.

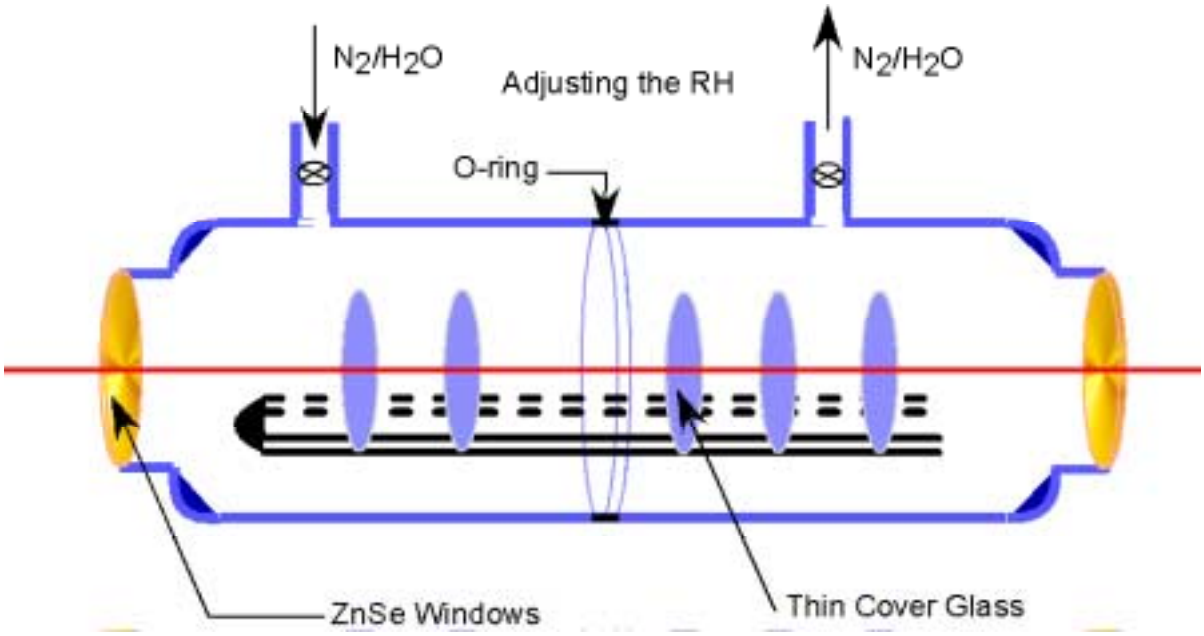

Figure 2.5. Borosilicate cover glass cell used to measure water coverage on the cover glass.

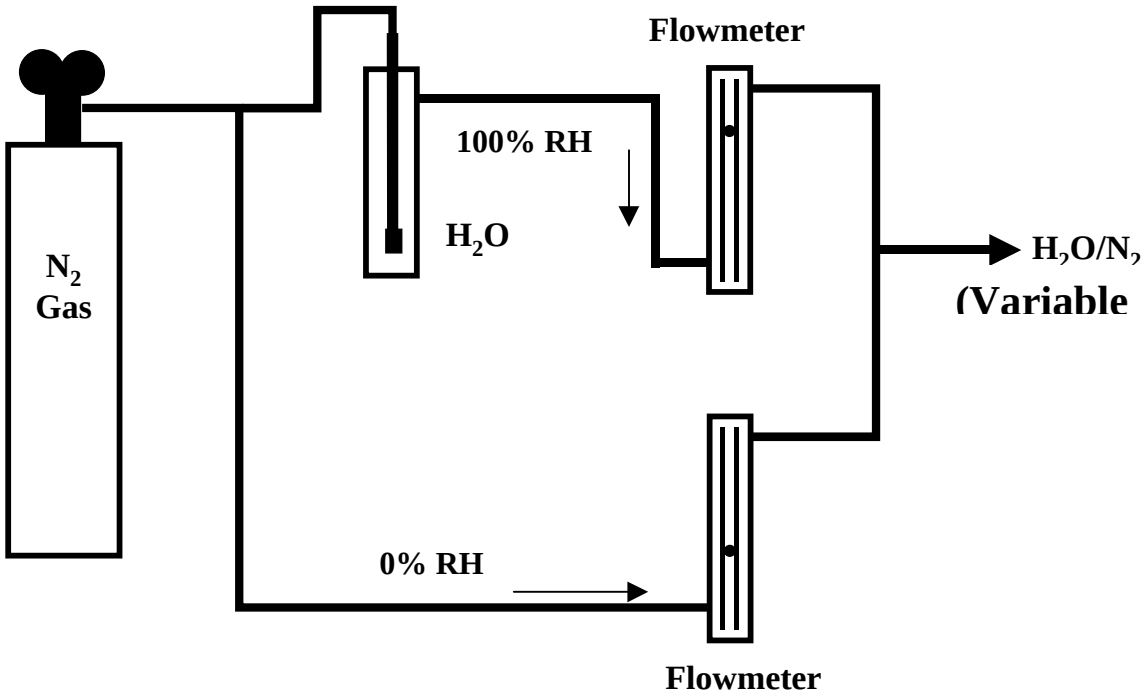

Figure 2.6. Set up used to generate N_2 (g) at different relative humidities.

I.F. Description of Airshed Model

The CIT Airshed model was used in order to evaluate the effects of possible renoxification in an urban region. The model is applied to the South Coast Air Basin of California to simulate conditions present during the 1987 South Coast Air Quality Study (SCAQS) on August 27–28, 1987. It incorporates a size-resolved and chemically resolved aerosol model within a three-dimensional detailed gas-phase model. The model includes the chemistry and physics of 133 gas species and 35 aerosol species distributed into 8 bin sizes. Furthermore, the model includes gas-phase and aerosol species with gas-to-particle transfer treated dynamically rather than simply assuming equilibrium. The most recent emissions inventories of particles in the South Coast Air Basin of California are included. We have improved the treatment of convective processes in the urban airshed model and the dynamics of secondary organic aerosol formation. A typical 24-hour run to simulate aerosol dynamics on the South Coast Air Basin of California using the CIT model requires nine hours of computational time when using 32 processors simultaneously. (A detailed description of the model may be found elsewhere (Meng *et al.*, 1998). Previous applications of the model to the SCAQS episode have yielded insights into the coupling between ozone and particulate matter (Meng *et al.*, 1997). In a similar fashion, the CIT Airshed model is now being used to assess the impact of surface reactions that may lead to the recycling of NO_x back to the gas-phase.

A total of 8 simulations were performed. The **Base Case** represents simulation of the SCAQS episode using a standard VOC-NO_x gas-phase chemical mechanism coupled with a detailed dynamic inorganic/organic aerosol model. All emissions, initial conditions, meteorological and solar data are input into model in order to reflect conditions present during the episode. Modifications to the model in the other simulations were as follows:

I.F.1. 100% Land Reaction

The effect of a chemical reaction of deposited nitric acid (HNO_3) with ambient nitric oxide (NO) to form nitrous acid (HONO) and nitrogen dioxide (NO_2),

$$HNO_{3(g,dep)} + NO_{(g)} \rightarrow HONO_{(g)} + NO_{2(g)} \qquad \text{(I.1)}$$

was simulated in the model. The rate of reaction (1) was chosen to be the rate-limiting of either the full rate of deposition rate of gas phase nitric acid or the rate of turbulent diffusion/collision of nitric oxide with an idealized "flat" terrestrial surface. Although this rate is arbitrary, our chosen simplification of the reaction rate is upheld by the following observations:

- An adequate determination of the true surface area of the South Coast Air Basin would undoubtedly yield a higher value than the assumption of a flat surface area.
- During intervals where the NO turbulent diffusion/collision rate becomes rate-limiting, an accumulation of nitric acid on surfaces is to be expected.
- Particulate nitrate that has deposited or settled to the terrestrial surface may provide added sites for reaction (1) to occur.
- Finally, the purpose of these initial simulations is insight on the magnitude that such a NO_x recycling mechanism may have to the gas-phase and aerosol-phase dynamics of an urban airshed.

I.F.2. 10% Land Reaction

Another set of simulations was carried out in which it was assumed that 10%, rather than 100%, of the HNO_3 deposited out reacted via reaction (I.1).

I.F.3. Svensson

The rate for the reaction between nitrogen dioxide and water vapor,

$$NO_2 + NO_2 + H_2O \rightarrow HNO_3 + HONO \qquad \text{(I.2)}$$

has been determined by Svensson and coworkers to depend on the S/V ratio of their chemical reactor. The resulting rate could be expressed in the form

$$-\,d[NO_2]/dt = (5.6\times10^{-9}(S/V) + 2.3\times10^{-9})\,[NO_2]\,[H_2O] \qquad \text{(Eq. I.1)}$$

where the surface area-to-volume ratio, S/V, is in units of m^{-1} and the second order rate constant term is in units of ppm^{-1} min^{-1}. This expression is valid for temperatures near 25°C, and was shown in our earlier studies of NO_2 hydrolysis in a small, borosilicate glass chamber to be a good representation of our data as well. This expression was incorporated into the model using the S/V ratio of atmospheric particles in air (i.e., the surface area of particulate matter expressed in m^2 contained in a m^3 of air) in substitution of a previous estimated rate of

$$- d[NO_2]/dt = 2\, k_1\, [NO_2]\, [H_2O] \qquad \text{(Eq. I.2)}$$

where

$$k_1 = 1.76\times10^{-6}/T \qquad \text{(Eq. I.3)}$$

and T is the ambient temperature in Kelvin. At 25°C the effective rate constant for (Eq. I.2) is $k = 2\, k_1 = 1.15 \times10^{-8}$ ppm^{-1} min^{-1}. In order for the rate as determined by (Eq. I.1) to be equal or greater to this value, the S/V ratio of aerosol would have to be equal or greater to 1.6 m^{-1}, respectively.

II. MATERIALS

II.A. HONO Generator

Synthesis of HONO is carried out by the reaction of HCl (g) with $NaNO_2$ (s) in the presence of water. The apparatus is depicted in Figure 2.7. N_2 gas is flowed over an aqueous solution of 5.2 M HCl at 0°C and then up through a bed of ~20 g "free-flowing" $NaNO_2$ powder supported on a 2 in. (~5 cm) diameter porous glass frit. A modified stir plate was used to mechanically stir the $NaNO_2$ powder to ensure even exposure of the powder to the HCl reactant. In the absence of stirring, small holes appear in the powder layer through which unreacted HCl can escape. The product mixture contains HONO with H_2O and NO_2 impurities. Unreacted HCl is sometimes present as well.

Some advantage was obtained by using "free-flowing" over the crystallized $NaNO_2$ powder. The term "free-flowing" refers to powder, which has been sifted by the manufacturer to remove large clumps resulting from the uptake of water by the hygroscopic $NaNO_2$.

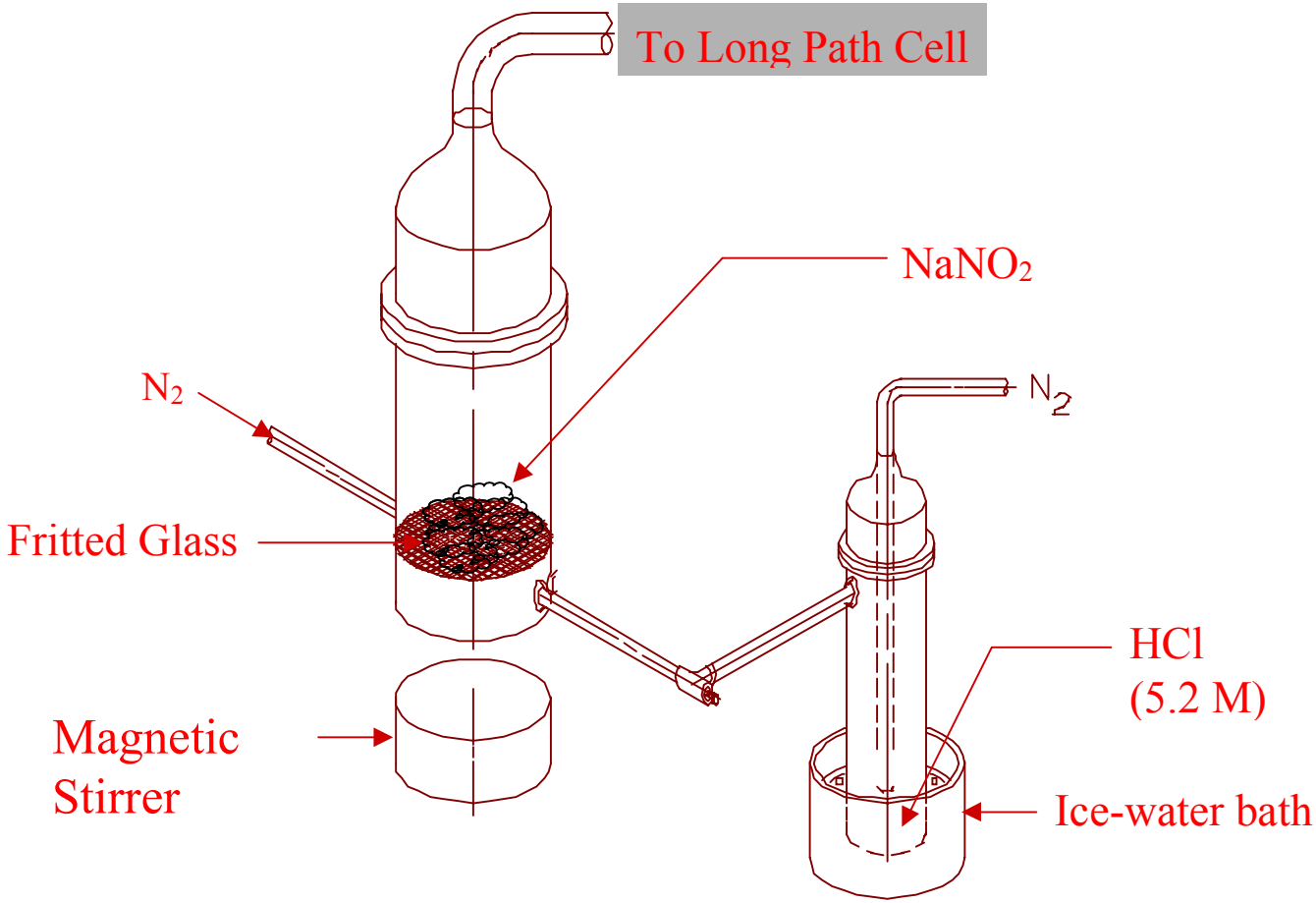

Figure 2.7. HONO Generation Apparatus

II.B. Gas Synthesis and Solution Preparation

Nitrosyl chloride was synthesized using a mixture of ~100 Torr Cl_2 (Matheson, 99.5%) and ~200 Torr NO (Matheson, 99%). The mixture was first condensed at 77 K in the cold finger of a 5 L bulb, then allowed to warm to room temperature. Reaction to form ClNO occurs primarily in the liquid phase as the mixture warms up. After several such reaction cycles, the gaseous ClNO was condensed at 195 K with a dry ice-acetone bath and the excess NO was pumped away.

Nitric oxide used in these experiments (Matheson 99 %) was passed through an acetone/dry ice bath trap at 195 K to remove impurities such as HNO_3. In some other experiments, NO was passed through a liquid N_2 trap at a relatively high rate to remove NO_2 and N_2O impurities as well as HNO_3.

Nitrogen dioxide was synthesized by mixing in a 5 L bulb, excess O_2 (Oxygen Service Company, 99.993%) with NO (Matheson, 99%) which had been passed through a trap at 196 K to remove impurities such as HNO_3. It was then purified by condensing the mixture at 195 K and pumping away the excess O_2. NO_2 was stored in a glass bulb covered with a dark cloth to prevent photolysis in room lights.

Gaseous HCl (Scott Specialty Gases, 99.995%) was used as a reactant in the titration. Gaseous nitric acid was obtained from the vapor above a 1:2 mixture of concentrated HNO_3 (69.3 % HNO_3, Fisher Chemical) and H_2SO_4 (95.7 %, Fisher Chemical). Nitrous oxide (99.99 %, Liquid Carbonic) was also used for experiments. He (Liquid Carbonic, 99.999 %) was used as a buffer gas for some experiments.

The binary $HNO_3 – H_2O$ and ternary $HNO_3 – H_2SO_4 – H_2O$ solutions were prepared by mixing 69.3 wt % HNO_3 (Fisher Scientific, ACS Certified Plus) and/or 96.0 wt % H_2SO_4 (Fisher Scientific, ACS Certified Plus) with 18 MΩ·cm water from a Barnstead/Nanopure Ultrapure Water System. The $NaHSO_3$ solution was prepared by dissolving the salt (Fisher Scientific, Certified ACS Grade) in Nanopure water.

3. RESULTS

I. MEASUREMENT OF HONO

I.A. HONO Titration by the Reaction HONO + HCl → ClNO + H_2O

I.A.1. Current Measurement Techniques for HONO

A sensitive and specific method for quantifying HONO in laboratory systems, as well as for measuring its *in-situ* atmospheric concentration, is differential optical absorption spectroscopy (DOAS). This method can reliably distinguish the UV/visible absorption spectrum of HONO from that of NO_2, which is generally also present. The accuracy of DOAS relies on a HONO reference spectrum which must be generated by a high-purity source of HONO. Although various methods of gaseous HONO generation have been reported (*Braman and de la Cantera*, 1986; *Taira and Kanda*, 1990; *Febo et al.*, 1995), generation of HONO containing low levels of impurities, particularly NO_2, is difficult. Another issue in accurately quantifying HONO is the availability of accurate UV/visible cross sections for HONO. In addition, while DOAS is experimentally straightforward, data analysis is more complex, and the technique has not become as widespread in use as other laboratory methods such as FTIR.

Other methods for HONO quantification include the use of denuders with NO_x detectors. Denuders with Na_2CO_3-glycerine and NaCl remove HONO + HNO_3 and HNO_3 alone, respectively, then a catalyst converts the remaining nitrogen oxides to NO for quantification by a NO_x detector such as a chemiluminescence detector. This method relies on the efficiency and specificity of the denuders. Alternatively, wet chemical techniques can be used including ion chromatography of the nitrite ions obtained from HONO dissolution, or reduction of the nitrite ions to NO followed by chemiluminescence detection. Finally, atmospheric pressure ionization mass spectrometry was used, for example by Spicer et al. (1993), who measured HONO using MS-MS of the Cl^-·HONO adduct formed when CCl_4 is added to the discharge region in which the ions are generated. This is a highly sensitive and specific method, but has not found widespread use due to its complexity.

I.A.2. New Technique for Quantification of HONO

We present a unique procedure for HONO titration experiments carried out in the environmental chamber. The experiment utilizes the gas phase reaction of HONO with excess HCl to produce ClNO, reaction (I.1).

$$HONO + HCl \rightarrow ClNO + H_2O \qquad (I.1)$$

A total of six titration experiments were performed using continuous, simultaneous measurements with UV/visible and IR spectroscopy. The HONO generation apparatus described above was used to flow a HONO/N_2 mixture into the evacuated environmental chamber to an initial pressure varying from ~65 Torr to ~550 Torr and N_2 was added to a total pressure of 700 Torr. Wall loss of HONO was then monitored for 15 to 30 min by FTIR

and DOAS. The titration experiment was initiated by flushing an excess of HCl (g) from a passivated glass cell of known volume into the chamber through a side panel using N_2 to a total pressure of 750 Torr. The amount of excess HCl used was at least ten times the initial HONO concentration, which was determined in real time by DOAS using the HONO cross sections of Bongartz et al. (1991, 1994). The loss of HONO due to reaction with HCl was followed with time by DOAS and FTIR, and ClNO formation was followed by FTIR. At longer times, the loss of ClNO in the chamber was measured by following it with time after most of the HONO had reacted. NO_2 impurities were measured using DOAS. The ClNO and NO_2 concentrations were determined by calibration with pure samples of ClNO and NO_2.

Another potential source of ClNO in these experiments is the reaction of HCl with NO_2, present as an impurity in the HONO synthesis. To investigate the products of this reaction, several experiments were carried out in which known concentrations of NO_2 and HCl were flushed into the chamber, followed by filling to 1 atm with humid N_2 to replicate conditions of a typical titration experiment. NO_2 was followed by both DOAS and FTIR, while ClNO was followed by FTIR.

I.A.3. Analysis of UV/Visible and FTIR Data

Analysis of the data is described in detail in Appendix A. In brief, a model spectrum (UV/visible or FTIR) can be described by equation (Eq. I.1).

$$F(\lambda) = \sum_j \left(a_j \times S_j(\lambda)\right) + P(\lambda) \qquad \text{(Eq. I.1)}$$

where $S_j(\lambda)$ are reference absorption spectra of known concentrations, a_j are scaling factors for the reference spectra, and $P(\lambda)$ is a polynomial to fit broad or background features (*Gomer et al.*, 1995). The recorded spectra consist of the sum of the broad features and the structured features of the absorber(s), thus the spectra were fitted mathematically to determine the contributions of each species to the total spectrum. This was accomplished by minimizing the residuals between each experimental spectrum and a linear combination of the reference spectra of all the contributing species to obtain a model spectrum, $F(\lambda)$, based on equation (Eq. I.1). The scaling factors, a_j, obtained for each species by this fitting procedure are proportional to concentration. They are multiplied by the concentration of each reference spectrum used to obtain the actual concentration of the experimental spectrum.

HONO and NO_2 concentrations in the UV/visible spectra were determined by fitting the spectra with HONO and NO_2 reference spectra and a third order polynomial in the 340-380 nm region (see Appendix A). The published cross sections of Bongartz et al. (1991, 1994) were used for HONO after first converting to 0.27 nm resolution by convolution with the instrument function of the grating spectrograph. The cross sections of Bongartz et al. (1991, 1994) are in excellent agreement with more recent studies of Stutz et al. (2000) but for reasons which are not clear, not with those of Brust et al., (2000). IR spectra were analyzed using polynomials of zero to second order to simulate the baseline and with reference spectra for HONO, HNO_3, and H_2O. The use of an aqueous solution of HCl for the synthesis of HONO gave water vapor in the chamber initially so that the relative humidity during the

experiments varied from ~10% to 30%. This water vapor caused interferences in the IR spectra near both HONO and ClNO. The interfering rotational structure from water vapor was accounted for by fitting the experimental spectra to a reference water spectrum taken at a similar water vapor concentration.

Typical IR spectra showing the loss of HONO and production of ClNO are shown in Figure 3.I.1. The HONO band centered at 1263 cm^{-1} (ν_3, *trans*-HONO) is shown in Figure 3.I.1a at t = 0, as well as at 1 h, and 3 h after HCl addition. Figure 3.I.1b shows the corresponding production of ClNO (ν_1, centered at 1799 cm^{-1}) at the same times. UV/visible spectra showing HONO loss are shown in Figure 3.I.2 at approximately the same times. The fitting procedure described above was applied to the spectra in Figures 3.I.1 and 3.I.2, followed by subtraction of the interfering compounds leaving the HONO and ClNO spectra shown.

I.A.4. Stoichiometry of Reaction of HONO With HCl

Reactions (I.1), (I.2), and (I.3) describe this system:

$$\text{HONO} + \text{HCl} \xrightarrow{k_1} \text{ClNO} + \text{H}_2\text{O} \qquad \text{(I.1)}$$

$$\text{ClNO} \xrightarrow{k_2} \text{Products} \qquad \text{(I.2)}$$

$$\text{HONO} \xrightarrow{k_3} \text{Products} \qquad \text{(I.3)}$$

For each experiment, the change in the concentrations of ClNO (determined by FTIR) and HONO (determined by DOAS) were calculated relative to the time when HCl was added. The increase in [ClNO] was plotted against the decrease in [HONO] for equal time intervals and the slope was obtained for each experiment. Using a numerical integration program, ACUCHEM (*Braun et al.*, 1988), the HONO and ClNO time traces resulting from reactions (I.1), (I.2), and (I.3) were modeled with the additional losses, k_2 and k_3, set to experimentally observed values as well as with these losses set to zero. Comparison of the two kinetics model runs shown in Figure 3.I.3 indicates that loss effects from reactions (I.2) and (I.3) are negligible until ~54 min.; thus, all stoichiometry plots were obtained using data from ≤54 min. A typical stoichiometry plot is shown in Figure 3.I.4 with a slope of 1.28 ± 0.02 (2σ). A slope of unity indicates that one ClNO forms for every HONO destroyed, i.e., a one-to-one stoichiometry for reaction (I.1).

The slopes obtained for these stoichiometry plots are shown in Table 3.I.1 for all experiments, with the average equal to 0.9 ± 0.4 (2σ). Although there is low precision between experiments, on average one ClNO molecule forms for every HONO molecule reacted. This is consistent with the results of Fenter and Rossi (1996), who observed a one-to-one stoichiometry for reaction of HONO with HCl on an ice substrate.

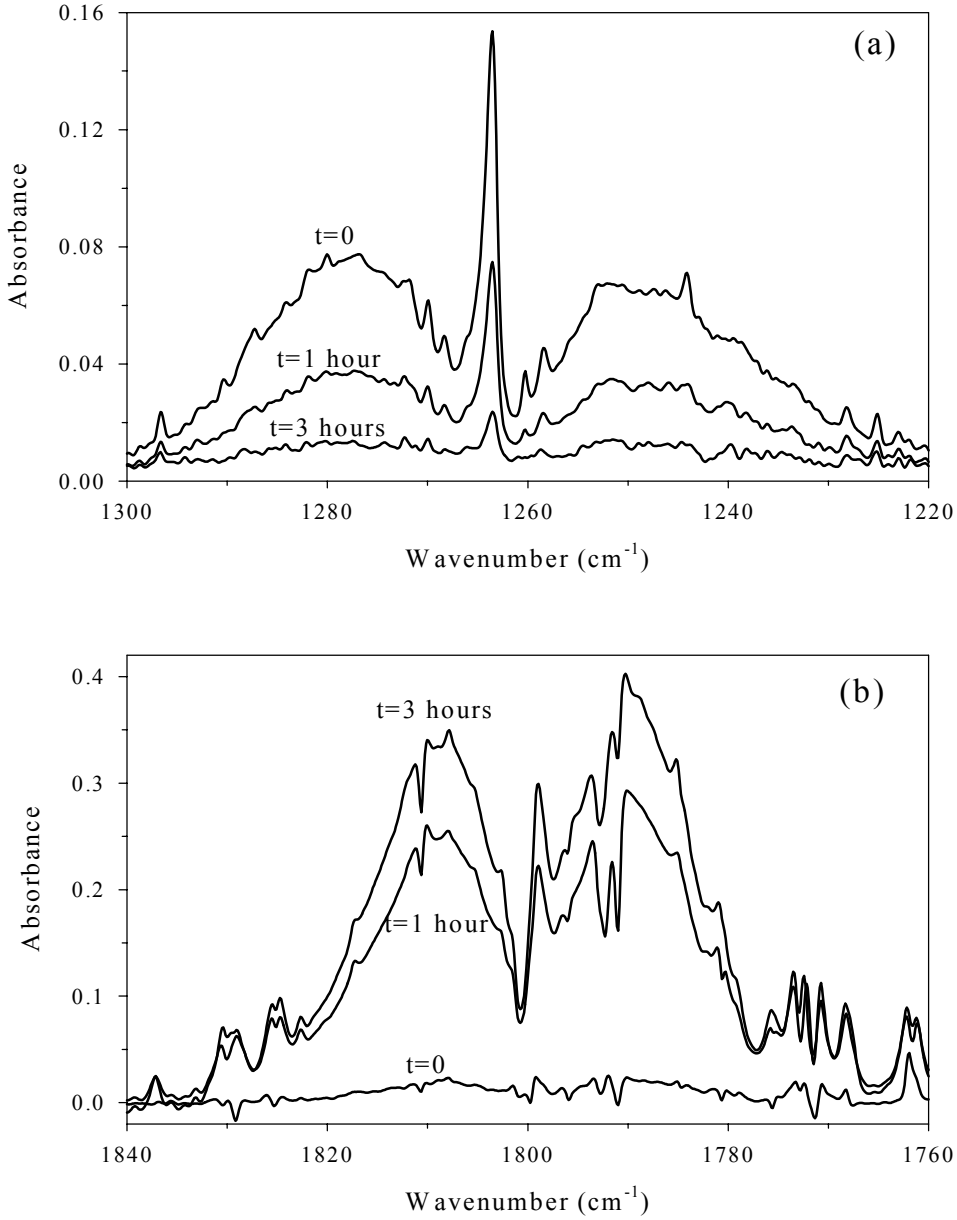

Figure 3.I.1. Infrared spectra showing the loss of HONO and increase in ClNO with time during a typical experiment (#2). (a) The ν_3 band of *trans*-HONO, centered at 1263 cm^{-1}, is shown at t = 0, before excess HCl (7.93×10^{14} molecules cm^{-3}) had been added, and also 1 h and 3 h after HCl had been added. (b) The ν_1 band of ClNO, centered at 1799 cm^{-1}, is shown for the same times as those in (a). At t = 0, $[ClNO]_0 = 2.1\times10^{13}$ molecules cm^{-3}; at t = 1 h, [ClNO] = 5.2×10^{13} molecules cm^{-3}; and at t = 3 h, [ClNO] = 6.8×10^{13} molecules cm^{-3}. Spectra were obtained by simultaneously fitting for HONO, HNO_3, H_2O, and a polynomial, followed by subtraction of HNO_3, H_2O, and the polynomial.

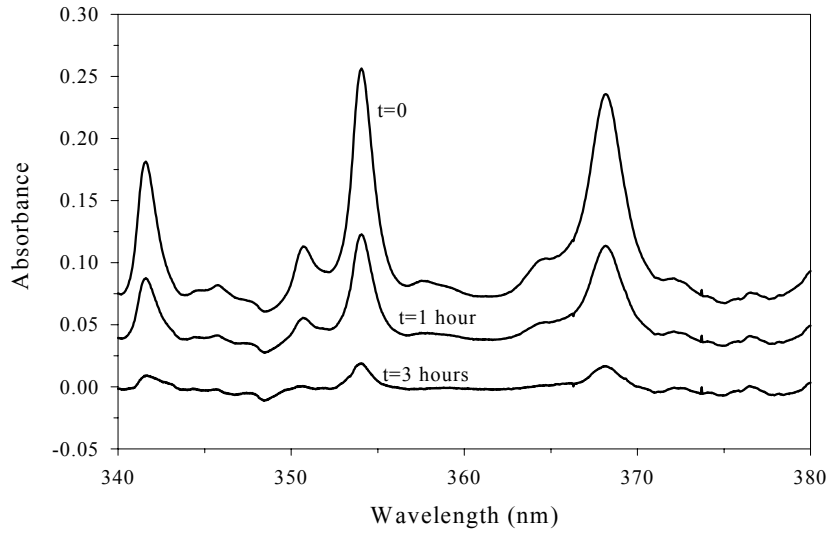

Figure 3.I.2. UV/visible spectra of gaseous HONO corresponding to approximately the same times as the IR spectra shown in Figure 3.I.1. Spectra were obtained by simultaneously fitting for HONO, NO_2, and a polynomial, followed by subtraction of NO_2 and the polynomial. At t = 0, $[HONO]_0 = 7.6\times10^{13}$ molecules cm^{-3}; at t = 1 h, $[HONO] = 3.6\times10^{13}$ molecules cm^{-3}; and at t = 3 h, $[HONO] = 9.3\times10^{12}$ molecules cm^{-3}. Spectra are offset on y-axis for clarity.

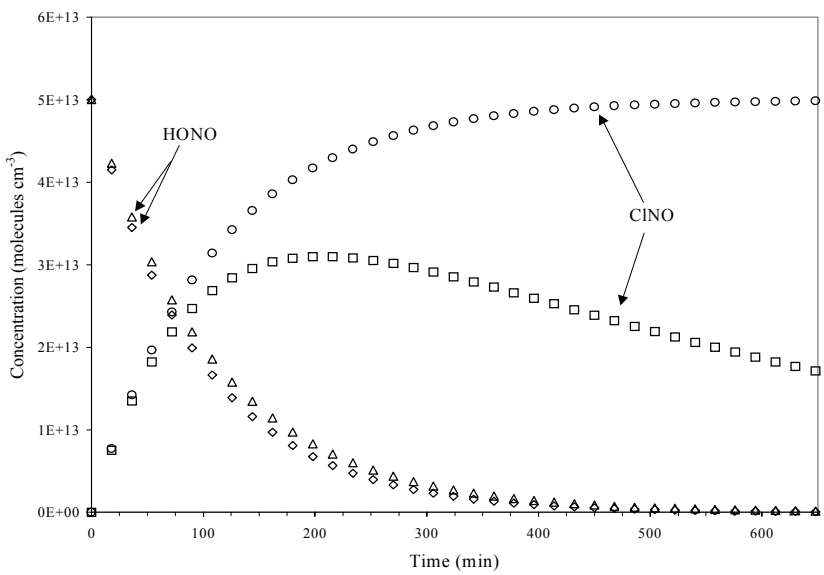

Figure 3.I.3. Kinetics modeling plots to show the difference in time profiles for HONO and ClNO with and without additional (wall) losses taken into account (see text). Triangles (Δ) show HONO loss due only to reaction (I.1). Diamonds (◊) show HONO with additional loss (reaction (I.3)). Circles (o) show ClNO production due only to reaction (I.1). Squares (□) show ClNO production with additional loss (reaction (I.2)). The difference between the two model runs is negligible before ~54 min.

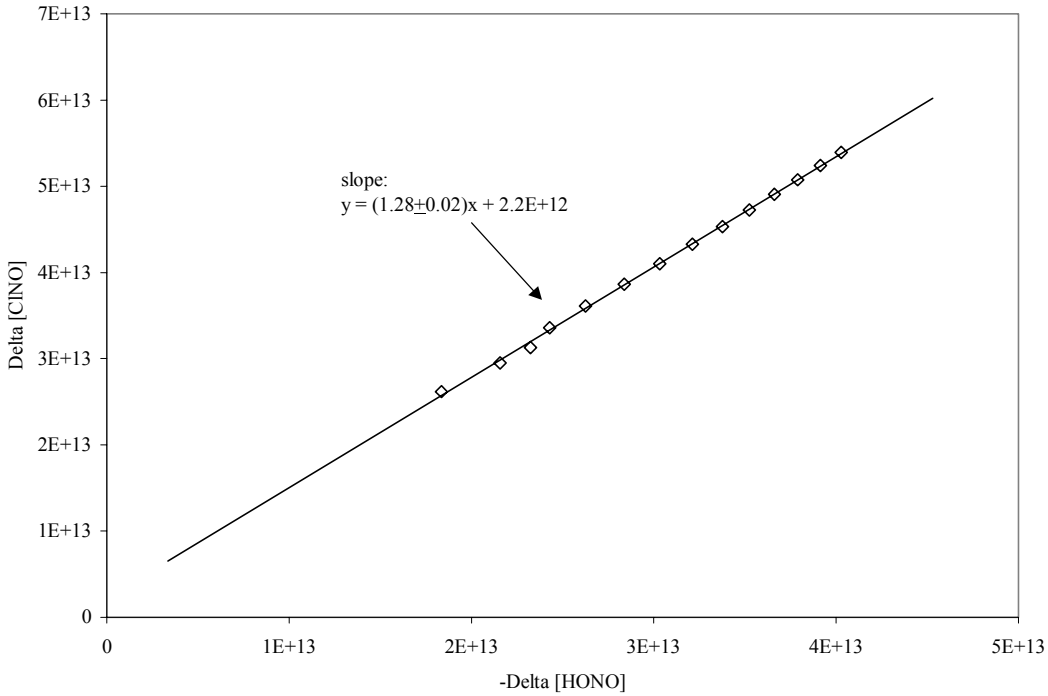

Figure 3.I.4. Typical stoichiometry plot showing the net production of ClNO versus the net decrease in HONO for equal time intervals. The slope gives the stoichiometry of reaction (I.1) for experiment #1.

Table 3.I.1. Summary of Stoichiometry and Kinetics Data for HONO Titration Experiments.

Exp. No.	Stoichiometry Plot Slope (−Δ[ClNO]/Δ[HONO])	k_1 from FTIR analysis of HONO[a] (cm^3 $molecule^{-1}$ s^{-1})	k_1 from DOAS analysis of HONO (cm^3 $molecule^{-1}$ s^{-1})
1	1.3	3.05×10^{-19}	2.91×10^{-19}
2	0.76	2.01×10^{-19}	2.21×10^{-19}
3	0.77	1.83×10^{-19}	2.16×10^{-19}
4	1.0	1.21×10^{-19}	1.23×10^{-19}
5	0.74	1.19×10^{-19}	1.07×10^{-19}
6	0.66	1.90×10^{-19}	1.61×10^{-19}
	0.9 ± 0.4 (2σ)	$(1.86 \pm 1.36)\times10^{-19}$ (2σ)	$(1.87 \pm 1.39)\times10^{-19}$ (2σ)

[a] Each rate constant in column 3 is an average of the rate constants obtained from the natural log plots using the three HONO IR peaks centered at 790 cm^{-1}, 852 cm^{-1}, and 1263 cm^{-1}.

Other minor pathways for ClNO formation in this system were considered. The reaction of NO_2, present as an impurity in the HONO mixture, with HCl was examined as a possible source of ClNO:

$$2\ NO_2 + HCl \rightarrow ClNO + HNO_3 \qquad \text{(I.4)}$$

To test this possibility, concentrations of HCl, NO_2, and H_2O typical of those in a titration experiment (#1) were introduced into the chamber and the formation of ClNO was followed with time. The experiment was performed using 11 ppm NO_2 and 34 ppm HCl at 11% relative humidity and resulted in a very small yield of ClNO, ~2% of the total ClNO formed under the same initial conditions during the titration experiment (#1). Thus, reaction of NO_2 with HCl only slowly produces relatively small amounts of ClNO and cannot be a significant source of ClNO in these HONO + HCl experiments.

I.A.5. Kinetics of Reaction of HONO With HCl

The time dependence of HONO during the reaction of HONO with HCl can be used to measure the rate constant for reaction (I.1). The time dependence of HONO was described by its loss by the reaction with HCl, reaction (I.1), as well as its loss to the walls and photodissociation by the Xe arc lamp, reaction (I.3). HCl was used in excess, so that its concentration remained approximately constant (≤ 6% loss over the times studied here, as discussed in Section I.A.6). Thus, the integrated rate equation for HONO is given by equation (Eq. I.2),

$$[HONO] = [HONO]_o \, e^{-(k_1[HCl]_o + k_3)t} \qquad \text{(Eq. I.2)}$$

where k_1 is the second order rate constant for the reaction of HONO with HCl, k_3 is the first order rate constant for HONO wall loss and photodissociation, $[HCl]_o$ is the initial HCl concentration, and $[HONO]_o$ is the initial HONO concentration before addition of excess HCl. To obtain k_1 from equation (Eq. I.2), $\ln(a_{HONO})$, where a_{HONO} are the scaling factors in equation (Eq. I.1), was plotted versus time, the slope of which is equal to $-(k_1[HCl]_o+k_3)$. The first order loss of HONO, k_3, was obtained experimentally by following HONO by FTIR and DOAS before HCl had been added for each experiment. $[HCl]_o$ is known for each experiment, thus k_1 was determined for each experiment from the slope after addition of HCl. Values of k_3 ranged from $(1.8–6.5) \times 10^{-5}$ s^{-1} in these experiments and are given in Table 3.I.2.

Table 3.I.2. Summary of Kinetic Data for HONO Titration Experiments.

Exp. No.	k_2 from FTIR analysis of ClNO (s^{-1})	k_3 from FTIR analysis of HONO (s^{-1})
1	1.3×10^{-5}	1.8×10^{-5}
2	2.2×10^{-5}	3.6×10^{-5}
3	1.8×10^{-5}	4.5×10^{-5}
4	7.4×10^{-6}	5.6×10^{-5} [b]
5	1.7×10^{-5} [a]	6.5×10^{-5} [b]
6	1.5×10^{-5}	5.3×10^{-5} [b]

[a] Experiment 5 had insufficient data at long times to measure the wall loss of ClNO. Thus, the average k_2 from other experiments was used, $k_2^{ave} = 1.69\times10^{-5}$ s^{-1}.

[b] A significant amount of unreacted HCl was present at the beginning of these experiments which may have affected the rate of HONO loss before excess HCl addition.

Figure 3.I.5 shows typical plots of ln (a_{HONO}) versus time using the HONO infrared peaks at 790 cm^{-1}, 852 cm^{-1}, and 1263 cm^{-1}. Table 3.I.1 summarizes the values obtained for k_1 by FTIR (column 3). Column 4 of Table 3.I.1 gives the values of k_1 obtained using the same analysis but using the DOAS HONO data. The average values for k_1 using the two measurement methods for HONO, $k_1 = (1.9 \pm 1.4)\times10^{-19}$ cm^3 $molecule^{-1}$ s^{-1} (2σ) by FTIR and $k_1 = (1.9 \pm 1.4)\times10^{-19}$ cm^3 $molecule^{-1}$ s^{-1} (2σ) using DOAS, are in excellent agreement, although the errors are large. The overall rate constant using both analytical techniques for HONO analysis is $k_1 = (1.9 \pm 1.3)\times10^{-19}$ cm^3 $molecule^{-1}$ s^{-1} (2σ).

Karlsson and Ljungström (1996) studied the reverse reaction, ClNO hydrolysis, and reported an upper limit for the rate constant for reaction (I.-1),

$$ClNO + H_2O \xrightarrow{k_{-1}} HONO + HCl \qquad \text{(I.-1)}$$

to be $k_{-1}(296\ K) \leq (7.4 \pm 2.4)\times10^{-22}$ cm^3 $molecule^{-1}$ s^{-1}. Using the calculated value of the equilibrium constant of $K_1(296\ K) = 8.0\times10^{-5}$ based on the published Gibbs free energy for the more stable *trans*-HONO (*Chase et al.*, 1985), the upper limit for the rate constant of the forward reaction (I.1) is thus $k_1(296\ K) \leq 9.3\times10^{-18}$ cm^3 $molecule^{-1}$ s^{-1}. Our measured value of $k_1 = (1.9 \pm 1.3)\times10^{-19}$ cm^3 $molecule^{-1}$ s^{-1} (2σ) for a temperature of 297±1 K is consistent with this reported upper limit.

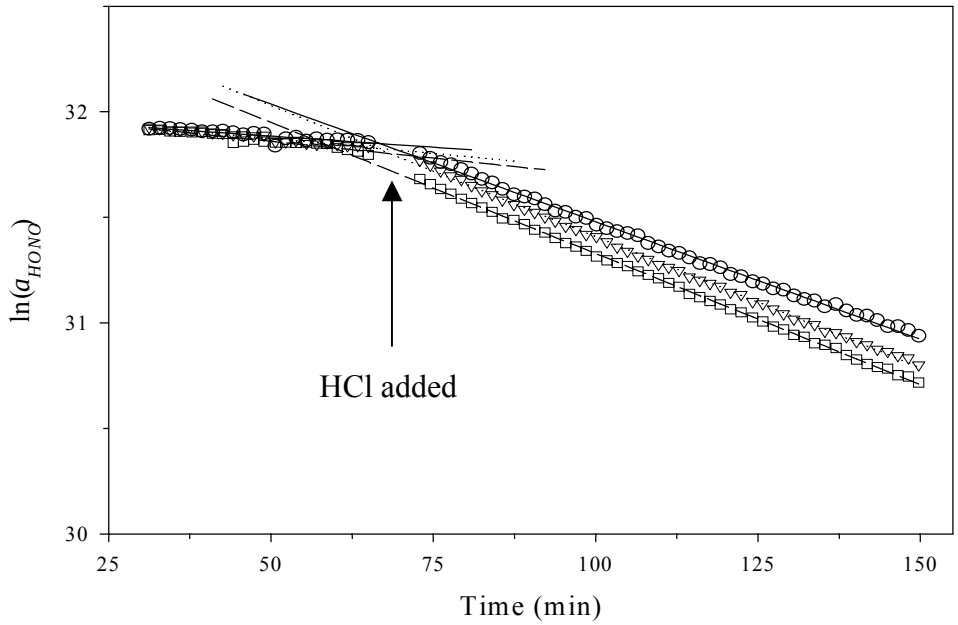

Figure 3.I.5. Typical plots of ln(a_{HONO}) versus time. Data shown are for experiment #3 in which $[HCl]_0 = 8.48\times10^{14}$ molecules cm^{-3}. Least squares analysis for the 790 cm^{-1} peak (o) yielded $k_3 = (3.5 \pm 0.8)\times10^{-5}$ s^{-1} and $k_1 = (1.8 \pm 0.1)\times10^{-19}$ cm^3 $molecule^{-1}$ s^{-1}. For the 852 cm^{-1} peak (∇), $k_3 = (4.7 \pm 0.4)\times10^{-5}$ s^{-1} and $k_1=(1.9 \pm 0.1)\times10^{-19}$ cm^3 $molecule^{-1}$ s^{-1}. For the 1263 cm^{-1} peak (□), $k_3=(5.3 \pm 0.7)\times10^{-5}$ s^{-1} and $k_1 = (1.8 \pm 0.1)\times10^{-19}$ cm^3 $molecule^{-1}$ s^{-1}. The symbols do not lie on top of each other because different reference HONO spectra were used for each infrared peak.

I.A.6. HONO Quantification

The time dependence of the concentration of ClNO was determined by its production in reaction (I.1) and the loss due to reaction (I.2). The integrated rate equation for ClNO, with taken as [HCl] constant, is given by equation (Eq. I.3).

$$[ClNO] = \frac{k_1[HONO]_0[HCl]_0}{k_2 - k_1[HCl]_0 - k_3}\left(e^{-(k_1[HCl]_0 + k_3)t} - e^{-k_2 t}\right) + [ClNO]_0 \qquad \text{(Eq. I.3)}$$

where equation (Eq. I.3), k_2 is the rate constant for first order ClNO loss and $[ClNO]_0$ is the initial ClNO concentration. The slow hydrolysis of ClNO, reaction (I.-1), was treated as first order ClNO loss included in the parameter k_2 due to the high concentrations of water present. While $[ClNO]_0$ should theoretically be zero, in some cases some unreacted HCl passed through the HONO generation apparatus, causing small amounts of ClNO to form before the addition of excess HCl. The value of $[HONO]_0$ is treated as unknown and is obtained by regression analysis of the ClNO data.

The experimental ClNO data were fitted to equation (Eq. I.3) using regression analysis in which the value of $[HONO]_o$ was optimized, while $[HCl]_o$, k_1, k_2, and k_3 were

fixed at the values measured in that experiment. The value of k_2 in equation (Eq. I.3) was determined by plotting ln[ClNO] versus time for later times in the experiment when ≥ 95% of the initial HONO had reacted. Under these conditions, new formation of ClNO was minimal and ClNO loss was dominant. Values of k_2 ranged from $(0.7–2) \times 10^{-5}$ s^{-1} for all experiments and are given in Table 3.I.2.

The effect of a decrease in HCl concentration during a titration was examined by kinetically modeling the system with and without HCl wall loss using ACUCHEM (*Braun et al.*, 1988). The loss of HCl was described using a first order rate constant of 1×10^{-5} s^{-1}, typical of the loss measured by FTIR during the titration experiments. Figure 3.I.6 shows these kinetics modeling results which indicate that the profiles of HONO and ClNO did not change significantly as a result of adding HCl loss to the kinetics model. These resulting time profiles of ClNO with and without HCl loss were then fitted using regression analysis with typical parameter values of $[HCl]_0 = 9.35\times10^{14}$ molecules cm^{-3}, $k_1 = 1.86\times10^{-19}$ cm^3 $molecule^{-1}$ s^{-1}, $k_2 = 2.97\times10^{-5}$ s^{-1}, and $k_3 = 1.69\times10^{-5}$ s^{-1}, while the parameter $[HONO]_0$ was optimized for both cases. As indicated by the regression lines in Figure 3.I.6, the small change in HCl concentration over the time of an experiment (≤ 6%) did not significantly affect the value of $[HONO]_0$ determined by regression (< 2%).

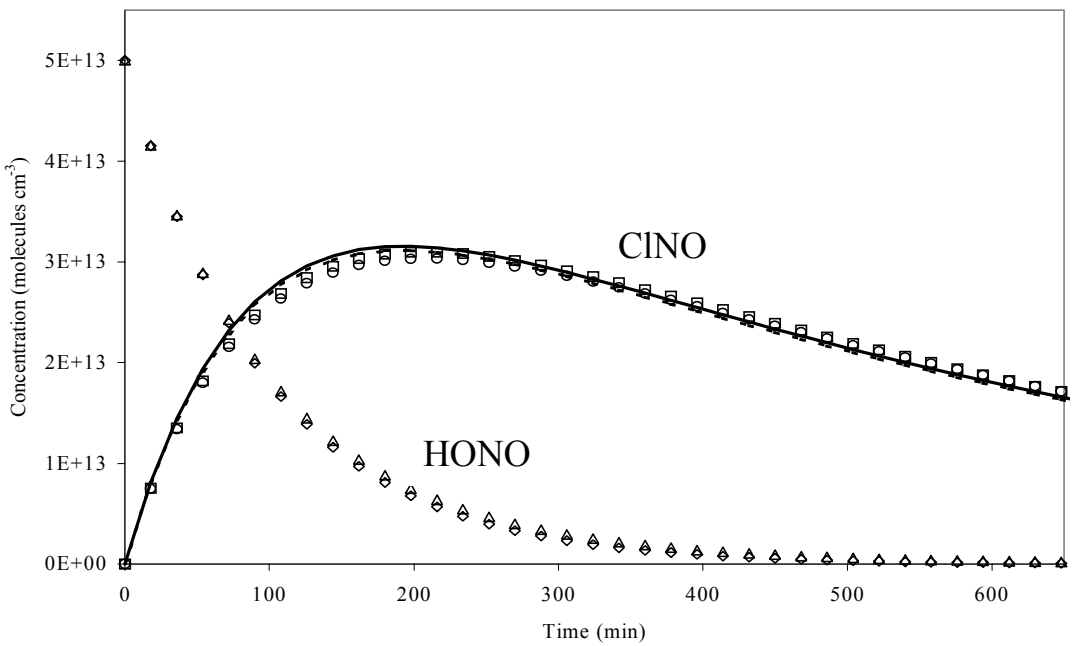

Figure 3.I.6. Kinetics modeling results using ACUCHEM (*Braun et al.*, 1988) showing the effect of adding HCl wall loss to the system. Diamonds (◊) represent HONO without HCl wall loss and triangles (Δ) represent HONO with HCl wall loss. Squares (□) represent ClNO without HCl wall loss with a solid regression line, and circles (o) represent ClNO with HCl wall loss with a dashed regression line.

Figure 3.I.7 shows typical experimental data for the decrease in HONO (determined by DOAS) and production of ClNO (determined by IR) with time. Also shown is the regression of the ClNO data using equation (Eq. I.3) with $[HONO]_0$ treated as an adjustable parameter whose value is determined by optimizing the fit to the data (solid lines). In Figure 3.I.7, the fitting procedure gave $[HONO]_0 = 9.35\times10^{13}$ molecules cm^{-3}, in good agreement with the value of 1.05×10^{14} molecules cm^{-3} determined by DOAS.

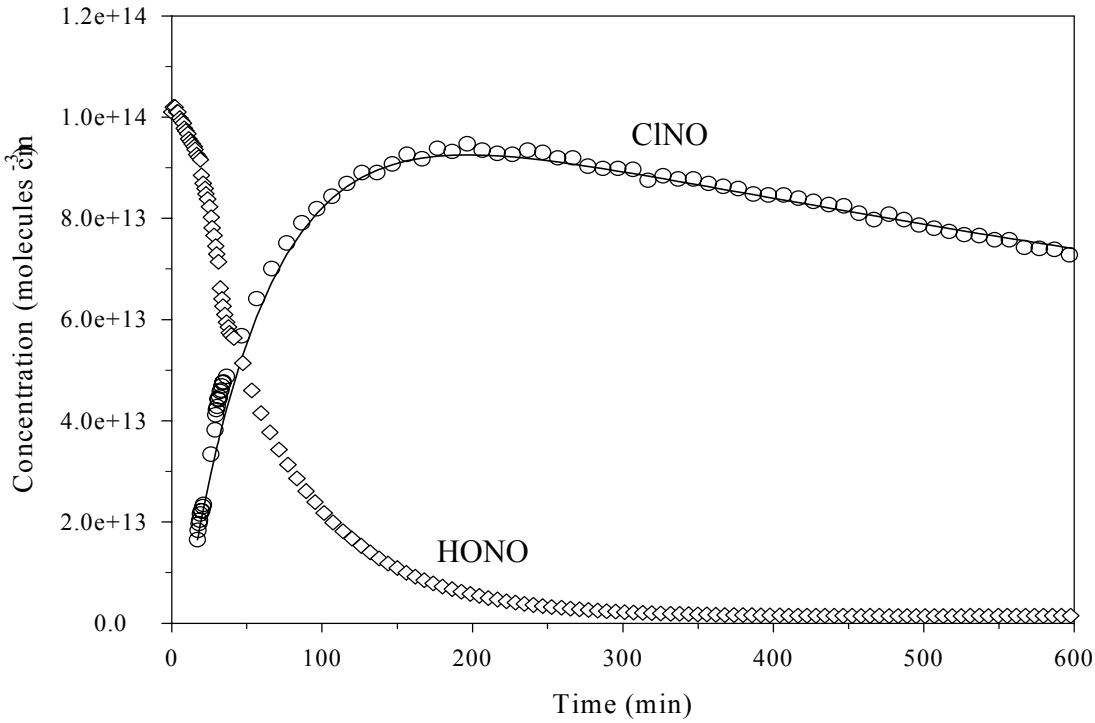

Figure 3.I.7. Time profiles for HONO measured by DOAS (diamonds (◊)) and ClNO by FTIR (circles (o)) during a typical experiment (#1). $[HCl]_0 = 9.35\times10^{14}$ molecules cm^{-3}. Regression of the ClNO data is shown as the solid line. Parameters used in regression: $k_1 = 3.1\times10^{-19}$ cm^3 $molecule^{-1}$ s^{-1}, $k_2 = 1.3\times10^{-5}$ s^{-1}, and $k_3 = 1.8\times10^{-5}$ s^{-1}. The parameter $[HONO]_0$ was optimized by the fit, giving $[HONO]_0 = 9.35\times10^{13}$ molecules cm^{-3}.

Table 3.I.3 summarizes the initial HONO concentrations obtained by the titration method as well as those determined by DOAS using the cross sections of Bongartz et al. (1991, 1994). The values determined by the titration method deviate from those determined by DOAS in individual experiments by –26 to +23%. However, the average deviation over all experiments is only 1%, but with a large uncertainty (39%, 2σ). The experiments with the highest deviations, experiments 4 – 6, were those in which dry, "free-flowing" $NaNO_2$ was used in the HONO generation, resulting in some unreacted HCl passing through the generator and into the chamber before the titration began. The average of the percent deviations, however, is close to zero, indicating that the $[HONO]_0$ values determined by the titration deviate both positively and negatively, i.e., there is no apparent systematic error.

Table 3.I.3. Summary of $[HONO]_0$ Data for HONO + HCl Titration Experiments.

Exp. No.	$[HCl]_0$ (molecules cm^{-3})	$[HONO]_0$ (molecules cm^{-3}) from DOAS analysis[a]	$[HONO]_0$ (molecules cm^{-3}) determined by titration	Percent Deviation $\left(\frac{col3-col4}{col3}\right)\bullet 100\%$
1	9.35×10^{14}	1.05×10^{14}	9.35×10^{13}	11 %
2	7.93×10^{14}	7.55×10^{13}	7.15×10^{13}	5 %
3	8.48×10^{14}	6.84×10^{13}	6.61×10^{13}	3 %
4	8.41×10^{14}	3.59×10^{13}	4.52×10^{13}	-26 % [c]
5	8.53×10^{14}	3.28×10^{13}	4.07×10^{13} [b]	-24 % [c]
6	8.41×10^{14}	2.10×10^{13}	1.61×10^{13}	23 % [c]
				average = -1 % ± 39 % (2σ)

[a] These values of $[HONO]_0$ were determined using the revised UV/visible cross sections of Bongartz et al. (1991, 1994) at the point just before addition of excess HCl.

[b] Experiment 5 had insufficient data at long times to measure the wall loss of ClNO. Thus, the average k_2 from the other experiments was used, $k_2^{ave} = 1.69\times10^{-5}\ s^{-1}$.

[c] A significant amount of unreacted HCl was present at the beginning of these experiments which may have affected the rate of HONO loss before excess HCl addition.

The gas phase reaction of HONO with HCl to produce ClNO has not been reported in the literature to the authors' knowledge. However, the heterogeneous reaction of HONO with HCl on ice and concentrated sulfuric acid solution substrates has been studied by several groups with a one-to-one stoichiometry as found in the present studies (*Zhang et al.*, 1996; *Fenter and Rossi*, 1996; *Burley and Johnston*, 1992; *Longfellow et al.*, 1998). In our studies, a heterogeneous component cannot be ruled out since some reaction may occur on the walls of the chamber. However, for the purposes of using this reaction to measure HONO, this is not an issue.

While the spectroscopic techniques used here detect only gaseous species, a possible contribution from a wall reaction was investigated by carrying out three titration experiments in a 7.6 L, glass long path cell (S/V = 40 m^{-1}). The rate constant obtained for reaction (I.1) in this cell was found to be $k_1^{(7.6L\ cell)} \cong (3 \pm 2)\times10^{-19}\ cm^3\ molecule^{-1}\ s^{-1}$ (2σ), within experimental error of that obtained in the much larger chamber. If reaction (I.1) occurred primarily at the surface, the measured rate constant would be expected to depend on S/V or possibly on surface area. While the data obtained from these experiments do not provide enough information about the mechanism of reaction (I.1) at the molecular level, they suggest that a surface reaction does not predominate.

I.B. Infrared Absorption Cross-Sections of Nitrous Acid (HONO)

We report here FTIR absorption cross-sections for HONO determined for the first time by simultaneous FTIR and DOAS measurements, using the revised UV/visible cross-sections of Bongartz et al. (1991,1994). This approach avoids the problem of indirectly determining the HONO concentration. In the event of future revisions to the UV cross-sections, the FTIR cross-sections reported here can easily be rescaled accordingly.

Experiments were conducted in the environmental chamber. HONO was introduced into the chamber as it was produced, and the chamber was filled until the relative humidity was between 10 – 30%. In order to study a range of concentrations, six experiments were carried out in which an initial concentration of HONO was reacted with an excess of HCl. This slow (*Wingen et al.*, 2000) gas-phase reaction proceeded over a period of hours, producing a range of HONO concentrations. Two additional experiments used the reverse of (I.1) to produce HONO *in situ*. ClNO was added to the chamber, which was subsequently filled with 750 Torr of N_2 at a controlled humidity. Initial HONO concentrations varied between 0.5 and 3.5 ppm; NO_2 impurities between 0.5 and 10 ppm. All spectra were taken at approximately 750 Torr total pressure in N_2. Conditions for each experiment are summarized in Table 3.I.4.

I.B.1. Reference Spectra

Concentrations of impurities such as HNO_3, NO_2, and H_2O were determined by fitting a reference spectrum of the pure gas (recorded in our chamber) to the experimental spectrum. Measured NO_2 pressures were corrected for N_2O_4 using the equilibrium constant (*DeMore et al.*, 1997) $[N_2O_4]/[NO_2]^2 = 2.5 \times 10^{-19}$ cm^3 molecule^{-1}. Our infrared spectra gave an average cross-section (0.5 cm^{-1} resolution, base 10) of $(5.1 \pm 0.9) \times 10^{-20}$ cm^2 molecule^{-1} for the NO_2 band at 2910 cm^{-1}, in good agreement with the value of Sakamaki et al. (1983) of 4.67×10^{-20} cm^2 molecule^{-1}. Our HNO_3 calibration gave an integrated base 10 cross-section of $(8.48 \pm 0.34) \times 10^{-17}$ cm molecule^{-1} over the range 840-930 cm^{-1}, in good agreement with the value 8.13×10^{-17} cm molecule^{-1} obtained for the same range by Hjorth et al. (1987). The high water concentrations present (2000-6000 ppm) meant that absorption was not linear with respect to concentration, so the reference spectrum used for analysis was chosen to be as close as possible to the actual concentration used in the experiment. The water reference spectra were obtained from mixtures of dry and humidified UHP N_2.

Table 3.I.4. Experimental Conditions for Infrared Cross-Section Measurements[a].

Experiment	Method of HONO Synthesis[b]	$[HONO]_{max}$ 10^{13} molecule cm^{-3}	$[NO_2]_{max}$ 10^{13} molecule cm^{-3}	$[HNO_3]_{max}$ 10^{13} molecule cm^{-3}	$[H_2O]_{max}$ 10^{16} molecule cm^{-3}	10^{-11} c_ν[c] 1263	852	790
2	$NaNO_2$+HCl	6.9	11.	0.4	14.	242.	1.68	1.94
3	$NaNO_2$+HCl	8.3	14.	1.0	14.	243.	1.70	1.94
4	ClNO+H_2O	1.5	0.15	<0.1	14.	226.	1.70	1.79[d,e]
5	ClNO+H_2O	1.2	0.14	<0.1	7.0	231.	1.73	1.96[e]
6	$NaNO_2$+HCl	2.9	1.6	0.4	7.0	229.	1.72	1.92
7	$NaNO_2$+HCl	2.5	1.6	0.4	4.0	245.	1.68[e]	2.02
8	$NaNO_2$+HCl	4.0	1.6	0.4	3.0	234.	1.71	2.02
9	$NaNO_2$+HCl	4.0	1.6	0.2	3.0	233.	1.66	1.90

[a] All experiments were done in ~750 Torr N_2 and 23 °C. Details are given in the Materials and Methods section and by *Wingen et al.* (2000). Experiment #1 was not used in the present analysis so is omitted here.

[b] $NaNO_2$+HCl: This reaction was used to generate gaseous HONO, which was flowed into the chamber. ClNO+H_2O: Gaseous ClNO and H_2O were introduced into the chamber and HONO production from the reverse of reaction (I.1) was followed with time. See text for details.

[c] The concentration associated with reference ν, from equation (Eq. I.3). Reference spectra were initially scaled differently, so c_ν does not have the same order of magnitude for each absorption band. *y*-intercepts were fixed to zero except where noted.

[d] The HONO 790 cm^{-1} band did not give reliable results for this experiment due to large changes in the baseline over time.

[e] *y*-intercept was floated in order to get an acceptable fit.

I.B.2. Data Analysis

Spectral analysis was done using the program MFC (*Gomer et al.* 1995). The details of the analysis are described in Appendix A and elsewhere (*Platt and Hausmann*, 1994; *Stutz and Platt*, 1996).

UV and IR HONO references $S_{HONO}^{UV,IR}(\lambda)$ were created from spectra of the experiments summarized in Table 3.I.4. Interfering absorbances were subtracted where necessary. The amount of a reference to be subtracted was determined by fitting the reference to the experimental spectrum in a nearby region that contained no HONO absorption. $S_{HONO}^{UV}(\lambda)$ was determined from a single UV reference spectrum, while averaging was used to correct for possible subtraction errors in the IR spectra. Eight selected HONO spectra, one from each experiment, were averaged to create the three $S_{HONO,\nu}^{IR}(\lambda)$ (ν=1263 cm^{-1}, 852 cm^{-1}, or 790 cm^{-1}). $S_{HONO}^{UV}(\lambda)$ was calibrated by fitting it to the published spectrum of Bongartz et al. (1991, 1994). The literature spectrum was convoluted with our instrument lineshape to produce a spectrum $S_{HONO}^{LIT}(\lambda)$ with the correct resolution (0.27 nm) to match our experimental spectra. Fitting our reference $S_{HONO}^{UV}(\lambda)$ to the convoluted literature spectrum $S_{HONO}^{LIT}(\lambda)$ gave the absolute HONO concentration for $S_{HONO}^{UV}(\lambda)$. Figure 3.I.8 shows the DOAS reference spectrum $S_{HONO}^{UV}(\lambda)$ compared to the literature reference $S_{HONO}^{LIT}(\lambda)$ (*Bongartz et al.* 1991, 1994) and to a reference spectrum of NO_2.

In all experiments, UV and IR spectra were recorded simultaneously. The HONO concentration, $C_{HONO}(t)$, was determined by fitting the UV/visible HONO reference spectrum, $S_{HONO}^{UV}(\lambda)$, to the experimental spectrum corresponding to time *t*. The IR spectra were fit according to equation (Eq. I.1) using the three uncalibrated references $S_{HONO,\nu}^{IR}(\lambda)$, producing three time profiles $a_{HONO,\nu}(t)$, where $a_{HONO,\nu}$ are scaling parameters for the HONO references and ν is either 1263 cm^{-1}, 852 cm^{-1}, or 790 cm^{-1}.

For each experiment, then, an absolute concentration-time profile $C_{HONO}(t)$ and three relative absorbance-time profiles (from FTIR) were obtained. The constant of proportionality, c_ν, could then be determined by a weighted linear regression for the best fit to the equation

$$C_{HONO}(t) = c_\nu a_{HONO,\nu}(t) \qquad \text{(Eq. I.4)}$$

where $C_{HONO}(t)$ is obtained by DOAS and the y-intercept is specified to be zero. $a_{HONO,\nu}(t)$ is a unitless coefficient so that c_ν has units of concentration and gives the concentration of HONO represented by the reference $S_{HONO,\nu}^{IR}(\lambda)$. Floating the y-intercept produced only small changes in the values of c_ν which were less than our detection limit and fluctuated around zero, thus indicating no systematic errors.

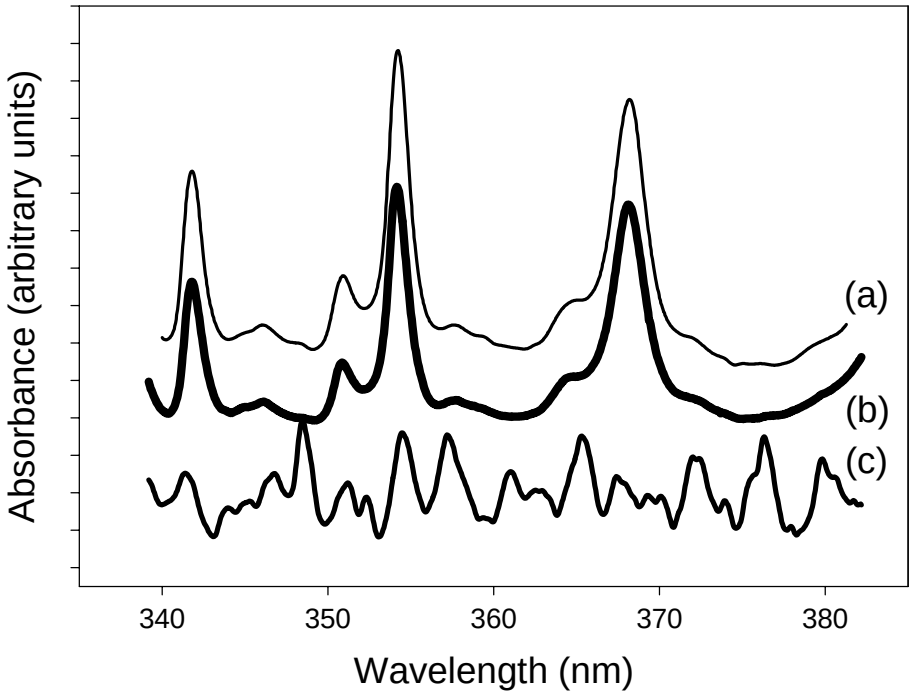

Figure 3.I.8. DOAS (UV) spectra of HONO and NO_2. (a) Spectrum of HONO from Bongartz et al. (1991, 1994). (b) HONO reference spectrum used in this work. (c) NO_2 reference spectrum used in this work. Comparing (a)-(c) shows that there is no significant contribution of NO_2 to spectrum (b).

Figure 3.I.9 shows the results of the regression (Eq. I.4) for a typical experiment, #6. These are similar to Beer-Lambert law plots, although the axes are reversed from the usual orientation and the x-axis is in relative, not absolute, absorbance units. As can be seen from Table 3.I.5, the values of c_v vary by less than 5% between experiments. The absorption cross-sections can then be easily determined:

$$\sigma_{HONO}^{IR}(\lambda) = \frac{S_{HONO,v}^{IR}(\lambda)}{c_v \ell} \qquad \text{(Eq. I.5)}$$

where $S_{HONO,v}^{IR}(\lambda)$ is the IR reference spectrum for HONO at one of three bands (1263 cm^{-1}, 852 cm^{-1}, or 790 cm^{-1}), c_v is the concentration of the reference, and ℓ is the infrared path length.

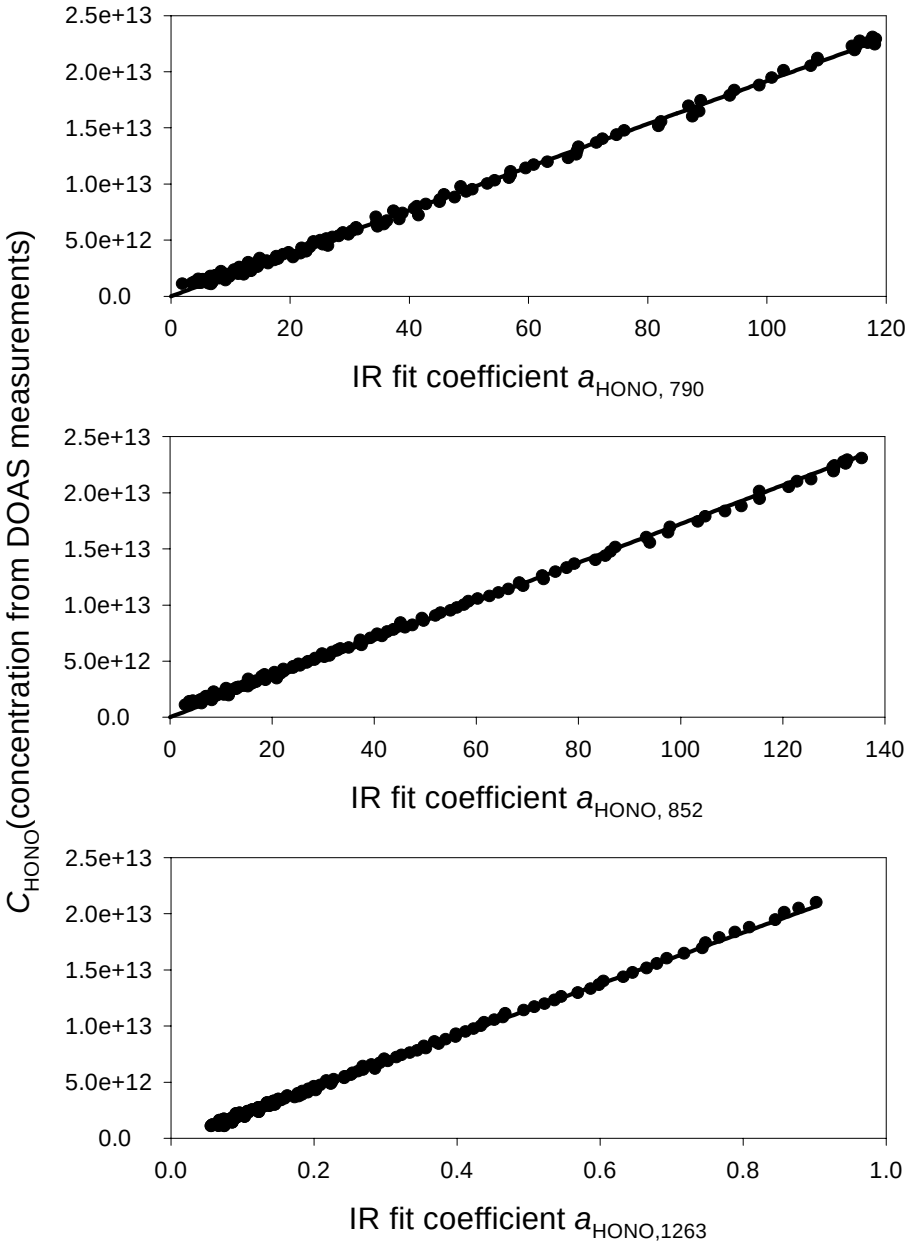

Figure 3.I.9. Linear regression fits of uncalibrated concentrations (from IR spectra) to absolute concentrations (from DOAS spectra). Data are from experiment 6.

The single point Q-branch cross-sections and integrated cross-sections are summarized in Tables 3.I.5 and 3.I.6. IR absorption cross-sections from the literature are included for comparison. All values are reported here as base 10 (i.e. $\sigma C\ell = \log_{10} I_0/I$, which is standard for most FTIR spectrometers). We have given both absolute and effective cross-sections. In the latter, the assumption is made that a particular absorbance is due to all the HONO in the sample, rather than just the *trans*- or *cis*-isomer. This reflects the way that most measurements are actually made, because it is difficult to independently determine the concentrations of the *trans*- and *cis*-isomers. The absolute cross-sections of the *trans*- and *cis*-isomers are then determined based on the equilibrium ratio *R* for *trans* vs. *cis*, which is temperature-dependent and is, unfortunately, not firmly established (*Bongartz et al.*, 1994). Previous studies have used different values of *R* and when converting the published values for comparison to our own, we have used the value of the ratio quoted in the actual study. The following relations were used:

$$\sigma_{cis}^{eff} = \sigma_{cis}\left(\frac{1}{1+R}\right) \qquad \sigma_{trans}^{eff} = \sigma_{trans}\left(\frac{R}{1+R}\right) \qquad \text{(Eq. I.6)}$$

In calculating absolute cross-sections from our own results, we have used *R*=2.3, calculated from data given in the JANAF thermochemical tables (*Chase et al.*, 1998).

During these studies we could only curve fit using 1024 data points simultaneously because of the particular software used. Because of this, each of the three HONO bands was fit independently. Subsequently, we obtained software that allowed us to fit all three bands simultaneously. There was no significant change in the 1263 cm^{-1} cross section, but those at 852 cm^{-1} and 790 cm^{-1} changed somewhat; this is likely due to a curving baseline in this lower wavenumber region. The data in Tables 3.I.5 and 3.I.6 are the revised cross sections (*Barney et al.*, 2000a).

Table 3.I.5. Infrared Absorption Cross-Sections: Q-Branch Intensity at Given Wavenumber.

	Effective[b] Cross Section σ (10^{-19} cm^2 molecule^{-1}, Base 10)				Absolute[c] Cross Section σ (10^{-19} cm^2 molecule^{-1}, Base 10)			
	790	852	1263	Trans/Cis Ratio Used	790	852	1263	$\frac{Q_{1263}}{Q_{852}}$
This Work[a,d]	2.8±0.6	2.7±0.3	3.7±0.4	2.30	4.0±0.8	9.0±0.9	5.2±0.5	0.58
Chan et al. (1976a)	--	3.79±0.38	4.84±0.48	2.29	--	12.5±1.3	6.93±0.70	0.56
Sakamaki et al. (1983)	--	2.86	2.78	2.27	--	9.34	4.00	0.43

[a] Revised cross sections (*Barney et al.*, 2000a).

[b] Calculated from $\sigma = \frac{1}{\ell C_{HONO}} \log_{10}\left(\frac{I_0}{I}\right)$ where C_{HONO} is the total HONO concentration (*trans* plus *cis*).

[c] Corrected for the *trans*/*cis* ratio.

[d] Error bars are 1 standard deviation. Those of Chan et al. (1976a) are not stated, and Sakamaki et al. (1983) do not give error bars for their cross-sections.

Table 3.I.6. Infrared Absorption Cross-Sections: Integrated Band.

	Integrated Effective[b] Cross Sections *S* (10^{-18} cm molecule^{-1} Base 10)			Trans/Cis Ratio Used	Integrated Base 10 Absolute[c] Cross Sections *S* (10^{-18} cm molecule^{-1} Base 10)		
	740-820	820-900	1220-1300		740-820	820-900	1220-1300
This Work[a]	7.0±1.4[d]	6.3±0.6[d]	8.2±0.8	2.30	10.0±2.0	21±2.1	11.7±1.2
Kagann and Maki (1983)[d]			8.1±1.0	2.0			12.2±1.5

[a] Revised cross sections (*Barney et al.*, 2000a).

[b] Calculated from $S = \frac{1}{\ell C_{HONO}} \int_{band} \log_{10}\left(\frac{I_0(\bar{\nu})}{I(\bar{\nu})}\right) d\bar{\nu}$ where C_{HONO} is the total HONO concentration (*trans* plus *cis*).

[c] Corrected for the *trans*/*cis* ratio.

[d] The cutoff between the *trans*-ν_4 band at 790 cm^{-1} and the *cis*-ν_4 band at 852 cm^{-1} was taken to be 820 cm^{-1}. Kagann and Maki (1983) reported values for the cross-sections for the 790 cm^{-1} and 852 cm^{-1} bands of (6.5±1.0)×10^{-18} cm molecule^{-1} and (5.6±0.8)×10^{-18} cm molecule^{-1}, respectively. However, our values may not be directly comparable to theirs since the wavenumber region used for each band was not stated in that work.

As seen in Table 3.I.5, our results are 25-30% lower than those of Chan et al. (1976a). These authors measured the concentrations of NO, NO_2, and H_2O in their reactor and calculated the partial pressure of HONO using the best known estimate of the equilibrium constant for reactions (I.4) and (I.–4):

$$NO + NO_2 + H_2O \leftrightarrow 2HONO \qquad \text{(I.4,I.-4)}$$

They assumed that this gas phase reaction accounted for all HONO formation and loss in their chamber, with the small surface-to-volume ratio and high total pressure favoring homogenous reaction. However, HONO is also formed in other equilibria involving nitrogen oxides (*Lammell and Cape*, 1996) including (I.5,I.-5):

$$2NO_2 + H_2O \leftrightarrow HONO + HNO_3 \qquad \text{(I.5,I.-5)}$$

The presence of other pathways such as (I.5,I.-5) will introduce other species that must be accounted for in the equilibrium calculation. Becker et al. (1995) noted that other tunable diode laser line-strength measurements, in which HONO concentrations were calculated by the equilibrium method, differed from each other by as much as a factor of 3.

Sakamaki et al. (1983) determined cross-sections of HONO in their fluoropolymer-coated environmental chamber using a chemiluminescence NO_y analyzer as described by Cox (1974). This instrument measures either NO or total NO_y (defined as NO + NO_2 + HONO + HNO_3 + N_2O_3 + PAN + organic nitrates + ...) in a gas sample. A scrubber, consisting of a trap containing a 0.1 N aqueous solution of NaOH, was placed in-line before the NO_y analyzer. The trap was intended to remove HONO while leaving NO and NO_2 in the gas stream. Measurements were taken with the scrubber in-line and with the scrubber bypassed, and the difference in total NO_y was taken to be due to HONO. This technique had the disadvantage that some NO and NO_2 are taken up in the trap, with uptake fractions of approximately 20% and 40%, respectively, reported by Sakamaki et al. (1983) for their system. This was given by the authors as the primary source of uncertainty in their experiment.

As shown in Table 3.I.5, our value for the *cis*-ν_4 cross-section maximum at 852 cm^{-1} is in excellent agreement with that of Sakamaki et al. (1983); however, our value for the *trans*-ν_3 maximum is 33% larger. As seen from the ratio Q_{1263}/Q_{852}, this reflects a difference in the relative intensity of the two Q-branches, so it cannot be attributed to error in measuring HONO concentrations. However, our measured ratio of the Q-branch cross-sections is in very good agreement with Chan et al. (1976a). One cause of such a discrepancy might be a difference in the actual *trans*/*cis* ratio present during the experiments; the studies of Sakamaki et al. (1983) were done at 30 °C, while ours and those of Chan et al. (1976a) were carried out at 23 °C. However, the calculated (*Chase et al.*, 1998) *trans*/*cis* ratio changes by only 2% over this temperature range, so it cannot explain the large observed difference in the Q-branch ratios. It is more likely that these ratios are affected by differences in subtraction of water from the spectra.

I.B.3. Water Subtraction

Water has a large effect on determination of HONO Q-branch cross-sections because water absorptions underlie the Q-branches at both 852 cm^{-1} and 1263 cm^{-1}. Water subtraction is especially difficult because at high partial pressures water absorption is not linear with respect to concentration. We have found it is possible to successfully subtract water by using a reference spectrum taken at very nearly the same partial pressure of water that was present during the experiment. Figure 3.I.10a shows the region around the 1263 cm^{-1} band before and after subtraction of water; the water vapor concentration in this case was approximately 4×10^{16} molecule cm^{-3}, about 1000 times the HONO concentration. At higher water concentrations, subtraction becomes more difficult, and the resultant spectrum may contain residual water lines, as shown in Figure 3.I.10b, where $[H_2O] \approx 1.5\times10^{17}$ molecule cm^{-3}. The effect of these lines can be determined by examining the Q-branch absorbance ratio Q_{1263}/Q_{852}. The different water lines underlying these two Q-branches make this ratio very sensitive to water interference.

Table 3.I.7 shows the absorbance of HONO and of water (A_{HONO} and A_{H_2O} respectively) and the absorbance ratio of HONO to water at the 1263 cm^{-1} and 852 cm^{-1} bands for some typical spectra. If A_{HONO}/A_{H_2O} is large, small errors in water subtraction will make little difference in the ratio Q_{1263}/Q_{852}. This is the case for the first two spectra listed, where the water absorbance at either Q branch is no more than ~20% of the HONO absorbance. In the third case listed, the water peak is approximately 40% as large as the HONO absorbance, and for this case a significant difference in Q_{1263}/Q_{852} is seen. This difference in Q-branch ratios is of similar magnitude to that described above between our results and those of Sakamaki et al. (1983), and provides a likely explanation for the discrepancy.

I.B.4. High-Resolution Studies

Kagann and Maki (1983) measured the spectra of equilibrium mixtures of NO, NO_2, and H_2O. They calculated the concentration of *trans*-HONO based on the equilibrium of reaction (I.4,I.-4) as well as several other equilibria in which N_2O_3 and N_2O_4 are formed, but apparently not reaction (I.5,I.-5). Their results cannot be compared to those of Sakamaki et al. (1983) and Chan et al. (1976a) because Kagann and Maki did not report Q-branch maxima. However, our integrated base 10 band intensity of $(7.2 \pm 0.7) \times 10^{-18}$ cm $molecule^{-1}$ for the *trans*-ν_3 band at 1263 cm^{-1} is in good agreement with their reported value of $(8.1 \pm 1.0) \times 10^{-18}$ cm $molecule^{-1}$.

Becker et al. (1995) have published TDLS line intensities, but we cannot compare these to our results because their reported high-resolution lines cover only a small part of the P-branch near 1255 cm^{-1}. To our knowledge, theirs is the only TDLS study in which line intensities were reported.

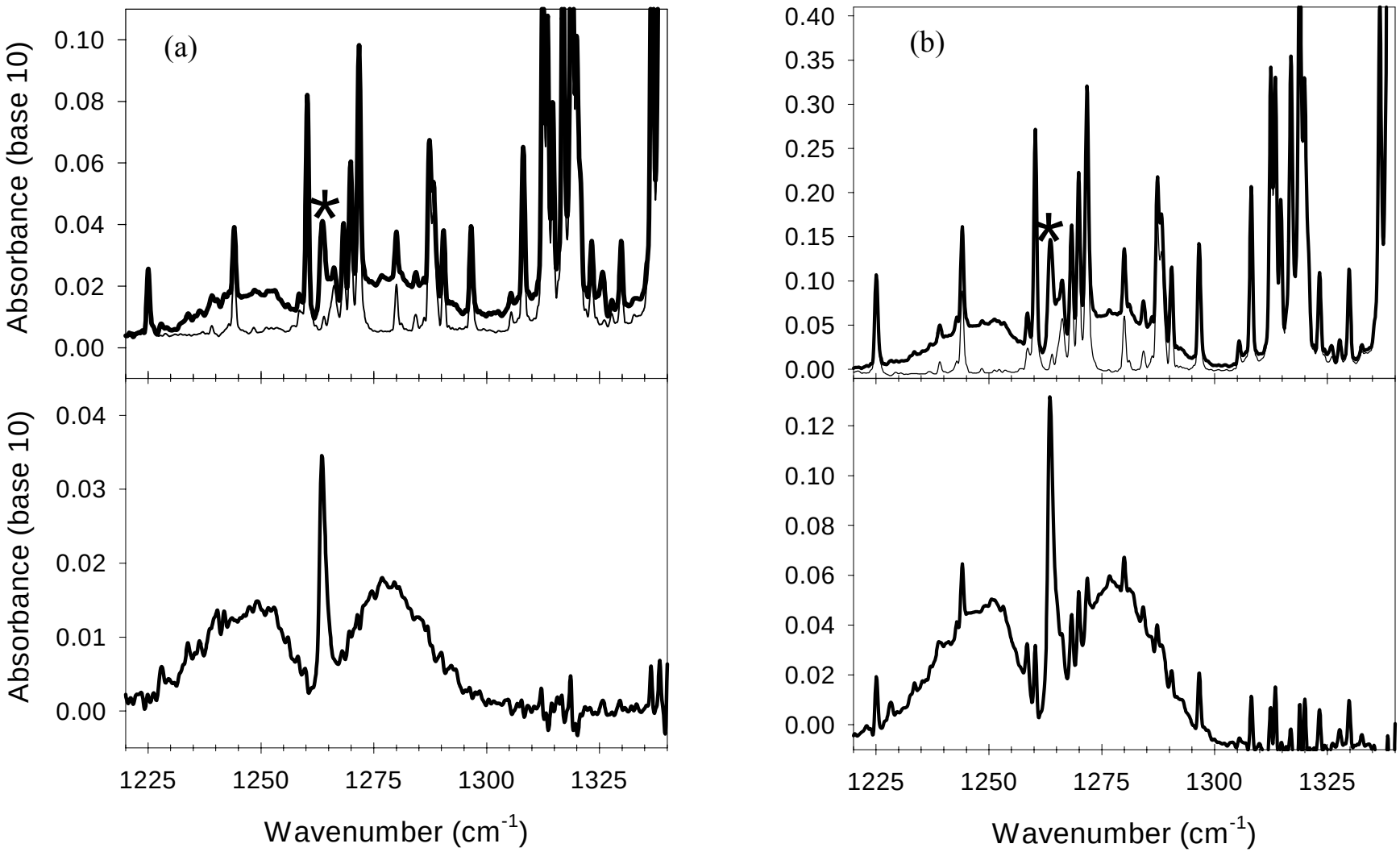

Figure 3.I.10. Water subtraction. In upper plots, asterisk (*) indicates position of HONO Q-branch. (a) Low water vapor concentration; subtraction works very well. (b) Higher water vapor concentration; some residual water lines remain in spectrum. In both of these cases the HONO absorption at the Q-branch is large relative to the water absorption, so the Q-branch intensity remains fairly accurate. The thin line is the water reference spectrum in each case.

Table 3.I.7. Absorbance Ratios of HONO to Water for Q-Branches of Typical Spectra.

	852 cm^{-1}			1263 cm^{-1}			
$[H_2O]$ 10^{17} molecule cm^{-3}	A_{HONO} 10^{-3} abs. units	A_{H_2O} 10^{-3} abs. units	$\frac{A_{HONO}}{A_{H_2O}}$	A_{HONO} 10^{-3} abs. units	A_{H_2O} 10^{-3} abs. units	$\frac{A_{HONO}}{A_{H_2O}}$	$\frac{Q_{1263}}{Q_{852}}$
1.6	100.	11.	9.1	130.	5.1	25	0.56
0.39	25.	1.3	19.	35.	7.2	4.9	0.61
0.72	23.	9.3	2.5	21.	7.9	2.7	0.40

$$\frac{Q_{1263}}{Q_{852}} = \frac{1}{R}\frac{A_{HONO}(1263)}{A_{HONO}(852)}$$

where the *trans/cis* ratio R=2.30.

I.B.5. Model References

Q-branch peak and band-integrated intensities are commonly used in IR work to determine concentration. The Q-branch intensity is usually determined from a single point, so this quantity is much more sensitive to noise than the broader P- or R-branches, and the intensity of all three branches is sensitive to the choice of baseline. Band integration is also very sensitive to the choice of baseline, especially when signal-to-noise is low. When using either method, the baseline must be carefully determined for each individual spectrum. This becomes especially cumbersome when analyzing kinetics data, in which a single experiment may produce dozens or even hundreds of spectra.

As one example of a comparison between two of these methods, we have shown in Table 3.I.8 the sensitivity of least-squares fitting and Q-branch absorbance to water subtraction errors. Multiple fits of the 1263 cm^{-1} band of a single spectrum were calculated, each time subtracting a different multiple of the same water reference spectrum. Table 3.I.8 shows that calculations of the HONO concentration based on Q-branch absorbance are much more sensitive to errors in water subtraction. The small errors (≤ 7% even with no water subtraction at all) are expected for the large concentration of HONO (8.38×10^{13} molecule cm^{-3}) in the test spectrum. Much larger errors result for smaller concentrations of HONO. We have found that least-squares fitting using reference spectra is greatly preferable to integration or Q-branch measurements in many situations, and that because it is not as strongly dependent on the location of the baseline or on the intensity of any one peak, it can extend the effective sensitivity of IR measurements to much lower concentrations.

To facilitate least-squares analysis, we have provided model references based on our experimental spectra. There are advantages to more traditional methods, however: Q-branch intensities are very useful for quickly estimating concentrations, and band integrations are resolution-independent. For this reason, we have also reported the Q-branch cross-sections and the integrated absorbances in Tables 3.I.5 and 3.I.6.

Figure 3.I.11 shows our actual reference spectra for the *trans*-ν_3 band at 1263 cm^{-1} and *cis*-ν_4 band at 852 cm^{-1}, recorded at 0.5 cm^{-1} resolution with 1 level of zerofilling. These HONO references can be described well by a small set of Gaussian functions. Figure 3.I.11 shows these simulated spectra $S(\bar{\nu})$:

$$S(\bar{\nu}) = \sum_{m=1}^{M} \alpha_m e^{-\beta_m (\bar{\nu} - \gamma_m)^2} \qquad \text{(Eq. I.7)}$$

The parameters α_m, β_m, and γ_m determine the intensity, width, and position, respectively, of the *m*th Gaussian function. The smallest number of functions which gave a good fit to the data was M=5. The choice of Gaussian functions was based on similarity to the experimental spectra, but does not have any physical significance. The optimum values of the parameters, given in Table 3.I.9, were determined by least-squares fitting.

Table 3.I.8. Sensitivity of Q-Branch Total Absorbance and Least-Squares Fit Methods to Water Subtraction Errors.

Fraction of H_2O Reference Subtracted[a]	% Error in H_2O Subtraction	% Change in Measured HONO Concentration	
		Least-Squares	Total Absorbance
0.0	-100	-3.2	-6.6
0.5	-44	-1.5	-2.8
0.7	-22	-0.88	-1.4
0.8	-11	0.00	-0.26
0.9	0	0.00	0.00
1.0	11	0.29	0.70
1.1	22	0.59	2.7
1.4	56	1.5	3.1
1.8	100	2.9	5.4

[a] The best subtraction coefficient for the water vapor reference was determined by a least-squares fit to be 0.9. In the sensitivity test, different amounts of the water reference were subtracted, and the % change in calculated [HONO] is shown for both the least-squares fit and the total absorbance methods. The test spectrum used represented 8.38×10^{13} molecule cm^{-3} of HONO (as determined by DOAS).

Table 3.I.9. Parameters Used to Generate Model Reference Spectra.[a]

	852 cm^{-1}			1263 cm^{-1}		
m	α_m 10^{-19} cm^2 $molecule^{-1}$	β_m cm^2	γ_m cm^{-1}	α_m 10^{-19} cm^2 $molecule^{-1}$	β_m cm^2	γ_m cm^{-1}
1	1.40 ± 0.01[b]	0.007 ± 0.0001	866.94 ± 0.08	1.76 ± 0.01	0.0062 ± 0.0001	1278.0 ± 0.1
2	0.59 ± 0.05	0.032 ± 0.003	840.9 ± 0.1	1.1 ± 0.2	0.012 ± 0.002	1249.8 ± 0.1
3	1.31 ± 0.06	2.3 ± 0.2	852.25 ± 0.02	1.1 ± 0.1	0.87 ± 0.29	1264.5 ± 0.2
4	0.98 ± 0.01	0.0043 ± 0.0003	830.7 ± 0.5	0.71 ± 0.1	0.0037 ± 0.0007	1239.8 ± 3.1
5	1.16 ± 0.05	0.35 ± 0.02	852.92 ± 0.04	2.6 ± 0.3	2.4 ± 0.3	1263.52 ± 0.03

[a] These parameters are used with equation (Eq. I.7) to produce model references. References can be used to analyze spectra with any other software which can perform a linear least-squares fit between two sets of data.

[b] Error bars are 1 standard deviation and reflect only the uncertainty associated with the nonlinear fit. See Table 3.I.5 for the error bars of the actual measured cross-sections.

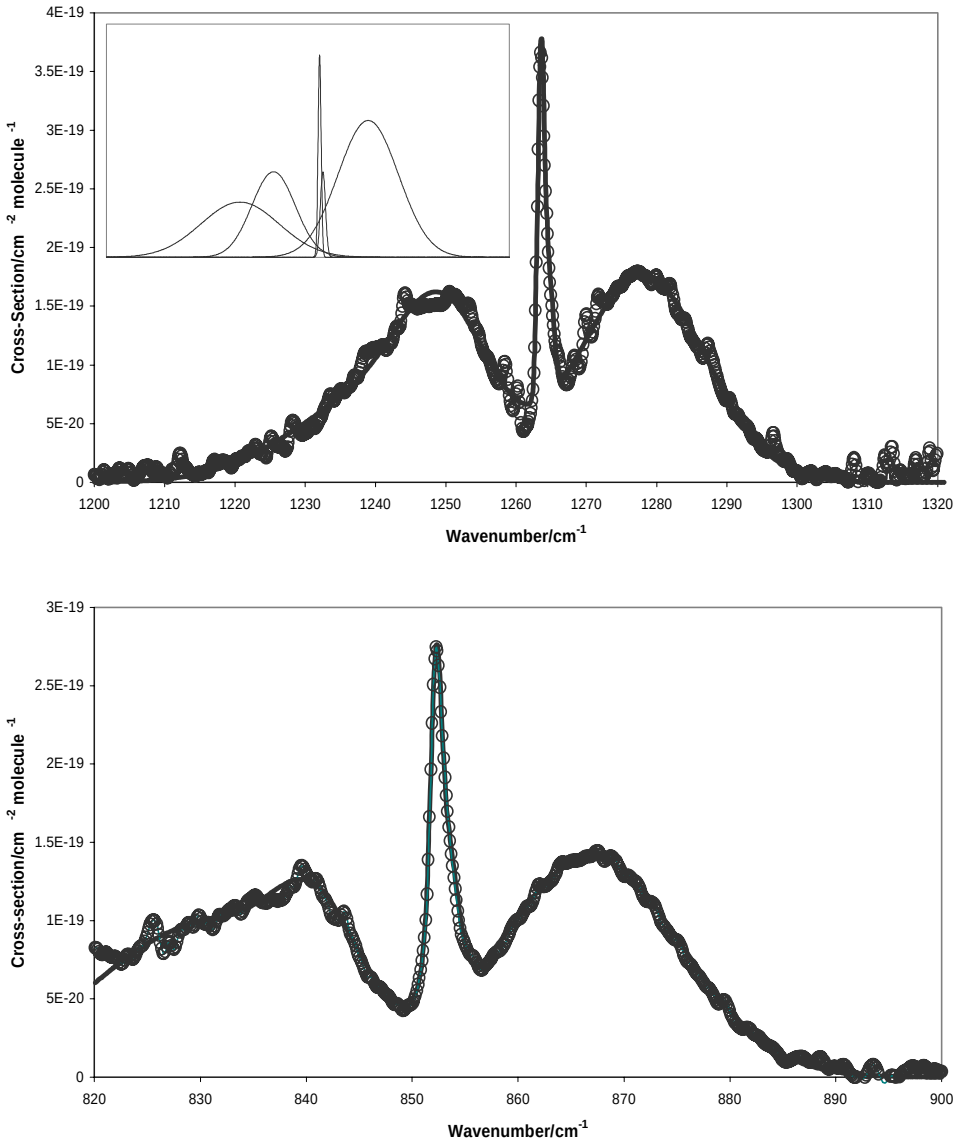

Figure 3.I.11. (a) Actual *trans*-ν_3 reference spectrum (circles) compared to 5-Gaussian model spectrum (solid line). Inset shows the five Gaussian functions used. (b) The actual and model *cis*-ν_4 references. Spectra were recorded at 0.5 cm^{-1} resolution with 1 level of zero filling.

Figure 3.I.12 compares the HONO concentration-time profiles for a typical experiment (#5) using in one case the measured HONO spectra, and in the other case the simulated spectra determined by the Gaussian fit approach. The agreement between the two is excellent, differing by less than 5% in all cases.

I.B.6. Uncertainty, Detection Limit, and Linearity

A conservative estimate of our uncertainties was calculated by propagating the errors in the regression from equation (Eq. I.4) and the spectral fit (Appendix A, Eq. A.5), as well as errors due to water subtraction and to the uncertainty in the DOAS measurements and in the IR and UV path length. Our conclusion is that the limiting source of error in our experiments is the signal-to-noise ratio of our IR HONO spectra, which is on the order of about 10% for each band. This gives the 1σ error bars quoted in Tables 3.I.5 and 3.I.6. We used different HONO sources ($ClNO + H_2O$ and $HCl + NaNO_2$) to reduce the possibility of systematic error relating to impurities, and Table 3.I.4 shows that our reproducibility for c_ν between the two types of experiments was about 5%, consistent with our error estimate. The errors associated with the maximum UV cross-sections of Bongartz et al. (1991, 1994), from their Table II, range from 0.9-1.8% (1σ), so these do not contribute very significantly to our error. Although some recent measurements (e.g. *Pagsberg et al.* (1997), *Brust et al.* (2000)) give slightly different values, the Bongartz et al. (1991, 1994) cross-sections are in good agreement with a recent measurement by Stutz et al. (2000) in which very high-purity (almost NO_2-free) samples of HONO were used.

Our IR detection limit at 52.53 m is between 50-80 ppb, and the IR measurements are in very good (≤10%) agreement with the DOAS measurements for HONO concentrations of 75 ppb and higher. Figure 3.I.9 shows the absorbance to be linear in the absorbance regimes used in our experiments. This linearity was found to hold up to the highest concentration-path length products (3.4 ppm at 52.53 m path length).

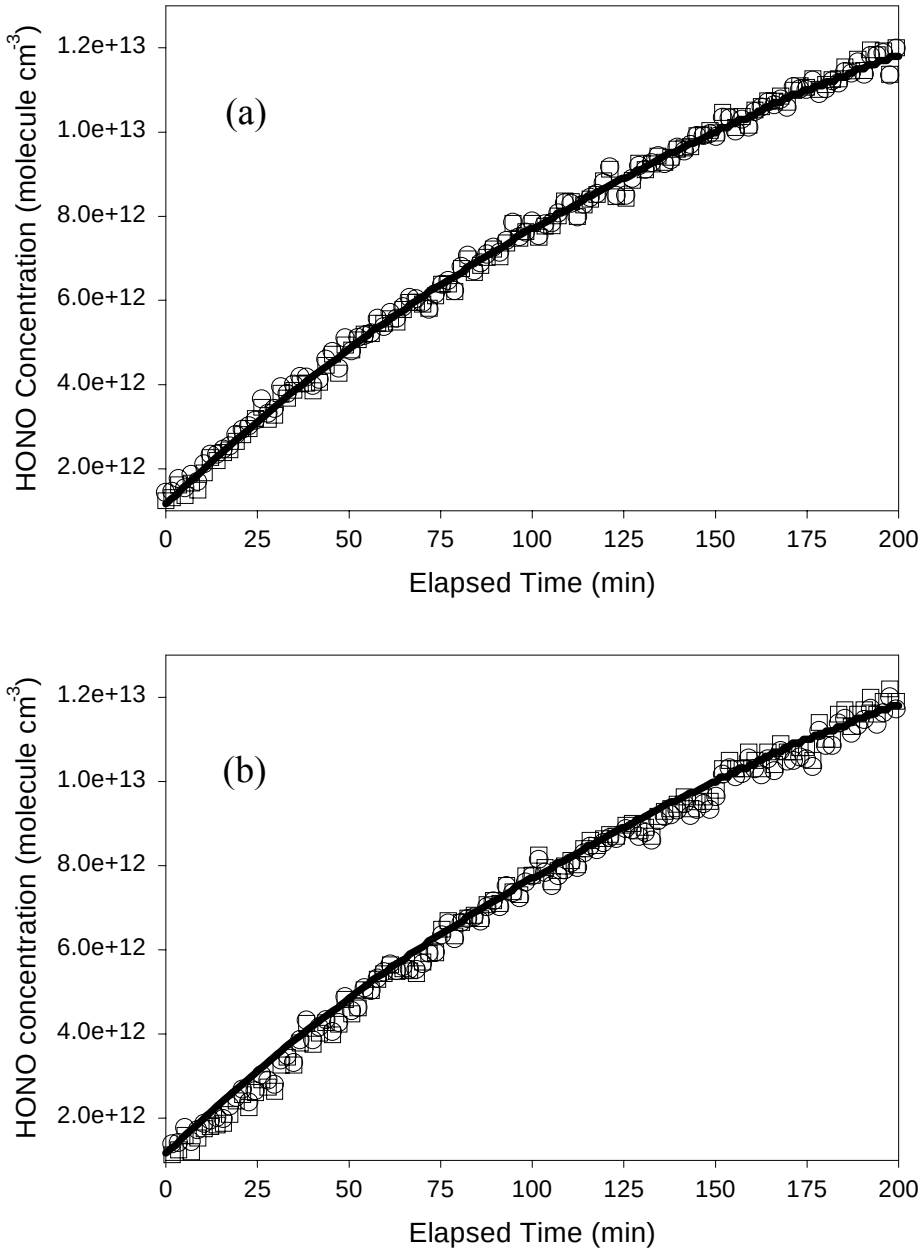

Figure 3.I.12. Comparison of HONO concentrations for experiment no. 5 determined from actual (squares) reference spectra (a) for 1263 cm^{-1} peak, (b) for 852 cm^{-1} peak, to simulated reference spectra (circles). The concentrations determined by DOAS are shown as a heavy line.

II. KINETICS OF HONO FORMATION

Heterogeneous hydrolysis of NO_2 by reaction (II.1) is currently considered a major source of HONO in the atmosphere. The formation of HONO from NO_2 hydrolysis provides a mechanism for reduction and interconversion of nitrogen oxides in the atmosphere. However, despite numerous investigations, the mechanism of reaction of NO_2 with water vapor is still highly debated and poorly understood.

$$2\ NO_2 + H_2O \xrightarrow{surface} HONO + HNO_3 \qquad \text{(II.1)}$$

II.A. NO_2 Hydrolysis - The Effect of Aerosol

To determine the effects of the presence and type of aerosol on NO_2 hydrolysis, experiments were performed in the 561 L environmental chamber using the aerosol generator. NO_2 was introduced into the chamber by filling a glass flow cell of known volume with a known amount of NO_2, then flushing this NO_2 into the chamber with nitrogen gas. A neutral aerosol, Na_2SO_4, and an acidic aerosol, $(NH_4)_2SO_4$, were chosen for two NO_2 hydrolysis experiments, and a third experiment was performed with no added aerosol at approximately the same relative humidity. Table 3.II.1 shows the experimental conditions for these aerosol experiments.

Table 3.II.1. Experimental Conditions for NO_2 Hydrolysis in Chamber With and Without Aerosol.

No.	$[NO_2]_0$ (10^{14} molecules cm^{-3})	Initial Relative Humidity	Aerosol Type	Aerosol Concentration
1	9.37	90%	Na_2SO_4	2.1×10^5 cm^{-3} [a]
2	9.63	90%	$(NH_4)_2SO_4$	2.2×10^5 cm^{-3} [b]
3	9.49	85%	none	-

[a] Na_2SO_4 aerosol had an initial surface area of 7.7×10^{10} nm^2 cm^{-3} and initial volume of 6.5×10^{12} nm^3 cm^{-3}.

[b] $(NH_4)_2SO_4$ aerosol had an initial surface area of 9.7×10^{10} nm^2 cm^{-3} and initial volume of 9.0×10^{12} nm^3 cm^{-3}.

Figure 3.II.1 shows the decay of NO_2 and formation of HONO in the absence and presence of the two types of aerosol. The decrease in NO_2 was, within experimental error, unaffected by the presence of aerosol. Formation of HONO was observed in all three cases, and was also unaffected by the presence of either type of aerosol. The HONO yield, defined by $\Delta[HONO]/\Delta[NO_2]$, was 22% on average for all three experiments. The sudden decreases in NO_2 and HONO at approximately 18 h are due to sampling from the chamber to determine aerosol number density and distribution.

In order to observe an effect due to the presence of aerosol in our environmental chamber, it was determined that the reaction probability (γ) of NO_2 with aqueous surfaces must

be $\gamma \geq 10^{-2}$. If this were the case, approximately 50% of the reaction would take place on the chamber walls and 50% on the surfaces of the aerosol. Thus, a reaction probability of $\gamma \geq 10^{-2}$ would result in a much faster decay of NO_2 and formation of HONO in the presence of aerosol. A reaction probability of $\gamma \leq 10^{-3}$ would result in a change of ≤ 10% in the presence of aerosol, a change which may not be detected in this system. As shown in Figure 3.II.1, the NO_2 decay in each case is approximately equal, i.e. the presence of acidic aerosol, $(NH_4)_2SO_4$, or neutral aerosol, Na_2SO_4, made essentially no difference in the decay of NO_2. This suggests an upper limit for the reaction probability for NO_2 on aqueous surfaces of $\gamma \leq 10^{-3}$.

Because these experiments showed that most of the NO_2 hydrolysis must be occurring on the chamber walls rather than on the aerosol particles, subsequent studies were carried out using the smaller glass cell which had a higher surface area to volume (S/V) ratio. In this case, the glass chamber walls provided the surface for the heterogeneous chemistry. However, since silica is a main component not only of glass but also of many particles suspended in air and surfaces found in polluted urban areas, the results are highly relevant to the formation of HONO in air.

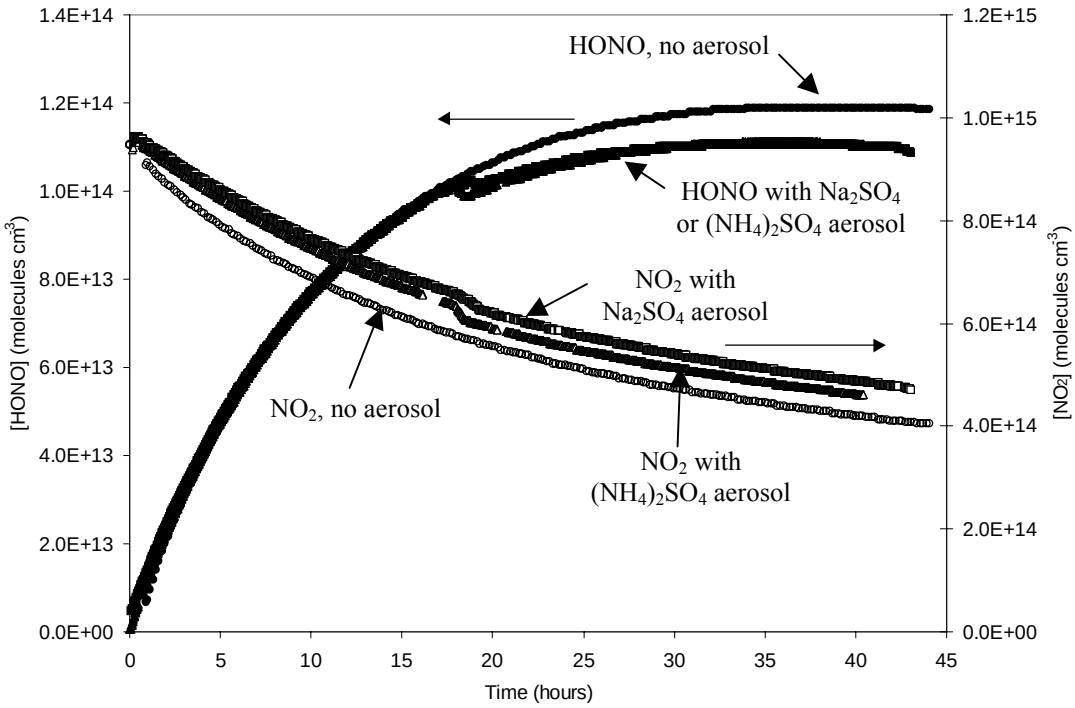

Figure 3.II.1. Hydrolysis of NO_2 and formation of HONO in the environmental chamber in the presence and absence of aerosol. o NO_2 decay in the absence of aerosol; ● HONO formation in the absence of aerosol. □ NO_2 decay in the presence of Na_2SO_4 aerosol; ■ HONO formation in the presence of Na_2SO_4 aerosol. Δ NO_2 decay in the presence of $(NH_4)_2SO_4$ aerosol; ▲ HONO formation in the presence of $(NH_4)_2SO_4$ aerosol. In the experiments with aerosol, the sudden decreases in HONO and NO_2 at approximately 18 h are due to sampling from the chamber to determine aerosol number density.

II.B. Experiments in the Long Path Cell

The experiments described below were designed to follow the reaction of NO_2 in the presence of water under the heterogeneous influence of the long path cell in order to compare to previous work in the literature. This is a critical step in elucidating the reaction mechanism for HONO formation. The reaction order with respect to NO_2 and H_2O are addressed, and product formation under these conditions is discussed.

Nitrogen dioxide hydrolysis experiments were performed in both the long path infrared cell and environmental chamber. Nitrogen dioxide concentrations in the range of $(0.77–2.3) \times 10^{15}$ molecules cm^{-3} (31–93 ppm) were obtained in the long path cell by expanding the appropriate amount of a mixture of NO_2 in N_2 into the evacuated cell (~10^{-5} Torr). Water vapor was added to the cell to give initial relative humidities of ~20%, 50%, and 80%. Since the addition of water vapor initiates the heterogeneous reaction, NO_2 was added first, followed by dry N_2, and finally humid N_2. The reactant and products were followed with time starting immediately after the addition of the reactants and proceeding for up to 6 h. A total of 22 hydrolysis experiments were performed in which the initial NO_2 concentration and initial relative humidity were varied. Table 3.II.2 summarizes the initial conditions of all NO_2 hydrolysis experiments performed in the long path cell ($S/V = 40\ m^{-1}$).

The initial conditions of an additional experiment performed in the 561 L chamber were $[NO_2]_0 = 8.1\times10^{14}$ molecules cm^{-3} and 49.9% relative humidity at 25°C (3.8×10^{17} molecules cm^{-3} H_2O).

Figure 3.II.2 shows typical FTIR spectra taken during an NO_2 hydrolysis experiment. This particular experiment (#12, Table 3.II.2) had an initial NO_2 concentration of 77.3 ppm (1.90×10^{15} molecules cm^{-3} NO_2) and an initial relative humidity of 48.1% at ~25°C (3.71×10^{17} molecules cm^{-3} H_2O). The decay of NO_2 and formation of HONO were observed with time, as seen by the decreasing NO_2 absorption at 2910 cm^{-1} (Fig. 3.II.2a) and increasing HONO absorptions at 790 cm^{-1}, 852 cm^{-1}, and 1263 cm^{-1} (Fig. 3.II.2b). N_2O formation was also observed during some of the experiments, as shown in Figure 3.II.3 (also for experiment 12). Plots of the concentrations of NO_2, HONO, and N_2O (also an observed product) versus time were created for each experiment in order to observe the overall reaction sequence. Figure 3.II.4 is an example of a plot of these time profiles for experiment 12.

Table 3.II.2. Summary of NO_2 Hydrolysis Experiments Performed in the Long Path Cell.

Exp.	Temperature (°C)	Relative Humidity (%)	$[H_2O]_0$ (10^{17} molecules cm^{-3})	$[NO_2]_0$ (10^{15} molecules cm^{-3})
		Low Relative Humidity		
1	24	18.8	1.37	0.768
2	24	20.9	1.52	0.765
3	24	21.1	1.54	1.46
4	24	19.9	1.45	1.44
5	23	20.9	1.44	1.90
6	23	20.3	1.40	1.91
		Intermediate Relative Humidity		
7	23	48.9	3.36	0.748
8	23	48.8	3.36	0.768
9	24	49.3	3.59	0.760
10	24	48.1	3.50	1.42
11	24	47.9	3.49	1.43
12	25	48.1	3.71	1.90
13	24	48.4	3.52	1.94
14	22	53.5	3.47	1.45
		High Relative Humidity		
15	23	78.9	5.43	0.753
16	21	80.0	4.90	0.763
17	22	80.1	5.20	0.831
18	21	79.2	4.85	1.45
19	22	76.4	4.96	1.54
20	23	79.9	5.49	1.96
21	25	79.5	6.12	2.08
22	22	79.3	5.15	2.32

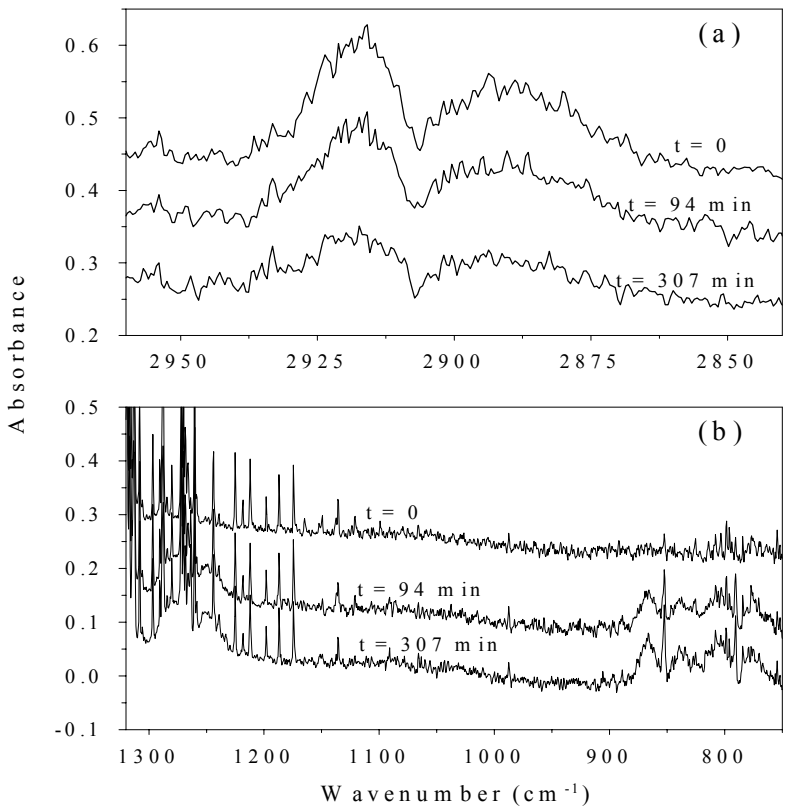

Figure 3.II.2. FTIR spectra of (a) decrease of NO_2, and (b) formation of HONO during a typical NO_2 hydrolysis experiment (experiment 12). Spectra are offset on the y-axis for clarity.

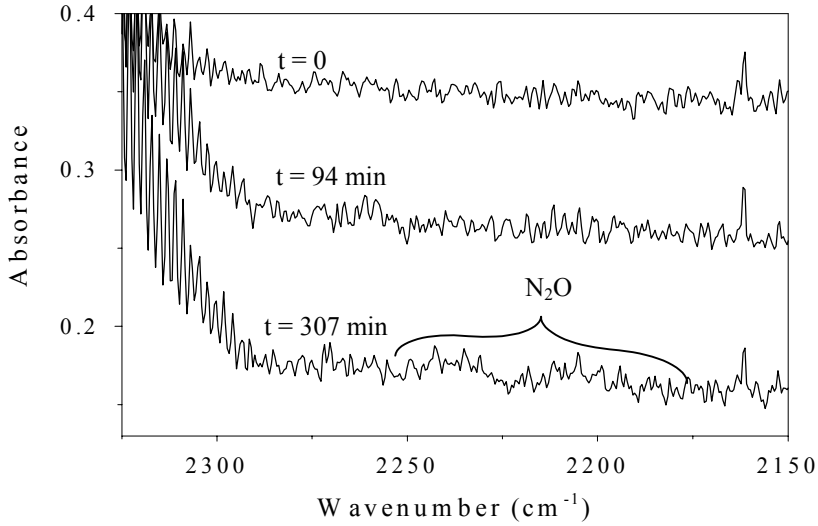

Figure 3.II.3. FTIR spectra showing the formation of small amounts of N_2O (experiment 12).

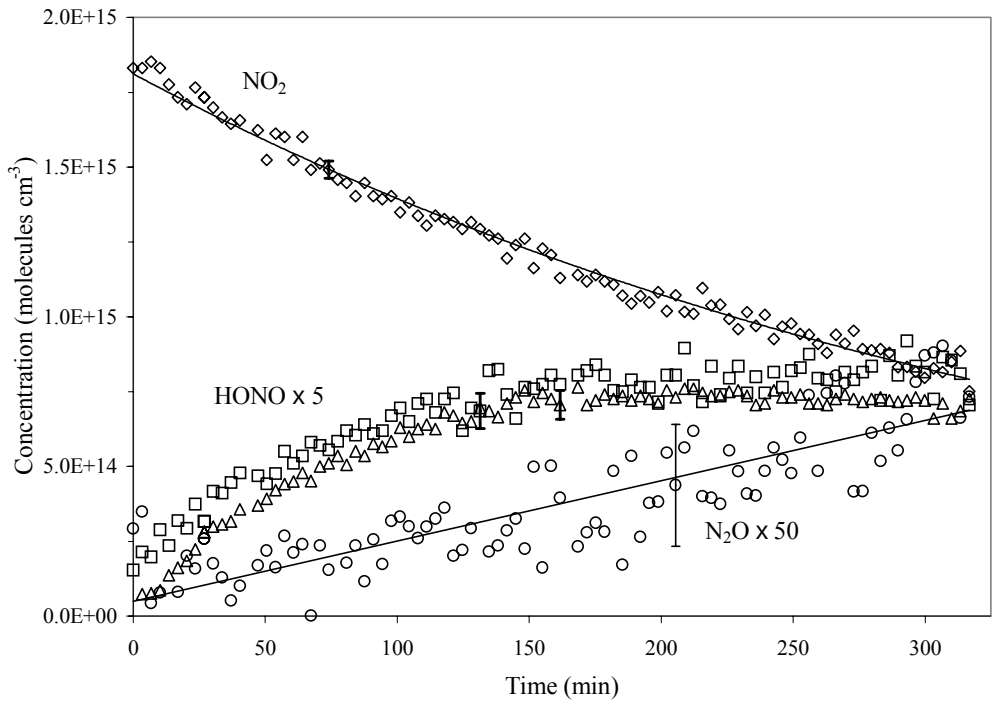

Figure 3.II.4. Time profiles of NO_2, HONO, and N_2O during hydrolysis of NO_2 (experiment 12). Diamonds (◊) represent NO_2, squares (□) represent HONO (×5) at 852 cm^{-1}, triangles (Δ) represent HONO (×5) at 1263cm^{-1}, and circles (o) represent N_2O (×50). The error bars shown are typical and represent 2σ, derived from the error reported in the least squares fitting procedure of the infrared spectra.

II.B.1. Reaction Order and Kinetics

If reaction (II.1) is an elementary process as written, its stoichiometry suggests that its rate should depend on the square of the NO_2 concentration. Several studies have shown, however, that the reaction is first order with respect to NO_2, indicating that reaction (II.1) as written is not an elementary process (*Sakamaki et al.*, 1983; *Pitts et al.*, 1984a; *Svensson et al.*, 1987; *Jenkin et al.*, 1988; *Febo and Perrino*, 1991; *Bambauer et al.*, 1994). Equation (Eq. II.1) shows the conventional, gas phase rate equation for reaction of NO_2 with H_2O:

$$Rate = \frac{-d[NO_2]}{dt} = k[NO_2]^n[H_2O]^m \qquad \text{(Eq. II.1)}$$

If the reaction is first order in NO_2, $n = 1$, a plot of $\ln[NO_2]$ versus time would be linear with slope $k[H_2O]$. A second order reaction in NO_2, $n = 2$, will have a linear plot of $[NO_2]^{-1}$ versus time. Using this rate model, variables expected to affect heterogeneous reactions, such as surface-to-volume ratio, appear in the rate constant, k.

Typical plots to determine NO_2 reaction order are shown in Figures 3.II.5(a–c) for experiments initiated at ~20%, 50%, and 80% relative humidity. The experiments initiated at ~20% and 50% relative humidity showed equally linear fits for both first- and second order plots up to 350 min, as shown in Figures 3.II.5a and 3.II.5b. These plots make it difficult to distinguish between first- and second order with respect to NO_2. In contrast, experiments initiated at ~80% relative humidity showed reasonably linear second order plots for only a limited time, deviating drastically from linearity after ~100–200 min, while first order plots remained linear for the entire extent of the reaction, up to 800 min (13 h). Figure 3.II.5c shows an example of the deviation from second order in NO_2 after ~150 min. The results of these studies suggest that heterogeneous hydrolysis of NO_2 can be equally well matched by first or second order kinetics at shorter reaction times where secondary reactions are less important.

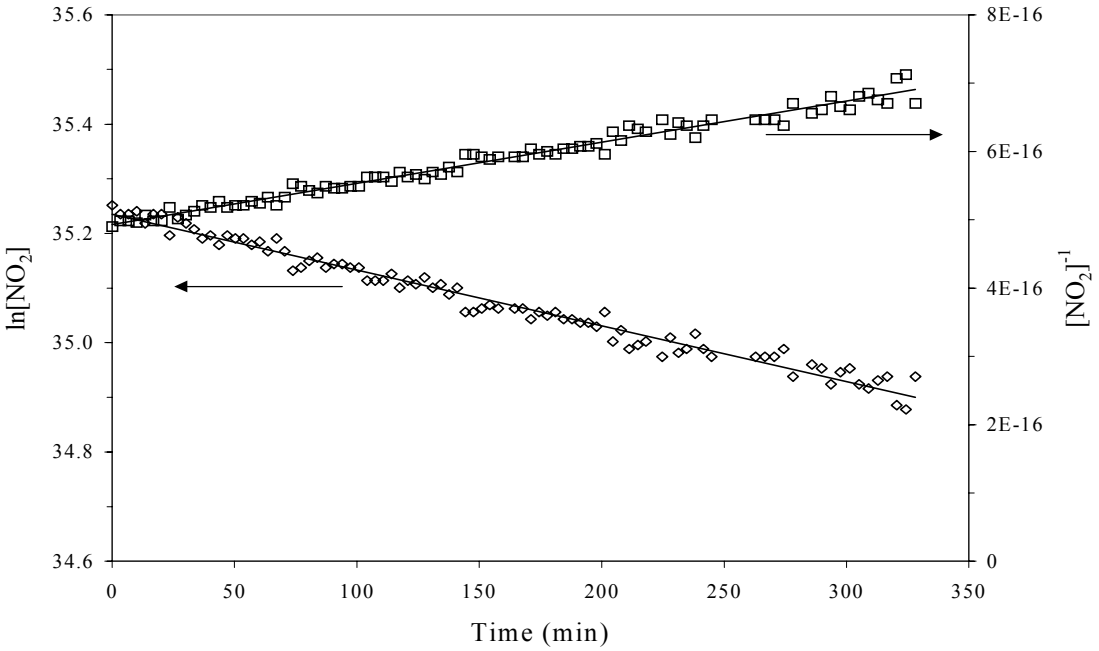

Figure 3.II.5a. Plots to determine reaction order with respect to NO_2 for a typical low relative humidity experiment (#6). Initial conditions for this experiment were $[NO_2]_0 = 1.9\times10^{15}$ molecules cm^{-3} and 20.3% relative humidity (1.40×10^{17} molecules cm^{-3} at 23°C).

Another method of investigating the reaction order in NO_2 is to plot the initial rate of HONO formation against $[NO_2]_o$ or $[NO_2]_o^2$. For the range of NO_2 concentrations covered in these experiments, our data plotted in this manner could again be equally well fit to either first or second order kinetics.

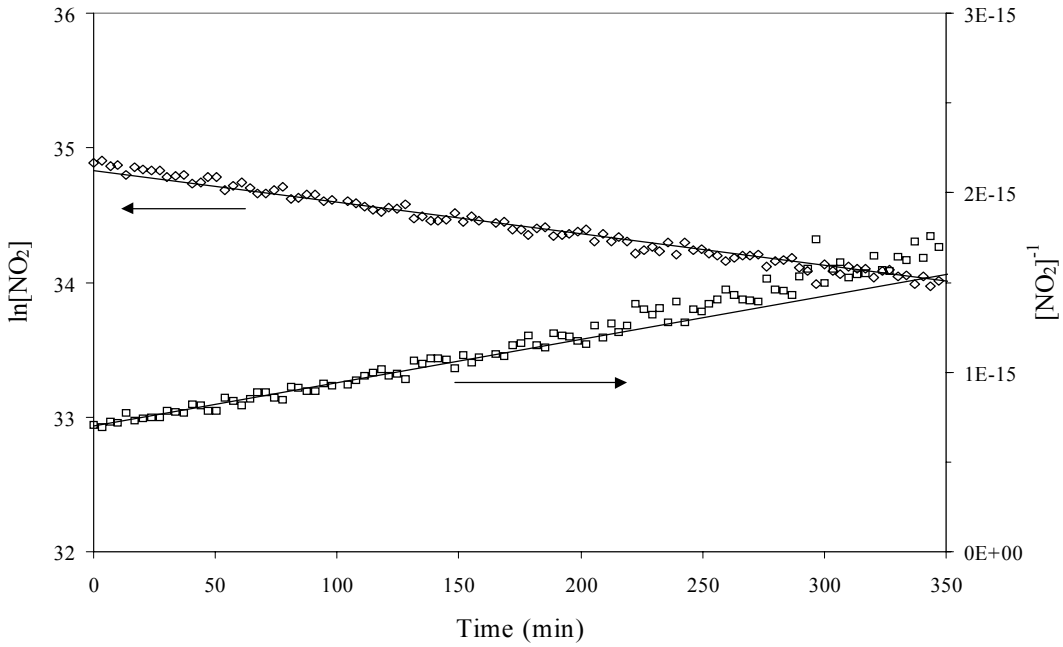

Figure 3.II.5b. Plots to determine reaction order with respect to NO_2 for a typical medium relative humidity experiment (#11). Initial conditions for this experiment were $[NO_2]_o = 1.4\times10^{15}$ molecules cm^{-3} and 47.9% relative humidity (3.49×10^{17} molecules cm^{-3} at 24°C).

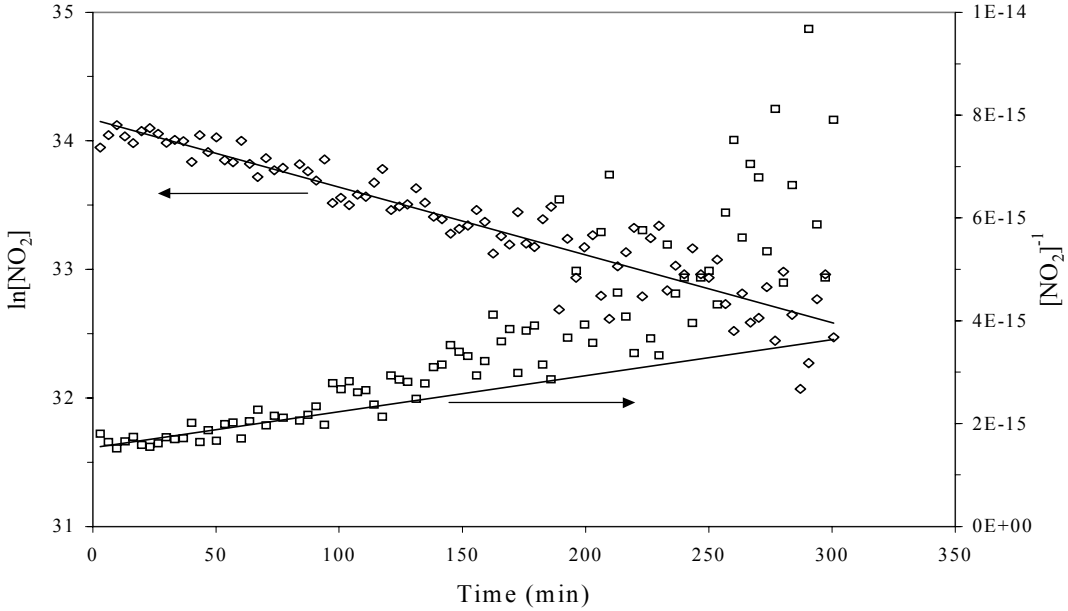

Figure 3.II.5c. Plots to determine reaction order with respect to NO_2 for a typical high relative humidity experiment (#19). Initial conditions for this experiment were $[NO_2]_o = 1.5\times10^{15}$ molecules cm^{-3} and 76.4% relative humidity (4.96×10^{17} molecules cm^{-3} at 22°C).

The additional experiment performed in the 561 L chamber resulted in equally good fits to first- and second order NO_2 kinetics, as shown in Figure 3.II.6. Although the relative humidity in this experiment is the same as that shown in Figure 3.II.5b, the surface area to volume ratio of the larger chamber was much lower, thus a complete comparison of the kinetics for the two chambers is not possible. A first order NO_2 decay constant of $(1.2 \pm 0.1)\times10^{-5}$ s^{-1} was obtained for the experiment in the larger chamber. Again, first order dependence on $[NO_2]$ indicates that reaction (II.1) as written, is not an elementary process.

The dependence of the rate on the initial H_2O concentration was examined by plotting the first order decay rate constants of NO_2 from each experiment versus initial H_2O concentration. The first order decay rate constants for NO_2, $k'=k[H_2O]^m$ (Eq. II.1), were obtained from the slopes of the plots of $\ln[NO_2]$ versus time at early times when $[H_2O]$ was essentially constant. Figure 3.II.7 shows this plot, in which the values of k' have an obvious dependence on the water concentration for each experiment. This figure also shows a least squares fit to the data from all 22 experiments (all symbols) and a fit in which the data points with large amounts of scatter (open symbols) have been omitted. The experiments represented by open symbols had large amounts of scatter in their time profiles, presumably due to the fast reaction times at these higher water vapor concentrations, resulting in large errors in their calculated rate constants. However, the trend is clear in both cases that the reaction is enhanced by water vapor. Table 3.II.3 shows the values of k' for all experiments and the averages at different relative humidities. To determine the relationship between k' and $[H_2O]$, the data points in Figure 3.II.7 were compared. The values of k' in the experiments performed at ~50% relative humidity, $(3.4–3.7) \times 10^{17}$ molecules cm^{-3} H_2O, are ~2.7 times larger than those performed at ~20% relative humidity, $(1.4–1.5)\times10^{17}$ molecules cm^{-3} H_2O (~2.4 times lower $[H_2O]$), suggesting an approximately linear relationship between the rate and $[H_2O]$, i.e., indicating that reaction (II.1) is approximately first order with respect to H_2O under these conditions. Reaction orders of unity with respect to water in the hydrolysis of NO_2 have also been found by Sakamaki et al. (1983), Pitts et al. (1984a), Svensson et al. (1987), and Jenkin et al. (1988). The values of k' at ~80% relative humidity are higher than expected from the increase in $[H_2O]$; an increase of $[H_2O]$ by a factor of $\sim1.6 \pm 0.1$ leads to an average increase in k' by a factor of $\sim2.5 \pm 1.0$. However, given the scatter in the data at high relative humidities, this increase in rate may be within experimental error of that expected.

Overall bimolecular rate constants for reaction (II.1) were calculated for each experiment from the corresponding first order rate constants, k', by dividing k' by the initial water vapor concentration, $[H_2O]_0$. $[H_2O]_0$ was assumed to be constant in determining values of k', since they were calculated from the linear portion of the data, i.e., earlier times in Figures 3.II.5(a–c). The resulting bimolecular rate constants for reaction (II.1) are included in Table 3.II.3, with an average of $k_1 = (1.8 \pm 1.6)\times10^{-22}$ cm^3 $molecule^{-1}$ s^{-1} (2σ).

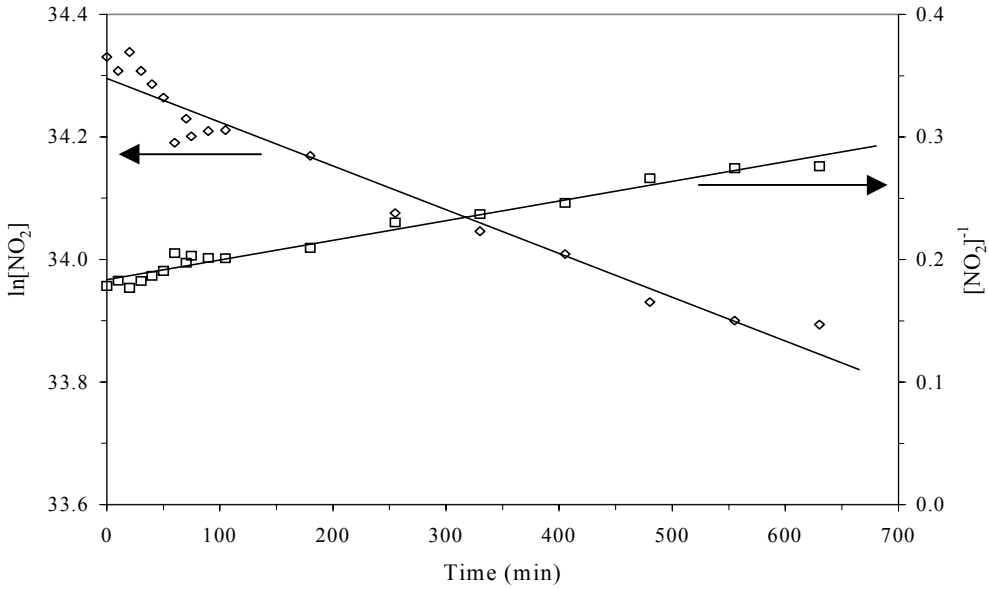

Figure 3.II.6. Plots of $\ln[NO_2]$ and $[NO_2]^{-1}$ versus time for the hydrolysis experiment performed in the 561 L chamber. Initial conditions were $[NO_2]_0 = 8.1\times10^{14}$ molecules cm^{-3} and 49.9% relative humidity (3.8×10^{17} molecules cm^{-3} H_2O at 25°C).

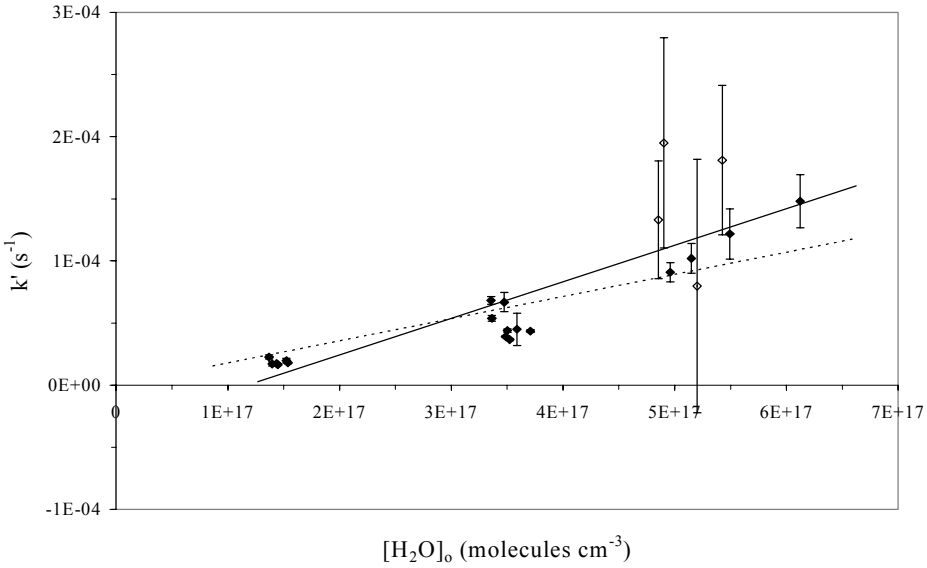

Figure 3.II.7. Plot of the decay constant of NO_2 versus initial $[H_2O]$. The solid line is a least squares fit of all data points, while the dotted line fits the data from experiments which had the least scatter in the time profiles (see text). Open symbols (◊) indicate the experiments with a high degree of scatter in time profiles. Closed symbols (♦)are experiments with low scatter in time profiles.

Table 3.II.3. Summary of Rate Constants for NO_2 Hydrolysis Experiments.

Exp.	k' (10^{-6} s^{-1} ± 2σ[a])	k (10^{-22} cm^3 $molecule^{-1}$ s^{-1})
Low Relative Humidity: (1.4–1.5) × 10^{17} molecules cm^{-3}		
1	0.23 ± 0.02	1.65 ± 0.12
2	0.20 ± 0.02	1.29 ± 0.12
3	0.18 ± 0.01	1.16 ± 0.05
4	0.16 ± 0.01	1.13 ± 0.05
5	0.17 ± 0.005	1.20 ± 0.03
6	0.17 ± 0.01	1.22 ± 0.04
average[c]	0.19 ± 0.05	1.28 ± 0.38
Intermediate Relative Humidity: (3.4–3.7) × 10^{17} molecules cm^{-3}		
7	0.54 ± 0.02	1.60 ± 0.06
8	0.68 ± 0.03	2.03 ± 0.09
9	0.45 ± 0.01	1.25 ± 0.04
10	0.44 ± 0.01	1.25 ± 0.04
11	0.39 ± 0.01	1.12 ± 0.02
12	0.44 ± 0.01	1.18 ± 0.03
13	0.37 ± 0.01	1.04 ± 0.03
14	0.67 ± 0.01	1.92 ± 0.02
average[c]	0.50 ± 0.24	1.42 ± 0.76
High Relative Humidity: (4.9–6.1) × 10^{17} molecules cm^{-3}		
15[b]	1.81 ± 0.6	3.3 ± 1.1
16[b]	1.95 ± 0.85	4.0 ± 1.7
17[b]	0.80 ± 0.10	1.5 ± 2.0
18[b]	1.33 ± 0.47	2.7 ± 1.0
19	0.91 ± 0.08	1.8 ± 1.6
20	1.22 ± 0.20	2.21 ± 0.37
21	1.48 ± 0.21	2.42 ± 0.35
22	1.02 ± 0.12	1.98 ± 0.23
average[c]	1.32 ± 0.83	2.50 ± 1.64
		1.8 ± 1.6 overall average

[a] Errors (2σ) were derived from the error in the slope of the least squares fits.
[b] These experiments had a high degree of scatter in the time profiles resulting in larger errors in rate constant calculations.
[c] The averages and 2σ standard deviations were calculated.

II.B.2. Dependence of Kinetics on Surface Area-to-Volume Ratio

Svensson et al. (1987) developed a rate equation for the heterogeneous hydrolysis of NO_2 in laboratory studies which is dependent upon the ratio of surface area to volume, equation (Eq. II.2):

$$\frac{-d[NO_2]}{dt} = \left[\left(\frac{S}{V}\right)(5.6 \pm 0.9)\times 10^{-9} + (2.3 \pm 6.5)\times 10^{-9}\right][NO_2][H_2O] \qquad \text{(Eq. II.2)}$$

where the surface area-to-volume ratio, S/V, is in units of m^{-1} and the overall bimolecular rate constant, k_1, given by equation (Eq. II.3), is in units of ppm^{-1} min^{-1}:

$$k_1\ (ppm^{-1}\ min^{-1}) = \left(\frac{S}{V}\right)(5.6 \pm 0.9)\times 10^{-9} + (2.3 \pm 6.5)\times 10^{-9} \qquad \text{(Eq. II.3)}$$

The experimental apparatus used in the studies described here had a surface-to-volume ratio of S/V = 40 m^{-1}. Based on this S/V, the calculated rate constant is $k_1 = (2.3 \pm 0.4)\times 10^{-7}$ ppm^{-1} min^{-1} or $k_1 = (1.5 \pm 0.3)\times 10^{-22}$ cm^3 $molecule^{-1}$ s^{-1}, in good agreement with the rate constant of $(1.8 \pm 1.6)\times 10^{-22}$ cm^3 $molecule^{-1}$ s^{-1} obtained from the experiments in the 32.0 m long path cell. The additional experiment performed in the 561 L chamber, S/V = 8 m^{-1}, had a first order NO_2 decay constant of $(1.2 \pm 0.1)\times 10^{-5}$ s^{-1} (2σ) with an initial water vapor concentration of $[H_2O]_0 = 3.8\times 10^{17}$ molecules cm^{-3}, corresponding to an overall bimolecular rate constant of $k_1 = (3.2 \pm 0.3)\times 10^{-23}$ cm^3 $molecule^{-1}$ s^{-1} (2σ). For S/V = 8 m^{-1}, equation (Eq. II.3) predicts $k_1 = (4.7 \pm 0.1)\times 10^{-8}$ ppm^{-1} min^{-1} or $k_1 = (3.2 \pm 0.9)\times 10^{-23}$ cm^3 $molecule^{-1}$ s^{-1}, in excellent agreement with that from the experiment performed in the larger chamber. This suggests the potential to parameterize this S/V dependence in airshed models, discussed in Section V.

In short, we have confirmed that the kinetics of the heterogeneous hydrolysis of NO_2 in our systems are generally consistent with others reported in the literature. However, our data suggest that at least in the early stages of the reaction it may be second order in NO_2 rather than first order. A possible cause of the apparent NO_2 reaction order change is reaction (II.2) or (II.3):

$$HONO\ (g) + HONO\ (g) \rightarrow NO_2 + NO + H_2O \qquad \text{(II.2)}$$

$$HONO\ (g) + HNO_3\ (surface) \rightarrow 2\ NO_2 + H_2O \qquad \text{(II.3)}$$

Reaction (II.2) may be important during NO_2 hydrolysis, especially when the HONO concentration reaches a maximum, at 50 – 300 min in these experiments depending on the relative humidity. The self-reaction of HONO to form NO_2, reaction (II.2), would cause the decrease of NO_2 to appear slower. Similarly, reaction (II.3) would regenerate NO_2 and make the heterogeneous hydrolysis appear slower. Note that (II.3) is the reverse of (II.1), suggesting that

the reaction may approach equilibrium at longer reaction times. Investigations of the mechanism were continued and are discussed in detail in Section III.

II.B.3. Product Yields – Nitrous Acid and Nitrous Oxide

The formation of HONO was observed in all experiments. An increase followed by a decrease in the HONO concentration was observed in those experiments followed to longer times, ≥400 min. The time at which the maximum yield of HONO occurred varied with the initial water concentration, consistent with a slower reaction rate at lower [H_2O]. For example, the experiments performed at the lowest water concentrations, ~20% relative humidity, showed maximum HONO concentrations between ~250 min and 400 min. The yield of HONO in these experiments, defined by 2×Δ[HONO]/Δ[NO_2] according to the stoichiometry of reaction (II.1), verified by Febo and Perrino (1991), was 10–20%. Experiments at intermediate [H_2O], ~50% relative humidity, had earlier and larger maximum HONO concentrations, with yields of 15–40% after 100–300 min. The highest [H_2O] experiments had maximum [HONO] at the earliest times, 50–100 min, but the yield was often lower relative to 50% relative humidity experiments at these times, at 10–20%. This indicates that HONO was being removed by secondary reactions.

The production and decay of HONO from NO_2 hydrolysis can be described by reactions (II.4) and (II.5), respectively:

$$2\ NO_2 + H_2O \xrightarrow{k_a} HONO + HNO_3 \qquad \text{(II.4)}$$

$$HONO \xrightarrow{k_b} \text{Products} \qquad \text{(II.5)}$$

The integrated rate expression developed from reactions (II.4) and (II.5) is given by equation (Eq. II.4):

$$[HONO]_t = \frac{[NO_2]_0}{k_b - k_a}\left(e^{-k_a t} - e^{-k_b t}\right) \qquad \text{(Eq. II.4)}$$

in which k_a is the rate constant describing HONO formation and k_b is that for HONO decay (*Wiesen et al.*, 1995). The time profiles of HONO were fitted to equation (Eq. II.4) using nonlinear regression. Figure 3.II.8 shows three such fits for experiments 15, 19, and 22, in which the rate of HONO formation and the HONO yield increase with initial NO_2 concentration. The values of k_a were also obtained from the slopes of plots ln[HONO] against time at early times, <45 min. These plots are shown in Figure 3.II.9 for experiments 15, 19, and 22. The slopes obtained show a linear dependence of HONO formation on $[NO_2]_0$, as shown in Figure 3.II.10. These results are consistent with the results of Wiesen et al. (1995) and verify that reaction (II.1) is first order with respect to NO_2.

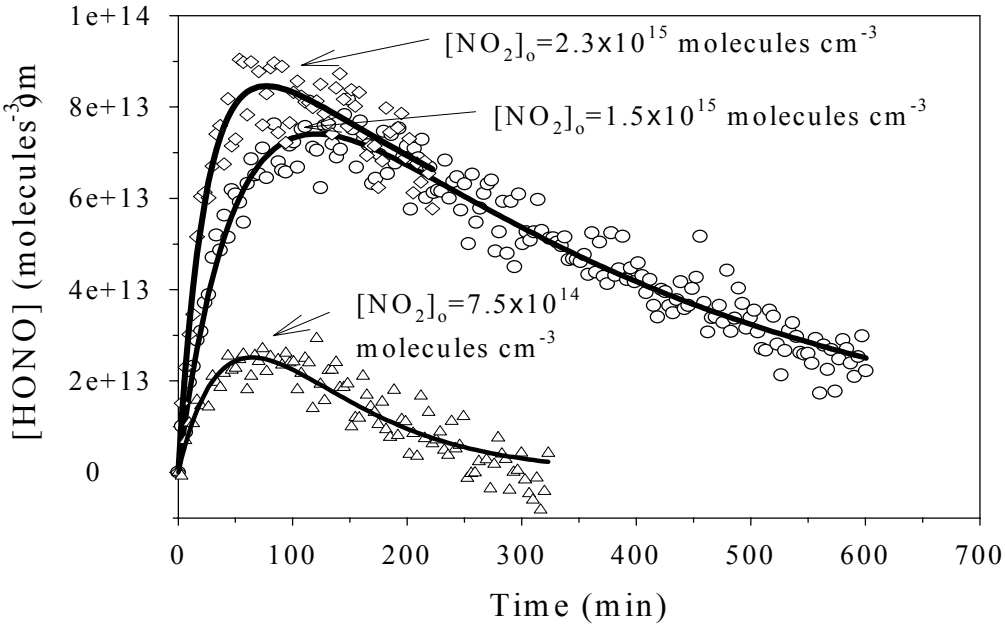

Figure 3.II.8. Plots of HONO time traces for three experiments at high water vapor concentrations (experiments 15 (Δ), 19 (O), and 22 (◊)). Solid lines represent fits to the data using equation (Eq. II.4).

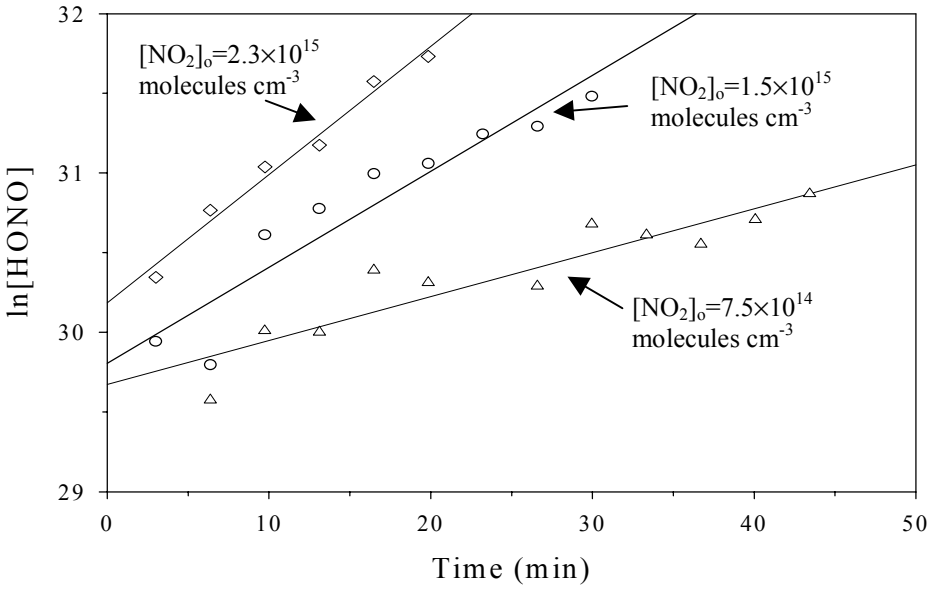

Figure 3.II.9. Plots of ln[HONO] versus time to obtain the HONO formation rate constants, k_a, from reaction (II.1) for experiments 15 (Δ), 19 (O), and 22 (◊)). The values of k_a are 4.6×10^{-4} s^{-1} (Δ), 1.0×10^{-3} s^{-1} (O), and 1.3×10^{-3} s^{-1} (◊), which show a linear dependence on the NO_2 concentration.

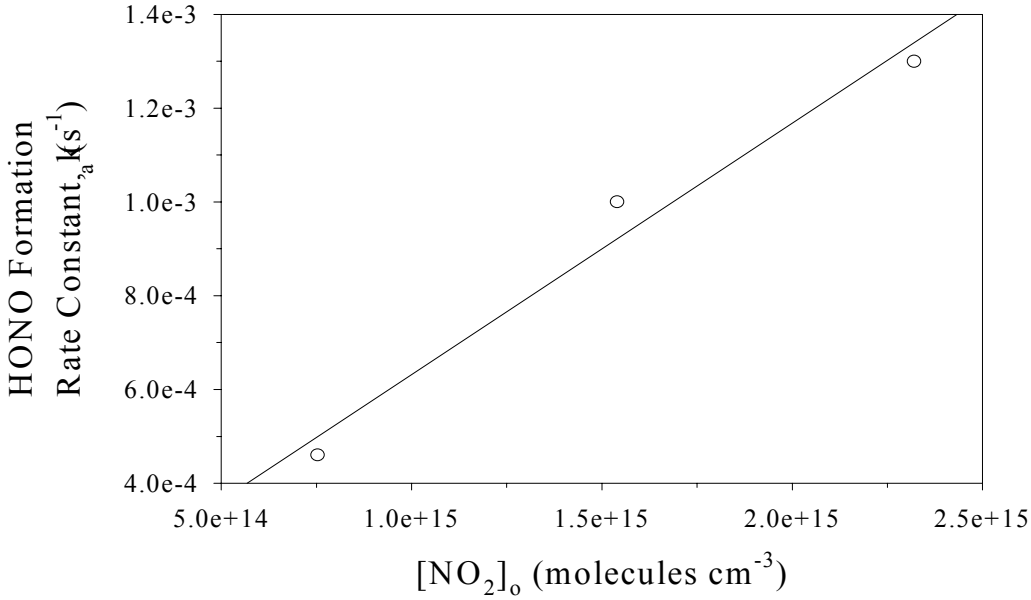

Figure 3.II.10. Plot of the HONO formation rate constant, k_a (s^{-1}), versus initial NO_2 concentration for experiments 15, 19, and 22 showing a linear dependence.

It is important to know if the decay of HONO regenerates oxides of nitrogen, e.g. NO and NO_2 via reaction (II.2). In this case, the net removal of NO_x from the atmosphere will be less than predicted from experimental studies. Although regeneration of NO_2 cannot be seen in this system due to the presence of large amounts initially, NO and other species such as N_2O can be seen.

The presence of NO (IR band centered at 1876 cm^{-1}) is difficult to observe due to the presence of the complex rotational structure of water vapor in the region 1250–1900 cm^{-1}. However, the least squares fitting procedure, described in a previous section, was used to search for NO. Several of the NO_2 hydrolysis experiments have been analyzed to date revealing NO formation, in agreement with the occurrence of reaction (II.2).

The formation of N_2O was observed in experiments in which $[H_2O]_0 \geq 3.5\times10^{17}$ molecules cm^{-3}, i.e., the ~50% and 80% relative humidity experiments. This N_2O formation is in agreement with Wiesen et al. (1995) and Kleffmann et al. (1998a,b) who reported N_2O formation during hydrolysis of NO_2 on the acidic surfaces of quartz and glass reaction chambers. Although the internal cell walls in the 32.0 m long path cell were not directly treated with acid, the surfaces were likely to be acidic due to the formation of nitric acid in this reaction, which remains adsorbed to the cell walls.

The yield of N_2O was defined by $2\times\Delta[N_2O]/\Delta[NO_2]$ due to the need for two nitrogen atoms to form one molecule of N_2O. The N_2O yield after 400 min was ≤ 2% in the experiments at the lowest water vapor concentrations. The detection limit for N_2O in the 32.0 m long path cell was determined to be 2.7×10^{12} molecules cm^{-3} N_2O. The formation of N_2O above this

detection limit in experiments with $[H_2O]_0 \geq 3.5\times10^{17}$ molecules cm^{-3} was continuous, as shown in Figure 3.II.4. N_2O yields were 1–9%, with larger yields observed in experiments at higher initial water vapor concentrations. This is shown in Figure 3.II.11 in which a plot of N_2O formation versus time is shown for three experiments with similar initial NO_2 concentrations, but varying initial relative humidities. The formation of N_2O is seen to increase with increasing initial water concentration. Figure 3.II.12 shows a plot of N_2O concentration versus time for experiments 15, 19, and 22, indicating that the N_2O formation rate also increases with the initial NO_2 concentration.

Thus, HONO decays in experimental systems, and likely in the atmosphere as well, in part to NO and N_2O. The latter is unreactive in the troposphere and hence this N_2O formation represents a permanent tropospheric "sink" for HONO and NO_x.

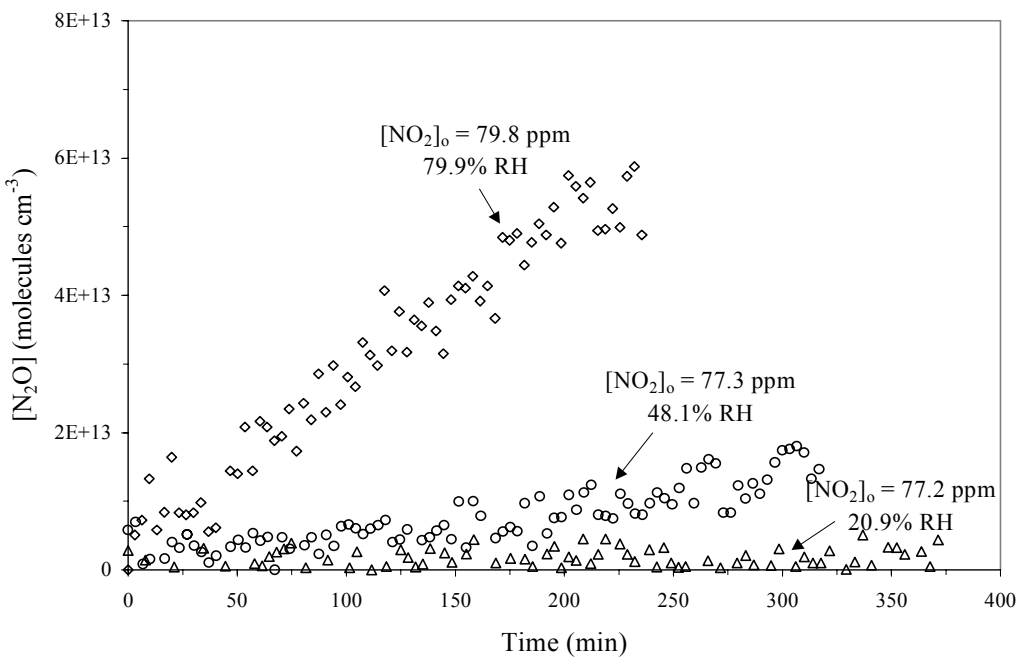

Figure 3.II.11. Nitrous oxide formation versus time for experiments 5 (Δ), 12 (O), and 20 (◊) showing the dependence of N_2O formation upon water concentration.

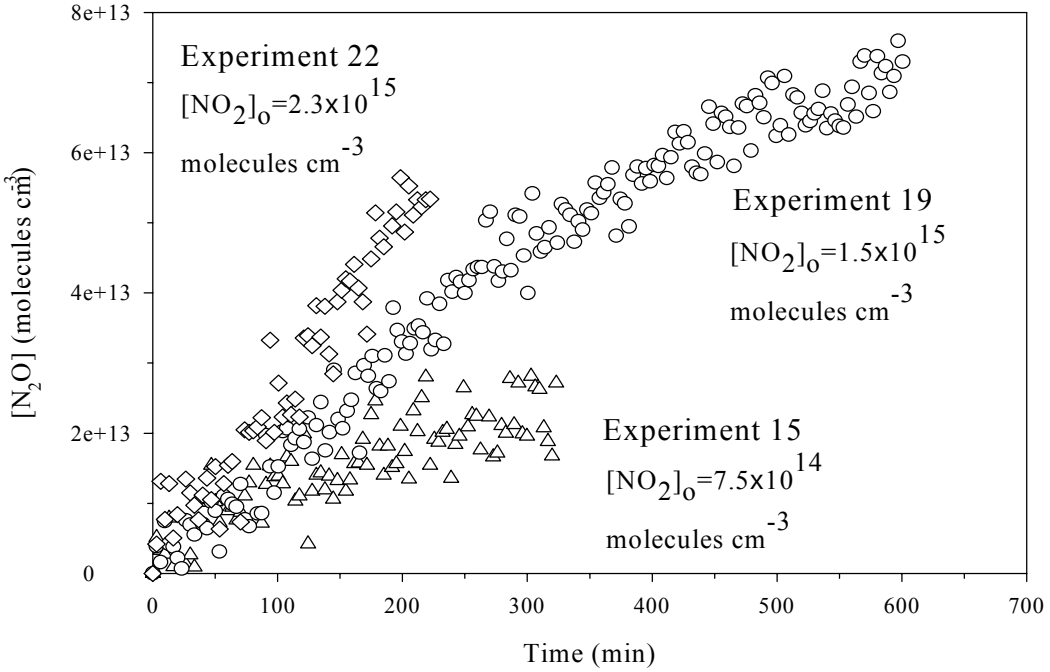

Figure 3.II.12. Plots of the time profiles of N_2O in experiments 15 (Δ), 19 (O), and 22 (◊)) showing the increase in the rate of N_2O formation with $[NO_2]_0$.

III. MECHANISM OF HONO FORMATION

As discussed in the previous section, the hydrolysis of NO_2 on surfaces explains the formation of HONO observed when NO_2 was injected into large environmental chambers in the presence of water vapor (*Sakamaki et al.*, 1983; *Pitts et al.*, 1984a; *Svensson, et al.*, 1987; *Jenkin et al.*, 1988; *Bambauer et al.*, 1994; *Mertes and Wahner*, 1995; *Kleffmann et al.*, 1998a,b).

$$2\ NO_2 + H_2O \xrightarrow{surface} HONO + HNO_3 \qquad \text{(III.1)}$$

While HONO has been observed in the gas phase, the corresponding amount of HNO_3 shown in reaction (III.1) has not. The reason has been proposed to be that HNO_3, which is notoriously "sticky," remains adsorbed on the surface. This is consistent with the observations of nitrate in washings of the surface post-reaction (*Svensson et al.*, 1987), but direct observations of HNO_3 during the reaction have not been reported. The following sections describe several experiments designed to observe HNO_3 adsorbed on glass surfaces.

Silica surfaces such as powders or porous glass are known to hold adsorbed water readily because of their polar surface –Si-OH groups (*Kiselev and Lygin*, 1975). While this adsorbed water can be removed by heating under vacuum, and indeed the surface can be dehyroxylated at sufficiently high temperatures, heating at lower temperatures leaves adsorbed water on the surface. As a result, such surfaces can be used as supports for water to study surface reactions involving water, such as reaction (III.1).

III.A. N_2O_4 Enhancement on Porous Glass at Room Temperature: A Key Intermediate in Heterogeneous Hydrolysis of NO_2?

We report here FTIR studies of the uptake of NO_2 onto porous glass at room temperature and show that NO_2 exists preferentially in the form of the dimer, N_2O_4, on the surface compared to the gas phase. In the presence of water on the surface, surface-adsorbed HNO_3 is formed and detected directly by FTIR.

Figure 3.III.1a shows the gas phase spectrum when 2.9 Torr NO_2 is added to the cell, along with N_2, to a total pressure of 508 Torr at room temperature. Strong peaks in the 1600 - 1650 cm^{-1} region are due to NO_2. The smaller peak at ~1750 cm^{-1} is due to the dimer, N_2O_4, which is in equilibrium with NO_2. Using the equilibrium constant (*DeMore et al.*, 1997) K_p = 2.5 x 10^{-19} cm^3 $molecule^{-1}$ for the reaction

$$2\ NO_2 \leftrightarrow N_2O_4 \qquad \text{(III.2,III.-2)}$$

the concentrations of N_2O_4 and NO_2 under these conditions are 2×10^{15} and 9×10^{16} molecules cm^{-3}, respectively.

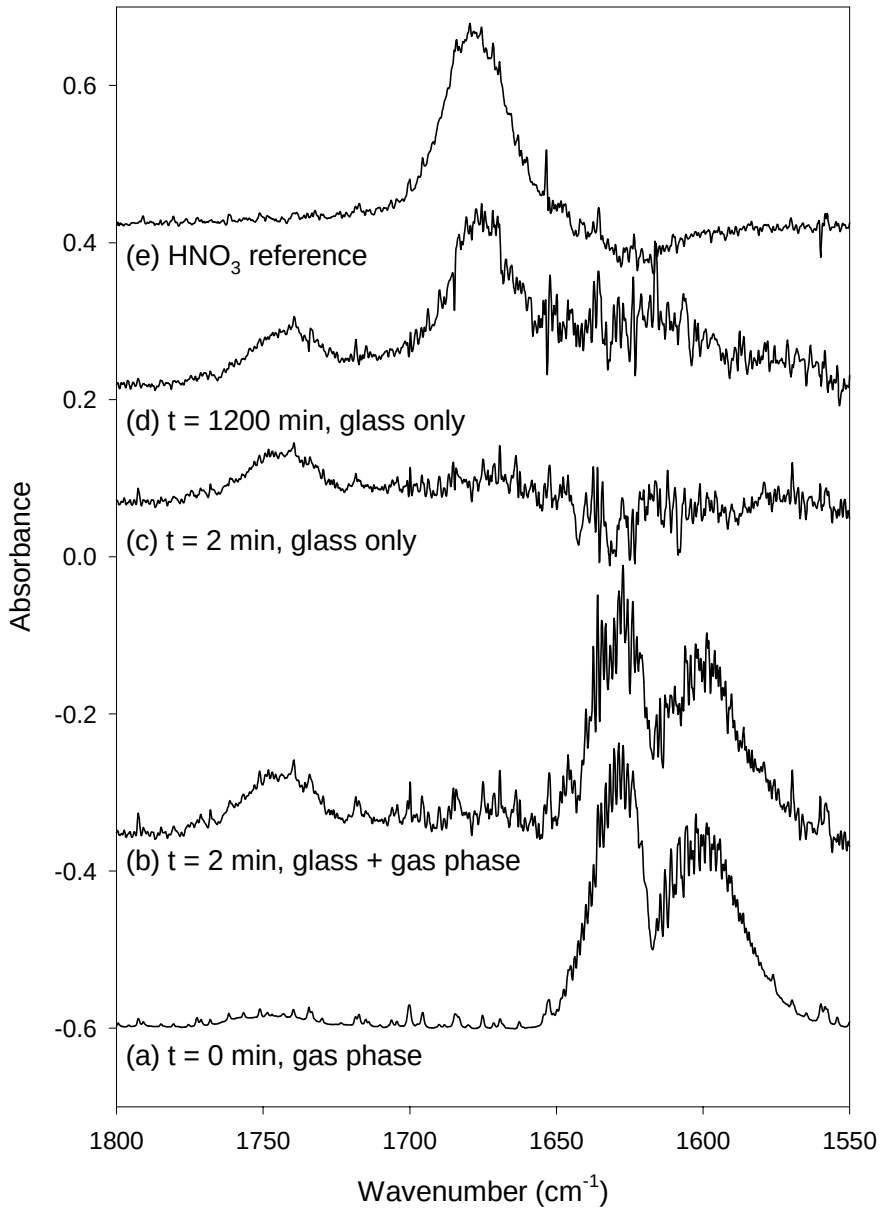

Figure 3.III.1. FTIR spectra of 2.9 Torr NO_2 in N_2 (total pressure 508 Torr) (a) gas phase only, (b) gas phase plus porous glass and surface-adsorbed species, (c) subtracted spectrum (b) - (a) showing the spectrum due to the adsorbed species, and (d) same as (c) but 20 hours later; (e) Reference spectrum of HNO_3 on porous glass; 0.57 Torr HNO_3 was added to the cell for 5 min. and then pumped away before recording the spectrum. The porous glass had been heated under vacuum before the exposure to NO_2.

Figure 3.III.1b shows the spectrum when the porous glass with the surface-adsorbed species is lowered into the infrared beam. This represents the sum of the gas phase and surface-adsorbed species on the porous glass. Figure 3.III.1c shows the difference between Figures 3.III.1b and 3.III.1a, i.e. the spectrum of the porous glass and the adsorbed species present at approximately the same time that the gas phase spectrum in Figure 3.III.1a was obtained. The band due to adsorbed N_2O_4 at 1740 cm^{-1} is clearly seen, while that due to NO_2 is not evident. The slightly negative bands in the NO_2 region reflect imperfect subtractions which are common for strong bands, particularly in regions where water vapor absorptions also occur as is the case for this region; there is also a small loss (~5%) of NO_2 from the gas phase between the times the spectra in Figures 3.III.1a and 3.III.1b were taken.

Figure 3.III.1d shows the spectrum of the porous glass and adsorbed species 20 hours later. There is a new absorption centered at ~1680 cm^{-1}. The assignment of this band to HNO_3 is confirmed by a reference spectrum (Fig. 3.III.1e) in which a clean plate of porous glass was exposed to gaseous HNO_3 for 5 min. The gaseous HNO_3 was pumped away before the reference spectrum was taken.

Figure 3.III.2 shows the results of a similar experiment but where the porous glass plate had been left exposed to room air overnight and was then used without prior heating. In room air, the porous glass takes up large amounts of water. For example, a peak at 5260 cm^{-1} was observed due to surface adsorbed water (*Kiselev and Lygin*, 1975) for this sample, but not for that used for the experiments in Figure 3.III.1. Figure 3.III.2a shows the spectrum of the gas; Figure 3.III.2b that of the gas plus the porous glass; and Figure 3.III.2c the difference, all recorded immediately after introduction of NO_2 into the cell. In contrast to the relatively "dry" porous glass in Figure 3.III.1c, the HNO_3 absorption is much larger than that of N_2O_4 on the surface, suggesting that the reaction with water on the surface to form HNO_3 has occurred even at the shortest reaction times.

In the gas phase, N_2O and NO were observed as reaction products under all conditions and in the "wet" case, HONO was also observed. For example, Figure 3.III.3 shows the gas phase spectrum in the 2200 cm^{-1} region taken at about the same time as that in Figure 3.III.1d. Superimposed on the narrow rotational bands of CO_2 (due to changes in purging of the air in the light beam) is a set of broad peaks, which can be seen by comparison to a reference spectrum (shown by the heavy line) to be due to gaseous N_2O, which increases linearly with time. The concentration after 1200 min. is 2×10^{16} molecules cm^{-3}, compared to a loss of NO_2 of ~7×10^{16} molecules cm^{-3} during this period. NO first increases and then decreases, with a peak concentration of ~2.5×10^{16} molecules cm^{-3} after 200 min. and 1×10^{16} molecules cm^{-3} at 1200 min.

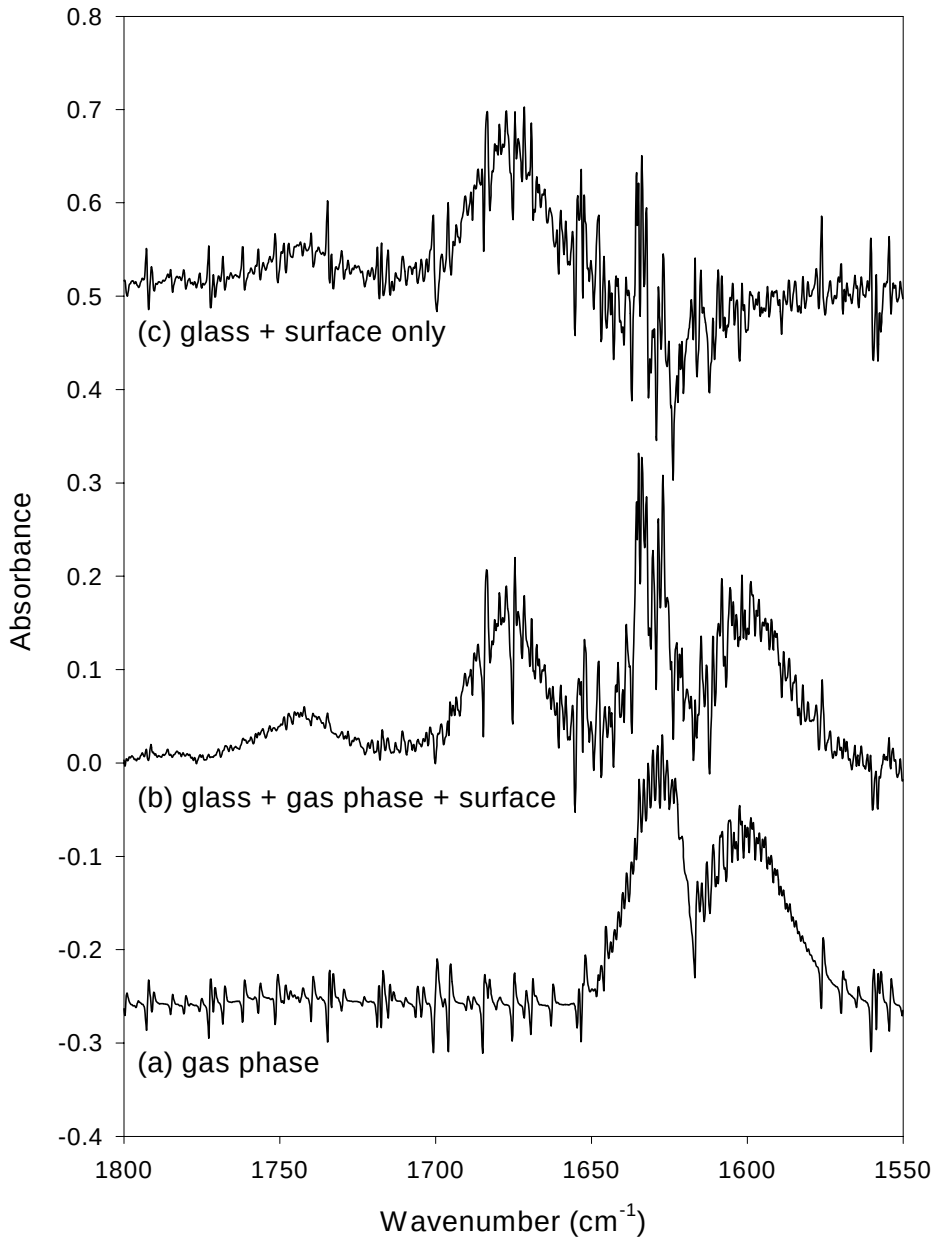

Figure 3.III.2. FTIR spectra of 3.3 Torr NO_2 in N_2 (total pressure 573 Torr) (a) gas phase only, (b) gas phase plus porous glass and surface-adsorbed species, (c) subtracted spectrum (b) - (a) showing the spectrum due to the adsorbed species. The porous glass was not heated to remove adsorbed water prior to exposure to NO_2.

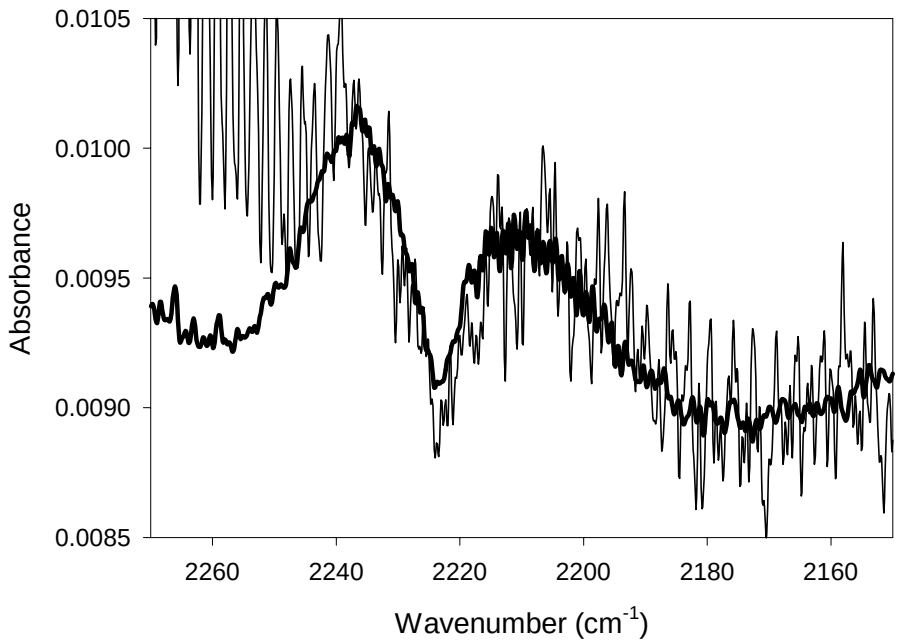

Figure 3.III.3. Gas phase spectrum taken under same experimental conditions as Fig. 3.III.1d. The heavy line is a reference spectrum of gas phase N_2O. Other absorptions are due to CO_2 outside the cell.

Figure 3.III.4 shows the gas phase spectrum in the 1250 cm^{-1} region during the experiment using "wet" glass shown in Figure 3.III.2. When the peak due to gaseous N_2O_4 is subtracted, a small band at 1263 cm^{-1} is detectable, which by comparison to a reference spectrum (*Barney et al.*, 2000b; shown by the heavy line) is due to gaseous HONO at a concentration of ~ 1 x 10^{15} cm^{-3}. In experiments where the porous glass had been heated under vacuum to remove surface water prior to introducing NO_2, gas phase HONO was not observed, even at similar levels of NO_2 loss. The NO and N_2O concentrations measured at these short reaction times were ~3 x 10^{16} cm^{-3} and 5 x 10^{15} cm^{-3}, respectively, and hence were again the major gas phase products.

In short, when water is present on the porous glass surface, NO, N_2O and HONO are formed at the same time that HNO_3 is generated on the surface. It should be noted that this chemistry is likely occurring on all of the surfaces of the reaction cell, not just the porous glass surface. However, "blank" runs in which NO_2 was followed with time in the cell in the absence of the porous glass showed that the loss of NO_2 was much smaller (~7% compared to 52% loss over 200 min), indicating that most of the chemistry observed was heterogeneous.

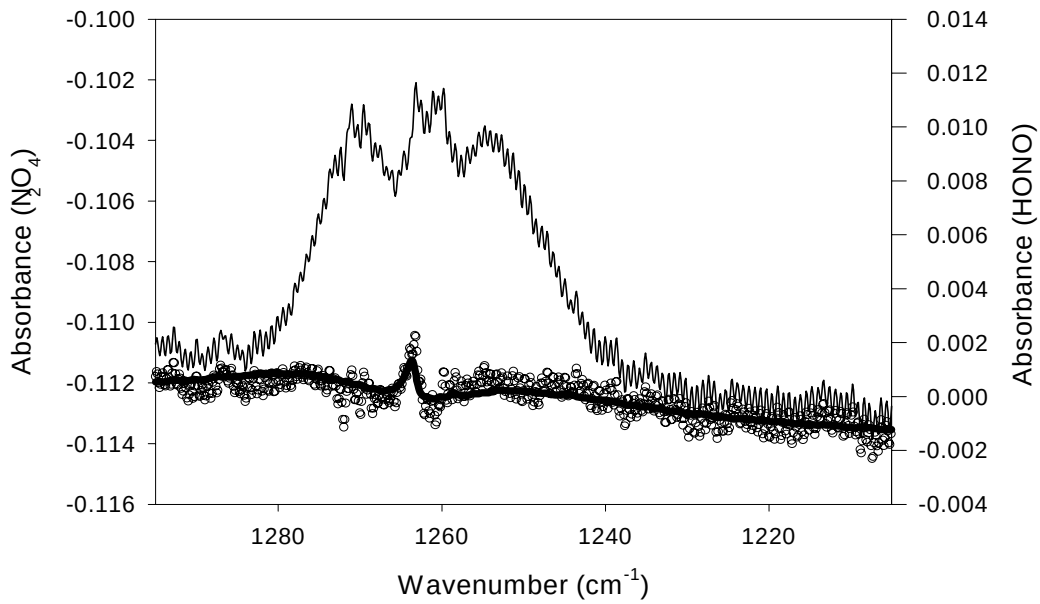

Figure 3.III.4. Gas phase spectrum taken under the same experimental conditions as in Fig. 3.III.2. The open circles show the spectrum remaining after the contribution of N_2O_4 has been subtracted out and the heavy line is a reference spectrum of gaseous HONO.

III.A.1. Dependence on Surface Water Content

Figures 3.III.5 and 3.III.6 show the time dependence of the gas-phase species observed in the porous glass cell under both wet and dry conditions. In Figure 3.III.5 the decay of NO_2 on porous glass under dry (a) and wet (b) conditions is compared to the decay in a "blank" experiment, where NO_2 is added to a similarly prepared cell but without the porous glass present. In the dry case (Fig. 3.III.5a), the NO_2 uptake is much larger when the porous glass is present indicating that most of the chemistry takes place on the porous glass surface. In the wet case (Fig. 3.III.5b), there is little difference in uptake. Sufficient water is present on the porous glass so the pores have become filled such that the internal surfaces are no longer exposed to the gas phase. With the internal surfaces unavailable, the total surface area contributed by the porous glass is only a few cm^2, thus its presence is expected to make little difference in the uptake.

Figure 3.III.6 shows the behavior of other gas-phase species. NO is the primary product, in both cases reaching a peak early in the reaction and then dropping off. N_2O increases linearly throughout the whole reaction. HONO is observed only under wet conditions. NO_2 drops off quickly at the beginning and slowly thereafter. This may reflect the surfaces becoming saturated, but may also indicate that NO_2 is regenerated through some other reaction. The production and subsequent decay of NO in the wet case suggests that it is involved in secondary chemistry, possibly reforming NO_2. Atmospheric HONO concentrations are often correlated with [NO] (*Sjodin and Ferm*, 1985; *Notholt et al.*, 1992; *Winer and Biermann*, 1994; *Calvert et al.*, 1994), therefore we investigated the possibility of N_2O_3 as an intermediate formed by the reaction of NO with NO_2.

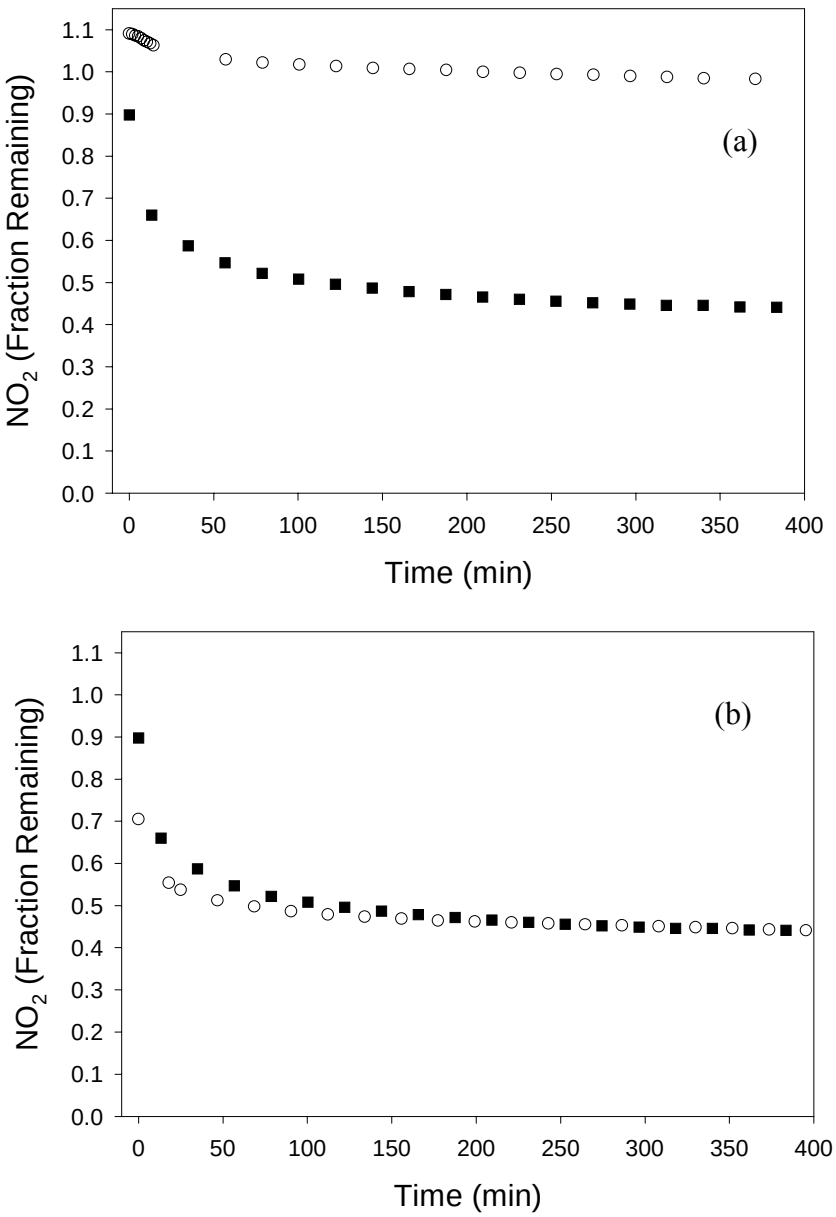

Figure 3.III.5. Uptake of NO_2 under dry and wet conditions. Squares: uptake on glass and cell walls. Circles: uptake on cell walls only. (a) Cell and glass evacuated at 280 °C for 35 minutes. (b) Cell and glass evacuated at 280 °C, then exposed to 10 Torr H_2O for 40 min. In cell-only case for (a), fraction values slightly greater than 1 reflect a small (10%) difference between pressure measurement of initial NO_2 and spectroscopic measurements.

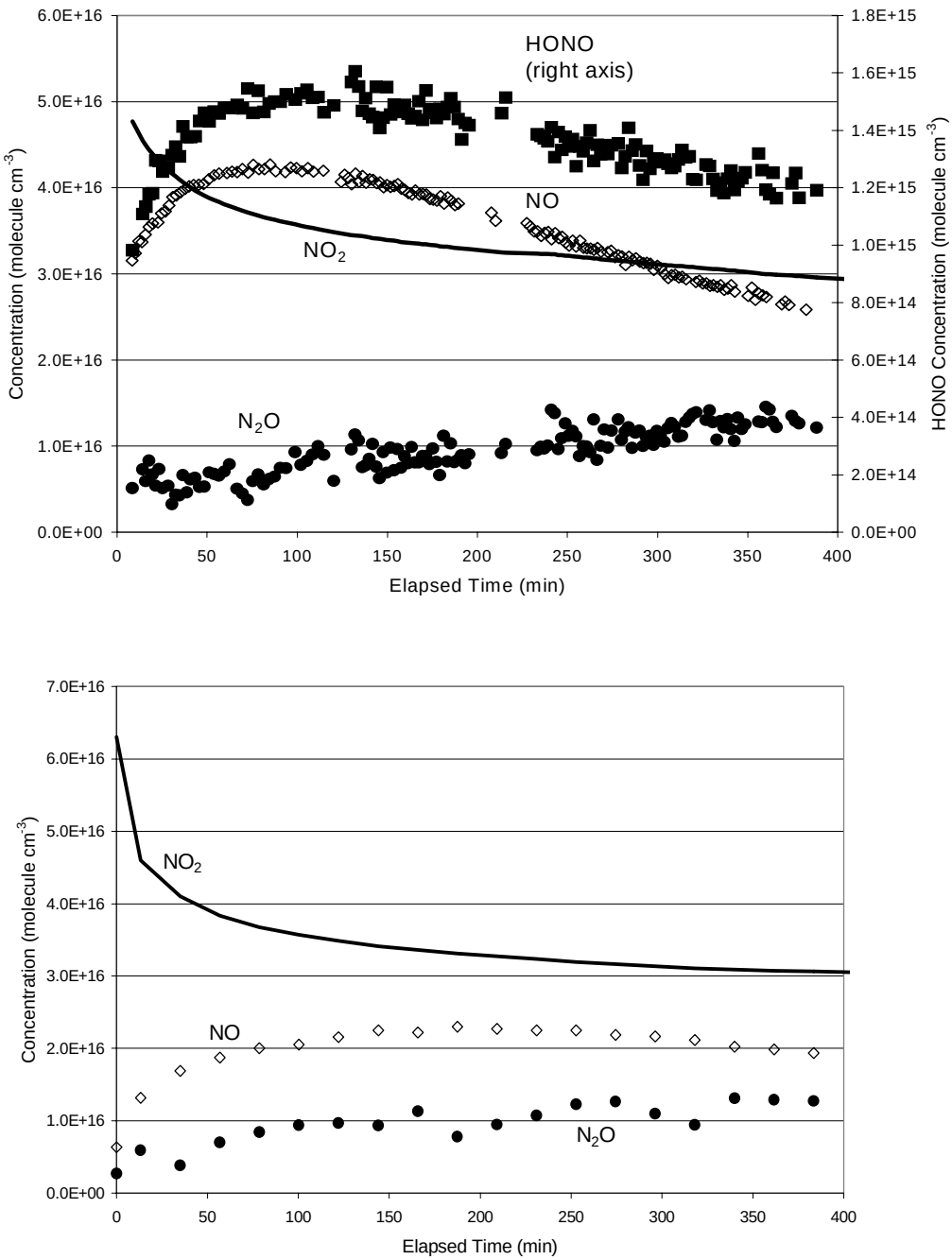

Figure 3.III.6. Gas phase species from wet (upper) and dry (lower) porous glass experiments. Heavy line: NO_2 decay. Open diamonds: NO production. Filled circles: N_2O production. Filled squares: HONO production (use right axis).

III.B. FTIR Study of N_2O_3 on Porous Glass at Room Temperature

Like N_2O_4, N_2O_3 is also a possible intermediate in the formation of nitrous acid in the reaction of NO, NO_2 and water, reaction (III.4,III.-4).

$$NO + NO_2 + H_2O \leftrightarrow 2\ HONO \qquad \text{(III.4,III.-4)}$$

Reaction (III.4) is known to be too slow in the gas phase to be responsible for any correlation between atmospheric concentrations of HONO with NO and NO_2 (*Atkinson*, 1986) but the kinetics are enhanced in the presence of surfaces (*Wayne and Yost*, 1951; *Graham and Tyler*, 1972; *Chan et al.*, 1976a,b; *Kaiser and Wu*, 1977a, *Sakamaki et al.*, 1983; *Pitts et al.*, 1984a). While N_2O_3 has been identified on gold surfaces with or without co-condensed water (*Bartram and Koel*, 1989; *Wang and Koel*, 1998; *Sato et al.*, 2000), in low-temperature matrices, (*Snyder and Hisatsune*, 1955; *Fateley et al.*, 1959; *Hisatsune et al.*, 1960; *Varetti and Pimentel*, 1971; *Nour et al.*, 1983; *Chewter et al.*, 1988; *Simon et al.*, 1992; *Horakh et al.*, 1995) in liquid xenon (*Holland and Maier*, 1983), and in the gas phase (*D'Or and Tarte*, 1953; *Bibart and Ewing*, 1974; *Kagann and Maki*, 1984), it has not, to our knowledge, been reported on surfaces at room temperature. We report here the results of FTIR studies in which N_2O_3 adsorbed on porous glass (a silica surface in the porous glass cell) has been identified at room temperature from the reaction of NO and NO_2.

III.B.1. Evidence for N_2O_3 Adsorbed on Porous Glass

Figure 3.III.7 shows infrared spectra when a set amount of NO_2 and increasing amounts of NO were added to the cell with the suspended porous glass plate. These spectra include both the gas phase and species adsorbed on the porous glass. As expected, the gas phase NO_2 and NO bands centered at 1618 and 1876 cm^{-1}, respectively, are clearly visible. The band at 1740 cm^{-1} is due to N_2O_4 (both gas phase and adsorbed) which is in equilibrium with NO_2.

A broad band at ~1677 cm^{-1}, assigned to nitric acid adsorbed on the porous glass (*Goodman et al.*, 1999; *Barney and Finlayson-Pitts*, 2000b; *Mochida and Finlayson-Pitts*, 2000), was also observed. The nitric acid is mainly due to hydrolysis of NO_2 on the hydrated silica surface (*Barney and Finlayson-Pitts*, 2000b), perhaps with some contribution from small amounts of impurity HNO_3 in NO_2. The surface-adsorbed HNO_3 decreases upon the addition of NO, due to the rapid reaction of the surface species with NO to form NO_2, (see Section III.C.) (*Mochida and Finlayson-Pitts*, 2000; *Saliba et al.*, 2000). In addition, a broad peak can be seen growing under the P-branch of the NO rotational bands.

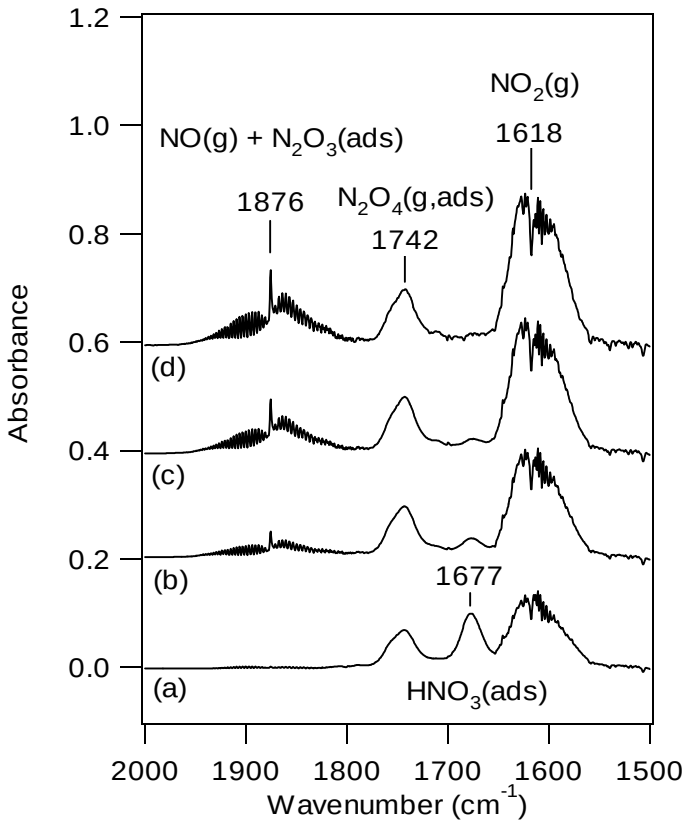

Figure 3.III.7. Infrared spectra of combined gas and adsorbed species after the introduction of (a) NO_2/N_2O_4 (1.7×10^{17} molecule cm^{-3}) into the reaction cell containing the porous glass followed by NO at concentrations of (b) 3.0×10^{17}, (c) 6.4×10^{17}, and (d) 9.5×10^{17} molecule cm^{-3}, respectively.

Figure 3.III.8a shows the combined spectrum of gases and surface-adsorbed species in the 1500-2000 cm^{-1} region for a typical experiment. Figure 3.III.8b is the spectrum of the gas phase only, obtained by lifting the porous glass sample out of the infrared beam. By subtracting from Figure 3.III.8b the contributions of NO, NO_2 and N_2O_4, a weak band centered at 1830 cm^{-1} is observed, as shown in Figure 3.III.8c. This band compares well with the ν_1 stretch of N_2O_3 in the gas phase (*D'Or and Tarte*, 1953; *Bibart and Ewing*, 1974; *Kagann and Maki*, 1984). Using $K = 0.59$ atm^{-1} for the equilibrium of NO and NO_2 with N_2O_3, and correcting the NO_2 concentration for the equilibrium amount of N_2O_4, the gas phase N_2O_3 concentration is calculated to be 7×10^{15} molecules cm^{-3}. This is in reasonable agreement with a concentration of 5×10^{15} molecule cm^{-3} calculated using the integrated band intensity reported by Kagann and Maki (1984), particularly given the relatively small amounts of N_2O_3 and the need to ratio out or subtract the contributions of the porous glass and other gases present in the cell. Another N_2O_3 peak around 1650 cm^{-1} was not clearly discernible due to the difficulty in perfectly subtracting the strong NO_2 absorption. The integrated band intensities for gas phase NO_2 (*Devi et al.*, 1982) and N_2O_3 (*Kagann and Maki*, 1984) are similar, (636 ± 25) cm^{-2} atm^{-1} and (660 ± 111) cm^{-2} atm^{-1}, respectively (both base 10). The much larger gas phase NO_2 infrared band compared to that

for N_2O_3 (Fig. 3.III.8) is consistent with its much higher concentration, 3×10^{17} vs. $(5\text{-}7) \times 10^{15}$ molecule cm^{-3} for N_2O_3.

Figure 3.III.8d shows the spectrum of the surface-adsorbed species, obtained by subtracting the gas spectrum in Figure 3.III.8b from the combined "gas + surface-adsorbed" spectrum in Figure 3.III.8a. In addition to N_2O_4 and HNO_3 on the surface, two broad peaks at ~1870 and ~1600 cm^{-1} were observed. As expected for surface species, rotational structure is not evident. The peaks at ~1870 and 1600 cm^{-1} correspond to those reported for solid *asym*-N_2O_3 at low temperatures (*Snyder and Hisatsune*, 1955; *Varetti and Pimentel*, 1971; *Fateley et al.*, 1959; *Hisatsune et al.*, 1960; *Bartram and Koel*, 1989; *Wang and Koel*, 1998), and hence we assign them to the nitrosyl NO stretch (1870 cm^{-1}) and the nitro NO stretch (~1600 cm^{-1}) of *asym*-N_2O_3 adsorbed on the porous glass. These absorption peaks were observed only when both NO and NO_2 were present. No surface absorptions due to NO or NO_2, respectively, were observed when these gases were introduced individually into the cell (although as reported in earlier studies (*Barney and Finlayson-Pitts*, 2000b), N_2O_4 and HNO_3 are formed on the surface from NO_2). Hence, attribution of these bands to species such as the *cis*-N_2O_2 dimer of NO observed on Zeolites (*Chao and Lunsford*, 1971; *Vaylon and Hall*, 1993) or to NO_2 strongly bonded to the surface with the partial loss of an electron (*Chao and Lunsford*, 1971) can be ruled out. In contrast to the gas phase absorption spectrum, the peak due to adsorbed N_2O_3 on the surface is larger than that of NO_2. Thus, the amount of N_2O_3 on silica surfaces is apparently enhanced compared to that of NO_2, as was observed for NO_2/N_2O_4 on silica surfaces (*Barney and Finlayson-Pitts*, 2000b).

Additional evidence for assignment of the 1870 and 1600 cm^{-1} peaks to surface-adsorbed N_2O_3 was obtained using ^{15}N-labelled NO and NO_2. As seen in Figure 3.III.9a, both of these peaks shifted to lower wavenumbers by approximately 30 - 40 cm^{-1}. Similar shifts have been observed for solid N_2O_3 at low temperatures where the 1870 cm^{-1} band shifted by ~32 cm^{-1} from the ^{14}N to the ^{15}N compound, while the second band shifted to lower wavenumbers by ~40 cm^{-1} (*Hisatsune et al.*, 1960; *Nour et al.*, 1983).

In short, both the peak positions and their shifts when ^{15}N is used support the assignment of the peak at 1830 cm^{-1} to the nitrosyl-NO stretching mode of *asym*-N_2O_3, and that around 1600 cm^{-1} to the nitro-NO stretching mode of *asym*-N_2O_3 (*Hisatsune et al.*, 1960; *Nour et al.*, 1983). To the best of our knowledge, this is the first time that N_2O_3 has been directly observed using infrared spectroscopy on a surface at room temperature.

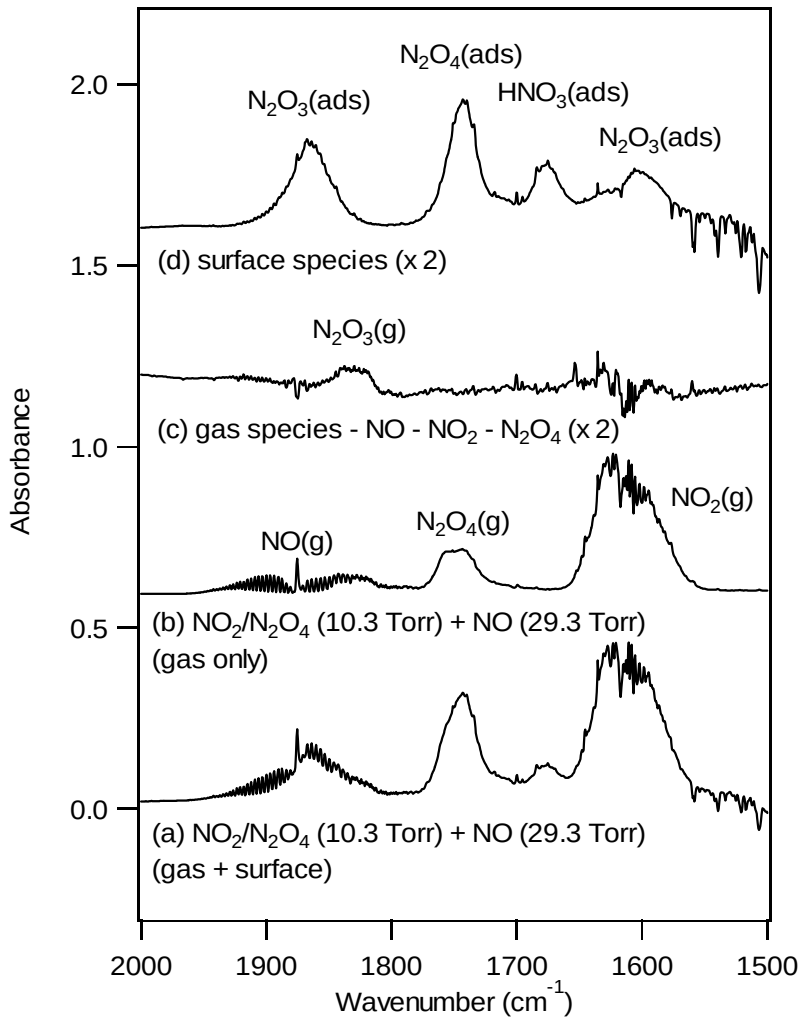

Figure 3.III.8. Infrared spectra of (a) gas and surface species after the introduction of 3.3×10^{17} molecule cm^{-3} of NO_2/N_2O_4 and 9.5×10^{17} molecule cm^{-3} of NO into the cell containing the porous glass; (b) gas phase under the same conditions as for (a); (c) difference spectrum obtained by subtraction of NO(g), NO_2(g) and N_2O_4(g) bands from (b); (d) difference spectrum between (a) and (b), showing only surface-adsorbed species. The total intensities in parts (c) and (d) have been multiplied by two for clarity.

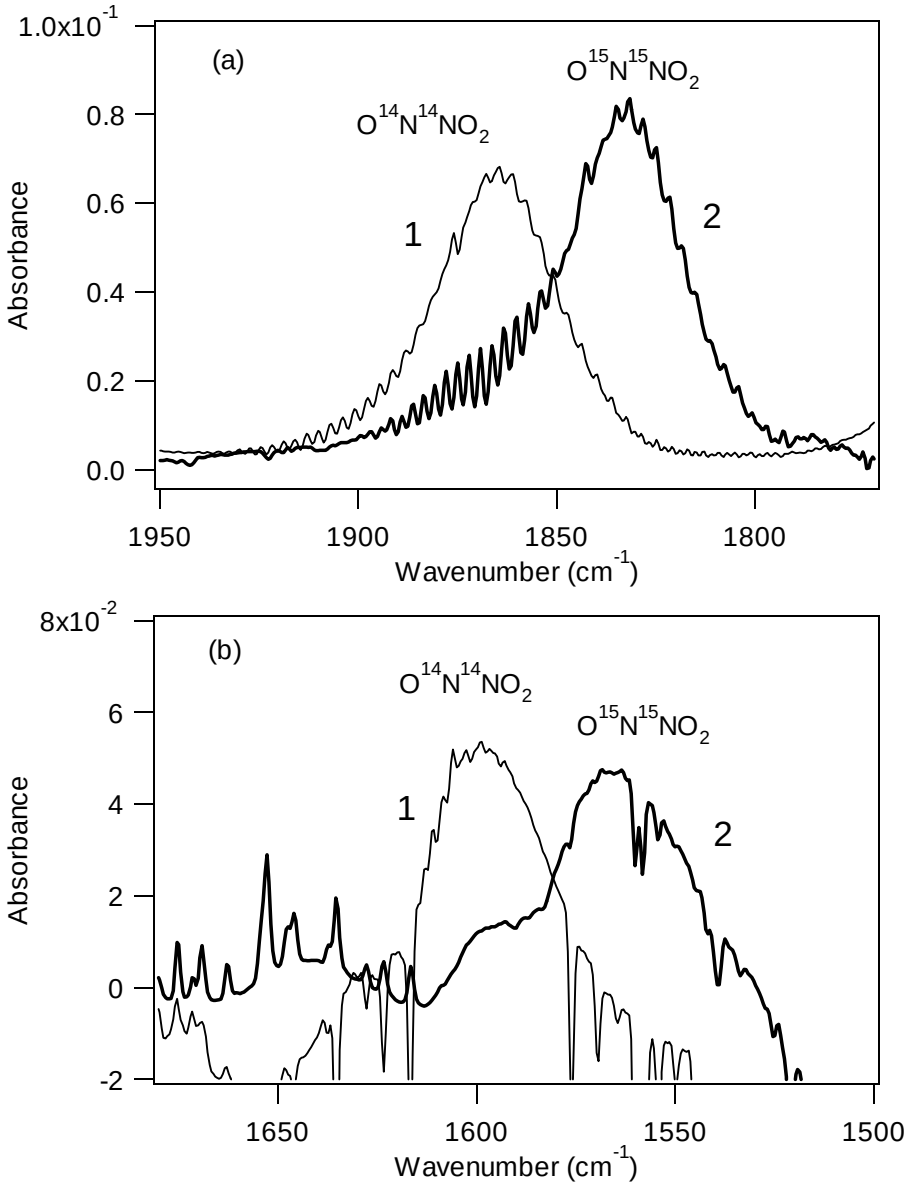

Figure 3.III.9. Infrared bands of surface-adsorbed N_2O_3 with two isotopes, ^{14}N and ^{15}N. (a) with (1) ^{14}NO (9.7×10^{17} molecules cm^{-3}) and $^{14}NO_2$ (1.6×10^{17} molecule cm^{-3}) or (2) ^{15}NO (1.1×10^{18} molecules cm^{-3}) and $^{15}NO_2$(1.7×10^{17} molecules cm^{-3}) in the cell; (b) with (1) ^{14}NO (1.1×10^{18} molecules cm^{-3}) and $^{14}NO_2$ (2.4×10^{17} molecules cm^{-3}) or (2) ^{15}NO (1.1×10^{18} molecules cm^{-3}) and $^{15}NO_2$ (1.7×10^{17} molecules cm^{-3}) in the reaction cell. The concentrations for NO_2 given are total NO_2 and the N_2O_4 in equilibrium with it.

III.B.2. Dependence of Gas and Surface-Adsorbed N_2O_3 on Gas Phase NO and NO_2

Figure 3.III.10a shows the concentration of gas phase N_2O_3, calculated using the integrated band intensity for the ν_1 stretch at 1830 cm^{-1} reported by Kagann and Maki (1984) as a function of the initial NO concentration at two different initial concentrations of NO_2. As expected from the equilibrium $NO + NO_2 + M \leftrightarrow N_2O_3 + M$, the gas phase intensity increases linearly with the NO concentration; the concentrations determined from the infrared band intensities are consistent within experimental error with those calculated using the equilibrium constant and the initial concentrations of NO and NO_2. (The small slope when NO_2 was not added and small non-zero intercepts are due to the difficulty in obtaining complete subtraction of the strong porous glass and gas phase NO absorptions in this region; in addition, some NO_2 is formed in the cell when NO is added, due to its reaction with small amounts of HNO_3 left adsorbed on the surface (*Mochida and Finlayson-Pitts*, 2000) from previous runs). Figure 3.III.10b shows that the intensity of the peak at 1870 cm^{-1} assigned to surface-adsorbed N_2O_3 also increases linearly with NO. (The band at 1600 cm^{-1} was too weak to provide a meaningful correlation with the gas phase species).

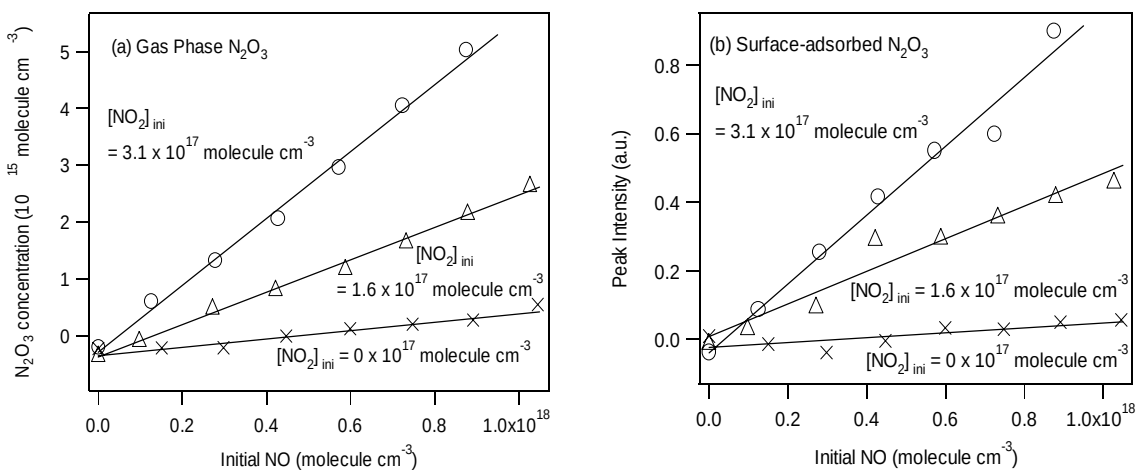

Figure 3.III.10. Measured (a) gas phase concentrations of N_2O_3 measured using the 1830 cm^{-1} band and (b) integrated intensities of the band at 1870 cm^{-1} due to surface-adsorbed N_2O_3 when increasing amounts of NO are added to an initial NO_2/N_2O_4 mixture at the initial concentrations of NO_2 shown which have been corrected for the $2NO_2 \leftrightarrow N_2O_4$ equilibrium.

Figure 3.III.11 shows the analogous plots for N_2O_3 as a function of the initial gas phase NO_2 concentration, which was calculated from the total pressure of NO_2/N_2O_4 and the equilibrium constant for the $2\ NO_2 \leftrightarrow N_2O_4$ reaction, $K_{eq} = 2.5 \times 10^{-19}$ cm^3 $molecule^{-1}$ (*DeMore et al.*, 1997). While the gas phase N_2O_3 varies linearly with NO_2, the peak intensity at 1870 cm^{-1} for the adsorbed species falls off at higher NO_2 concentrations. Given that N_2O_4 is enhanced on

the surface relative to the gas phase (*Barney and Finlayson-Pitts*, 2000b), a possible explanation is that N_2O_4 competes with N_2O_3 for the surface sites at the higher concentrations, leading to the observed fall-off in the surface N_2O_3. If this is the case, then the difference between the expected ideal linear behavior shown by the dotted lines and the observed peak intensities, represented as ΔI_{N2O3} in Figure 3.III.11b, should be proportional to the amount of surface N_2O_4 and hence to gas phase N_2O_4 or $[NO_2]^2$. Figure 3.III.12 shows a plot of this difference, ΔI_{N2O3}, as a function of the square of the NO_2 pressure for the two different concentrations of NO. The linearity of these plots shows that competition for surface sites between N_2O_4 and N_2O_3 is indeed responsible for the non-linear dependence of surface-adsorbed N_2O_3 on the gas phase NO_2 concentration seen in Figure 3.III.11b.

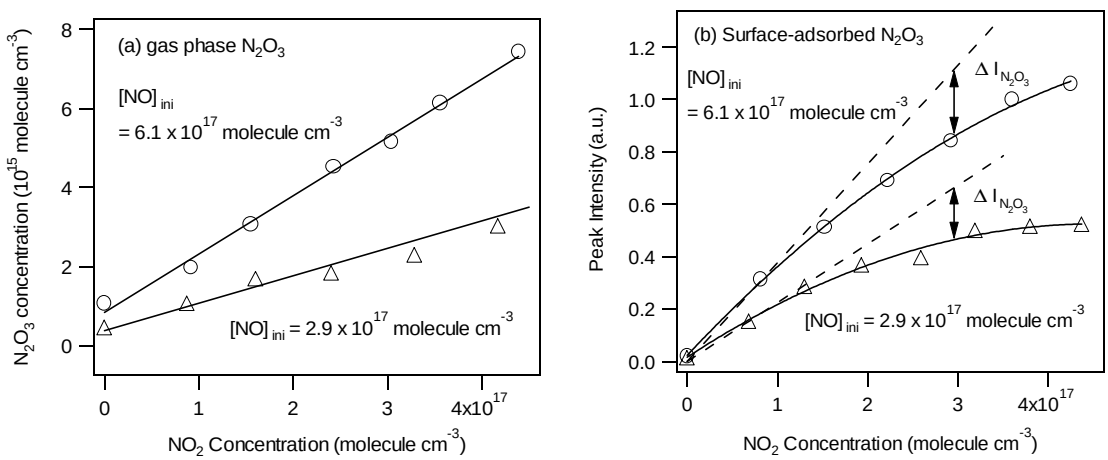

Figure 3.III.11. Measured (a) gas phase concentrations of N_2O_3 using the 1830 cm^{-1} band, and (b) integrated intensities of the band at 1870 cm^{-1} due to surface-adsorbed N_2O_3 when increasing concentrations of NO_2/N_2O_4 are added to either 2.9 or 6.1×10^{17} molecule cm^{-3} NO in the cell. The concentrations of NO_2 have been corrected for the $2NO_2 \leftrightarrow N_2O_4$ equilibrium.

III.B.3. Effects of Added Water Vapor

Reaction (III.4) may involve adsorbed N_2O_3 as an intermediate, which then reacts with water on the surface. N_2O_3 is the anhydride of HONO, and is known to react in aqueous solution with H_2O to form HONO (*Grätzel et al.*, 1970):

$$N_2O_3 + H_2O \leftrightarrow 2\ HONO \qquad \text{(III.5,III.-5)}$$

To test whether surface-adsorbed N_2O_3 reacts with water vapor, the porous glass was first heated to 520 K for several hours under vacuum; this decreased the peak height due to water at 3400 cm^{-1} by a factor of approximately 30. N_2O_3 was generated on the surface in the usual manner

and water vapor was then added to the cell. The dotted line in Figure 3.III.13a shows the initial spectrum of the gas and surface species. The solid line shows the spectrum after water vapor in 650 Torr He was added to the cell. The N_2O_4 peak decreased and that of adsorbed HNO_3 increased, as expected from previous studies in this laboratory (*Barney and Finlayson-Pitts*, 2000b). (The apparent increase in the NO and NO_2 is due to pressure effects on the bands). However, as seen in Figure 3.III.13b, the 1870 cm^{-1} N_2O_3 peak did not change significantly upon the addition of water vapor.

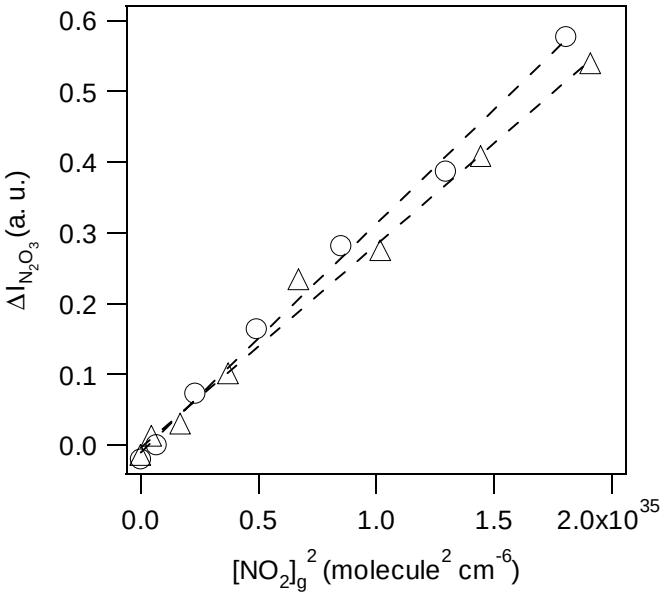

Figure 3.III.12. The difference (ΔI_{N2O3}) shown in Figure 3.III.11 as a function of square of the NO_2(g) concentration. Circles and triangles are plots at NO concentrations of 2.9 and 6.1×10^{17} molecule cm^{-3}, respectively.

The lack of change in the surface-adsorbed N_2O_3 when water vapor is added may be attributed to one or more factors. One possibility is that the amount of N_2O_3 lost from the surface by hydrolysis is too small to be observed. We estimate that the loss would have to be ≥ 20 % in order to be readily observed in these experiments. Another possibility is that the symmetrical form of N_2O_3, i.e. ONONO, reacts more rapidly with water than the asymmetrical form, $ONNO_2$, to form HONO. This is reasonable since the reaction of H_2O with *sym*-N_2O_3 presumably occurs with a more-favored 6-membered transition state compared to a 5-membered transition state for *asym*-N_2O_3. A small amount of *sym*-N_2O_3 adsorbed on the surface would not be detectable in these experiments, particularly given the overlap of its absorption bands with other species such as HNO_3 and N_2O_4 in our system (*Nour et al.*, 1983; *Wang et al.*, 1997). A third possibility is that surface-N_2O_3 is replenished rapidly from gas phase NO and NO_2 as it reacts with water.

The formation of gas phase HONO was followed with time under the experimental conditions similar to the ones shown in Figure 3.III.13. Despite the lack of change in surface-adsorbed N_2O_3 , gas phase HONO was formed (Fig. 3.III.14). However, the amount of HONO

formed without the porous glass plate in the cell was about twice that when the porous glass plate was present. This initially puzzling result may be due to the fact that the effective surface area for the reaction on the porous glass plate is much closer to its geometric surface area than to the measured BET surface area. In that case, most of the heterogeneous chemistry is actually occurring on the walls of the reaction cell, rather than on the porous glass plate. Following the surface species on the porous glass plate using FTIR provides a means of directly following the chemistry occurring on all of the cell surfaces. The smaller amount of HONO formed in the presence of the porous glass may be due to two factors: (1) a heterogeneous loss of HONO by reaction with HNO_3 on the porous glass plate suggested by studies of the reaction of surface-adsorbed HNO_3 with NO in this system (*Mochida and Finlayson-Pitts*, 2000), and/or (2) efficient uptake of water vapor by the porous glass so that the surfaces of the reaction cell are actually drier when it is suspended in the cell.

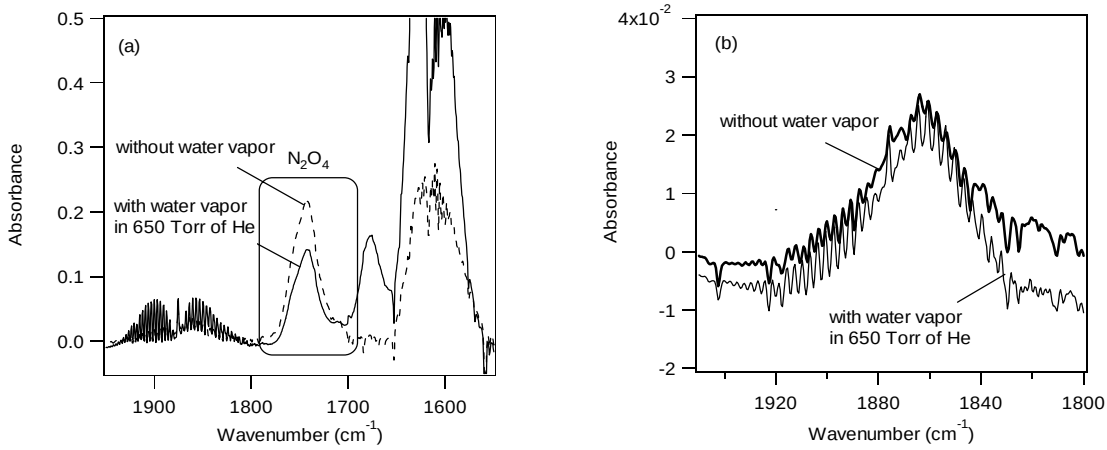

Figure 3.III.13. Infrared spectra of (a) the gas phase plus surface-adsorbed species before adding water (dotted line) and after adding water vapor, and (b) spectrum of surface-adsorbed N_2O_3 before and after the addition of water vapor. The initial concentration of NO was 3.0×10^{17} molecule cm^{-3} and NO_2 was 2.5×10^{17} molecule cm^{-3}. The water vapor concentration added to the cell in 650 Torr of He was 6.6×10^{17} molecules cm^{-3}. The cell with the porous glass had been heated to 520 K for several hours prior to introducing the gases.

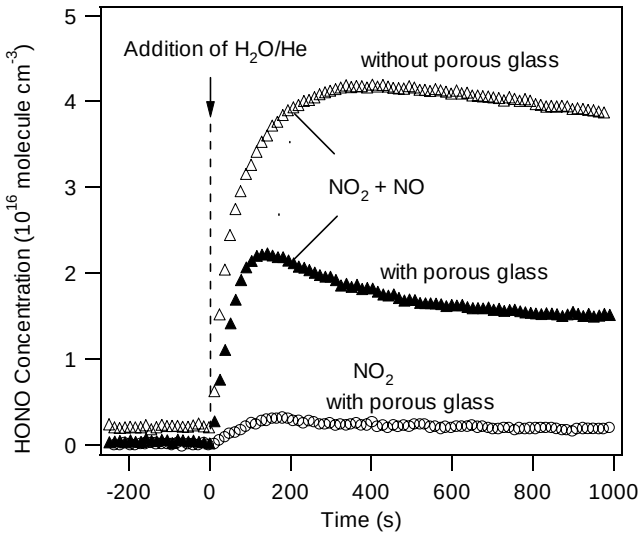

Figure 3.III.14. Time-concentration profiles of HONO with 1.1×10^{18} molecules cm^{-3} of NO and 1.6×10^{17} molecules cm^{-3} of NO_2 in the cell before and after the addition of 6.6×10^{17} molecules cm^{-3} of water vapor in 650 Torr of He. ▲ represents HONO with the porous glass suspended in the cell and Δ represent HONO without the porous class in the cell. Smaller amounts of HONO generated with only NO_2 in the cell with the porous glass are represented by O.

Finally, it may be that N_2O_3 is not an intermediate in HONO formation, *i.e.* the reaction of NO and NO_2 at the surface, and not N_2O_3, leads to HONO formation. This could, in principle, occur as a single step or through a sequence of reactions. For example, gas phase NO_2 is known to react with surface-adsorbed water on the porous glass, forming HNO_3 on the surface (*Barney and Finlayson-Pitts*, 2000b). This HNO_3 can react with NO rapidly, likely forming HONO and NO_2 (*Mochida and Finlayson-Pitts*, 2000).

$$2\ NO_2(g) + H_2O \xrightarrow{surface} HONO(g) + HNO_3(ads) \qquad \text{(III.6)}$$

$$NO(g) + HNO_3(ads) \xrightarrow{surface} HONO(g) + NO_2(ads) \qquad \text{(III.7)}$$

$$NO(g) + NO_2(g) + H_2O \xrightarrow{surface} 2\ HONO(g) \qquad \text{(Net Reaction)} \qquad \text{(III.8)}$$

In short, the mechanism of the observed formation of HONO from the heterogeneous reaction of NO, NO_2 and water and whether it involves N_2O_3 as an intermediate on the surface is not clear. However, this reaction is unlikely to be a significant source of HONO in air.

III.C. FTIR Study of the Reaction of Gaseous NO with HNO_3 on Silica Surfaces: Implications for Conversion of HNO_3 to Photochemically Active NO_x in the Atmosphere.

Nitric acid adsorbed on surfaces may also be a source of HONO in the atmosphere through its reaction with NO. In fact, a heterogeneous reaction of NO with HNO_3 was suggested by Besemer and Nieboer (1985) as a source of HONO to explain the concentration-time profiles of major species generated in smog chamber studies of mixtures of NO_x with CO and propane.

To the best of our knowledge, there has been no systematic study of the *heterogeneous* reactions of HNO_3 with gas phase nitrogen compounds. A major reason may be the difficulty in measuring both surface adsorbed and gas phase species simultaneously.

In the work reported here, the heterogeneous reaction of surface-adsorbed HNO_3 with gaseous NO on a "wet" porous glass surface was investigated using transmission FTIR spectroscopy. Both gas and surface-adsorbed species were identified from their infrared absorption bands and followed as a function of time. Isotopically labeled ^{15}NO was also used in some experiments to investigate the source of nitrogen atoms in the NO_2 product. We show that the heterogeneous reaction of HNO_3 with NO on silica surfaces proceeds significantly faster than in the gas phase, as suggested by observations in earlier gas phase studies (*Smith*, 1947; *Jaffe and Ford*, 1967; *Kaiser and Wu*, 1977b; *Streit et al.*, 1979). This reaction is shown to be a potentially important reduction process for HNO_3 back to NO_x as well as a source of HONO in polluted urban atmospheres.

III.C.1. Formation of NO_2 by Exposure of HNO_3 Adsorbed on Porous Glass to Gas Phase NO

Figure 3.III.15a shows a spectrum of surface-adsorbed HNO_3. A peak that does not show significant rotational structure was observed at 1677 cm^{-1}, in agreement with previous studies by Goodman et al. (1999) and Barney and Finlayson-Pitts (2000b). A similar peak has been observed for undissociated nitric acid in water solutions (*Querry and Tyler*, 1980; *Biermann et al.*, 2000). The concentration of gas phase HNO_3, measured using its 1711 cm^{-1} band, was small compared to the amount of surface adsorbed HNO_3. For instance, when the amount of surface adsorbed HNO_3 was 1×10^{19} molecules (based on measurements by ion chromatography), the gas phase HNO_3 was 2.2×10^{15} molecules cm^{-3}, corresponding to a total of 1.7×10^{17} gas phase HNO_3 in the cell (cell volume = 79 cm^3).

Figure 3.III.15(b-1d) shows typical spectra from reaction of adsorbed HNO_3 with gaseous NO. Figure 3.III.15b is the spectrum of both gas and surface species after 60 min reaction time; the surface HNO_3 has decreased, while NO_2 and N_2O_4 have increased. Figure 3.III.15c is the gas phase spectrum which shows only NO_2 and small amounts of N_2O_4. Figure 3.III.15d is the difference spectrum (Fig. 3.III.15d = 3.III.15b-3.III.15c) which shows only surface-adsorbed species. While essentially all of the NO_2 is in the gas phase, roughly half of the intensity of the N_2O_4 band around 1750 cm^{-1} is due to the surface-adsorbed species. The gas phase NO is not consumed completely, and its steady-state concentration is ~7 % of its initial value.

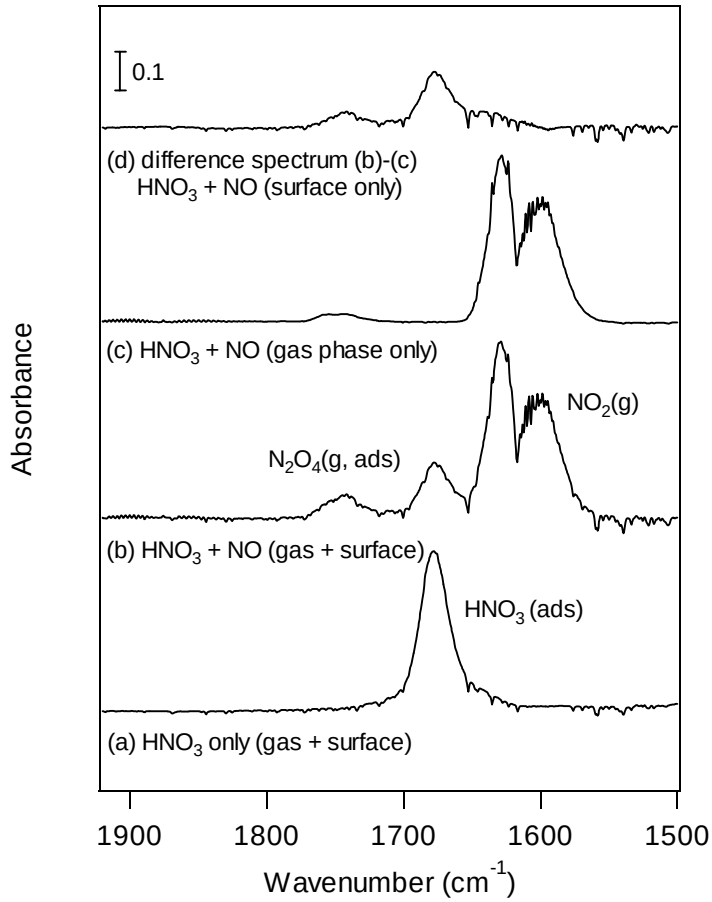

Figure 3.III.15. FTIR spectra of (a) surface species after the introduction of HNO_3; the porous glass has 9.4×10^{18} adsorbed molecules of HNO_3 (determined by ion chromatography); (b) spectrum of gas plus surface species 60 min after introduction of NO (6.7×10^{16} molecules cm^{-3}) along with 460 Torr of He to the reaction cell; (c) the gas phase spectrum under the same conditions as (b); (d) the difference spectrum between (b) and (c) due to surface adsorbed species. The absorbance scale is the same for all spectra.

The initial conditions for a series of experiments designed to measure the changes in the gas and surface species are summarized in Table 3.III.1. The reaction stoichiometries between the initial concentrations and steady state are also summarized.

Small amounts of HONO were also formed in the gas phase. As shown in Figure 3.III.16, the HONO peak at 1263 cm^{-1} was identified after surface-adsorbed HNO_3 was exposed to NO. This peak corresponds to approximately 2×10^{14} molecules cm^{-3} of HONO, an amount that is significantly greater than what is observed as a trace impurity in the NO (Fig. 3.III.16c). The small yields of HONO suggest that if the reaction of NO with HNO_3 is the source of HONO, removal of HONO by rapid secondary reactions must be occurring simultaneously in this system.

Although the NO also had small amounts of NO_2 and N_2O impurities, Figure 3.III.17 shows that there were no secondary reactions of these trace contaminants with the surface HNO_3.

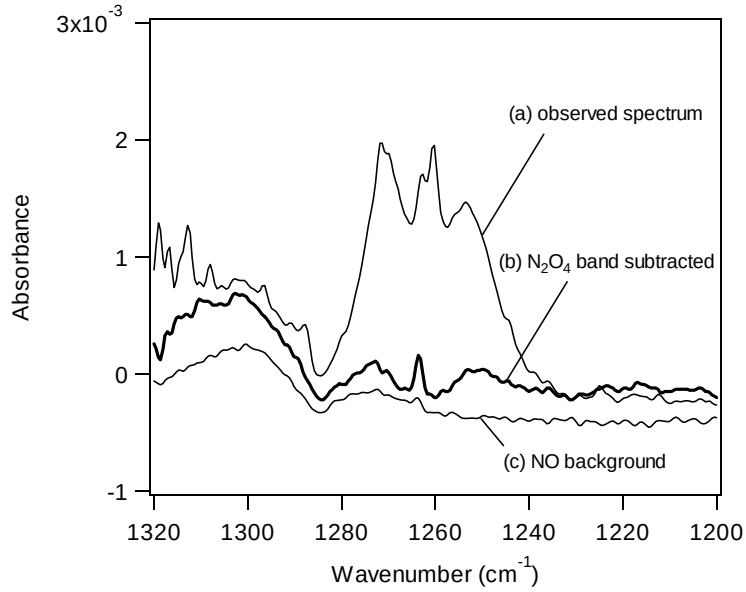

Figure 3.III.16. Gas phase infrared spectra (a) after 120 min during the reaction of adsorbed HNO_3 (initially 9×10^{18} molecules) with 6.5×10^{16} molecules cm^{-3} NO; (b) after subtraction of the ν_{11} band of N_2O_4 from (a), showing the ν_3 band of gas phase *trans*-HONO whose intensity corresponds to a concentration of $\sim 2 \times 10^{14}$ molecules cm^{-3}; (c) of NO alone.

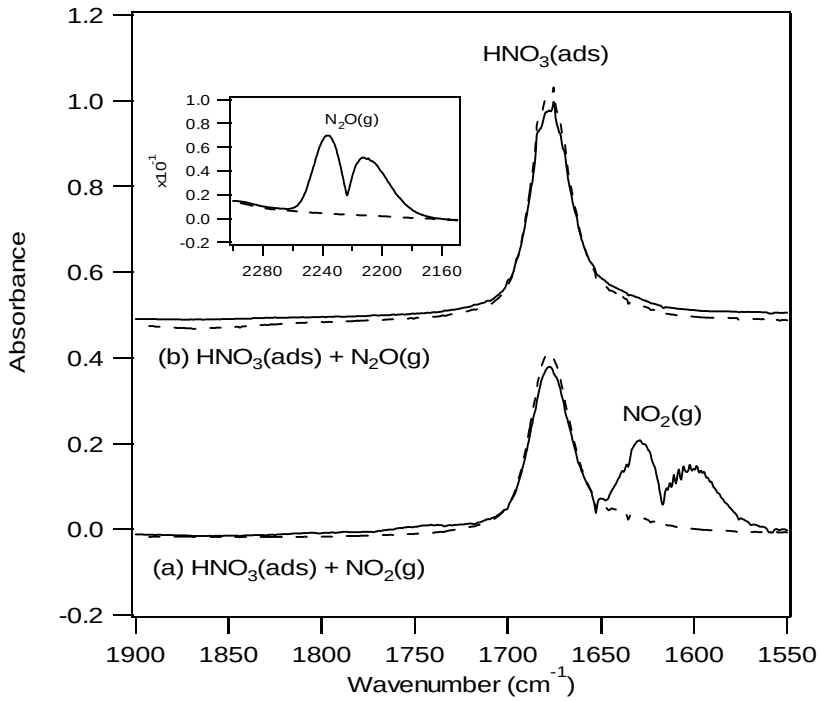

Figure 3.III.17. Infrared spectra of surface-adsorbed HNO_3 with some gaseous nitrogen oxides. (a) Dashed line: Adsorbed HNO_3 (9×10^{18} molecules) on porous glass. Solid line: after introduction of 6.5×10^{16} molecules cm^{-3} of NO_2. (b) Dashed line: adsorbed HNO_3 (1.1×10^{19} molecules) on porous glass. Solid line: after introduction of 6.5×10^{16} molecules cm^{-3} of N_2O.

III.C.2. Possible Reaction Mechanisms

The experimental observations are consistent with the following heterogeneous reactions, suggested in the previous section:

$$NO(g) + HNO_3(ads) \xleftrightarrow{surface} HONO + NO_2 \qquad \text{(III.7,III.-7)}$$

$$HONO + HNO_3(ads) \xleftrightarrow{surface} 2\ NO_2 + H_2O \qquad \text{(III.-6,III.6)}$$

$$2\ HONO \xleftrightarrow{surface} NO + NO_2 + H_2O \qquad \text{(III.-8,III.8)}$$

Both reactions (III.7) plus (III.-6), or two times (III.7) plus (III.-8) give the net reaction

$$NO + 2\ HNO_3 \xrightarrow{surface} 3\ NO_2 + H_2O \qquad \text{(III.9)}$$

This net reaction is consistent, within experimental error, with the measured reaction stoichiometries shown in Table 3.III.1 for $\Delta HNO_3/\Delta NO = 1.9 \pm 0.3$, $\Delta NO_2/\Delta NO = 2.2 \pm 0.3$, $\Delta HNO_3/\Delta NO_2 = 0.9 \pm 0.2$ and $\Delta NO_2/(\Delta NO + \Delta HNO_3) = 0.8 \pm 0.1$ (2σ). Note that the yield of

NO_2 has been underestimated because the gas and surface-adsorbed N_2O_4 have not been taken into account in calculating these ratios. This is supported by separate studies using a long path (38.4 m) gas cell whose walls were doped with HNO_3. NO in N_2 at 50% relative humidity was then added. The stoichiometry $\Delta NO_2/\Delta NO$ was measured to be 3.5 ± 0.5 (2σ) at NO concentrations down to 26 ppm where N_2O_4 formation is not important, unlike the present studies at higher concentrations where N_2O_4 is observed (*Saliba et al.*, 2000).

The heterogeneous formation of NO_2 by reaction (III.7) has been suggested by several authors attempting to study the gas phase reaction (*Smith*, 1947; *Jaffe and Ford*, 1967; *Kaiser and Wu*, 1977b; *Streit et al.*, 1979). This reaction in the gas phase is approximately thermoneutral, ΔH^0= -1.5 kJ mol^{-1}, and it is common for such reactions to proceed more rapidly on surfaces (*Fairbrother et al.*, 1997).

In order to confirm the proposed mechanism, isotopically labeled ^{15}NO was used as a reactant in some experiments. At steady-state, both isotopes $^{14}NO_2$ and $^{15}NO_2$ were identified as products by the $\nu_3+\nu_1$ band at 2907 and 2859 cm^{-1}, respectively. Both isotopomers were also confirmed from their parent peaks at m/z = 46 and 47 using mass spectrometry. This provides clear evidence that the nitrogen atom in surface adsorbed HNO_3 is involved in the reaction with NO. However, because of the fast interconversion between NO and NO_2 (*Sharma et al.*, 1979), which we also observed in separate experiments, it was not possible to trace the fate of ^{14}N and ^{15}N as a function of time; at steady-state, the ratio of $^{15}N/^{14}N$ of nitrogen compounds reached the same value as the ratio of ^{15}NO and $H^{14}NO_3$ initially present in the reaction cell.

Table 3.III.1. Initial Reactant HNO_3 and NO and Measured Stoichiometry for Reactants and Product NO_2

Run	HNO_3(ini)[a]	HNO_3(ss)[a]	ΔHNO_3 [b]	NO(ini) [c]	NO(ss) [c]	ΔNO [d]	ΔNO_2 [e]	$\frac{\Delta HNO_3}{\Delta NO}$	$\frac{\Delta HNO_3}{\Delta NO_2}$	$\frac{\Delta NO_2}{\Delta NO}$	$\frac{\Delta NO_2(ss)}{\Delta NO+\Delta HNO_3}$
1	1.1×10^{19}	3.4×10^{18}	7.6×10^{18}	4.8×10^{18}	1.1×10^{18}	3.7×10^{18}	9.0×10^{18}	2.0	0.85	2.4	0.79
2	9.9×10^{18}	3.2×10^{18}	6.7×10^{18}	5.1×10^{18}	1.3×10^{18}	3.7×10^{18}	7.7×10^{18}	1.8	0.87	2.1	0.74
3	9.4×10^{18}	3.0×10^{18}	6.4×10^{18}	5.3×10^{18}	1.4×10^{18}	3.9×10^{18}	8.5×10^{18}	1.7	0.76	2.2	0.83
4	9.3×10^{18}	1.0×10^{18}	8.3×10^{18}	1.5×10^{19}	1.1×10^{19}	4.1×10^{18}	8.1×10^{18}	2.0	1.0	2.0	0.66
5	2.6×10^{18}	1.3×10^{17}	2.5×10^{18}	5.1×10^{18}	3.8×10^{18}	1.3×10^{18}	3.0×10^{18}	1.9	0.82	2.3	0.79
6	2.4×10^{18}	1.1×10^{17}	2.3×10^{18}	5.1×10^{18}	3.9×10^{18}	1.2×10^{18}	2.6×10^{18}	1.9	0.88	2.1	0.74
							AVERAGE	1.9	0.9	2.2	0.8
							2σ	0.3	0.2	0.3	0.1

[a] Number of HNO_3 molecules on the porous glass plate before (ini) and after (ss) the reaction.
[b] Number of HNO_3 molecules reacted.
[c] Number of NO molecules in the reaction cell before (ini) and after (ss) the reaction.
[d] Number of NO molecules reacted.
[e] Number of NO_2 molecules produced by the reaction; this does not take into account small amounts of N_2O_4 in equilibrium with the NO.

The presence of small amounts of HONO in the cell after the reaction of adsorbed HNO_3 with NO suggests that HONO is removed by a fast secondary reaction such as reactions (III.-6) and/or (III.-8). Reaction (III.-6), whose reverse reaction (III.6) is the well known HONO formation pathway on surfaces (*Sakamaki et al.*, 1983; *Pitts et al.*, 1984a; *Svensson et al.*, 1987; *Jenkin et al.*, 1988; *Febo and Perrino*, 1991; *Bambauer et al.*, 1994; *Mertes and Wahner*, 1995; *Kleffmann et al.*, 1998a,b, 1999), is reported to proceed slowly in the gas phase (*England and Corcoran*, 1975; *Kaiser and Wu*, 1977a; *Streit et al.*, 1979; *Wallington and Japar*, 1989) and is not important under our experimental conditions. However, Wallington and Japar (1989) report evidence that reaction (III.-6) occurs heterogeneously as well. In the studies of Streit et al. (1979), the gas phase reaction (III.11) of HNO_3 with HONO was found to be faster than reaction (III.10) of HNO_3 with NO. If the same is true for the analogous heterogeneous reactions (III.-6) and (III.7), HONO may be removed rapidly by reaction (III.-6) as it is formed.

$$NO(g) + HNO_3(g) \rightarrow HONO(g) + NO_2(g) \qquad \Delta H° = -1.5 \text{ kJ mol}^{-1} \qquad \text{(III.10)}$$

$$HONO(g) + HNO_3(g) \rightarrow 2\ NO_2(g) + H_2O(g) \qquad \Delta H° = +39.2 \text{ kJ mol}^{-1} \qquad \text{(III.11)}$$

HONO is also known to be in equilibrium with NO and NO_2 in the gas phase via reaction (III.-8,III.8) (*Wayne and Yost*, 1951; *Graham and Tyler*, 1972; *Chan et al.*, 1976a,b; *Cox and Derwent*, 1976, 1977; *Kaiser and Wu*, 1977a; *Sakamaki et al.*, 1983; *Pitts et al.*, 1984a). Kaiser and Wu (1977a) reported an upper limit for the gas-phase rate constant of $k_{-8} < 1\times10^{-20}$ cm^3 $molecule^{-1}$ s^{-1} which, at a HONO concentration of 10^{16} molecules cm^{-3}, would generate only $\sim10^{15}$ molecules of NO_2 in 20 s, much less than observed (Table 3.III.1). While the gas phase reaction cannot be important in our system, a heterogeneous self-reaction of HONO on the porous glass surface cannot be ruled out. However, regardless of whether reaction (III.-6) or (III.-8) is more important, HONO can be consumed heterogeneously, leading to additional NO_2 formation.

As seen in Table 3.III.1 and Figure 3.III.19, in the presence of an excess stoichiometric amount of HNO_3 compared to NO (runs 1 - 3), HNO_3 levels off at nonzero levels at longer reaction times, with approximately 25% of the initial NO remaining unreacted. This suggests that NO and HNO_3 may be regenerated in secondary reactions. In the case of NO, the bimolecular reaction (III.-8) of HONO on surfaces generates NO, and the hydrolysis of NO_2 on surfaces, reaction (III.6), is well-known to generate HNO_3 (*Sakamaki et al.*, 1983; *Pitts et al.*, 1984a; *Svensson et al.*, 1987; *Jenkin et al.*, 1988; *Febo and Perrino*, 1991; *Bambauer et al.*, 1994; *Mertes and Wahner*, 1995; *Kleffmann et al.*, 1988a,b, 1999; *Finlayson-Pitts and Pitts*, 2000).

In order to explain their smog chamber results, Besemer and Nieboer (1985) proposed that a reaction of NO with a species, likely HNO_3, on the walls of their reaction chamber produces HONO with the overall reaction being $2\ NO + HNO_3 \rightarrow 3\ HONO$. In their studies, the HONO was photolyzed as it was formed, so that secondary reactions such as (III.-6) and (III.-8) were likely not important under their experimental conditions.

III.C.3. Kinetics of Reaction of HNO_3(ads) + NO(g) on Porous Glass

In order to examine how fast this reaction proceeds on silica surfaces, the decay of adsorbed HNO_3 and production of gaseous NO_2 were measured as a function of reaction time. A typical sequence of spectra is shown in Figure 3.III.18 and a typical time evolution of HNO_3 and gaseous NO_2 in Figure 3.III.19. The reaction reaches a steady-state in several seconds to several tens of seconds, depending on the initial concentrations of NO and adsorbed HNO_3. The pseudo first-order rate constant for loss of HNO_3 was found to be the same with or without He carrier gas in the cell.

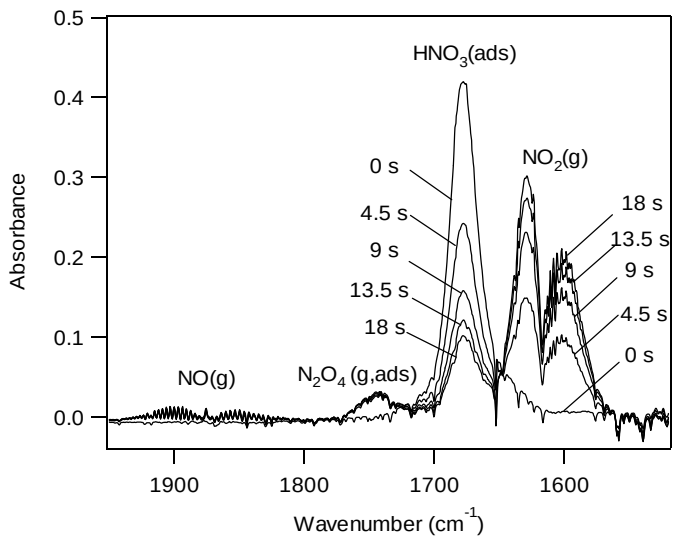

Figure 3.III.18. Infrared spectra of the combination of gas and adsorbed species after the reaction of surface adsorbed HNO_3 with gas phase NO at various reaction times. The initial concentration of gas phase NO was 6.7×10^{16} molecules cm^{-3} and the number of adsorbed HNO_3 determined by ion chromatography was 9×10^{18} molecules. The total pressure was 450 Torr in He carrier gas.

Figure 3.III.20a shows the pseudo-first order rate constants (k^I) for the initial decay of surface-adsorbed HNO_3 as a function of the initial NO concentration when the total amount of initial adsorbed HNO_3 is constant at either 0.8 or 9×10^{18} molecules. The values of k^I were derived from the initial slope of plots of $\ln(N_{HNO3})$ vs time. The rate of HNO_3 decay ($d\,N_{HNO3}/dt$, in molecule s^{-1}) is given by $k^I N_{HNO3}$ and increases proportionally with NO (Fig. 3.III.20b), i.e. reaction (III.7) is first order in NO.

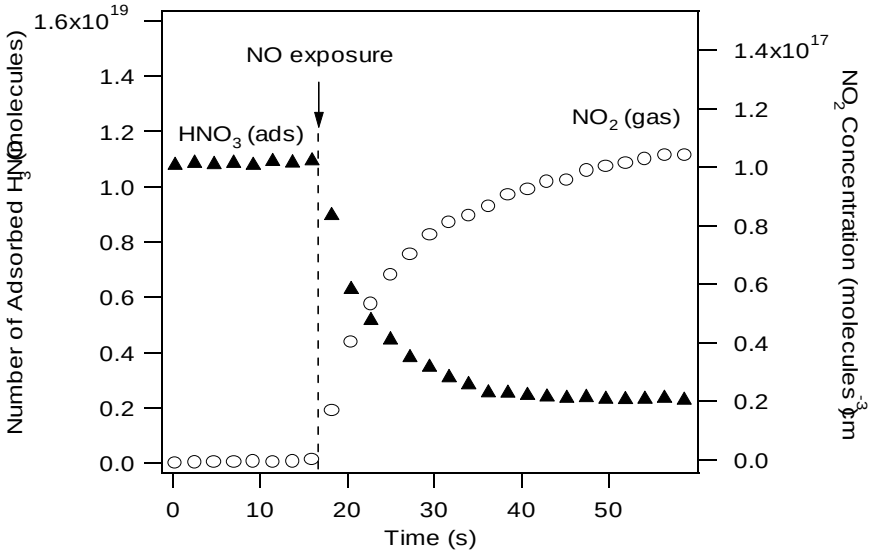

Figure 3.III.19. The time evolution of surface-adsorbed HNO_3 (1.1×10^{19} molecules) and gaseous NO_2 product measured using infrared bands at 1677 cm^{-1} and 1620 cm^{-1}, respectively, when NO (6.1×10^{16} molecules cm^{-3}) was added to the cell in the presence of 450 Torr He.

The HNO_3 decay was also followed at a constant gas phase NO concentration of 6×10^{16} molecules cm^{-3} with varying amounts (5×10^{17} molecules to 1.1×10^{19} molecules) of surface-adsorbed HNO_3. Figure 3.III.21a shows a negative dependence of the measured pseudo-first order rate constants for HNO_3 decay as a function of the initial number of adsorbed HNO_3 molecules, $N_{HNO3,\ ini}$. When expressed in the form $k^I = k^{II}(N_{HNO3})$, a value of b = -0.5 gives the best fit to the data. To explore the possible effects of surface-water, some experiments were carried out in which the outer portion of the cell containing the porous glass was heated to ~520 K while under vacuum for several hours. The integrated band intensity of the water peak at ~3500 cm^{-1} decreased by approximately a factor of two. This did not substantially alter the measured reaction stoichiometries. As seen in Figure 3.III.21a, the HNO_3 pseudo-first order rate constants at the lower initial coverages increased somewhat, but in all cases by less than 50%. However, this does not rule out a role for surface water in the reaction, since the infrared spectrum of the porous glass indicated there were still substantial amounts of water available on the surface.

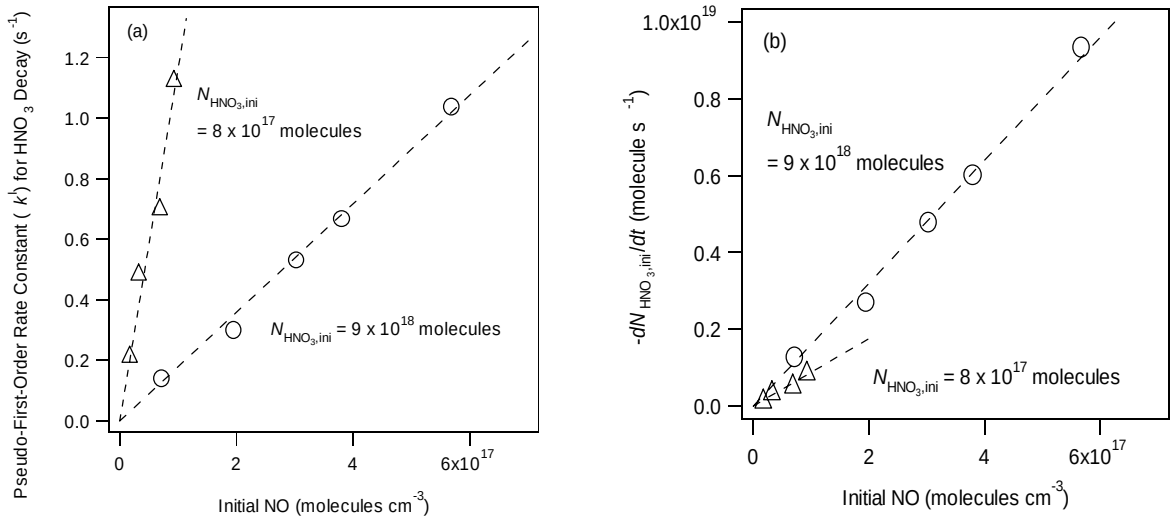

Figure 3.III.20.(a) The observed pseudo-first order rate constants for HNO_3 decay on porous glass as a function of the initial NO concentration in the gas phase at two different initial amounts of adsorbed HNO_3. (b) Same as (a) but plotted in terms of the rate, $-dN_{HNO3}/dt$ (molecules s^{-1}).

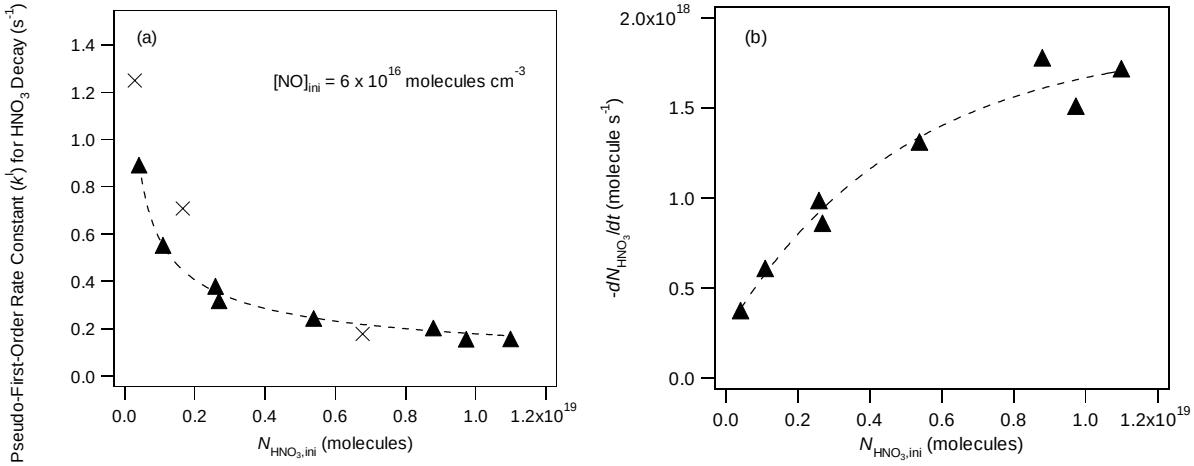

Figure 3.III.21.(a) Measured pseudo-first order rate constants for HNO_3 decay as a function of initial adsorbed HNO_3 on the porous glass at a constant NO concentration of 6×10^{16} molecules cm^{-3} (total of 5×10^{18} molecules available for reaction in the cell). ▲ porous glass pumped on but not heated. ✕ porous glass heated prior to reaction to remove some adsorbed water; (b) Same as (a) but plotted in terms of the rate, $-dN_{HNO3}/dt$.

The initial rate of HNO_3 decay, *i.e.* $dN_{HNO3}/dt = k^I N_{HNO3,\,ini}$ in molecule s^{-1}, as a function of the initial adsorbed HNO_3, (Fig. 3.III.21b) shows that the rate increases with $N_{HNO3,ini}$, at low surface HNO_3, but drops off at higher surface coverages. This suggests that HNO_3 adsorbs to individual sites on the surface at low coverages, but completely covers the surface, forming multilayers at higher amounts of surface HNO_3. Given the porous nature of the surface, this multilayer formation may occur at least partially in the pores. At the lower coverages, the rate should depend linearly on the surface HNO_3 since increased amounts are available for reaction with gas phase NO. However, at the point of complete coverage or multilayer formation, only a constant amount of surface HNO_3 is available for reaction and the rate should become independent of the initial surface HNO_3, as appears to be the case (Fig. 3.III.21b).

The fraction of available surface sites covered by HNO_3 initially under our experimental conditions can, in principle, be estimated from the measured BET surface area of 28.5 m^2. The adsorption site for HNO_3 may be surface -Si-OH groups. A fully hydroxylated surface has approximately 5×10^{14} Si-OH surface groups cm^{-2} (*Kiselev and Lygin*, 1975; *Zhuravlev*, 1993; *Sneh et al.*, 1996). If one HNO_3 is taken up per Si-OH group, a total of 1.4×10^{20} adsorption sites should be available. In this case, the HNO_3 coverages in these experiments would represent less than 10 % of the surface adsorption sites. However, given the larger size of the HNO_3 molecule compared to N_2 used for the surface area measurements, and the possibility of water in the pores, all of the area inside the pores may not be available for uptake of HNO_3. It is therefore not unreasonable that high surface coverages and multilayers are obtained at the highest amounts of HNO_3 used in these studies.

III.D. Reaction of Adsorbed Nitric Acid With Gaseous Nitric Oxide in the Long Path Cell

As shown in the preceding section, gaseous NO in the Torr concentration range reacts with HNO_3 on "wet" silica surfaces. Once this was established, it became important to (1) extrapolate these studies to lower NO concentrations, approaching atmospheric conditions (*Saliba et al.*, 2000), (2) evaluate the possibility of these reactions thermodynamically (*Fairbrother et al.*, 1997), and (3) define the chemical and physical changes occurring to HNO_3(ads) as a function of the change in the relative humidity (*Schnitzer et al.*, 1999).

This section summarizes studies designed to address these issues. Experiments were carried out using the long path cell and lower concentrations of gaseous nitric oxide at different relative humidities. We propose using thermodynamic calculations, the likely role played by the surface and with the help of some IR reflectance measurements, a model for the liquid-gas interface reaction is suggested.

III.D.1 Effect of Relative Humidity

Surface HNO_3 could not be followed directly in the long path cell system but the loss of NO and formation of NO_2 and other gas phase products could be measured using FTIR. In this set of experiments, gaseous HNO_3 was admitted to the cell to adsorb on the surfaces. It was then

pumped out and this conditioning/adsorbing process repeated at least three times. NO concentrations in the range of (0.2 - 40.0) $\times 10^{15}$ molecule cm^{-3} (8 - 1630 ppm) were obtained in the cell by expanding the appropriate amount of a mixture of NO in N_2 into the evacuated cell. Initial relative humidities of 0, 20, 30, 40, 50 and 70% were used and the reactant and products were followed with time starting immediately after the addition of the reactants and proceeding up to 350 min.

Figure 3.III.22 shows a typical set of data for the NO decay and NO_2 increase as a function of time for a 0% RH experiment. Past the first 100 min, a small amount of NO_2 was observed and only at high initial NO concentrations. No loss in NO was detected and no systematic behavior could be deduced from the loss in NO_2. Hence, in the absence of water the reaction between NO and adsorbed HNO_3 is insignificant.

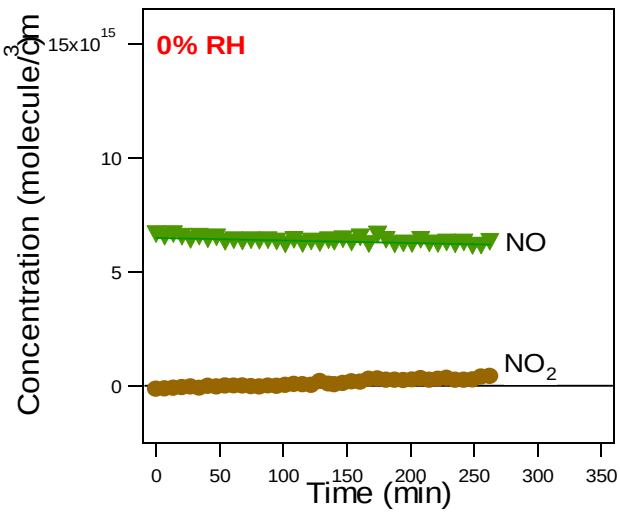

Figure 3.III.22. Decay of gas phase NO and formation of NO_2 in the long path cell whose walls had first been exposed to HNO_3. The relative humidity was 0% and the total pressure was 1 atm in N_2. Data are shown for an initial NO concentration of 2.2 $\times 10^{16}$ molecule cm^{-3}.

At 20 and 30% relative humidity (Fig. 3.III.23 a,b), four different initial NO concentrations were introduced into the cell containing adsorbed HNO_3. Almost no change in the NO concentration was detected and only a small increase in the NO_2 concentration in the first 200 min of the reaction was observed.

At 40% and 50% relative humidity, several different NO concentrations were introduced into the cell containing HNO_3 (ads). The change in NO and NO_2 concentrations for different experiments are summarized in Tables 3.III.2 and 3.III.3. Figure 3.III.24a,b shows typical concentration-time profiles for the decay of NO in the cell at 40% and 50% relative humidity. The reaction in both cases seemed to be accelerated so that nitric oxide decayed with time while NO_2 increased. NO_2 was the major product detected and only small concentrations of HONO ($\sim 10^{14}$ cm^{-3}) were observed. The stoichiometry $\Delta[NO_2]/\Delta[NO]$ was calculated from the slopes of

the lines obtained when NO and NO_2 were plotted as a function of time between 0 and 300 minutes and the change in NO and NO_2 concentrations within the same time. The average stoichiometry calculated over the experimental runs at 40% and 50% RH was 3.44 ± 0.4 (2σ) and 3.5 ± 0.5 (2σ), respectively.

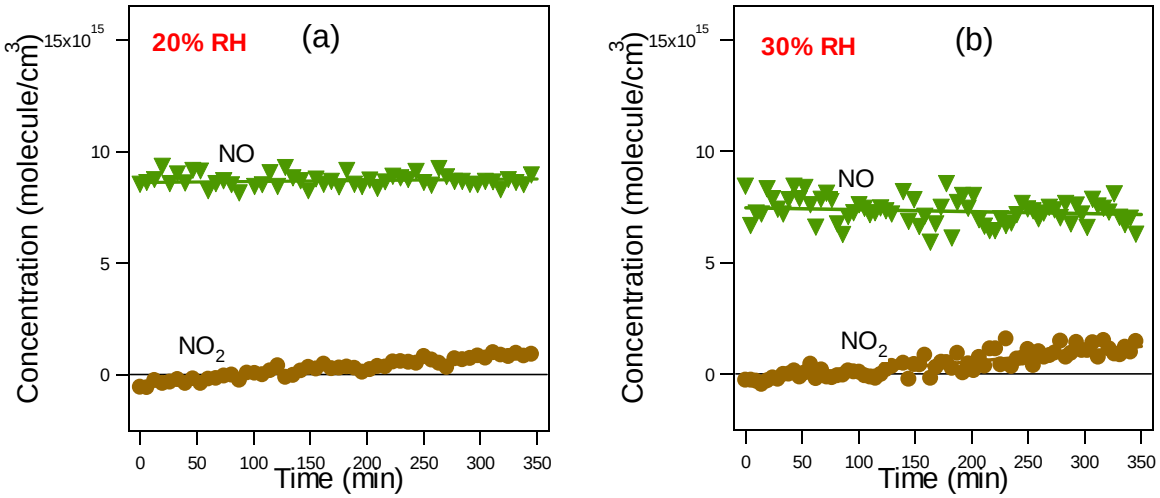

Figure 3.III.23. Decay of gas phase NO and formation of NO_2 in the long path cell whose walls had first been exposed to HNO_3 for (a) 20% relative humidity and (b) 30% relative humidity. The total pressure was 1 atm in N_2. Data are shown for an initial NO concentration of 8.6×10^{15} and 8.42×10^{15} molecule cm^{-3}, respectively.

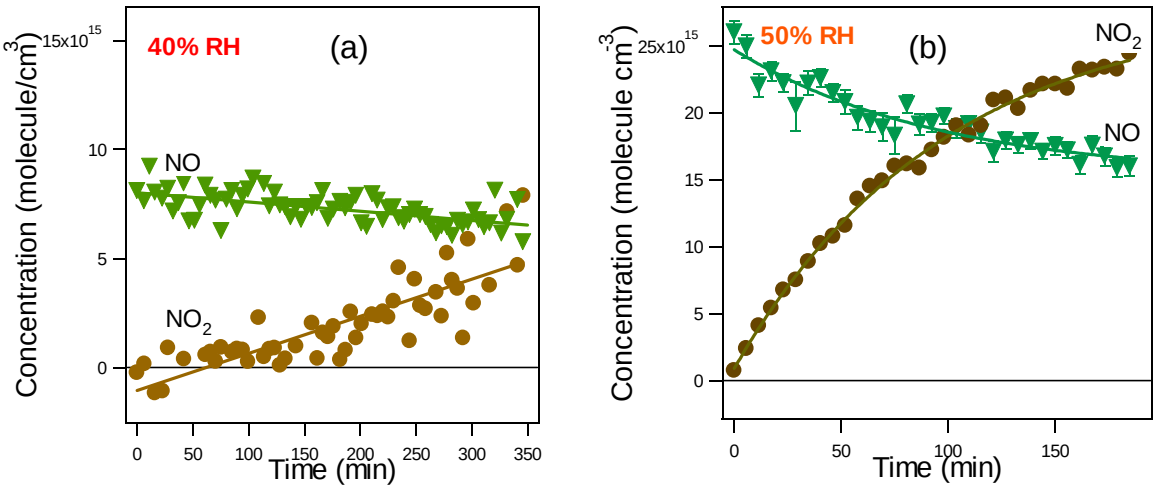

Figure 3.III.24. Decay of gas phase NO and formation of NO_2 in the long path cell whose walls had first been exposed to HNO_3 for (a) 40% relative humidity and (b) 50% relative humidity. The total pressure was 1 atm in N_2. Data are shown for an initial NO concentration of 8.0×10^{15} and 2.6×10^{16} molecule cm^{-3}, respectively.

Table 3.III.2. Summary of Long Path Cell FTIR Measurements of the Decay of NO and Formation of NO_2 in the Reaction of NO with HNO_3 Adsorbed on the Cell Walls[a].

Experiment # (40% RH)	$[NO]_0$ (10^{15} molecule cm^{-3})	$\Delta[NO]/\Delta t$ (10^{12} molecule cm^{-3s-1})	$\Delta[NO_2]/\Delta t$ (10^{12} molecule $cm^{-3}s^{-1}$)	$\frac{\Delta[NO_2]}{\Delta[NO]}$
1	2.59	-0.78	1.81	2.31
2	8.00	-4.24	15.3	3.61
3	11.0	-5.86	22.2	3.79
4	15.0	-10.6	32.9	3.09
			Average (±2σ)	3.44± 0.37

[a] $\Delta[NO_2]/\Delta[NO]$ was calculated from the slopes of the lines obtained when NO and NO_2 were plotted as a function of time between 0 and 300 minutes.

Table 3.III.3. Summary of Long Path Cell FTIR Measurements of the Decay of NO and Formation of NO_2 in the Reaction of NO with HNO_3 Adsorbed on the Cell Walls[a].

Experiment # (50% RH)	$[NO]_0$ (10^{15} molecule cm^{-3})	$\Delta[NO]/\Delta t$ (10^{15} molecule cm^{-3})	$\Delta[NO_2]/\Delta t$ (10^{15} molecule cm^{-3})	$\frac{\Delta[NO_2]}{\Delta[NO]}$
1	0.65	0.50	1.03	2.05
2	3.20	0.70	2.70	3.86
3	7.00	1.50	5.50	3.67
4	8.20	2.20	6.90	3.14
5	14.3	2.80	10.0	3.57
6	22.0	5.00	16.0	3.20
7	40.0	8.00	26.8	3.35
			Average (±2σ)	3.5 ± 0.5

[a] $\Delta[NO_2]/\Delta[NO]$ was calculated from the change in NO and NO_2 concentrations between 0 and 300 minutes.

At 70% RH, a change in NO and NO_2 concentrations was observed as well. However, quantifying the loss of NO and the formation of NO_2 was difficult due to the overlap of water bands with the NO and NO_2 bands in the 1400 - 1700 cm^{-1} region. Figure 3.III.25 shows a typical concentration-time profile for the change in NO and NO_2 concentrations in the cell at 70 % RH. The stoichiometry, $\Delta[NO_2]/\Delta[NO]$, averaged over 4 experimental runs was 4.47 ± 0.96 (2σ). Although the error is large, the results suggest that the reaction in this case follows the same order as those at 40% and 50% RH.

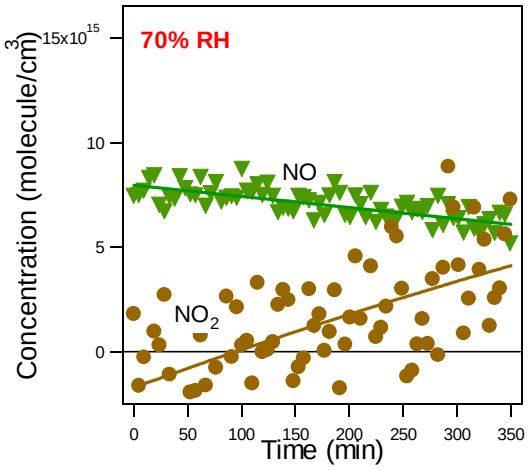

Figure 3.III.25. Decay of gas phase NO and formation of NO_2 in the long path cell whose walls had first been exposed to HNO_3. The relative humidity was 70% and the total pressure was 1 atm in N_2. Data are shown for an initial NO concentration of 7.44 $\times 10^{15}$ molecule cm^{-3}.

Figure 3.III.26 shows the rate of NO_2 formation in the long path cell as a function of the initial NO concentrations at 50 % RH. The linear relation indicates that the increase in NO_2 at lower concentrations, is proportional to NO and so the rate of the HNO_3 - NO reaction is first order in NO.

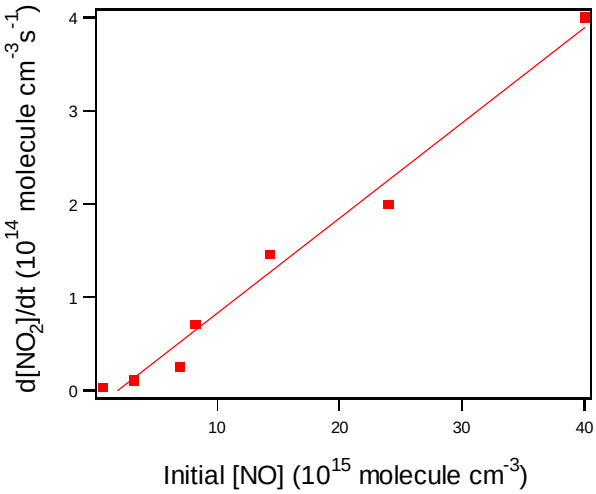

Figure 3.III.26. Rate of NO_2 formation as a function of initial NO concentration in the long path cell at 1 atm pressure and 50% RH.

It is important to mention that blank runs of NO introduced alone in the cell without coating the walls with HNO_3 (after disassembling and cleaning the cell walls) and HNO_3 alone without the introduction of NO at different relative humidities led to no reaction in the system.

In short, the HNO_3(ads)-NO reaction was greatly influenced by the relative humidity of the medium. At 25°C, the reaction was so slow as to be almost undetectable at 0 and 20% RH, but was highly accelerated with an increase in the relative humidity of the cell to 50% RH. This suggests that water is directly involved in the reaction and/or that it has an indirect effect by altering the surface.

III.D.2. Thermodynamic Considerations

Based on thermodynamic calculations detailed in Table 3.III.5, the gas phase reaction between HNO_3 and NO is unfavorable under normal conditions ($\Delta H^0 > 0$) (the values used in these calculations are summarized in Table 3.III.4). This is in agreement with Fairbrother et al. (1997), who suggested that this reaction is only possible in the atmosphere under certain catalytic conditions. Table 3.III.5 shows the reactions between HNO_3 in all its possible states, i.e. the liquid and aqueous phase, and the tri- and monohydrate forms in the liquid and solid phases, with NO in the gas phase. Most are not thermodynamically favorable or are nearly thermoneutral. However, in our experiments product formation was observed on the scale of minutes to hours, hence adsorption phenomena and surface reactions must lead to new physical states of H_2O and HNO_3.

Table 3.III.4. Thermodynamic Values Retrieved from NBS Tables (1982).

Substance	Enthalpy (kJ/mol)	Free Energy (kJ/mol)	Entropy (J/mol deg)
HONO(g)	-79.5	-46.0	254.1
HNO_3(g)	-135.1	-74.7	266.4
HNO_3(l)	-174.1	-80.7	155.6
HNO_3(aq)	-207.4	-111.2	146.4
NO_3^-(aq)	-205.0	-108.7	146.4
$HNO_3.H_2O$(l)	-473.5	-328.8	216.9
$HNO_3.3H_2O$(l)	-1056.0	-811.1	347.0
NO_2(g)	33.2	51.3	240.1
NO_2^-(aq)	-104.6	-32.2	-
NO(g)	90.2	86.5	210.8
H_2O(l)	-285.8	-237.1	70.0
H_2O(g)	-241.8	-228.6	188.9
$HNO_3.H_2O$(s)	-505.8		196.5
$HNO_3.3H_2O$(s)	-1095.2		87.8

Table 3.III.5 Reaction Thermodynamics for Reactions of HNO_3 in Various Forms with NO.

Equation	Enthalpy (kJ/mol)	Free Energy (kJ/mol)	Entropy (J/mol deg)	Free Energy (kJ/mol)
$HNO_3(g) + NO(g) \rightarrow HONO(g) + NO_2(g)$	-1.4	-6.5	17.0	-6.5
$HNO_3(g) + HONO(g) \rightarrow 2NO_2(g) + H_2O(g)$	39.2	-5.3	148.6	-5.1
$2HNO_3(g) + NO(g) \rightarrow 3NO_2(g) + H_2O(g)$	37.8	-11.8	165.6	-11.5
$HNO_3(l) + NO(g) \rightarrow HONO(g) + NO_2(g)$	37.6	-0.5	127.8	-0.5
$HNO_3(l) + HONO(g) \rightarrow 2NO_2(g) + H_2O(l)$	34.2	-7.8	140.5	-7.7
$2HNO_3(l) + NO(g) \rightarrow 3NO_2(g) + H_2O(l)$	71.8	-8.3	268.3	-8.2
$HNO_3(g) + NO(g) \rightarrow HONO(g) + NO_2(g)$	-1.4	-6.5	17.0	-6.5
$HNO_3(g) + HONO(g) \rightarrow 2NO_2(g) + H_2O(l)$	-4.8	-13.8	29.7	-13.7
$2HNO_3(g) + NO(g) \rightarrow 3NO_2(g) + H_2O(l)$	-6.2	-20.3	46.7	-20.1
$HNO_3(aq) + NO(g) \rightarrow HONO(g) + NO_2(g)$	70.9	30.0	137.0	30.1
$HNO_3(aq) + HONO(g) \rightarrow 2NO_2(g) + H_2O(l)$	67.5	22.7	149.7	22.9
$2HNO_3(aq) + NO(g) \rightarrow 3NO_2(g) + H_2O(l)$	138.4	52.7	286.7	53.0
$HNO_3.H_2O(l) + NO(g) \rightarrow HONO(g) + NO_2(g) + H_2O(l)$	51.2	10.5	136.5	10.5
$HNO_3.H_2O(l) + HONO(g) \rightarrow 2NO_2(g) + 2H_2O(l)$	47.8	3.2	149.2	3.3
$2HNO_3.H_2O(l) + NO(g) \rightarrow 3NO_2(g) + 3H_2O(l)$	99	13.7	285.7	13.9
$HNO_3.3H_2O(l) + NO(g) \rightarrow HONO(g) + NO_2(g) + 3H_2O(l)$	62.1	18.6	146.4	18.5
$HNO_3.3H_2O(l) + HONO(g) \rightarrow 2NO_2(g) + 4H_2O(l)$	58.7	11.3	159.1	11.3
$2HNO_3.3H_2O(l) + NO(g) \rightarrow 3NO_2(g) + 7H_2O(l)$	120.8	29.9	305.5	29.8
$HNO_3.H_2O(s) + NO(g) \rightarrow HONO(g) + NO_2(g) + H_2O(l)$	83.5	xx	156.9	36.7
$HNO_3.H_2O(s) + HONO(g) \rightarrow 2NO_2(g) + 2H_2O(l)$	80.1	xx	169.6	29.5
$2HNO_3.H_2O(s) + NO(g) \rightarrow 3NO_2(g) + 3H_2O(l)$	163.6	xx	326.6	66.2
$HNO_3.3H_2O(s) + NO(g) \rightarrow HONO(g) + NO_2(g) + 3H_2O(l)$	101.3	xx	405.6	-19.6
$HNO_3.3H_2O(s) + HONO(g) \rightarrow 2NO_2(g) + 4H_2O(l)$	97.86	xx	418.32	-26.8
$2HNO_3.3H_2O(s) + NO(g) \rightarrow 3NO_2(g) + 7H_2O(l)$	199.12	xx	823.94	-46.4

III.D.3. Water Coverage on the Cover Glass Surface

In order to investigate the role of water in the NO + HNO_3 reaction, the physical and chemical state of HNO_3 on the wet surface needs to be understood. A brief review is given here of the studies concerning the effect of the water concentration on the chemical and physical properties of HNO_3 solutions.

The behavior of nitric acid in solution has been extensively studied (*Redlich and Bigeleisen*, 1943; *Redlich*, 1946; *Miles*, 1961; *Davis and De Bruin*, 1964; *Schwartz and White*, 1981; *Hamill et al.*, 1988; *Koller and Hadzi*, 1991; *Molina et al.*, 1993). Nitric acid is a strong acid and is virtually entirely dissociated in dilute solutions (10 wt%) (*Miles*, 1961). As the concentration increases the degree of dissociation decreases and the concentration of hydrates increases. Nitric acid tri-(NAT) and monohydrate (NAM) are formed around 50 and 77 wt%, respectively. At the highest concentration (100 wt%), nitric acid undergoes a self-dehydration, which produces nitric acid, NO_2^+, NO_3^-, and water. Schnitzer et al. (1999) confirmed the ionic nature of nitric acid at the interface at low HNO_3 concentrations using a Sum Frequency Generation (SFG) technique. However, for concentrated HNO_3 solutions, the SFG measurements indicated an enrichment of the surface with molecular HNO_3 species and a lack of free OH water bands, suggesting that water is complexed and/or displaced from the surface. The excess of HNO_3 at the surface confirmed the studies of Hard et al. (1977) and Donaldson and Anderson (1999) that the surface tension of HNO_3 solutions decreases as the concentration of HNO_3 increases. This was further investigated in this laboratory and, as will be discussed below and in the next section, we determined the amount of water adsorbed on borosilicate cover glasses and found that molecular nitric acid is enriched at the surface, most likely in the monohydrate form.

The amount of H_2O absorbed on glass at different relative humidities (RH) was determined by transmission infrared spectroscopy. The glass samples were enclosed in the glass cell described in the Materials and Methods section.

Figure 3.III.27 shows the absorption bands of H_2O adsorbed on cover glass from 3800 to 2800 cm^{-1}. The number of layers (L) of adsorbed H_2O on glass can be calculated using the water bands in this wavenumber region and the following procedure.

The integrated cross section ($\bar{\sigma}$) of bulk water has been determined in previous studies (*Foster and Ewing*, 1999, 2000) to be 1.4×10^{-16} cm $molecule^{-1}$. From this value of $\bar{\sigma}$, the surface density (S) of adsorbed H_2O can be calculated using the measured integrated absorbance, $\tilde{A}$, using Figure 3.III.27 and equation (Eq. III.1).

$$S = \frac{2.303\tilde{A}}{N\bar{\sigma}} \qquad \text{(Eq. III.1)}$$

where $N = 10$ is the number of cover glass surfaces. The number of layers of adsorbed H_2O can be obtained by dividing the surface density S by the density of a monolayer ($S_{mono} = 1\times10^{15}$).

$$L = \frac{S}{S_{mono}} \qquad \text{(Eq. III.2)}$$

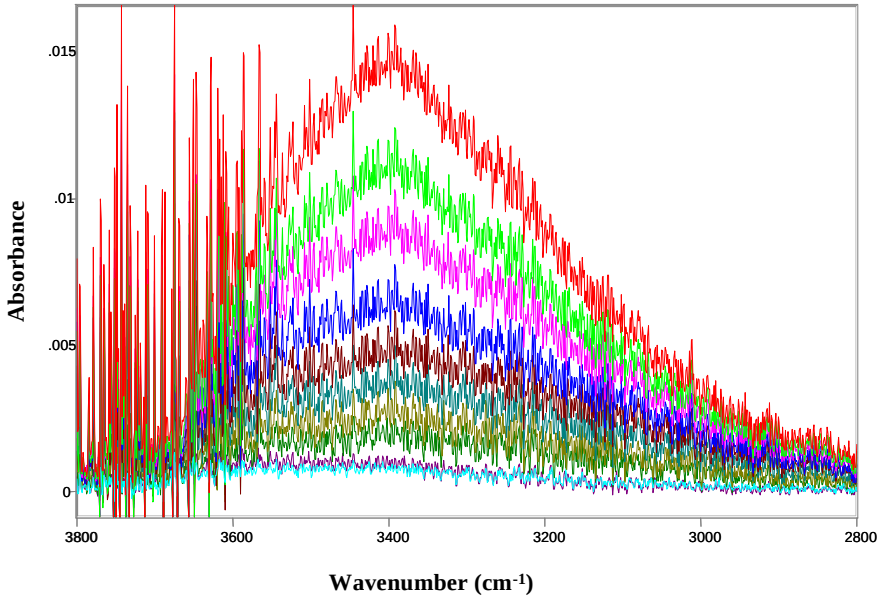

Figure 3.III.27. Absorption bands between 3800 to 2800 cm^{-1} of H_2O adsorbed on cover glass at different relative humidities.

Figure 3.III.28 shows the number of layers of adsorbed H_2O calculated as a function of RH (results are also summarized in Table 3.III.6).

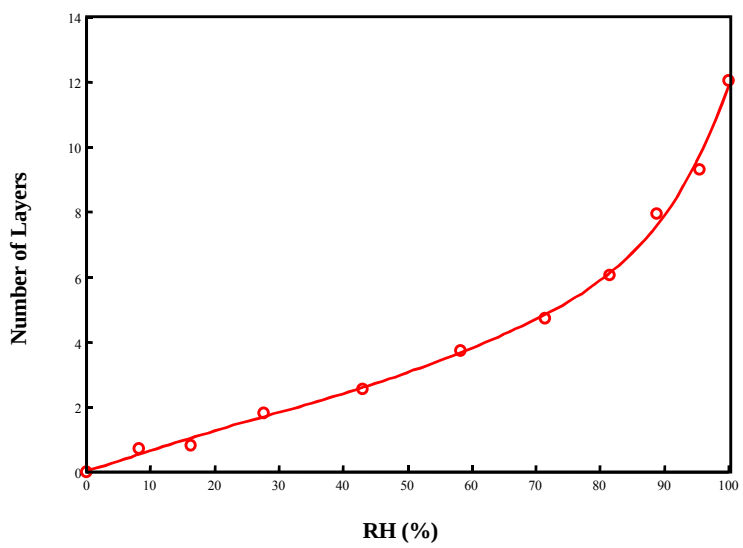

Figure 3.III.28. Number of layers of adsorbed H_2O on cover glass shown as a function of different relative humidities.

Table 3.III.6. Experimental Results for the Number of Layers at Different RH.

RH	Number of Layers
8.2	0.7
16.3	0.8
27.7	1.8
43.0	2.6
58.2	3.7
71.4	4.7
81.5	6.1
88.7	8.0
95.5	9.3
100.0	12.0

III.D.4. Estimate of HNO_3 Concentration on the Borosilicate Glass Walls of the Long Path Cell

In order to estimate the potential concentrations of HNO_3 in thin water films on the glass surfaces of the cell, we assume that the procedure used to produce HNO_3(ads) on the cell walls, introducing about 3 Torr of gaseous HNO_3 and then pumping it out several times, yielded a monolayer. Based on the amount of water on the cell walls at different RH (Table 3.III.6), dissolving the monolayer of HNO_3 in the water film at 20% RH would give a 78 wt% HNO_3 solution while at 50% RH, it would be 54 wt%. No HNO_3 was detected in the gas phase. Thus, based on these calculations, we conclude that at 20% RH, the concentration of molecular HNO_3 increases and the walls are enriched with nitric acid that is approaching the 100% phase, leading probably to the formation of the NO_2^+ and NO_3^- ions. At 50% RH, the ~μm-thick layer of HNO_3 is acting as a thin layer of a highly concentrated nitric acid solution containing predominantly molecular HNO_3 most likely in the monohydrate form at the interface as suggested by our group (next section) and others as well.

At 20% RH, a coverage of ~ 1 monolayer of water on the glass walls corresponds to $1x10^{15}$ molecules cm^{-2} of H_2O and at 50% RH an estimated coverage of ~3 monolayers will increase the number of H_2O molecules to $3x10^{15}$ molecules cm^{-2}.

IV. INFRARED SPECTROSCOPIC STUDIES OF BINARY SOLUTIONS OF NITRIC ACID AND WATER AND TERNARY SOLUTIONS OF NITRIC ACID, SULFURIC ACID AND WATER AT ROOM TEMPERATURE: EVIDENCE FOR MOLECULAR NITRIC ACID AT THE SURFACE

The results described in sections III.C. and III.D. suggest that molecular nitric acid present at the interface of a thin liquid film is responsible for the reaction with gas phase NO. Loss of NO and adsorbed HNO_3 and formation of gaseous NO_2 and smaller amounts of HONO were observed using FTIR with either a "wet" porous silica surface or a glass cell at 50% relative humidity but not at relative humidities of 0 or 20%. It is therefore of interest to understand the chemical and physical state of nitric acid at the air-water interface and in thin water films, in order to understand at the molecular level the mechanisms of such heterogeneous NO_x reactions.

We report here the results of single reflectance FTIR (SR-FTIR) studies of binary solutions of nitric acid in water ($HNO_3 – H_2O$), as well as ternary solutions of nitric acid, sulfuric acid and water ($H_2SO_4 – HNO_3 – H_2O$) at room temperature. As discussed in more detail below, SR probes not only the surface but also the bulk below to depths of the order of microns, depending on the particular solution and frequency of the radiation. Since the signal decays exponentially with depth from the interface, signals due to species at the air-solution interface are relatively stronger. For comparison to the literature, attenuated total reflectance (ATR) spectra were also taken. These ATR spectra are similar to transmission spectra of bulk solutions (*Harrick*, 1967; *Marley et al.*, 1992). Thus, differences between the SR and ATR spectra reflect primarily differences in species at or near the interface.

IV.A. Spectra of Binary Solutions of HNO_3 and H_2O.

Figures 3.IV.1 and 3.IV.2 show SR and ATR spectra of various solutions of nitric acid in water. Spectra (a) through (f) are in decreasing order of concentration from 40 to 0.9 mol% HNO_3, while (g) is that for pure water. In both figures, absorption bands are observed in the most concentrated solutions at 951, 1307, 1435/1421, 1673/1662, 2670 and 2936 cm^{-1}; a broad peak is also seen at 3600 cm^{-1}. All but the latter peak are attributable to known absorption bands of molecular nitric acid: 2936 (2 ν_3), 2670 (2 ν_4), 1673 (ν_2), 1435 (ν_3), 1307 (ν_4) and 951 (ν_5) (*Querry and Tyler*, 1980; *Ritzhaupt and Devlin*, 1991; *Devlin et al.*, 1999; *Biermann et al.*, 2000). It is interesting to note that the spectrum in Figure 3.IV.1a corresponding to 40 mol% HNO_3 is very similar, especially in the region below 3000 cm^{-1}, to that reported for a solid amorphous thin film deposit of a 1:1 mixture of HNO_3:H_2O at lower temperatures and assigned to the monohydrate, $HNO_3 \cdot H_2O$ (*Ritzhaupt and Devlin*, 1977; *Tolbert and Middlebrook*, 1990; *Ritzhaupt and Devlin*, 1991; *Smith et al.*, 1991; *Devlin et al.*, 1999).

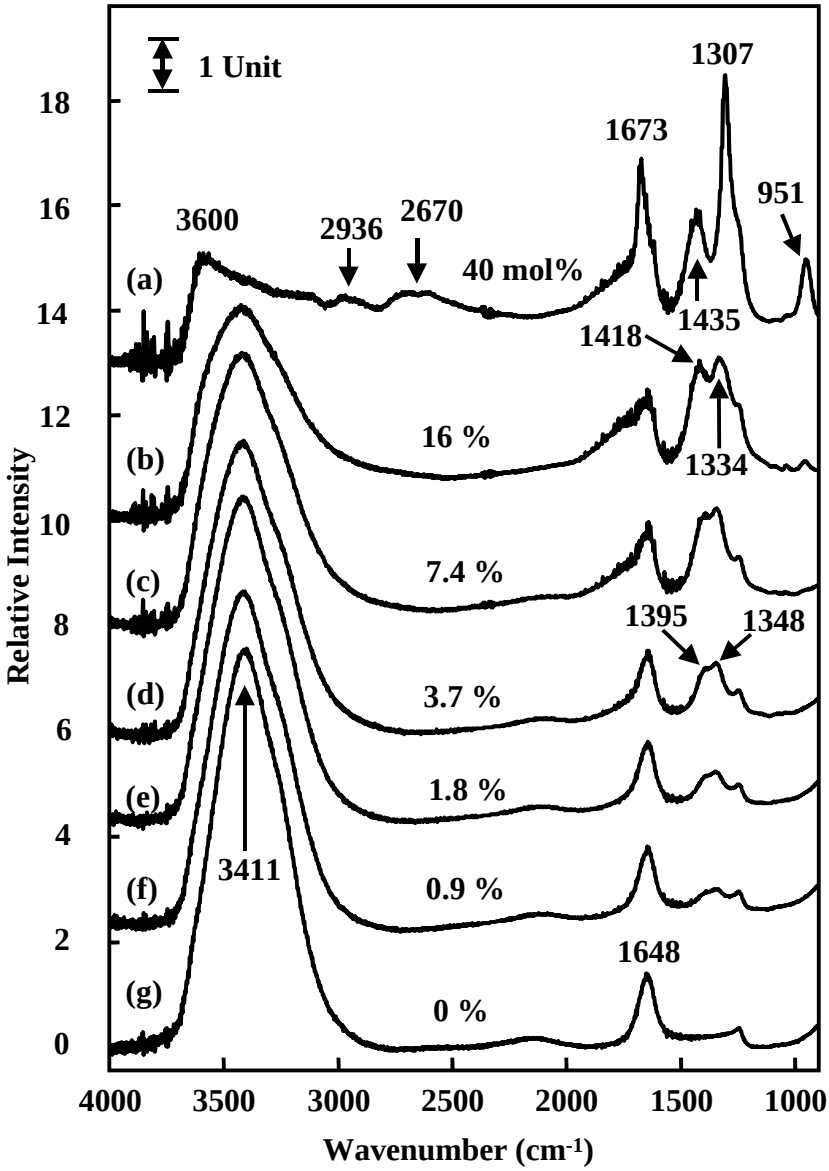

Figure 3.IV.1. SR spectra of $HNO_3 - H_2O$ solutions. The concentrations of HNO_3 for spectra (a)-(f) are 40, 16, 7.4, 3.7, 1.8 and 0.9 mol %, respectively. Spectrum (g) is for pure water.

It is well known that molecular nitric acid is largely undissociated at high concentrations. The degree of dissociation of HNO_3 varies from 0.17 at 40 mol % to 0.99 at 0.9 mol% HNO_3 (*Davis and De Bruin*, 1964). In addition, HNO_3 is known to form hydrates in these solutions, particularly the monohydrate and the trihydrate, with the relative amounts varying with the concentration of HNO_3 in solution (*Högfeldt*, 1963). At 40 mol %, for example, where the ratio of H_2O to HNO_3 is 3:2, the monohydrate $HNO_3 \cdot H_2O$ is the major form of the acid. Högefeldt

(1963) estimated that under these conditions, about 80% of the undissociated acid is in the form of the monohydrate, 12% is unhydrated HNO_3 and 8% is the trihydrate, $HNO_3 \cdot 3H_2O$. Hence, it is not surprising that the spectrum of the most concentrated solution is similar to that of the monohydrate at low temperatures.

In short, the infrared bands in the most concentrated solution are due to undissociated nitric acid hydrates, primarily the monohydrate. Ab initio calculations, supported by microwave spectroscopic measurements, show that when gas phase HNO_3 forms a 1:1 complex with water, most of the infrared bands are shifted by relatively small amounts, < 30 cm^{-1} (*Tao et al.*, 1996; *Canagaratna et al.*, 1998). However, the H-O stretch of nitric acid is predicted to red-shift by ~340 cm^{-1}, and the H-O-N bend is predicted to blue-shift by ~150 cm^{-1}. While these calculations are for gaseous species, qualitatively similar shifts might be expected in solution for the undissociated, unhydrated form compared to the monohydrate. The red-shifted H-O stretch would be difficult to observe because of overlapping water bands (indeed, even the unshifted 3410 cm^{-1} band in liquid nitric acid is generally not observed for the same reason) (*Querry and Tyler*, 1980). The H-O-N bend in gas phase nitric acid is at 1331 cm^{-1} and in liquid HNO_3, it appears at 1395 cm^{-1} (*McGraw et al.*, 1965; *Querry and Tyler*, 1980). In $HNO_3 - H_2O$ solutions, this H-O-N bend is observed at ~1430 cm^{-1}, blue-shifted by ~100 cm^{-1} compared to the gas phase (*Querry and Tyler*, 1980). Such a shift is qualitatively consistent with the effects of hydrogen-bonding with water[31] and with the ab initio calculations (*Tao et al.*, 1996).

As the concentration is reduced below 40 mol % [spectra (b) – (f)], the peaks in the 1300 – 1500 cm^{-1} region change in a manner consistent with conversion of molecular nitric acid to the nitrate ion, i.e., to the dissociated acid. The splitting of ~130 cm^{-1} between the two bands at 1435 (ν_3) and 1307 (ν_4) cm^{-1}, characteristic of the monohydrate $HNO_3 \cdot H_2O$ (*Ritzhaupt and Devlin*, 1977; *Tolbert and Middlebrook*, 1990; *Ritzhaupt and Devlin*, 1991; *Smith et al.*, 1991; *Devlin et al.*, 1999), decreases and is replaced by a broad band at ~1355 cm^{-1}.

Comparison to a SR spectrum of $NaNO_3$ and to literature spectra (*Marley et al.*, 1993) shows that this band is characteristic of the nitrate ion, NO_3^-, in aqueous solutions at room temperature. Simultaneously, the peak at ~1670 cm^{-1} due to molecular nitric acid (Fig. 3.IV.1a and 3.IV.2a) in the 40 mol % solution shifts toward lower wavenumbers and disappears into the peak at 1648 cm^{-1} due to liquid water. The same behavior has been reported in transmission studies of HNO_3-water solutions at room temperature as well (*Biermann et al.*, 2000).

In Figures 3.IV.1 and 3.IV.2, the absorption bands due to liquid water at ~3400 and 1648 cm^{-1} are clearly visible in the spectra of the more dilute solutions. However, as the nitric acid concentration is increased to 40 mol %, the strongest water peak is shifted from 3400 cm^{-1} toward higher wavenumbers characteristic of non-hydrogen bonded gas phase water which has the ν_3 asymmetric stretch at 3756 and the ν_1 symmetric stretch at 3652 cm^{-1} (*Herzberg*, 1945). This is reminiscent of recent studies of water adsorbed on NaCl at sub-monolayer coverages which minimized lateral interactions associated with hydrogen bonding and led to a blue-shift in the 3400 cm^{-1} water band (*Foster and Ewing*, 2000). In the present case of 40 mol % HNO_3, most of the water is tied up in the form of the hydrates as well as H_3O^+, whose ν_4 absorption band at 1742 cm^{-1} can be seen as a broad shoulder on the high wavenumber side of the 1673 cm^{-1}

nitric acid band (*Querry and Tyler*, 1980). Thus, the amount of free, hydrogen-bonded liquid water is relatively small, resulting in a decrease in the 3400 cm^{-1} band and a shift of the remaining infrared absorption due to water to higher wavenumbers.

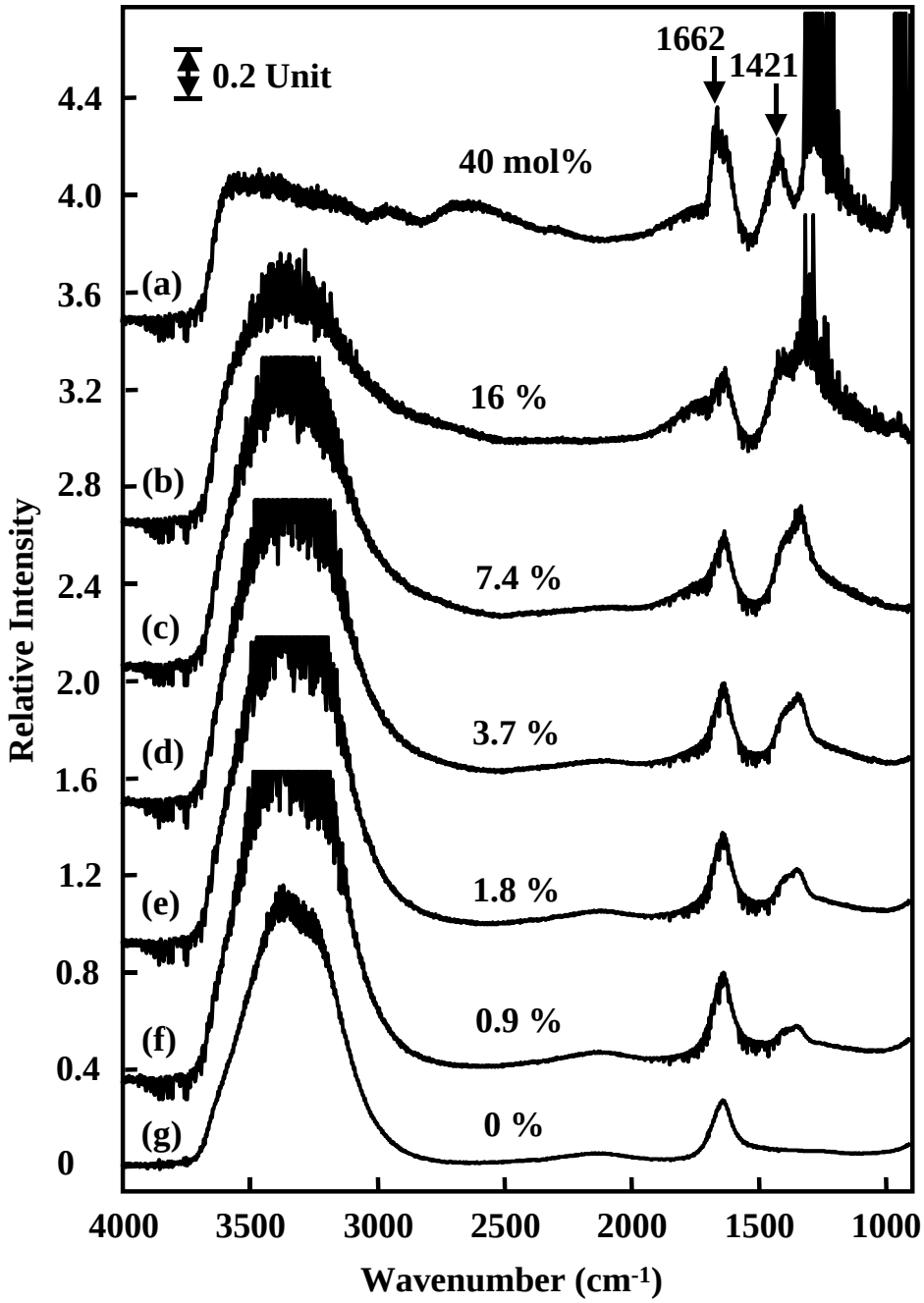

Figure 3.IV.2. ATR spectra of the HNO_3 solutions shown in Figure 3.IV.1.

In short, the major features of both the SR and ATR spectra are consistent with nitric acid being primarily dissociated in the more dilute solutions, and changing to undissociated HNO_3 mainly in the form of the monohydrate, $HNO_3 \cdot H_2O$, in the most concentrated solution.

Figure 3.IV.3 shows, however, that there are quantitative differences between the SR and ATR spectra of the most concentrated solution. The blue-shift in the 3400 – 3600 cm^{-1} region is more pronounced for the SR spectrum, suggesting less hydrogen-bonded liquid water in the surface film. In addition, the bands due to nitric acid at 1673, 1435, 1307 and 951 cm^{-1} are significantly more intense in the SR compared to the ATR spectrum. This comparison shows that molecular nitric acid must be enhanced at the surface of the most concentrated solution, since the contribution to absorption in SR spectra decreases exponentially with distance from the reflecting interface.

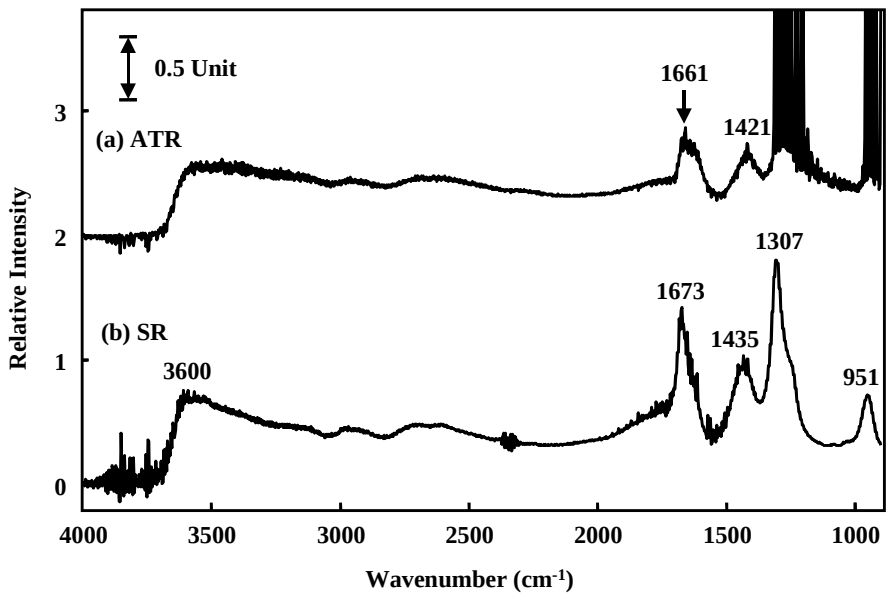

Figure 3.IV.3. Comparison of the (a) ATR and (b) SR spectra of the 40 mol % HNO_3 solution. Spectrum (a) is the same as Figure 3.IV.2a, and spectrum (b) is the same as Figure 3.IV.1a.

Because the ATR spectra have been corrected for the known wavelength dependence, the actual ATR spectra as recorded had stronger bands in the lower wavenumber region (*Harrick*, 1967; *Marley et al.*, 1992). To ensure that an artifact is not introduced by correcting the absorbance for the wavelength dependence, the ATR and SR spectra for the 3.7 mol % (2 M) HNO_3 solution, where the nitric acid is 95% dissociated, were compared. As seen in Figure 3.IV.4, the ATR corrected relative band intensities in the 900 – 1700 cm^{-1} region, which are due to water at ~1640 cm^{-1} and NO_3^- at 1355 cm^{-1}, are in excellent agreement with those in the SR spectrum. Hence the less intense peaks in the ATR spectrum of the 40 mol % HNO_3 solution in Figure 3.IV.3 cannot be an artifact from the wavelength correction.

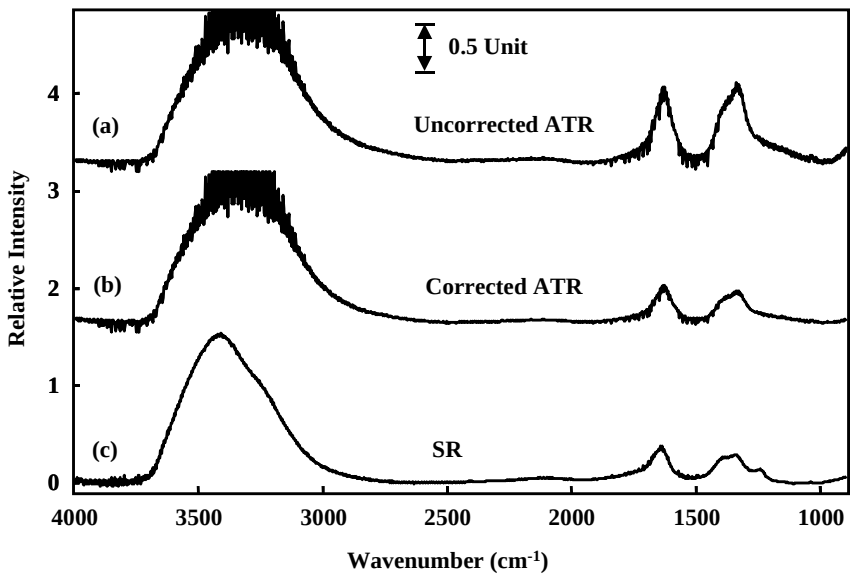

Figure 3.IV.4. Comparison of the ATR spectra for the 3.7 mol % HNO_3 – H_2O solution as recorded; (b) corrected for the wavelength dependence; (c) the SR spectrum. The agreement of the relative band intensities between (b) and (c) substantiates the wavenumber correction of the ATR spectrum.

This direct detection of the enhancement of HNO_3 at the interface is consistent with the surface tension measurements of Donaldson and Anderson (1999) who proposed that the decrease in surface tension with increasing nitric acid concentrations was indicative of a surface film of HNO_3. Similarly, Shultz and coworkers used SFG to show that at 40 mol % HNO_3, there is no detectable signal from the dangling –OH of water at the surface and the signal from hydrogen-bonded water is very small (*Schnitzer et al.*, 1999). They attributed this to the formation of either contact ion pairs or molecular nitric acid at the surface, although a direct signal due to the H-O stretch in nitric acid expected in the spectral region they studied was not detected. The studies reported here appear to be the first direct detection of enhanced HNO_3 at the interface of these concentrated solutions.

IV.B. Spectra of Ternary Solutions of HNO_3, H_2SO_4 and H_2O.

Figure 3.IV.5 shows a series of SR spectra of H_2SO_4 – HNO_3 – H_2O solutions in which the mol % H_2SO_4 is constant at 25% and varying concentrations of HNO_3 from 25 mol % in part (a) to 0 mol % in part (e) are present. Bands due to molecular nitric acid at ~1677 cm^{-1}, 1307 cm^{-1} and 951 cm^{-1} are again clearly observed in the more concentrated solutions. The bands at ~1196 and 1053 cm^{-1} seen both with and without HNO_3 are attributable to molecular H_2SO_4 and the bisulfate ion (*Biermann et al.*, 2000). The spectra of both H_2SO_4 – H_2O as well as H_2SO_4 – HNO_3 – H_2O are in agreement with spectra of such mixtures reported in the literature at room and low temperatures (*Adams and Downing*, 1986; *Middlebrook et al.*, 1993; *Anthony et al.*, 1995; *Iraci et al.*, 1995; *Bertram et al.*, 1996; *Anthony et al.*, 1997; *Biermann et al.*, 2000).

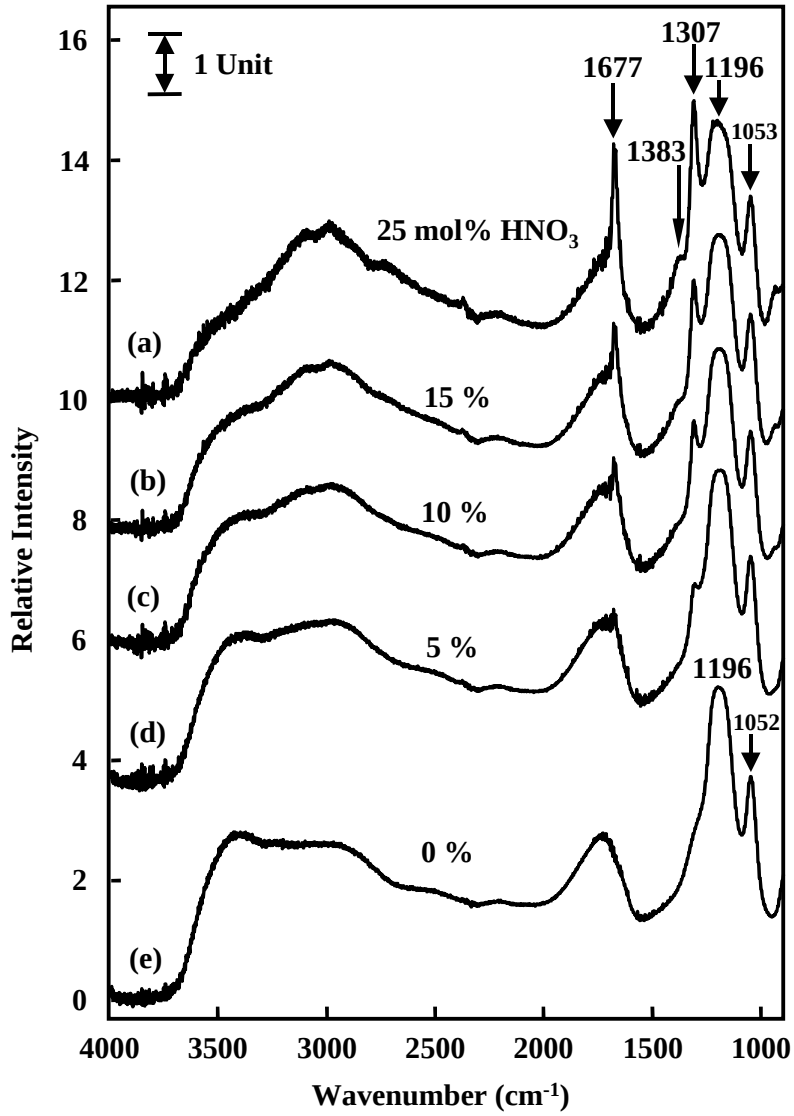

Figure 3.IV.5. SR spectra of ternary solutions of $H_2SO_4 – HNO_3 – H_2O$. The mol% H_2SO_4 is 25 % in all 5 solutions. The mol% HNO_3 is (a) 25, (b)15, (c) 10, (d) 5, and (e) 0.

Figure 3.IV.6 compares the SR spectra of a 28.5 mol % (12.3 M) $HNO_3 – H_2O$ solution (Fig. 3.IV.6a) to that of a ternary solution consisting of 25 mol % H_2SO_4, 25 mol % HNO_3 and 50 mol % H_2O. The $HNO_3 – H_2O$ solution is calculated to have the same concentration of undissociated nitric acid as in the $H_2SO_4 – HNO_3 – H_2O$ solution (*Davis and De Bruin*, 1964). While molecular nitric acid bands are clear in both cases, there are several significant differences in the spectra of the two solutions.

These differences can be seen more clearly in Figure 3.IV.6c which is the difference between the SR spectrum of the $H_2SO_4 – HNO_3 – H_2O$ solution (25 %: 25 %: 50 %) and that of the $H_2SO_4 – H_2O$ solution (25% : 75 %). The bands due to sulfuric acid are subtracted out, but

because there is more water in the $H_2SO_4 – H_2O$ solution, the strong water band around 3400 cm^{-1} is over-subtracted, leading to a negative band in this region. However, comparison of the remaining absorption bands to those assigned to undissociated HNO_3 in Figure 3.IV.6a show there is a red-shift in the 1437 cm^{-1} band, to 1383 cm^{-1} (the weak peaks at ~ 1140 and 1056 cm^{-1} may be due to incomplete subtraction of the contributions from sulfate and bisulfate ions). This band is the H-O-N bend of nitric acid. The gas phase fundamental for this bend appears at 1331 cm^{-1}, but consistent with the expected effects of hydrogen bonding on such a bending motion, the infrared absorption is shifted to 1395 cm^{-1} in the pure liquid and to 1429 cm^{-1} in water solutions (*Cohn et al.*, 1952; *Pimentel and McClellan*, 1960; *McGraw et al.*, 1965; *Querry and Tyler*, 1980; *Biermann et al.*, 2000). The observation that the band is at ~1383 cm^{-1} in the $H_2SO_4 – HNO_3 – H_2O$ solution suggests that the spectrum in Figure 3.IV.6c is due to anhydrous, undissociated molecular nitric acid. This is consistent with the similarity of this spectrum to one of nearly anhydrous nitric acid particles at low temperatures (*Devlin et al.*, 1999 and Devlin, personal communication).

Figure 3.IV.6d shows the difference spectrum in Figure 3.IV.6c but with the 3400 cm^{-1} water band corrected by an amount estimated to be equivalent to the 25 mol % difference in H_2O. It can be seen that there is then little in the way of absorption bands remaining in this region, in contrast to Figure 3.IV.6a where a blue-shifted band assigned to water is evident. This is also consistent with the nitric acid at the surface being anhydrous, rather than the monohydrate form.

Thus, for the ternary solution, the surface is again enhanced in undissociated nitric acid. However, the position of the H-O-N bending vibration suggests that the form is anhydrous HNO_3, in contrast to the $HNO_3 – H_2O$ solution where the monohydrate appears to be the primary species. This may be due to the fact that H_2SO_4 is known to form acid hydrates which tie up the water (*Phillips*, 1994). For example, it has been found in SFG studies that as the concentration of H_2SO_4 is increased, the signal from water at the interface decreases until there is essentially no signal due to water at sulfuric acid mole fractions ≥ 0.4 (*Baldelli et al.*, 1997, 1998, 1999; *Radüge et al.*, 1997).

The presence of a film of anhydrous HNO_3 when added to $H_2SO_4 – H_2O$ is consistent with the decreased surface tension of ternary solutions reported by Donaldson and Anderson (1999) and with the results of molecular scattering experiments which show that the residence time of HNO_3 on a D_2SO_4 surface is much longer than for HCl and HBr, allowing extensive H $\rightarrow$ D exchange to occur (*Morris et al.*, 2000). It is interesting, however, that Fairbrother and Somorjai (2000) reported evidence for enhanced nitrogen at the surface of sulfuric acid only at temperatures below 200 K.

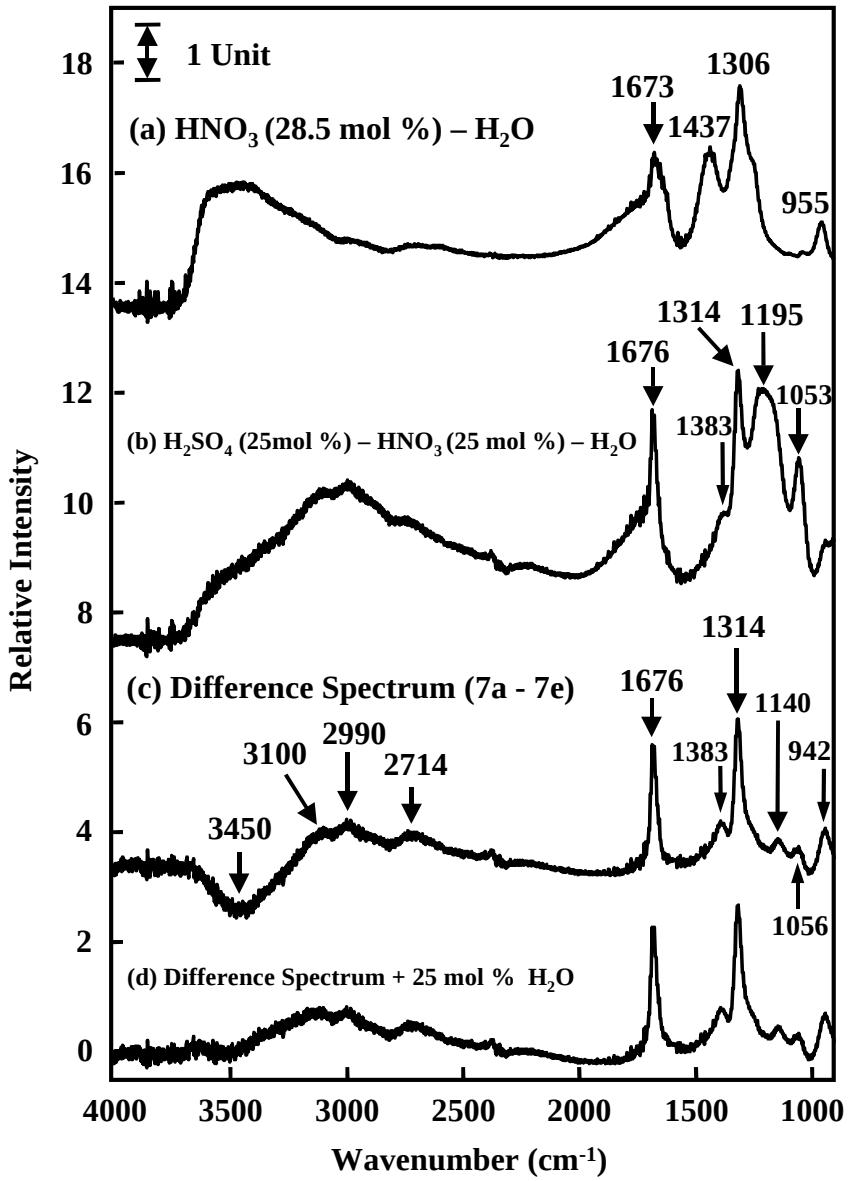

Figure 3.IV.6. Comparison of SR spectra of (a) 28.5 mol % HNO_3 – H_2O solution with (b) H_2SO_4 (25 mol %) – HNO_3 (25 mol %) – H_2O (50 mol %) as in Figure 3.IV.5a. The concentration of undissociated HNO_3 is the same in these two mixtures; (c) is the difference spectrum between H_2SO_4 (25 mol %) – HNO_3 (25 mol %) – H_2O (50 mol %) and H_2SO_4 (25 mol %) – H_2O (75 mol %), i.e. Figure 3.IV.5a – Figure 3.IV.5e; (d) difference spectrum in (c) with one third of water peak at 3400 cm^{-1} observed in Figure 3.IV.5e added back to adjust for the different amounts of water in the subtracted spectrum.

V. INITIAL AIRSHED MODELING RUNS

Time series plots for ozone, PM2.5 particulate nitrate, and HONO are presented for the Central Los Angeles and Riverside sites. In addition, all plots show reported measured values (Observations). Figures 3.V.1 - 3.V.4 show the plots for the Base Case, observations, 100% land reaction and 10% land reaction. Figures 3.V.5 - 3.V.8 show the plots for the Base Case, observations, and Svensson kinetics for HONO formation from NO_2 surface reaction.

The results can be summarized as follows:

- In Central LA, including the 100% land reaction gives a better match to the ozone peak on the second day of the simulation than does the base case; this mismatch between the base case and the observed values of O_3 has been the subject of considerable debate in the past. (Note, however, that the 100% land reaction then overpredicts for day 1).
- In Riverside, including the land reaction generates a predicted "double peak" for ozone, consistent with common observations in that area; the base case does not predict such double peaks.
- Significant increases in particulate nitrate are predicted for both locations with either 100% or 10% land reaction; this is to be expected because less HNO_3 is deposited out, leaving more available for forming particulate nitrate.

The surface hydrolysis of NO_2 to generate HONO,

$$2\ NO_2 + H_2O \rightarrow HONO + HNO_3 \qquad \text{(V.1)}$$

is often represented in current airshed models by a simple second order reaction of NO_2 with water (i.e. first order in NO_2 and first order in H_2O):

$$-\frac{d[NO_2]}{dt} = 2\,k_1\,[NO_2][H_2O] \qquad \text{(Eq. V.1)}$$

where the effective rate constant for (Eq. V.1) is $k = 2\ k_1 = 1.15 \times 10^{-8}\ ppm^{-1}\ min^{-1}$ at 25°C. However, this certainly cannot be the correct parameterization of HONO formation since it does not involve a term representing the available surface on which the reaction occurs.

In this project, we established that the rate of NO_2 loss in our experimental system was well matched by the parameterization proposed by Svensson et al. (1987). This involves two terms, one of which depends on the available surface-to-volume ratio of the reactor and one of which is independent of the surface:

$$-\frac{d[NO_2]}{dt} = \left[5.6\times10^{-9}\left(\frac{S}{V}\right) + 2.3\times10^{-9}\right][NO_2][H_2O] \qquad \text{(Eq. V.2)}$$

where the surface area-to-volume ratio, S/V, is in units of m^{-1} and the second order rate constant term is in units of $ppm^{-1}\ min^{-1}$. As a result, the Svensson et al. parameterization was introduced

into the airshed model in place of the original, or base case, formulation to assess the impact on predicted HONO levels. Figures 3.V.9 and 3.V.10 show the predicted HONO levels for Central Los Angeles and for Riverside for the base case and for the Svensson et al. parameterization. It is seen that in both cases, less HONO is predicted by the Svensson parameterization compared to the base case.

The reason for this is that the S/V value for particles in air is predicted by the model to be at its maximum 0.06 m^{-1}. This is sufficiently small that the first term which depends on S/V is small compared to the second, constant term. However, this second term has a rate constant that is about a factor of five smaller than assumed in the base case, leading to lower predicted HONO levels.

Clearly this is an area that needs much more work to define the appropriate parameterization to use for HONO production in models.

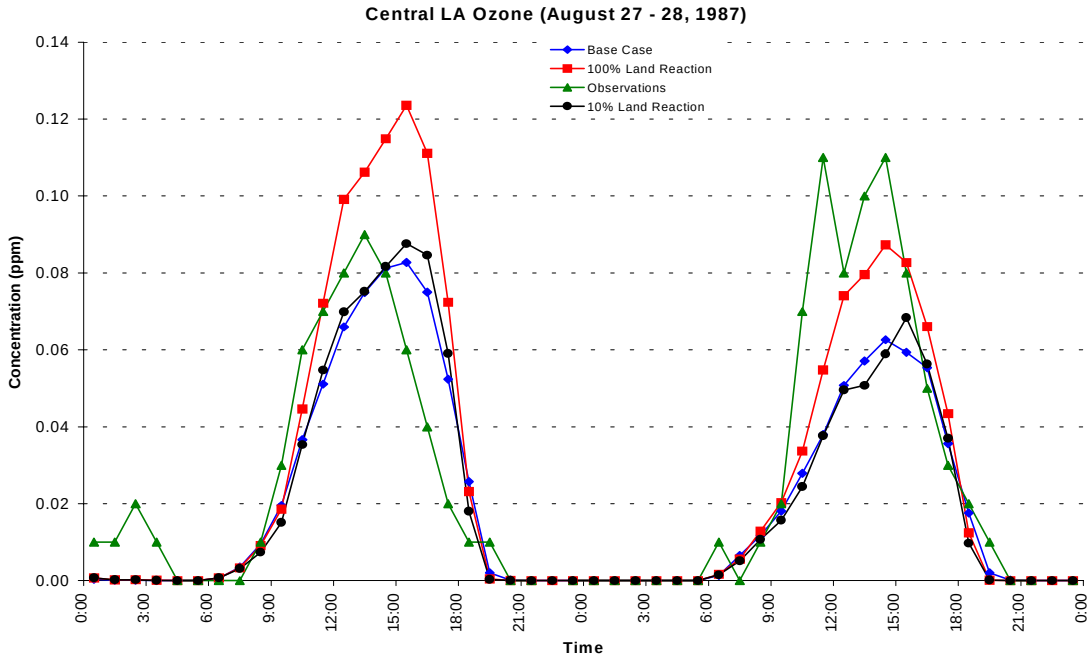

Figure 3.V.1. Model of ozone: Base Case, observations, 100% land reaction, and 10% land reaction for Central L.A.

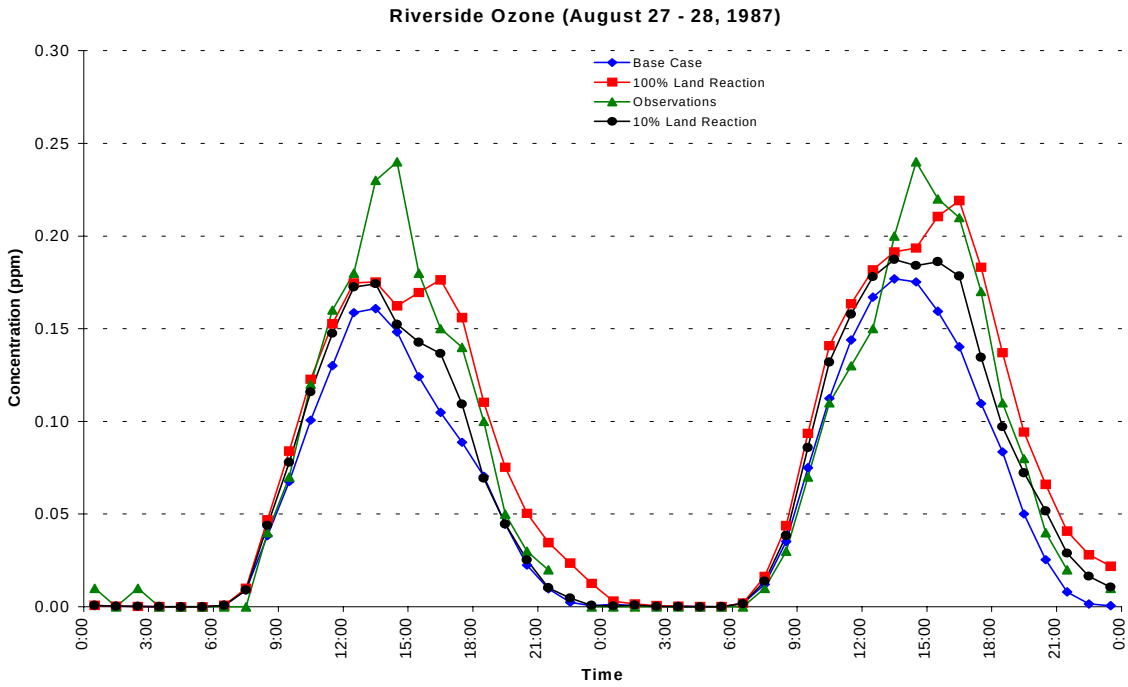

Figure 3.V.2. Model of ozone: Base Case, observations, 100% land reaction, and 10% land reaction for Riverside.

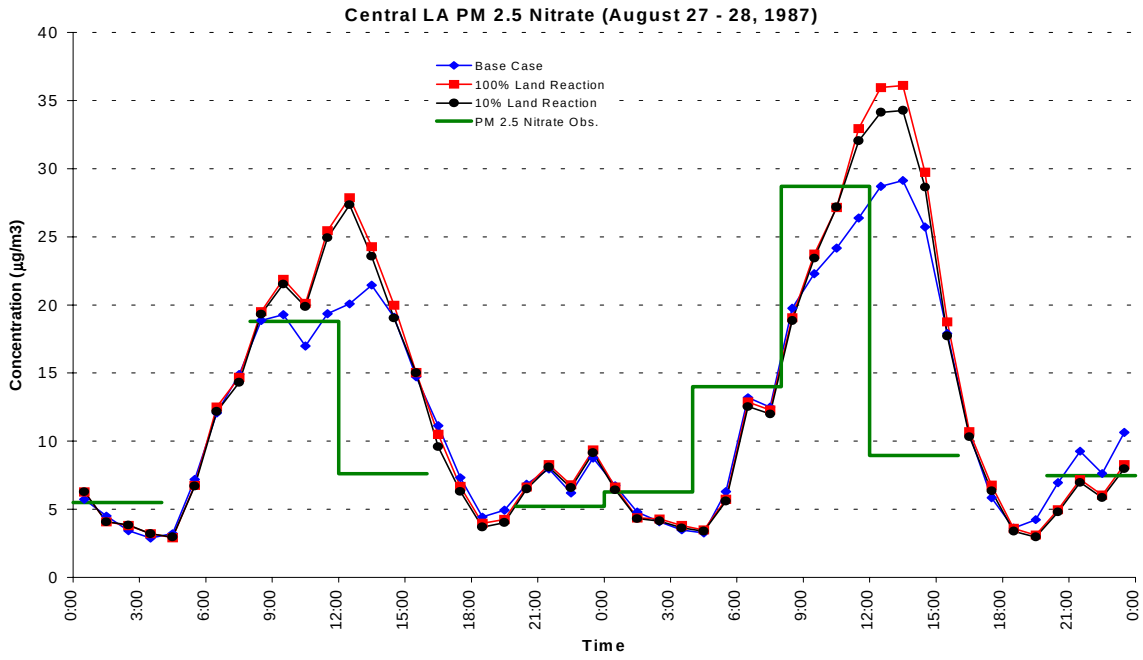

Figure 3.V.3. Model of PM 2.5 nitrate: Base Case, observations, 100% land reaction, and 10% land reaction for Central L.A.

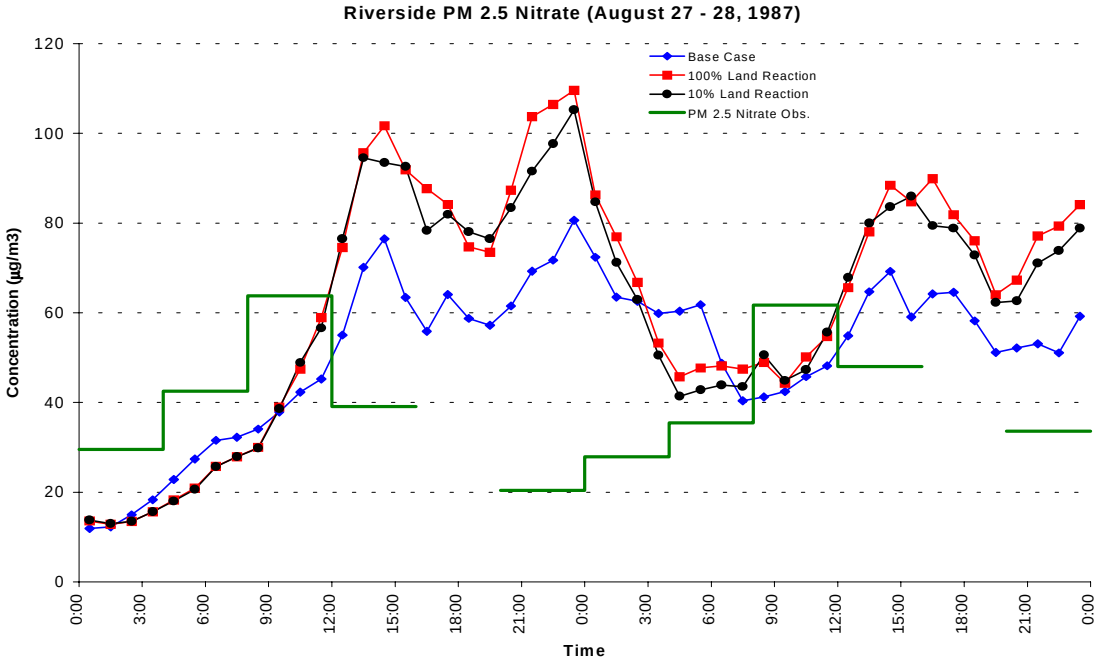

Figure 3.V.4. Model of PM 2.5 nitrate: Base Case, observations, 100% land reaction, and 10% land reaction for Riverside.

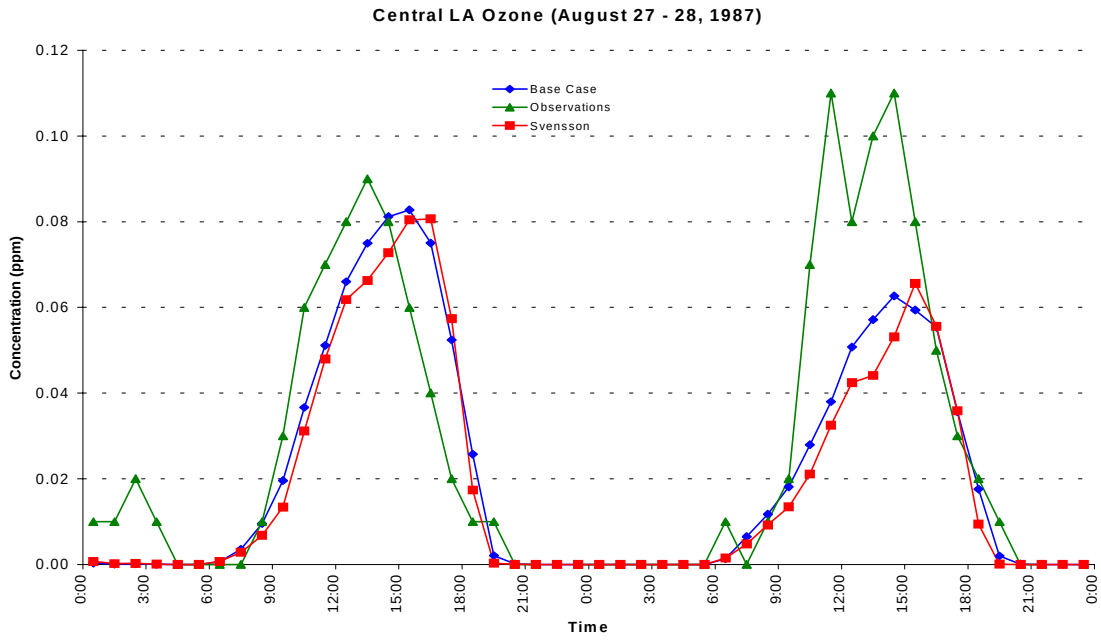

Figure 3.V.5. Model of ozone: Base Case, observations, and Svensson kinetics for Central L.A.

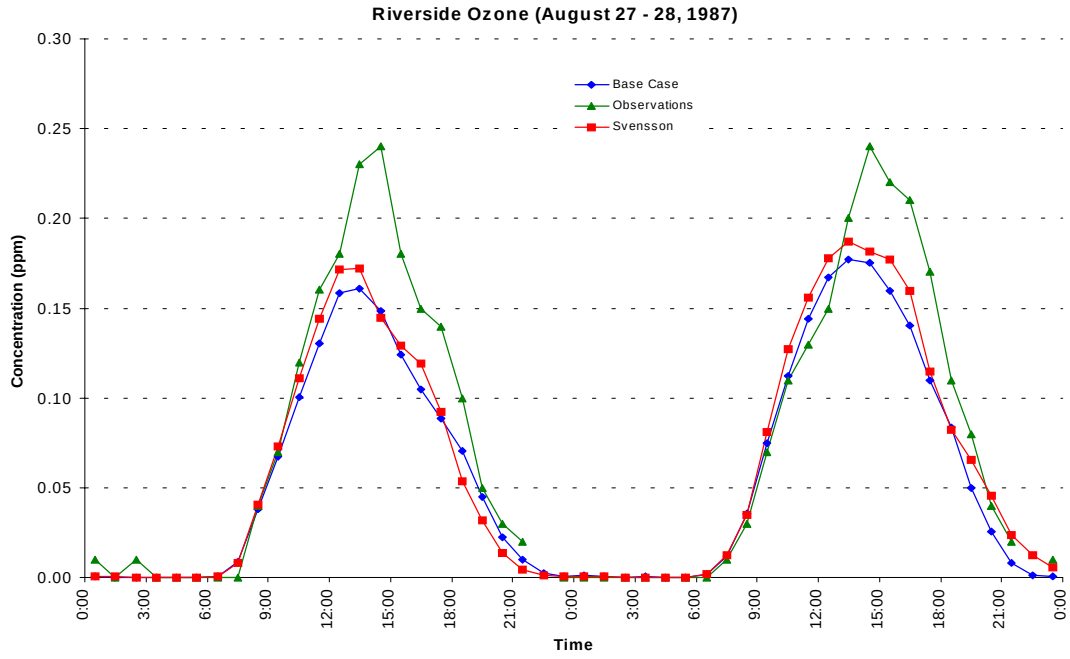

Figure 3.V.6. Model of ozone: Base Case, observations, and Svensson kinetics for Riverside.

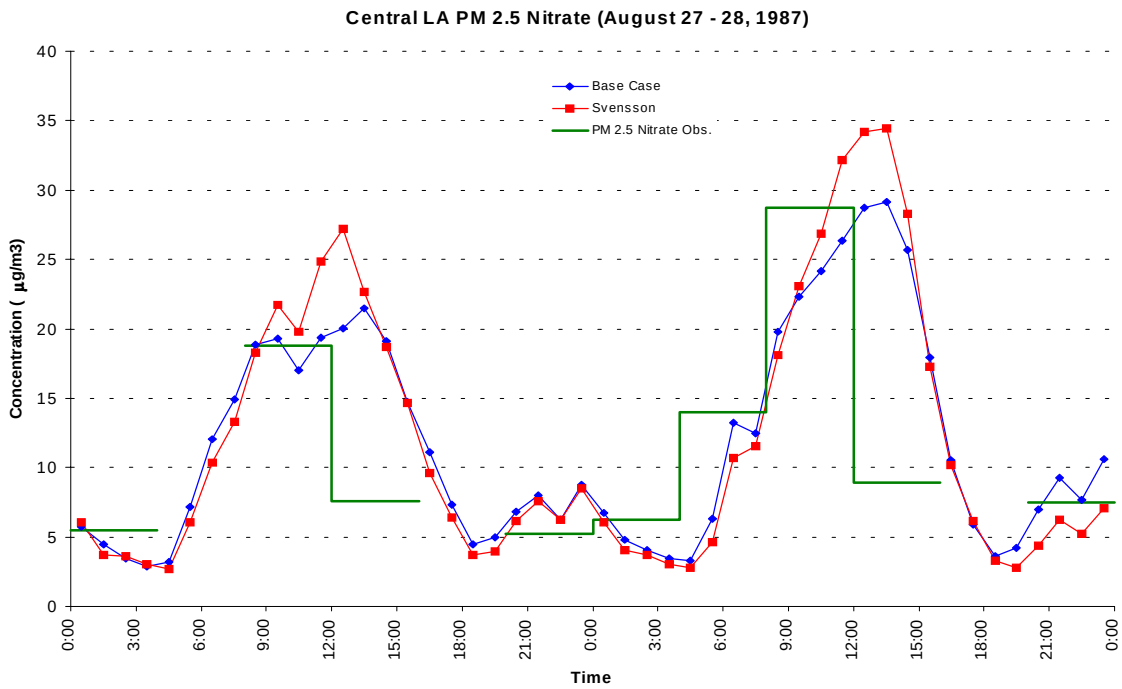

Figure 3.V.7. Model of PM2.5 nitrate: Base Case, observations, and Svensson kinetics for Central L.A.

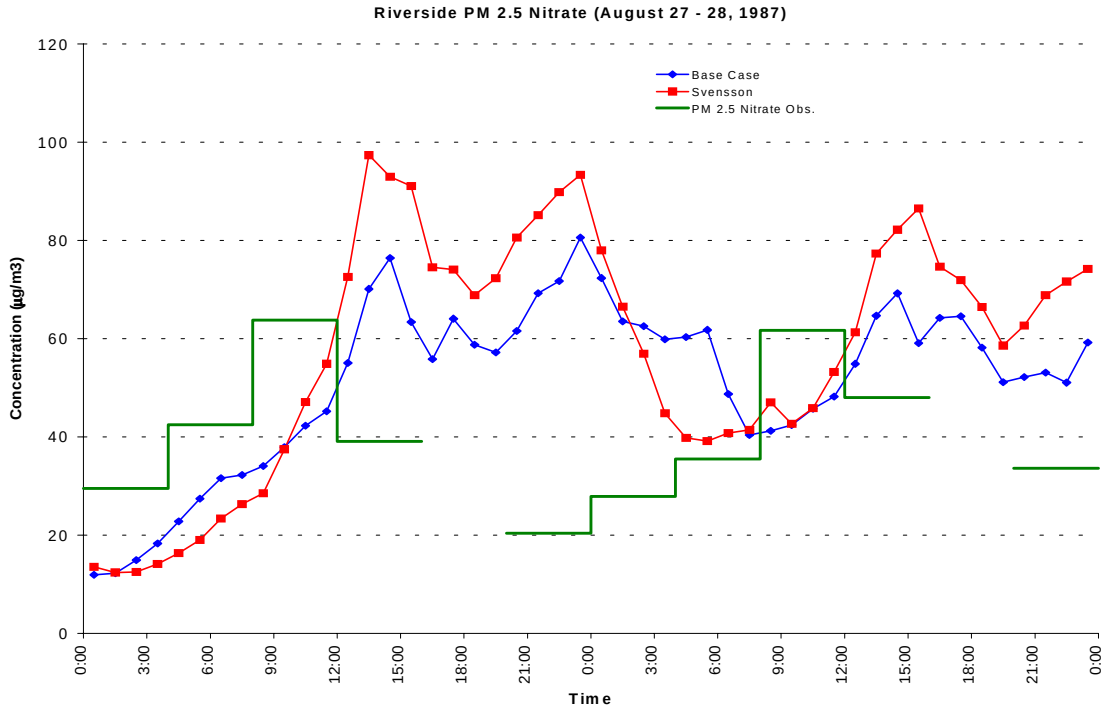

Figure 3.V.8. Model of PM2.5 nitrate: Base Case, observations, and Svensson kinetics for Riverside.

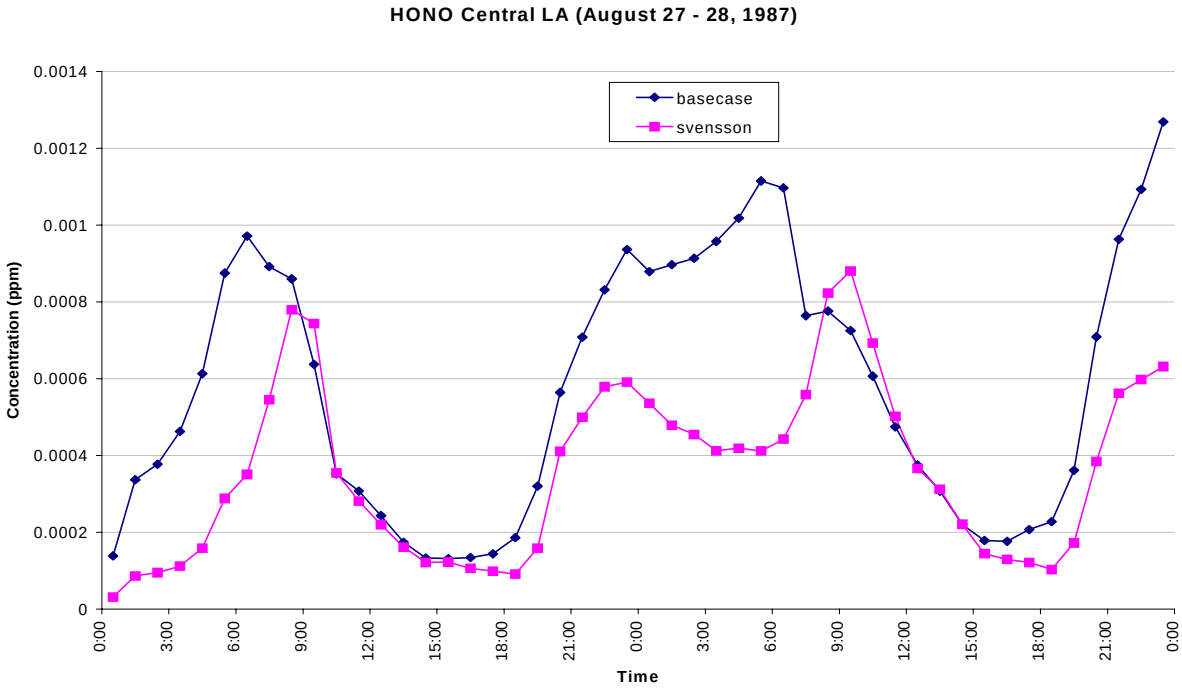

Figure 3.V.9. Model of HONO: Base Case and Svensson et al. (1987) parameterization for Central L.A.

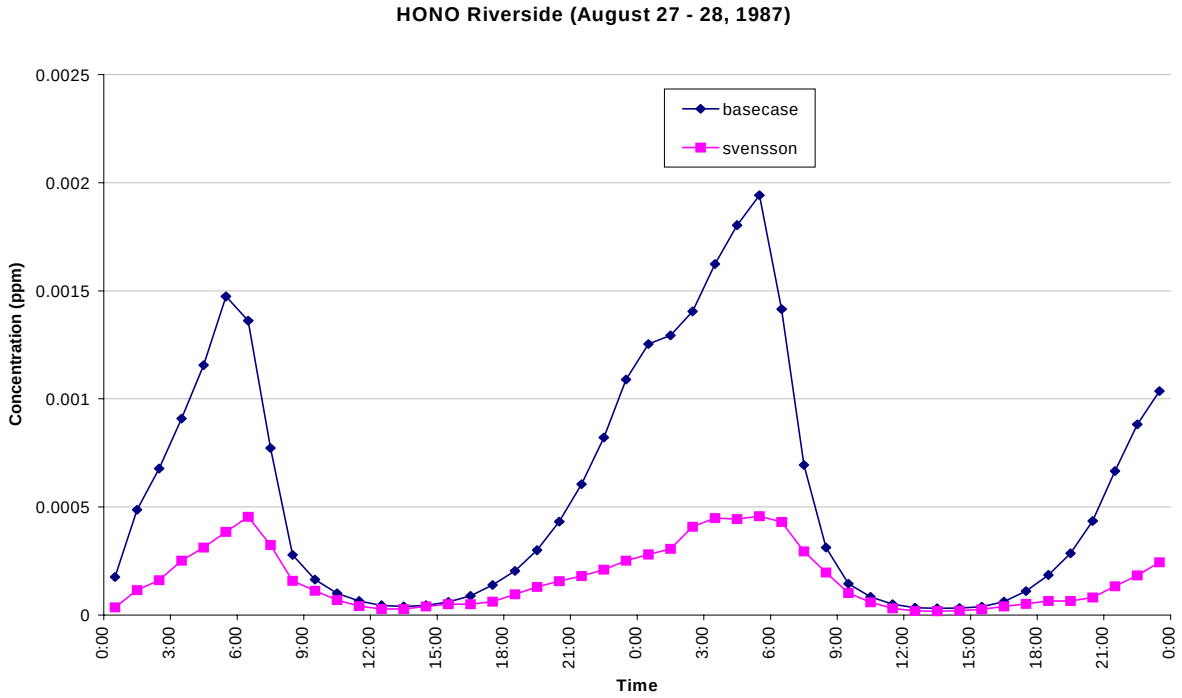

Figure 3.V.10. Model of HONO: Base Case and Svensson et al. (1987) parameterization for Riverside.

4. DISCUSSION

The research project encompassed a number of different studies of nitrous acid (HONO) in order to address its sources and sinks, since it is considered a key determinant in the tropospheric ozone and fine particle pollution. The results of these various approaches are discussed individually, and an overview is provided.

We considered first the synthesis of pure samples of HONO and then addressed new methods for its quantification. Hence, we can now measure HONO to within about ± 20% using either our newly measured IR absorption cross sections, or by titration with HCl and measurement of the ClNO formed. Infrared absorption cross-sections for nitrous acid were measured using HONO spectra recorded simultaneously by UV/visible and FTIR spectroscopy. We also reported both Q-branch intensities and integrated absorbances for the HONO modes *trans*-ν_3 (1263 cm^{-1}), *cis*-ν_4 (852 cm^{-1}), and *trans*-ν_4 (790 cm^{-1}). For *trans*-ν_3 and *cis*-ν_4 we also included synthetic reference spectra composed of Gaussian functions which gave an accurate reproduction of our experimental references. These functions can easily be generated by computer for ease of use in other laboratories. The gas phase reaction of HONO with HCl has not been reported in the literature to the best of our knowledge (although it should be noted that we cannot rule out a heterogeneous component of the reaction). However, the heterogeneous reaction of HONO with HCl on ice and concentrated sulfuric acid solution substrates has been studied by several groups with a one-to-one stoichiometry as found in the present studies (*Zhang et al.,* 1996*; Fenter and Rossi,* 1996*; Burley and Johnston,* 1992*; Longfellow et al.,* 1998, *Chu et al*. 2000). Although the reaction is slow, $k = (1.9 \pm 1.3)\times10^{-19}$ cm^3 $molecule^{-1}$ s^{-1} (2σ) at 297 K, it has been shown to be a useful method for quantifying HONO in laboratory systems, since calibration for ClNO can be readily carried out. FTIR has the advantage over UV/visible spectroscopy that it does not require the more complex data analysis associated with DOAS and allows the simultaneous determination of other species, such as HNO_3, which cannot be measured by DOAS. It is also a more direct and specific method than the denuder and NO_x detector approaches.

Second, we have made significant progress in understanding the mechanism of formation of HONO in the atmosphere from three different types of reactions.

$$2\,NO_2 + H_2O \xrightarrow{Surface} HONO + HNO_3 \qquad (1)$$

$$NO + NO_2 + H_2O \xrightarrow{Surface} 2\,HONO \qquad (2)$$

$$NO + HNO_3 \xrightarrow{Surface} HONO + NO_2 \qquad (3)$$

While all of these reactions are slow in the gas phase, they may be surface catalyzed and contribute to the atmospheric formation of HONO to various extent (*Chan et al.,* 1976a, b*; Kaiser and Wu,* 1977a*; Sakamaki et al.,* 1983*, Fairbrother et al.* 1997). We have shown here that reactions (1) and (3) are feasible sources of HONO in polluted urban atmospheres but the reaction (2) of NO, NO_2 and water is not.

Starting with reaction (1), a large amount of research focusing on the effects of surface area and type on NO_2 hydrolysis (*Sakamaki et al.,* 1983*; Pitts et al.,* 1984a*; Pitts et al.,* 1985*; Akimoto et al.,* 1987*; Svensson et al.,* 1987*; Jenkin et al.,* 1988*; Febo and Perrino,* 1991*; Junkermann and Ibusuki,* 1992*; Bambauer et al.,* 1994*; Mertes and Wahner,* 1995, *Weisen et al.* 1995, *Kleffmann et al.* 1998a, b) has been conducted. The rate of reaction (1) has been shown to be highly variable, depending upon the surface area and type of the reaction chamber in laboratory experiments. For example, Svensson et al. (1987) reported a linear increase in the rate constant for reaction (1) with increasing ratios of surface area to volume of the experimental apparatus used. They also reported large increases in the rate of NO_2 disappearance in a glass reaction cell when the glass was first treated with a dilute HCl solution, then rinsed with distilled water, and finally pumped thoroughly, and also when the cell was lined with stainless steel. This dependence of the rate constant upon surface area and type is expected for reactions which occur heterogeneously on the walls of the reaction chamber. As a result, the heterogeneous reaction (1) is often considered to be a major source of HONO in laboratory studies and in the atmosphere. However, this reaction is still not included in airshed models because the mechanisms and kinetics are not sufficiently well understood, despite almost two decades of work in this area.

It has been reported in a number of studies that reaction (1) is first order with respect to NO_2 (*Sakamaki et al*., 1983; *Pitts et al*., 1984; *Svensson et al*., 1987; *Jenkin et al*., 1988; *Febo and Perrino*, 1991; *Bambauer et al*., 1994). Pitts et. al. (1984a) proposed that the kinetics were consistent with a stepwise reaction involving a slow adsorption of NO_2 at the water surface, followed for example, by a rapid reaction of two surface adsorbed NO_2 with water. The uptake of NO_2 on liquid water (*Ponche et al.* 1993) is known to be slow, consistent with this hypothesis.

We have shown in the present studies that while the loss of NO_2 can be described as first order, the data are equally well matched by second order kinetics in the early stages of the reaction when secondary chemistry is minimized. In this case, the reactant may be N_2O_4, the dimer of NO_2:

$$2NO_2 \leftrightarrow N_2O_4 \qquad (4, -4)$$

Supporting evidence in N_2O_4 as the key intermediate in the formation of HONO by NO_2 surface hydrolysis was obtained using FTIR to follow the surface thin water film directly on exposure to NO_2. Enhanced N_2O_4 concentrations relative to the gas phase, and formation of nitric acid in the thin water film were observed. N_2O_4 has also been seen as an intermediate on the surface of ice at 86 K after exposure to NO_2 (*Wang and Koel,* 1998a, b), and upon heating, generates HONO and HNO_3 amongst other products. The formation of N_2O_4 on the ice surface is not unexpected, given that the equilibrium (4, -4) will shift to the right at lower temperatures

In determining the importance of reaction (1) in the atmosphere, the rate of NO_2 loss and yields of HONO were considered. The most important loss process for NO_2 is photolysis, with $k_{photolysis} \cong (3–9)\times10^{-3}$ s^{-1} (*Finlayson-Pitts and Pitts,* 1986, 2000). The average second order rate constant determined in this study in the long path cell with a surface area-to-volume ratio of 40 m^{-1} is $k_1 = (1.8 \pm 1.6)\times10^{-22}$ cm^3 $molecule^{-1}$ s^{-1}. Typical surface area-to-

volume ratios in the troposphere are in the range of 0.1 – 1.2 m^{-1} taking into account the surface area of the ground, buildings, roads, plants, and aerosols (*Lammel and Cape,* 1996). Using the rate equation for the reaction of NO_2 with water developed by Svensson et al. (1987) (Equation (I))

$$\frac{-d[NO_2]}{dt} = \left[\left(\frac{S}{V}\right)(5.6 \pm 0.9)\times 10^{-9} + (2.3 \pm 6.5)\times 10^{-9}\right][NO_2][H_2O] \qquad \text{(I)}$$

where the surface area-to-volume ratio, S/V, is in units of m^{-1} and the second order rate constant, k_1, given by Equation (II), is in units of ppm^{-1} min^{-1}:

$$k_1\ (ppm^{-1}\ min^{-1}) = \left(\frac{S}{V}\right)(5.6 \pm 0.9)\times 10^{-9} + (2.3 \pm 6.5)\times 10^{-9} \qquad \text{(II)}$$

an estimate of the rate constant at these surface-to-volume ratios gives a range for k_1 of $(2 - 6)\times 10^{-24}$ cm^3 $molecule^{-1}$ s^{-1} in the atmosphere. Choosing a condition of 50% relative humidity at 25°C (~4×10^{17} molecules cm^{-3}), the pseudo-first order rate constant for reaction (1) has a range of k' = $(0.8 - 2.4)\times 10^{-6}$ s^{-1}. To determine the relative importance of reaction (1), the fraction, F, of the pseudo-first order rate constant for reaction (1) over the sum of the pseudo-first order rate constants for the other NO_2 reactions (i.e., photolysis, and reaction with OH, O_3, NO_3, and H_2O) was calculated, Equation (III):

$$F = \frac{k_1[H_2O]}{k_1[H_2O] + k_{photolysis} + k_{OH+NO_2}[OH] + k_{O_3+NO_2}[O_3] + k_{NO_3+NO_2}[NO_3]} \qquad \text{(III)}$$

The values of k_{OH+NO_2}, $k_{O_3+NO_2}$, and $k_{NO_3+NO_2}$ were taken at 298 K (*DeMore et al.,* 1997) and the concentrations are typical of moderately polluted regions (*Finlayson-Pitts and Pitts,* 2000). Using these values, the fraction, F, of NO_2 expected to undergo hydrolysis is F = 3×10^{-4} or 0.03%. In addition, Equation (II) was developed to predict the hydrolysis rate constant under laboratory conditions in which reaction chamber surfaces were passivated by reactants and products. Surfaces in the atmosphere may become reactivated depending upon the weather conditions, thus Equation (II) may underestimate the NO_2 hydrolysis rate constant (*Calvert and Yarwood,* 1994). Under less polluted conditions, i.e., when [OH] and [O_3] are lower, or at lower temperatures when the NO_2 hydrolysis rate constant, k_1, has been shown to be larger, reaction (1) may play a more important role in removal of NO_2 from the atmosphere (*Svensson et al.,* 1987). This is especially true at night when the destruction of NO_2 and HONO by photolysis does not occur. For example, the fraction of NO_2 expected to undergo hydrolysis at night was calculated for remote locations in which [OH] ≤ 2×10^4 radicals cm^{-3} (*Eisele et al.,* 1996), [O_3] ≤ 1×10^{12} molecules cm^{-3}, and [NO_3] ≤ 1×10^8 radicals cm^{-3} (*Finlayson-Pitts and Pitts,* 2000). Assuming that photolysis does not occur at night, i.e., $k_{photolysis} = 0$, and that k_1 increases by a factor of 2 at 280 K (*Svensson et al.,* 1987), the fraction of NO_2 undergoing hydrolysis at night is F = 3%. Despite the fact that "F" seems small and so reaction (1) is considered a relatively minor loss

process for NO_2, it remains an important formation process for nitrous acid in the atmosphere (*Lammel and Perner,* 1988*; Febo and Perrino,* 1991*; Notholt et al.,* 1992*; Kitto and Harrison,* 1992*; Calvert et al.,* 1994*; Mertes and Wahner,* 1995*; Andrés-Hernández et al.,* 1996*; Lammel and Cape,* 1996).

While HONO has been detected using FTIR in the gas phase during the NO_2 hydrolysis reaction, the other major product of reaction (1), HNO_3 has not until the present studies. HNO_3 is a well-known "sticky" acid that remains adsorbed on the surface. This is consistent with the observations of nitrate in washings of the surface post-reaction (*Svensson et al.*, 1987), but direct observations of HNO_3 during the reaction have not been reported. Our observation of HNO_3 formation on the porous glass during the NO_2 reaction is the first direct confirmation of the production of HNO_3 in reaction (1).

Gaseous NO, N_2O and HONO were formed at the same time HNO_3 was identified on the porous glass surface in the presence of water and NO_2. The major gas phase reaction product from the surface N_2O_4 reaction is NO, regardless of whether the surface is "wet" or dry. When there is water on the surface, gas phase HONO is generated. Small amounts of N_2O are generated in both cases. Grassian and co-workers (*Miller and Grassian,* 1998*; Goodman et al.,* 1998*; Underwood et al.,* 1999) have also reported NO as a major gas phase product in the studies of the uptake of NO_2 on Al_2O_3, Fe_2O_3 and TiO_2. Small amounts (<1% of the gas phase products) of N_2O were also observed, but HONO was not (*Underwood et al.* 1999). This may be due to the rapid decomposition of HONO on these surfaces after it is generated. In fact it is well known that HONO undergoes a self-reaction (*Markovits et al.* 1981) to form N_2O_3:

$$2\ HONO \leftrightarrow N_2O_3 + H_2O \qquad (5, -5)$$

N_2O_3 is known to decompose to NO + NO_2. Hence formation of HONO followed by reaction (5) on the porous glass surface and decomposition of the N_2O_3 may be at least partially responsible for the NO observed in our system. Consistent with this, HONO has been observed to decompose into NO + NO_2 in a glass smog chamber (*Ten Brink and Spoelstra,* 1998).

Identifying NO and adsorbed HNO_3 in the same system lead us to propose a new mechanism for the formation of HONO in the atmosphere.

$$HNO_3(ads) + NO(g) \xrightarrow{surface} HONO(g) + NO_2(g) \qquad (3)$$

$$HNO_3(ads) + HONO(g) \xrightarrow{surface} 2NO_2 + H_2O(l) \qquad (6)$$

In the gas phase, two non-photochemical reduction pathways for HNO_3 have been reported, the reaction of HNO_3 with NO (*Smith* 1947*, Jaffe and Ford.* 1967*, Kaiser and Wu,* 1977a, b*, Streit et al.* 1979) (reaction (7)), and reaction (8) with nitrous acid (*Kaiser and Wu*, 1977a, b*, Streit et al.* 1979, *England and Corcoran,* 1975, *Wallington and Japar,* 1989).

$$HNO_3(g) + NO(g) \rightarrow HONO(g) + NO_2(g) \qquad \Delta H^0 = -1.5 \text{ kJ mol}^{-1} \quad (7)$$

$$HNO_3(g) + HONO(g) \rightarrow 2\ NO_2(g) + H_2O(g) \qquad \Delta H^0 = +39.2 \text{ kJ mol}^{-1} \quad (8)$$

The upper limits for these rate constants, $k_8 < 3.4 \times 10^{-22}$ cm^3 molecule^{-1} s^{-1} [15] and $k_9 < 7 \times 10^{-19}$ cm^3 molecule^{-1} s^{-1} (*Wallington and Japar,* 1989) imply that these reactions are not important in the atmosphere. HNO_3 is believed to be an end product of oxidation processes of nitrogen oxides in the atmosphere. Removal processes include reaction with OH and NH_3 (reversible) and photolysis, as well as wet and dry deposition, which tend to predominate in the lower troposphere (*Finlayson-Pitts and Pitts,* 2000). A number of researchers have suggested pathways whereby HNO_3 is reduced in the atmosphere, yielding photochemically active forms of NO_x (*Finlayson-Pitts and Pitts,* 2000). For example, Chatfield, (1994) hypothesized that the discrepancy between the measured ratio of $[HNO_3]/[NO_x] \sim 5$ in the free troposphere and the values of 15 – 100 predicted by model calculations could be due to liquid phase reactions of HCHO with HNO_3 in aerosols and cloud droplets. The conversion of HNO_3 into NO has been reported to proceed heterogeneously on soot surfaces at room temperature (e.g. *Rogaski et al.,* 1997), although at lower HNO_3 concentrations and temperatures, only physical adsorption may occur (*Rogaski et al.* 1997, *Choi and Leu,* 1998, *Disselkamp et al.* 2000, *Krichner et al.* 2000, *Longfellow et al*. 2000). Some model studies have suggested that if this reduction on soot occurs in the atmosphere, it could bring the measurements and models into better agreement (*Hauglustaine et al.,* 1996, *Lary et al.,* 1997).

However, with the use of the long path and the porous glass IR cells, we were able to study the heterogeneous reaction of HNO_3 on the borosilicate glass walls and on the silica surface, respectively. We found that the reaction between HNO_3 and NO was clearly enhanced relative to the gas phase reaction. It was also greatly influenced by the relative humidity of the medium. At 25°C, the reaction was so slow as to be almost undetectable at 0 and 20% RH, but was highly accelerated at a relative humidity of 50% RH. Extrapolation to atmospheric conditions suggests that this reaction could be a significant HNO_3 reduction process in the atmosphere and contribute to the lower than the model-predicted values in the ratio of HNO_3 to NO_x measured in the troposphere (*Chatfield* 1994) and perhaps to the high $[NO_x]/[HNO_3]$ ratio observed in snow packs (*Honrath et al.,* 1999, *Jones et al.,* 2000).

If the rate constants for HNO_3 decay measured in our laboratory systems can be extrapolated down to a polluted ambient NO concentration of 100 ppbv in polluted areas, *i.e.* 2.5×10^{12} molecules cm^{-3}, then the rate constants for HNO_3 decay on particles in air will be in the range of $\sim(1\text{-}3) \times 10^{-5}$ s^{-1}.

The importance of this heterogeneous reaction for the net loss of HNO_3 will depend on how much of the total HNO_3 in the atmosphere is adsorbed on particles relative to the amount in the gas phase, as well as the rates of the gas phase reactions of HNO_3. Chemical losses for gas phase HNO_3 include reaction with OH and photolysis, both daytime processes. Using the kinetics for the OH + HNO_3 reaction of Brown et al., (*Brown et al.,* 1999) the pseudo-first order loss rate for HNO_3 with respect to reaction with OH at 1×10^6 radicals cm^{-3} (1 atm pressure at

298 K) is 1.6×10^{-7} s^{-1} (HNO_3 lifetime of ~ 75 days). That for photolysis at a solar zenith angle of 50° at the earth surfaces is 3.4×10^{-7} s^{-1} (lifetime of 34 days), calculated using recommended actinic fluxes and absorption cross sections (*DeMore et al.* 1997). The lifetime with respect to deposition can be significantly shorter. However, under dry conditions above the boundary layer, deposition is less important.

Dentener et al (1996) have carried out global three-dimensional model studies of the uptake of HNO_3 and other gases on mineral aerosols and predict highly variable percentages of the total available HNO_3 which is on the mineral dust, varying from < 20 % to > 90 %. They assume that the major mechanism of uptake of gaseous HNO_3 is a neutralization reaction with particle components such as $CaCO_3$, which would leave nitrate, rather than adsorbed nitric acid, on the particles. However, if sufficient acidity were available to generate surface-adsorbed HNO_3, as might be the case in more polluted regions, the heterogeneous reaction with NO could be important. For instance, if 10% of the total HNO_3 were on the particles, the loss rates cited above imply that approximately 30% of the loss of HNO_3 in a volume of air containing 100 ppb NO could occur by the heterogeneous reaction. Furthermore, in urban areas, not only suspended particles but the surfaces of buildings, roads etc. may also adsorb HNO_3 and hence provide sites for the heterogeneous reaction with NO. Another possibility is uptake of HNO_3 into cirrus clouds and snow packs and its reaction with NO. Finally, although we have not directly observed the reaction, the reaction stoichiometry observed here suggests that the heterogeneous reaction (6) of gaseous HONO with surface adsorbed HNO_3 may also contribute to the reduction of HNO_3(ads) and to the removal of HONO in the atmosphere. This will depend on the rates of other processes for removal of HONO such as photolysis or advection away from the surface which are not important in our static experimental system.

In addition to regenerating photochemically active forms of NO_x from HNO_3, this heterogeneous reaction may be a significant source of HONO in urban atmospheres. For example, in a number of field studies where HONO as well as its precursors NO and NO_2 were measured, nighttime HONO concentrations were found to correlate best with the product $[NO][NO_2][H_2O]$ and possibly with a term for the concentration of particles available to enhance the heterogeneous reactions (*Sjodin and Ferm,* 1985**,** *Notholt et al.,* 1992**,** *Winer and Biermann,* 1994**,** *Calvert et al.,* 1994). This correlation is not expected if the heterogeneous reaction (1) of NO_2 with water is the source of HONO, as commonly believed based on laboratory studies. As a result, the heterogeneous reaction of NO and NO_2 with water (or of N_2O_3 formed from NO and NO_2) on particles has often been suggested as a potential HONO source. The studies reported here suggest an alternate explanation for the correlation with NO, *i.e.* that it is the direct reaction of NO with surface-adsorbed HNO_3 that generates HONO. The importance of this source depends on whether the subsequent reactions of HONO with adsorbed HNO_3 is also fast under atmospheric conditions, as appears to be the case under our experimental conditions. It may also be that other condensed forms of nitric acid such as NH_4NO_3 undergo a similar reaction and could serve as a source of HONO in air. Our studies have also provided for the first time some indication of "HNO_3(ads)" in reactions (3) and (6). It appears that nitric acid hydrates may be the major form of nitric acid at the air-water interface and that these are the reactive forms. Thus, no significant reaction of gaseous NO with HNO_3 was observed in the long path cell until the RH was sufficiently high to form the water film of concentrated nitric acid on the surface.

The amount of water on the surface was measured in separate experiments and the nature of the nitric acid at the interface and its enhancement compared to the bulk was established using single reflectance FTIR. These studies are in agreement with those of Donaldson and Anderson (1999) who recently reported that the surface tension of sulfuric acid -water and pure water was lowered upon addition of nitric acid. They attributed lowering of the surface tension to the presence of molecular nitric acid at the air-water interface. In addition, Schultz and coworkers (*Schnitzer et al.,* 1999) showed using sum frequency generation (SFG) that the disruption of the surface water hydrogen bonded network increased with the concentration of HNO_3 in bulk solution. They attributed this to nitric acid at the surface, although an infrared absorption band due to the H-O stretch of HNO_3 expected in the spectral region they measured was not observed. Nathanson and coworkers (*Morris et al.,* 2000) reported that the gaseous acids HCl and HBr impinging on a supercooled D_2SO_4 acid surface undergo relatively little H $\rightarrow$ D exchange, 11 and 22% respectively. However, when HNO_3 was used instead of HCl and HBr, an exchange of more than 95% was observed, along with a much longer residence time in/on the sulfuric acid. This again suggested a unique interaction for HNO_3 at the surface.

We showed that in concentrated binary HNO_3–H_2O and ternary H_2SO_4–HNO_3–H_2O solutions, molecular HNO_3 is readily available at the air-solution interface. In the case of the binary solutions, the form of the nitric acid is primarily the monohydrate. However, when H_2SO_4 is present, water preferentially complexes with H_2SO_4, leaving anhydrous HNO_3 at the surface. The thermodynamics for heterogeneous reactions of nitric acid (which are potential "renoxification" routes) (*Saliba et al.,* 2000*, Mochida and Finlayson-Pitts,* 2000), and possibly the kinetics and mechanisms as well, may depend on the form of HNO_3 present at the surface. Studies are currently underway to explore any such differences. It is also possible that the health effects associated with inhaled particles, particularly highly acidic sulfate particles, are determined in part by the availability of the highly oxidizing nitric acid on the particle surface.

For the purposes of comparing HONO formation from reactions (1), (2) and (3) at night in polluted urban atmospheres, we assume an air mass containing 10^4 particles cm^{-3} having a diameter of 1 μm. We also assume that NO and NO_2 concentrations are 100 ppb, typical of polluted urban areas at night, and a relative humidity of 50%. The mixing height is taken to be 100 m, and the ground is also considered available for these heterogeneous reactions. The surface area for the particles is 3.1×10^{-4} cm^2 per cm^3 air or 3.1 cm^2 total particle surface in a column of air of 100 m high and an area of 1 cm^2. The ground geometric surface area of 1 cm^2 is multiplied by two because of the increased area associated with the porosity of the soil and the buildings in urban areas. The total surface area (S) in this column is thus 5 cm^2. Clearly this assumption, and indeed the size and concentration of suspended particles, is somewhat arbitrary but provides a consistent set of conditions to compare the three mechanisms.

Reaction (3) of Surface-Adsorbed HNO_3 with NO: While HONO was removed by secondary reactions in the laboratory systems, this is less likely to occur under atmospheric conditions. For example, Besemer and Nieboer *(Besemer and Nieboer,* 1985) reported that the photochemical oxidation of CO and organics in a mixture with NO_x and air could be quantitatively modeled only if it was assumed that gas phase NO reacted with HNO_3 on the walls to form HONO, which then photolyzed to form OH. We therefore assume that the rate of

HONO generation from reaction (3) is obtained from the measured rate of HNO_3 decay in the porous glass studies, divided by two to account for reaction (6).

The measured pseudo-first order rate constant for the decay of surface-adsorbed HNO_3 in the presence of 3.3×10^{16} molecule cm^{-3} of NO is 0.49 s^{-1} (see results). Scaling this rate constant down to 2.5×10^{12} molecule cm^{-3} (100 ppb) gives a pseudo-first order rate constant of 3.7 x 10^{-5} s^{-1}. The rate for HONO generation would be half of this if it were not removed in subsequent reactions. If there are 1×10^{14} HNO_3 per cm^2, then the total rate of HNO_3 decay in the air column is 9.3×10^5 HNO_3 cm^{-3} s^{-1}, which if sustained, would generate about 1 ppb HONO in 8 hours.

Clearly this involves many assumptions, including that the surface coverage of HNO_3 on the particles and ground is similar to that on the porous glass and that HONO is not removed by secondary reactions in air as is the case in our laboratory system. However, even this crude estimate of potential HONO production is of the same order of magnitude as that measured for HONO in air *(Finlayson-Pitts and Pitts,* 2000*, and references therein*). Thus, this surface reaction of NO with adsorbed HNO_3 cannot be discounted as a source of HONO in air. Furthermore, it would be consistent with the field observations that HONO concentrations often appear to correlate better with $[NO][NO_2][H_2O]$ rather than $[NO_2][H_2O]$ *(Sjodin and Ferm,* 1985*; Notholt et al.,* 1992*; Calvert et al.,* 1994*; Winer and Biermann,* 1994).

Reaction (2) of NO and NO_2 with Water on Surfaces: In a separate set of studies carried out in the same cell used for the porous glass, *(Mochida and Finlayson-Pitts,* 2000) the formation of HONO was observed when water vapor was added to a mixture of NO and NO_2. These were at high NO and NO_2 concentrations because of the short path length of the cell. The initial rate of HONO formation without the porous glass present was measured to be 6.9×10^{14} molecule cm^{-3} s^{-1} at initial concentrations of NO, NO_2 and H_2O of 11, 1.6 and 6.6×10^{17} molecule cm^{-3}, respectively. Scaling this rate of HONO generation to the air column (S = 5 cm^2) with NO and NO_2 concentration of 100 ppb, and a water concentration equivalent to 50% relative humidity, the rate of HONO generation is estimated to be 2 molecules cm^{-3} s^{-1}. Over 8 hours, this gives a HONO concentration of only ~10^{-6} ppb; a value much smaller than the one obtained from the heterogeneous HNO_3 + NO reaction. Thus, it seems more likely that the dependence of HONO on NO concentrations in air originates from the heterogeneous HNO_3 reaction with NO, rather than NO + NO_2 with water at surfaces.

Reaction (1) of NO_2 with Water on Surfaces: Svensson and coworkers *(Svensson et al.,* 1987) found that the rate of reaction (1) in their laboratory system could be expressed by:

$$\frac{-d[NO_2]}{dt} = \frac{2d[HONO]}{dt} = \left[5.6\times10^{-9}\frac{S}{V} + 2.3\times10^{-9}\right][NO_2][H_2O] \quad \text{(I)}$$

S/V is the surface-to-volume ratio (m^{-1}), the concentrations are in ppm and the rates in ppm min^{-1}. Using the conditions assumed above, S/V in the air column is 0.05 m^{-1}. So, at an NO_2 concentration of 100 ppb and 50% RH, we calculate a rate of HONO formation of 0.12 ppb hr^{-1},

and a total HONO concentration of 0.9 ppb over 8 hours; a value similar to that from the heterogeneous reaction of HNO_3 with NO.

Reaction of NO_2 with Soot: The importance of the NO_2 reaction with soot as a HONO source in polluted areas is uncertain. If no surface deactivation occurs, this reaction could generate as much as 15 ppb overnight *(Aumont et al.,* 1999); however, given the likelihood of some surface deactivation, this appears to be an upper limit (*Smith et al.*, 1988, *Chughtai et al.* 1990a, b, *Tabor et al.*, 1993, *Tabor et al.*, 1994; *Ammann et al*. 1995, *Kalberer et al.*, 1996, *Rogaski et al.*, 1997; *Lur'e and Mikhno*, 1997, *Chughtai et al.* 1998, *Ammann et al.*, 1998; *Gerecke et al.*, 1998; *Aumont et al.*, 1999; *Kalberer et al.*, 1999a, b; *Longfellow et al.*, 1999, *Kleffmann et al.* 1999, *Ravishankara and Longfellow*,1999, *Kirchner et al.* 2000, *Al-Abadheh and Grassian*, 2000, *Stadler and Rossi*, 2000, *Alcala-Jornod et al.*, 2000).

There is a great deal of current interest in heterogeneous reactions in the atmosphere, and in particular, their potential role in the chemistry of oxides of nitrogen in the troposphere (*Finlayson-Pitts and Pitts,* 2000*, de Reus et al.,* 2000*, Dentener et al.,* 1996*, Raes et al.,* 2000). The surfaces with which tropospheric gases collide include not only airborne particles but also building materials and biological surfaces, all of which have water films. Thus, reactions at the air-water interface and in thin water films (*Saliba et al.,* 2000) on surfaces may be important in tropospheric chemistry. Experimental evidence for unique chemistry occurring at solution interfaces has been obtained, for example, in studies of the kinetics of uptake and reaction of Cl_2 with solutions containing bromide ions (*Hu et al.,* 1995). Similarly, Knipping et al. (2000) showed that OH radicals must react with chloride ions not only in the bulk solution of suspended concentrated NaCl particles, but also at the air-solution interface, generating Cl_2 at much lower acidities than are required for the bulk reaction.

In summary, the heterogeneous reactions involving NO_2 hydrolysis and HNO_3 adsorbed with NO gas were shown both to be potential major sources of HONO in the atmosphere. The kinetics and mechanisms study of the NO_2 hydrolysis reaction show that the reaction fits first order kinetics in NO_2, in agreement with a number of other studies. However, in the first several hours of the reaction, the data can be equally well fit by a second order process. These observations suggest that an intermediate such as N_2O_4 may be a key intermediate in the generation of HONO in the atmosphere. The major gas phase reaction product from the surface N_2O_4 reaction is NO, regardless of whether the surface is "wet" or dry. When there is water on the surface, gas phase HONO is generated. Small amounts of N_2O are generated in both cases. On the other hand, we showed that the heterogeneous reaction between NO + HNO_3 is also a major source of HONO in the atmosphere. This reaction is completely dependent on the state of HNO_3 on the surface , which for sufficiently concentrated HNO_3 solutions, is likely the monohydrate.

Incorporation of the laboratory results into an airshed model shows that the current parameterization of HONO formation in the model is not appropriate since it does not involve a surface term in the rate constant. However, incorporation of the Svensson et al. (1987) parameterization which is applicable to laboratory systems, including ours, is also not appropriate because under atmospheric conditions typical of Los Angeles, the surface dependent

term is much smaller than the constant term, again giving a rate constant that is essentially independent of surface. There is a strong need to reexamine the parameterization and to develop a new one, based on laboratory data, that will incorporate a surface dependent turn in the models.

Initial modeling runs in which the HNO_3 was assumed to undergo reaction with gaseous NO suggest that this reaction could potentially be important in reconverting HNO_3 back into photochemically active forms of NO_x. Such a recycling appears to improve the agreement of predicted with observed O_3 on day two of the simulation in Central Los Angeles and to predict double ozone peaks at downwind locations (Riverside, San Bernardino), which the base model does not. This reaction may also lead to increased particulate nitrate levels. These results are preliminary but do indicate that this chemistry may potentially be important in determining bulk ozone and particulate nitrate levels.

5. SUMMARY AND CONCLUSIONS

While the gas phase chemistry of oxides of nitrogen leading to the formation of ozone and particulate nitrate is reasonably well understood, the heterogeneous chemistry on surfaces is not. The goals of our laboratory studies were to elucidate the kinetics and mechanisms of some of the heterogeneous reactions of oxides of nitrogen that are relevant to the formation of ozone, particles and associated air pollutants and to carry out initial airshed model runs to assess whether or not such chemistry might be important in polluted urban airsheds in California.

Studies of the kinetics and mechanisms of the heterogeneous hydrolysis of nitrogen dioxide (NO_2) on surfaces,

$$2\ NO_2 + H_2O \xrightarrow{\text{surface}} HONO + HNO_3$$

were carried out using two chambers, a 561 L chamber equipped with FTIR and DOAS and an 8 L chamber equipped with FTIR. In addition, a smaller cell in which the chemistry occurred on a high surface area porous silica surface was used in which both the gas phase and surface species could be followed simultaneously. These studies showed that this reaction likely proceeds via the initial formation of its dimer (N_2O_4), followed by the reaction of the dimer with water. This is in contrast to previous studies of this reaction that ruled out the dimer as an important intermediate, and is inconsistent with the parameterization of this reaction in current airshed models. This reaction generates gas phase nitrous acid (HONO) whose generation in our experimental system was in agreement with a parameterization of HONO formation proposed earlier by Svensson and coworkers. However, this parameterization was shown to be inappropriate for inclusion in airshed models because of the very different surface-to-volume ratios for particles in air compared to the experimental system. A parameterization appropriate for airshed models remains to be developed.

The reaction of gas phase NO_2 with water on surfaces not only generates gas phase nitrous acid but also nitric acid, the latter remaining on the chamber surfaces. This results in a thin film of nitric acid and water on the surface that then plays a key role in secondary reactions in this system. The formation of this thin aqueous film of nitric acid and its properties were investigated using the porous silica surface as a support for the thin acid film and using single reflectance FTIR to probe the surface of nitric acid-water mixtures. Using these techniques, we showed that gaseous nitric oxide (NO) reacts with nitric acid in this surface film to regenerate NO_2. The overall reaction (but certainly not the mechanism) is:

$$2\ HNO_{3(surface)} + NO_{(g)} \rightarrow 3\ NO_2 + H_2O$$

The single reflectance FTIR data show that nitric acid is enhanced at the air-thin film interface and that its likely form is undissociated nitric acid complexed with one or more water molecules; it may be that the particular form of the nitric acid, *e.g.* dissociated versus undissociated, or complexed or uncomplexed with water, is what determines its chemistry at the air interface.

"Conventional wisdom" has been that once nitric acid is formed, it is not reduced in air back to photochemically active NO_2 and hence is not involved in the further formation of ozone. However, our results suggest that this may not be the case and further reactions of nitric acid on the surface may lead to its reduction back to NO_2, *i.e.*, a catalytic cycle may be contributing to the overall NO_x chemistry.

Preliminary airshed modelling predicts that this reaction of gaseous NO with surface nitric acid may be important with respect to the formation of both ozone and particulate nitrate in polluted urban airsheds in California; changes in both the concentrations and profiles of ozone and particulate nitrate were predicted when the reaction of gaseous NO with deposited nitric acid was included.

6. RECOMMENDATIONS

A great deal of experimental work is needed to elucidate this heterogeneous chemistry in order to include it in airshed models and to assess the impacts on various control strategies. For example,

- What is the most appropriate parameterization for HONO formation from the surface hydrolysis of NO_2 to use in airshed models?
- What is the mechanism of the photoenhancement of HONO formation that has been observed in studies by other researchers?
- What is the reaction probability for the reaction of gaseous NO with the surface film of nitric acid, and how is it affected by relative humidity, the nature of the surface etc?
- Are there other reactions of the nitric acid film, *e.g.* with CO, SO_2 or CH_4, that have been proposed by other researchers that may also generate NO_2 from HNO_3?
- Do forms of nitrate other than nitric acid such as ammonium nitrate undergo the same chemistry?
- Does the simultaneous presence of sulfuric acid in the thin films alter the molecular nature of nitric acid and hence its reactions?
- Does gas phase nitrous acid also react with nitric acid on the surface, and if so, does this affect how much nitrous acid is released into air by the surface hydrolysis of NO_2?
- Can this chemistry be integrated into a comprehensive model that will explain the experimental observations made by many research groups over the years on the behaviour of oxides of nitrogen in laboratory systems? How does this extrapolate to the urban air situation?

REFERENCES

Adams, R.W.; Downing, H.D., "Infrared Optical Constants of a Ternary System of 75% H_2SO_4, 10% HNO_3, and 15% H_2O", *J. Opt. Soc. Am. A*, *3*, 22-28, **1986**.

Akimoto, H.; Takagi, H.; Sakamaki, F., "Photoenhancement of the Nitrous Acid Formation in the Surface Reaction of Nitrogen Dioxide and Water Vapor: Extra Radical Source in Smog Chamber Experiments", *Int. J. Chem. Kinet.*, *19*, 539-551, **1987**.

Al-Abadleh, H.A., Grassian, V.H**.** "Heterogeneous Reaction of NO_2 on Hexane Soot: A Knudsen Cell and FT-IR Study", *J. Phys. Chem. A*, *104*, 11926-11933, **2000**.

Alcala-Jornod, C., van den Bergh, H., Rossi, M.J. "Reactivity of NO_2 and H_2O on Soot Generated in the Laboratory: A Diffusion Tube Study at Ambient Temperature", *Phys. Chem. Chem. Phys*, 2, 5584-5593, **2000**.

Ammann, M.; Baltensperger, U.; Bochert, U.K.; Eichler, B.; Gaggeler, H.W.; Jost, D.T.; Turler, A.; Weber, A.P., "Study of HI, HBr and NO_2 Adsorption On Graphite and Silver Aerosol Particles Using Short-Lived Isotopes", *J. Aerosol Sci.*, *26*, 61-70, **1995**.

Ammann, M.; Kalberer, M.; Jost, D.T.; Tobler, L.; Rossler, E.; Piguet, D.; Gaggeler, H.W.; Baltensperger, U., "Heterogeneous Production of Nitrous Acid on Soot in Polluted Air Masses", *Nature*, *395*, 157-160, **1998**.

Andrés-Hernández, M.D.; Notholt, J.; Hjorth, J.; Schrems, O., "A DOAS Study on the Origin of Nitrous Acid at Urban and Non-Urban Sites", *Atmos. Environ.*, *30*, 175-180, **1996**.

Anthony, S.E.; Tisdale, R.T.; Disselkamp, R.; Tolbert, M.A., "FTIR Studies of Low Temperature Sulfuric Acid Aerosols", *Geophys. Res. Lett.*, *22*, 1105-1108, **1995**.

Anthony, S.E.; Onasch, T.B.; Tisdale, R.T.; Disselkamp, R.S.; Tolbert, M.A., "Laboratory Studies of Ternary $H_2SO_4/HNO_3/H_2O$ Particles: Implications for Polar Stratospheric Cloud Formation", *J. Geophys. Res.*, *102*, 10777-10784, **1997**.

Atkinson, R., "Comment on "Measurements of Nitrous Acid in an Urban Area"", *Atmos. Environ.*, *20*, 408-409, **1986**.

Aumont, B.; Madronich, S.; Ammann, M.; Kalberer, M.; Baltensperger, U.; Hauglustaine, D.; Brocheton, F., "On the NO_2 + Soot Reaction in the Atmosphere", *J. Geophys. Res.*, *104*, 1729-1736, **1999**.

Baldelli, S.; Schnitzer, C.; Shultz, M.J.; Campbell, D.J., "Sum Frequency Generation Investigation of Water at the Surface of H_2O/H_2SO_4 Binary Systems", *J. Phys. Chem. B*, *101*, 10435-10441, **1997**.

Baldelli, S.; Schnitzer, C.; Shultz, M.J.; Campbell, D.J., "Sum Frequency Generation Investigation of Water at the Surface of H_2O/H_2SO_4 and H_2O/Cs_2SO_4 Binary Systems", *Chem. Phys. Lett.*, *287*, 143-147, **1998**.

Baldelli, S.; Schnitzer, C.; Campbell, D.J.; Shultz, M.J., "Effects of H_2SO_4 and Alkali Metal SO_4^{2-}/HSO_4^- Salt Solutions on Surface Water Molecules Using Sum Frequency Generation", *J. Phys. Chem. B*, *103*, 2789-2795, **1999**.

Bambauer, A.; Brantner, B.; Paige, M.; Novakov, T., "Laboratory Study of NO_2 Reaction with Dispersed and Bulk Liquid Water", *Atmos. Environ.*, *28*, 3225-3232, **1994**.

Barney, W.S.; Wingen, L.M.; Lakin, M.J.; Brauers, T.; Stutz, J.; Finlayson-Pitts, B.J., "Infrared Absorption Cross-Section Measurements for Nitrous Acid (HONO) at Room Temperature", *J. Phys. Chem. A*, *104*, 1692-1699, **2000a**.; *ibid*: Erratum.

Barney, W.S.; Finlayson-Pitts, B.J., "Enhancement of N_2O_4 on Porous Glass at Room Temperature: A Key Intermediate in the Heterogeneous Hydrolysis of NO_2?", *J. Phys. Chem. A*, *104*, 171-175, **2000b**.

Bartram, M.E.; Koel, B.E., "The Molecular Adsorption of NO_2 and the Formation of N_2O_3 on Au(111)", *Surf. Sci.*, *213*, 137-156, **1989**.

Becker, K.H.; Kleffmann, J.; Kurtenbach, R.; Wiesen, P., "Line Strength Measurements of Trans-HONO Near 1255 cm^{-1} By Tunable Diode Laser Spectrometry", *Geophys. Res. Lett.*, *22*, 2485-2488, **1995**.

Beckett, W.S.; Russi, M.B.; Haber, A.D.; Rivkin, R.M.; Sullivan, J.R.; Tameroglu, Z.; Mohsenin, V.; Leaderer, B.P., "Effect of Nitrous Acid on Lung Function in Asthmatics: A Chamber Study", *Environmental Health Perspectives*, *103*, 372-375, **1995**.

Bertie, J.E.; Lan, Z., "Infrared Intensities of Liquid XX: The Intensity of the OH Stretching Band of Liquid Water Revisited, and the Best Current Values of the Optical Constants of H_2O(l) at 25 ºC between 15,000 and 1 cm^{-1}", *Appl. Spectros.*, *50*, 1047-1057, **1996**.

Bertram, A.K.; Patterson, D.D.; Sloan, J.J., "Mechanisms and Temperatures for the Freezing of Sulfuric Acid Aerosols Measured by FTIR Extinction Spectroscopy", *J. Phys. Chem.*, *100*, 2376-2382, **1996**.

Besemer, A.C.; Nieboer, H., "The Wall as a Source of Hydroxyl Radicals in Smog Chambers", *Atmos. Environ.*, *19*, 507-513, **1985**.

Bibart, C.H.; Ewing, G.E., "Vibrational Spectrum of Gaseous N_2O_3*", *J. Chem. Phys.*, *61*, 1293-1299, **1974**.

Biermann, U.M.; Luo, B.P.; Peter, T., "Absorption Spectra and Optical Constants of Binary and Ternary Solutions of H_2SO_4, HNO_3 and H_2O in the Mid-Infrared at Atmospheric Temperatures", *J. Phys. Chem. A.*, *104*, 783-793, **2000**.

Bongartz, A.; Kames, J.; Welter, F.; Schurath, U., "Near-UV Absorption Cross Sections and Trans/Cis Equilibrium of Nitrous Acid", *J. Phys. Chem.*, *95*, 1076-1082, **1991**.

Bongartz, A.; Kames, J.; Schurath, U.; George, C.; Mirabel, P.; Ponche, J.L., "Experimental Determination of HONO Mass Accommodation Coefficients Using Two Different Techniques", *J. Atmos. Chem.*, *18*, 149-169, **1994**.

Braman, R.S.; de la Cantera, M.A., "Sublimation Sources for Nitrous Acid and Other Nitrogen Compounds in Air", *Anal. Chem.*, *58*, 1533-1537, **1986**.

Brauer, M.; Ryan, P.B.; Suh, H.H.; Koutrakis, P.; Spengler, J.D.; Leslie, N.P.; Billick, I.H., "Measurements of Nitrous Acid Inside Two Research Houses", *Environ. Sci. Tech.*, *24*, 1521-1527, **1990**.

Braun, W.; Herron, J.T.; Kahaner, D.K., "ACUCHEM: A Computer Program for Modeling Complex Chemical Reaction Systems", *Int. J. Chem. Kinet.*, *20*, 51-62, **1988**.

Brown, S.S.; Talukdar, R.K.; Ravishankara, A.R., "Reconsideration of the Rate Constant for the Reaction of Hydroxyl Radicals with Nitric Acid", *J. Phys. Chem. A*, *103*, 3031-3037, **1999**.

Brust, A.S.; Becker, K.H.; Kleffmann, J.; Wiesen, P., "UV Absorption Cross Sections of Nitrous Acid", *Atmos. Environ.*, *34*, 13-19, **2000**.

Burley, J.D.; Johnston, H.S., "Nitrosyl Sulfuric Acid and Stratospheric Aerosols", *Geophys. Res. Lett.*, *19*, 1363-1366, **1992**.

Calvert, J.G.; Yarwood, G.; Dunker, A.M., "An Evaluation of the Mechanism of Nitrous Acid Formation in the Urban Atmosphere", *Res. Chem. Intermed.*, *20*, 463-502, **1994**.

Canagaratna, M.; Phillips, J.A.; Ott, M.E.; Leopold, K.R., "The Nitric Acid - Water Complex: Microwave Spectrum, Structure, and Tunneling", *J. Phys. Chem. A*, *102*, **1998**.

Chan, W.H.; Nordstrom, R.J.; Calvert, J.G.; Shaw, J.H., "Kinetic Study of HONO Formation and Decay Reactions in Gaseous Mixtures of HONO, NO, NO_2, H_2O, and N_2", *Environ. Sci. Tech.*, *10*, 674-682, **1976a**.

Chan, W.H.; Nordstrom, R.J.; Calvert, J.G.; Shaw, J.H., "An IRFTS Spectroscopic Study of the Kinetics and Mechanism of the Reactions in the Gaseous System HONO, NO, NO_2, H_2O", *Chem. Phys. Lett.*, *37*, 441-446, **1976b**.

Chao, C.C.; Lunsford, J.H., "Adsorption of Nitric Oxide on Y-Type Zeolites. A Low-Temperature Infrared Study", *J. Am. Chem. Soc.*, *1971*, 6794-6800, **1971**.

Chase, M.W., Jr.; Davies, C.A.; Downey, J.R,. Jr., Frurip, D.J.; McDonald, R.A.; Syverud, A.N.; *J. Phys. Chem. Ref. Data*, *14* (Suppl. 1), **1985**.

Chase, M.W., Jr.; Davies, C.A.; Downey, J.R. Jr.; Frurip, D.J.; McDonald, R.A.; Syverud, A.N.; *J. Phys. Chem. Ref. Data*; 4th ed.; Monograph No. 9; Woodbury, NY, **1998**.

Chatfield, R.B., "Anomalous HNO_3/NO_x Ratio of Remote Tropospheric Air - Conversion of Nitric Acid to Formic Acid and NO_x", *Geophys. Res. Lett.*, *21*, 2705-2708, **1994**.

Chewter, L.A.; Smith, I.W.M.; Yarwood, G., "A High Resolution FTIR Spectroscopic Study of the $n\nu_1$ (n = 1-4) bands of N_2O_3", *Mol. Phys.*, *63*, 843-864, **1988**.

Choi, W.; Leu, M.T., "Nitric Acid Uptake and Decomposition on Black Carbon (Soot) Surfaces: Its Implications for the Upper Troposphere and Lower Stratosphere", *J. Phys. Chem. A.*, *102*, 7618-7630, **1998**.

Chu, L; Diao, GW; Chu, LT**.** "Heterogeneous interaction and reaction of HONO on ice films between 173 and 230 K", *J. Phys. Chem. A*, *104*, 3150-3158, **2000**.

Chughtai, A.R., Welch, W.F., Smith, D.M. "A Spectroscopic and Gravimetric Study of the Soot-NO_2/N_2O_4 Reaction at Various Temperatures", *Carbon*, *28*, 411-421, **1990**.

Chughtai, A.R., Welch, W.F., Akhter, M.S., Smith, D.M. "A Spectroscopic Study of Gaseous Products of Soot-Oxides of Nitrogen Water Reactions", *Appl. Spectrosc.*, *44*, 294-298, **1990**.

Chughtai, A.R.; Atteya, M.M.O., Kim, J., Konowalchuk, B.K., Smith, D.M. "Adsorption and Adsorbate Interaction at Soot Particle Surfaces", *Carbon*, *36*, 1573-1589, **1998**.

Cohn, H.; Ingold, C.K.; Poole, H.G., "Infra-red Spectrum of Nitric and of Deuteronitric Acid Vapor. Completion of Identification of the Fundamental Frequencies. Entropy of Nitric Acid. Barrier Resisting Rotation of the Hydroxyl Group", *J. Chem. Soc.*, , 4272-4282, **1952**.

Cox, R.A., *J. Photochem.*, *3*, 175, **1974**.

Cox, R.A.; Derwent, R.G., "The Ultraviolet Absorption Spectrum of Gaseous Nitrous Acid", *J. Photochem.*, *6*, 23-34, **1976/77**.

D'Or, L.; Tarte, P., "Sur le Spectre Infra-rouge et la Structure d l'Anhydride Nitreux", *Bul. Soc. Roy. Sci. Liege*, *22*, 276-284, **1953**.

Davis, W.J.; DeBruin, H.J., "New Activity Coefficients of 0-100% Aqueous Nitric Acid", *J. Inorg. Nucl. Chem.*, *26*, 1069-1083, **1964**.

DeMore, W.B.; Sander, S.P.; Golden, D.M.; Hampson, R.F.; Kurylo, M.J.; Howard, C.J.; Ravishankara, A.R.; Kolb, C.E.; Molina, M.J. *Chemical Kinetics and Photochemical Data for Use in Stratospheric Modeling*, Eval. No. 12, Pub. 97-4, **1997**.

Dentener, F.J.; Carmichael, G.R.; Zhang, Y.; Lelieveld, J.; Crutzen, P.J., "Role of Mineral Aerosol as a Reactive Surface in the Global Troposphere", *J. Geophys. Res.*, *101*, 22,869-22,889, **1996**.

deReus, M.; Dentener, F.; Thomas, A.; Borrmann, S.; Strom, J.; Lelieveld, J., "Airborne Observations of Dust Aerosol Over the North Atlantic Ocean During ACE2: Indications for Heterogeneous Ozone Destruction", *J. Geophys. Res.*, *105*, 15,263-15,275, **2000**.

Devi, V.M.; Fridovich, B.; Jones, G.D.; Snyder, D.G.S., "Tunable Diode Laser Spectroscopy of NO_2 at 6.2 mm", *J. Molec. Spectrosc.*, *93*, 179-195, **1982**.

Devlin, J.P.; Uras, N.; Rahman, M.; Buch, V., "Covalent and Ionic States of Strong Acids at the Ice Surface", *Isr. J. Chem.*, *39*, 261-272, **1999**.

Disselkamp, R.S.; Carpenter, M.A.; Cowin, J.P., "A Chamber Investigation of Nitric Acid-Soot Aerosol Chemistry at 298 K", *J. Atmos. Chem.*, *37*, 113-123, **2000**.

Dluhy, R.A., "Quantitative External Reflection Infrared Spectroscopic Analysis of Insoluble Monolayers Spread at the Air-Water Interface", *J. Phys. Chem.*, *90*, 1373-1379, **1986**.

Dluhy, R.A.; Stephens, S.M.; Widayati, S.; Williams, A.D., "Vibrational Spectroscopy of Biophysical Monolayers. Application of IR and Raman Spectroscopy to Biomembrane Model Systems at Interfaces", *Spectrochimica Acta Part A*, *51*, 1413-1447, **1995**.

Donaldson, D.J.; Anderson, D., "Does Molecular HNO_3 Adsorb onto Sulfuric Acid Droplet Surfaces?", *Geophys. Res. Lett.*, *26*, 3625-3628, **1999**.

Eisele, F.L.; Tanner, D.J.; Cantrell, C.A.; Calvert, J.G., "Measurements and Steady State Calculations of OH Concentrations at Mauna Loa Observatory", *J. Geophys. Res.*, *101*, 14665-14679, **1996**.

England, C.; Corcoran, W.H., "The Rate and Mechanism of the Air Oxidation of Parts-Per-Million Concentrations of Nitric Oxide in the Presence of Water Vapor", *Ind. Eng. Chem. Fundam.*, *14*, 55-63, **1975**.

Fairbrother, D.H.; Sullivan, D.J.D.; Johnston, H.S., "Global Thermodynamic Atmospheric Modeling: Search for New Heterogeneous Reactions", *J. Phys. Chem. A*, *101*, 7350-7358, **1997**.

Fairbrother, D.H.; Somorjai, G.A., "Equilibrium Surface Composition of Sulfuric Acid Films in Contact with Various Atmospheric Gases (HNO_3, CO_2, CH_2O, Cl_2, NO, NO_2)", *J. Phys. Chem. B*, *104*, 4649-4652, **2000**.

Fateley, W.G.; Bent, H.A.; Crawford Jr., B., "Infrared Spectra of Frozen Oxides of Nitrogen", *J. Chem. Phys.*, *31*, 204-217, **1959**.

Febo, A.; Perrino, C., "Prediction and Experimental Evidence for High Air Concentration of Nitrous Acid in Indoor Environments", *Atmos. Environ.*, *25A*, 1055-1061, **1991**.

Febo, A.; Perrino, C.; Gherardi, M.; Sparapani, R., "Evaluation of a High-Purity and High-Stability Continuous Generation System for Nitrous Acid", *Environ. Sci. Technol.*, *29*, 2390-2395, **1995**.

Febo, A.; Perrino, C.; Allegrini, I., "Measurement of Nitrous Acid in Milan, Italy, by DOAS and Diffusion Denuders", *Atmos. Environ.*, *30*, 3599-3609, **1996**.

Fenter, F.F.; Rossi, M.J., "Heterogeneous Kinetics of HONO on H_2SO_4 Solutions and on Ice: Activation of HCl", *J. Phys. Chem.*, *100*, 13765-13775, **1996**.

Finlayson-Pitts, B.J.; Pitts, J.N., Jr. *Atmospheric Chemistry: Fundamentals and Experimental Techniques*; Wiley, **1986**.

Finlayson-Pitts, B.J.; Pitts, J.N., Jr. *Chemistry of the Upper and Lower Atmosphere: Theory, Experiments and Applications*; Academic Press, **2000**.

Foster, M.; Ewing, G.E., "An Infrared Spectroscopic Study of Water Thin Films on NaCl (100)", *Surf. Sci.*, *427/428*, **1999**.

Foster, M.C.; Ewing, G.E., "Adsorption of Water on the NaCl(001) Surface. II. An Infrared Study at Ambient Temperatures", *J. Chem. Phys.*, *112*, 6817-6826, **2000**.

Gerecke, A.; Thielmann, A.; Gutzwiller, L.; Rossi, M.J., "The Chemical Kinetics of HONO Formation Resulting from Heterogeneous Interaction of NO_2 with Flame Soot", *Geophys. Res. Lett.*, *25*, 2453-2456, **1998**.

Gomer, T.; Brauers, T.; Heintz, F.; Stutz, J.; Platt, U.; MFC version 1.98, **1995**.

Goodman, A.L., Miller, T.M., Grassian, V.H. "Heterogeneous Reactions of NO_2 on NaCl and Al_2O_3 Particles", *J. Vac. Sci. & Tech. A* (Vacuum, Surfaces, and Films), *16*, 2585-90, **1998**.

Goodman, A.L.; Underwood, G.M.; Grassian, V.H., "Heterogeneous Reaction of NO_2: Characterization of Gas-Phase and Adsorbed Products from the Reaction, $2NO_2(g) + H_2O(a) \rightarrow HONO(g) + HNO_3(a)$ on Hydrated Silica Particles", *J. Phys. Chem. A*, *103*, 7217-7223, **1999**.

Graham, R.F.; Tyler, B.J., "Formation of Nitrous Acid in a Gas-Phase Stirred Flow Reactor", *J. Chem. Soc., Faraday Trans. I*, *68*, 683-688, **1972**.

Grätzel, M.; Taniguchi, S.; Henglein, A., "Pulseradiolytishe Untersuchung der NO-Oxydation und des Gleichgewichts $N_2O_3 \leftrightarrow NO + NO_2$ in Wäßriger Lösung", *Ber. Bunsen-Gesell Physik. Chem.*, *74*, 488-492, **1970**.

Hamill, P.; Turco, R. P.; Toon, O. B. "On the growth of Nitric and Sulfuric Acid Aerosol Particles Under Stratospheric Conditions", *J. Atmos. Chem.*, *7*, 287, **1988**.

Hard, S.; Johansson, K., "The Surface Tension of Concentrated Aqueous Solutions of 1.1-Electrolytes Measured by Means of Wilhelmy and Laser Scattering Methods", *Journal of Colloid and Interface Science*, *60*, 467-472, **1977**.

Harrick, N.J. *Internal Reflection Spectroscopy*; Interscience Publishers: New York, 1967.

Harrison, R.M.; Peak, J.D.; Collins, G.M., "Tropospheric Cycle of Nitrous Acid", *J. Geophys. Res.*, *101*, 14429-14439, **1996**.

Hauglustaine, D.A.; Ridley, B.A.; Solomon, S.; Hess, P.G.; Madronich, S., "HNO_3/NO_x Ratio in the Remote Troposphere During Mlopex 2 - Evidence For Nitric Acid Reduction On Carbonaceous Aerosols", *Geophys. Res. Lett.*, *23*, 2609-2612, **1996**.

Heikes, B.G.; Thompson, A.M., "Effects of Heterogeneous Processes on NO_3, HONO, and HNO_3 Chemistry in the Troposphere", *J. Geophys. Res.*, *88*, 10883-10895, **1983**.

Herzberg, G. *Molecular Spectra and Molecular Structure. II. Infrared and Raman Spectra of Polyatomic Molecules*; Vol. II, D. Van Nostrand Company, Inc.: Princeton, N. J., **1945**.

Hisatsune, I.C.; Devlin, J.P.; Wada, Y., "Infrared Spectra of Some Unstable Isomers of N_2O and N_2O_3*", *J. Chem. Phys.*, *33*, 714-719, **1960**.

Hjorth, J.; Ottobrini, G.; Cappellani, F.; Restelli, G., "A Fourier Transform Infrared Study of the Rate Constant of the Homogeneous Gas-Phase Reaction $N_2O_5 + H_2O$ and Determination of Absolute Infrared Band Intensities of N_2O_5 and HNO_3", *J. Phys. Chem.*, *91*, 1565-1568, **1987**.

Holland, R.F.; Maier II, W.B., "Infrared Absorption of Spectra of Nitrogen Oxides in Liquid Xenon. Isomerization of N_2O_3", *J. Chem. Phys.*, *78*, 2928-2941, **1983**.

Honrath, R.E.; Peterson, M.C.; Guo, S.; Dibb, J.E.; Shepson, P.B.; Campbell, B., "Evidence of NO_x Production Within or Upon Ice Particles in the Greenland Snowpack", *Geophys. Res. Lett.*, *26*, 695-698, **1999**.

Horakh, J.; Borrmann, H.; Simon, A., "Phase Relationships in the N_2O_3/N_2O_4 System and Crystal Structures of N_2O_3", *Chem. Eur. J.*, *1*, 389-393, **1995**.

Högfeldt, E., "The Complex Formation between Water and Strong Acids", *Acta Chem. Scand.*, *17*, 785-796, **1963**.

Hu, J.H.; Shi, Q.; Davidovits, P.; Worsnop, D.R.; Zahniser, M.S.; Kolb, C.E., "Reactive Uptake of Cl_2(g) and Br_2(g) by Aqueous Surfaces as a Function of Br^- and I^- Ion Concentration: The Effect of Chemical Reaction at the Interface", *J. Phys. Chem.*, *99*, 8768-8776, **1995**.

Iraci, L.T.; Middlebrook, A.M.; Tolbert, M.A., "Laboratory Studies of the Formation of Polar Stratospheric Clouds: Nitric Acid Condensation on Thin Sulfuric Acid Films", *J. Geophys. Res.*, *100*, 20969-20977, **1995**.

Jaffe, S.; Ford, H.W., "The Photolysis of Nitrogen Dioxide in the Presence of Nitric Acid at 3660 Å and 25°", *J. Phys. Chem.*, *71*, 1832-1836, **1967**.

Jenkin, M.E.; Cox, R.A.; Williams, D.J., "Laboratory Studies of the Kinetics of Formation of Nitrous Acid from the Thermal Reaction of Nitrogen Dioxide and Water Vapor", *Atmos. Environ.*, *22*, 487-498, **1988**.

Jones, A.E.; Weller, R.; Wolff, E.W.; Jacobi, H.W., "Speciation and Rate of Photochemical NO and NO_2 Production in Antarctic Snow", *Geophys. Res. Lett.*, *27*, 345-348, **2000**.

Junkermann, W.; Ibusuki, T., "FTIR Spectroscopic Measurements of Surface Bond Products of Nitrogen Oxides on Aerosol Surfaces - Implications for Heterogeneous HNO_3 Production", *Atmos. Environ.*, *26A*, 3099-3103, **1992**.

Kagann, R.H.; Maki, A.G., "Infrared Absorption Intensities of Nitrous Acid (HONO) Fundamental Bands", *J. Quant. Spectrosc. Radiat. Transfer*, *30*, 37-44, **1983**.

Kagann, R.H.; Maki, A.G., "Infrared Absorption Intensities for N_2O_3", *J. Quant. Spectrosc. Radiat. Transfer*, *31*, 173-176, **1984**.

Kaiser, E.W.; Wu, C.H., "A Kinetic Study of the Gas Phase Formation and Decomposition Reactions of Nitrous Acid", *J. Phys. Chem.*, *81*, 1701-1706, **1977a**.

Kaiser, E.W.; Wu, C.H., "Measurement of the Rate Constant of the Reaction of Nitrous acid with Nitric acid", *J. Phys. Chem.*, *81*, 187-190, **1977b**.

Kalberer, M.; Tabor, K.; Amman, M.; Parrat, Y.; Weingartner, E., Piguet, D., Rossler, E., Jost, D.T., Turler, A., Gaggeler, H.W., Baltensperger, U. "Heterogeneous Chemical Processing of (NO_2)-N-13 by Monodisperse Carbon Aerosols at Very Low Concentrations", *J. Phys. Chem.*, *100*, 15487-15493, **1996**.

Kalberer, M.; Ammann, M.; Arens, F.; Gaggeler, H.W.; Baltensperger, U., "Heterogeneous Formation of Nitrous Acid (HONO) on Soot Aerosol Particles", *J. Geophys. Res.*, *104*, 13825-13832, **1999**.

Kalberer, M., Ammann, M., Gaggeler, H.W., Baltensperger, U. "Adsorption of NO_2 on Carbon Aerosol Particles in the Low ppb Range", *Atmos. Environ.*, *33*, 2815-2822, **1999**.

Karlsson, R.S.; Ljungström, E.B., "Laboratory Study of ClNO: Hydrolysis", *Environ. Sci. Technol.*, *30*, 2008-2013, **1996**.

Kirchner, U., Scheer, V., Vogt, R**.** "FTIR Spectroscopic Investigation of the Mechanism and Kinetics of the Heterogeneous Reactions of NO_2 and HNO_3 with Soot", *J. Phys. Chem. A*, *104*, 8908-8915, **2000**.

Kirchstetter, T.W.; Harley, R.A.; Littlejohn, D., "Measurement of Nitrous Acid in Motor Vehicle Exhaust", *Environ. Sci. Technol.*, *30*, 2843-2849, **1996**.

Kiselev, A.V.; Lygin, V.I. *Infrared Spectra of Surface Compounds*; Wiley: New York, **1975**.

Kitto, A.-M.N.; Harrison, R.M., "Nitrous Acid and Nitric Acid Measurements at Sites in South-East England", *Atmos. Environ.*, *26A*, 235-241, **1992**.
Kleffmann, J.; Becker, K.H.; Wiesen, P., "Heterogeneous NO_2 Conversion Processes on Acid Surfaces: Possible Atmospheric Implications", *Atmos. Environ.*, *32*, 2721-2729, **1998a**.
Kleffmann, J.; Becker, K.H.; Wiesen, P., "Investigation of the Heterogeneous NO_2 Conversion on Perchloric Acid Surfaces", *J. Chem. Soc. Faraday Trans.*, *94*, 3289-3292, **1998b**.
Kleffmann, J.; Becker, K.H.; Lackhoff, M.; Wiesen, P., "Heterogeneous Conversion of NO_2 on Carbonaceous Surfaces", *Phys. Chem. Chem. Phys.*, *1*, 5443-5450, **1999**.
Knipping, E.M.; Lakin, M.J.; Foster, K.L.; Jungwirth, P.; Tobias, D.J.; Gerber, R.B.; Dabdub, D.; Finlayson-Pitts, B.J., "Experiments and Simulations of Ion-Enhanced Interfacial Chemistry on Aqueous NaCl Aerosols", *Science*, *288*, 301-306, **2000**.
Koller, J.; Hadzi, D. "AM1 and ab initio Calcuations on Nitric Acid Mono- and Trihydrates", *J. Molec. Struct*., *247*, 225, **1991**.
Krcho, D. In *The 3rd Biennial Engineering Mathematics and Applications Conference*: Adelaide, Australia, **1998**.
Lammel, G.; Perner, D., "The Atmospheric Aerosol as a Source of Nitrous Acid in the Polluted Atmosphere", *J. Aerosol Sci.*, *19*, 1199-1202, **1988**.
Lammel, G.; Cape, J.N., "Nitrous Acid and Nitrite in the Atmosphere", *Chem. Soc. Rev.*, *25*, 361-369, **1996**.
Lary, D.J.; Lee, A.M.; Toumi, R.; Newchurch, M.J.; Pirre, M.; Renard, J.B., "Carbon Aerosols and Atmospheric Photochemistry", *J. Geophys. Res.*, *102*, 3671-3682, **1997**.
Longfellow, C.A.; Imamura, T.; Ravishankara, A.R.; Hanson, D.R., "HONO Solubility and Heterogeneous Reactivity on Sulfuric Acid Surfaces", *J. Phys. Chem. A*, *102*, 3323-3332, **1998**.
Longfellow, C.A.; Ravishankara, A.R.; Hanson, D.R., "Reactive Uptake on Hydrocarbon Soot: Focus on NO_2", *J. Geophys. Res.*, *104*, 13833-13840, **1999**.
Longfellow, C.A.; Ravishankara, A.R.; Hanson, D.R., "Reactive and Nonreactive Uptake on Hydrocarbon Soot: HNO_3, O_3, and N_2O_5", *J. Geophys. Res.-Atmos.*, *105*, 24345-24350, **2000**.
Lure, B.A., Mikhno, A.V. "Interaction of NO_2 with Soot", *Kinet. Catal.*, *38*, 490-497, **1997**.
Markovitz, S, Schwartz, E., Newman, L., "Hydrolysis of Dinitrogen Trioxide in Dilute Acid Solution", *Inorg. Chem.*, *20*, 444-450, **1981**.
Marley, N.A.; Gaffney, J.S.; Cunningham, M.M., "Cylindrical Internal Reflectance Spectroscopy", *Spectroscopy*, *7*, 44-53, **1992**.
Marley, N.A.; Gaffney, J.S.; Cunningham, M.M., "Aqueous Greenhouse Species in Clouds, Fogs, and Aerosols", *Environ. Sci. Technol.*, *27*, 2864-2869, **1993**.
McGraw, G.E.; Bernitt, D.L.; Hisatsune, I.C., "Vibrational Spectra of Isotopic Nitric Acids", *J. Chem. Phys.*, *42*, 237-244, **1965**.
Meng, Z., Dabdub, D.,Seinfeld, J.H. "Chemical Coupling Between Atmospheric Ozone and Particulate Matter", *Science, 277*, 116-119, **1997**.
Meng, Z., Dabdub, D.,Seinfeld, J.H. "Size-Resolved and Chemically Resolved Model of Atmospheric Aerosol Dynamics", *J. Geophys. Res*., *103*, 3419-3425, **1998**.
Mertes, S.; Wahner, A., "Uptake of Nitrogen Dioxide and Nitrous Acid On Aqueous Surfaces", *J. Phys. Chem.*, *99*, 14000-14006, **1995**.
Middlebrook, A.M.; Iraci, L.T.; McNeill, L.S.; Koehler, B.G.; Wilson, M.A.; Saastad, O.W.; Tolbert, M.A., "Fourier Transform Infrared Studies of Thin H_2SO_4/H_2O Films:

Formation, Water Uptake and Solid-Liquid Phase Changes", *J. Geophys. Res.*, *98*, 20473-20481, **1993**.

Miles, F. D. in Nitric Acid Manufacture and Uses, Oxford University Press, London, New York**,** p.9-25, **1961**.

Miller, T.M.; Grassian, V.H., "Heterogeneous Chemistry of NO_2 on Mineral Oxide Particles: Spectroscopic Evidence for Oxide-Coordinated and Water-Solvated Surface Nitrate", *Geophys. Res. Lett.*, *25*, 3835-3838, **1998**.

Mochida, M.; Finlayson-Pitts, B.J., "FTIR Studies of the Reaction of Gaseous NO with HNO_3 on Porous Glass: Implications for Conversion of HNO_3 to Photochemically Active NO_x in the Atmosphere", *J. Phys. Chem. A*, *104*, 9705-9711, **2000**.

Molina, M. J.; Zhang, R.; Wooldridge, P. J.; McMahon, J. R.; Kim, J. E.; Chang, H. Y.; Beyer, K. D. "Physical Chemistry of the $H_2SO_4/HNO_3/H_2O$ System: Implications for Polar Stratospheric Clouds", *Science***,** *261*, 1418, **1993**.

Morris, J.R.; Behr, P.; Antman, M.D.; Ringeisen, B.R.; Splan, J.; Nathanson, G.M., "Molecular Beam Scattering from Supercooled Sulfuric Acid: Collisions of HCl, HBr and HNO_3 with 70 wt% D_2SO_4", *J. Phys. Chem. A.*, *104*, 6738-6751, **2000**.

Notholt, J.; Hjorth, J.; Raes, F., "Formation of HNO_2 On Aerosol Surfaces During Foggy Periods in the Presence of NO and NO_2", *Atmos. Environ.*, *26A*, 211-217, **1992**.

Nour, E.M.; Chen, L.-H.; Laane, J., "Interconversion Studies and Characterization of Asymmetric and Symmetric Dinitrogen Trioxide in Nitric Oxide Matrices by Raman and Infrared Spectroscopy", *J. Phys. Chem.*, *87*, 1113-1120, **1983**.

Ohta, K.; Ishida, H., "Comparison Among Several Numerical Integration Methods for Kramers-Kronig Transformation", *Appl. Spectros.*, *42*, 952-957, **1988**.

Pagsberg, P.; Bjergbakke, E.; Ratajczak, E.; Sillesen, A., "Kinetics of the Gas Phase Reaction OH + NO(+ M) → HONO (+ M) and the Determination of the UV Absorption Cross Sections of HONO", *Chem. Phys. Lett.*, *272*, 383-390, **1997**.

Perner, D.; Platt, U., "Detection of Nitrous Acid in the Atmosphere by Differential Optical Absorption", *Geophys. Res. Lett.*, *6*, 917-920, **1979**.

Phillips, L.F., "Surface Concentrations and Compound Formation in Aqueous Sulfuric Acid", *Aust. J. Chem.*, *47*, 91-99, **1994**.

Pimentel, G.C.; McClellan, A.L. *The Hydrogen Bond*; W. H. Freeman: San Francisco, **1960**.

Pitts, J.N., Jr.; Grosjean, D.; Cauwenberghe, K.V.; Schmid, J.P.; Fitz, D.R., "Photooxidation of Aliphatic Amines Under Simulated Atmospheric Conditions: Formation of Nitrosamines, Nitramines, Amides, and Photochemical Oxidant", *Environ. Sci. Tech.*, *12*, 946-954, **1978**.

Pitts, J.N., Jr.; Sanhueza, E.; Atkinson, R.; Carter, W.P.L.; Winer, A.M.; Harris, G.W.; Plum, C.N., "An Investigation of the Dark Formation of Nitrous Acid in Environmental Chambers", *Int. J. Chem. Kinet.*, *16*, 919-939, **1984a**.

Pitts, J.N., Jr.; Biermann, H.W.; Winer, A.M.; Tuazon, E.C.,., "Spectroscopic Identification and Measurement of Gaseous Nitrous Acid in Dilute Auto Exhaust", *Atmos. Environ.*, *18*, 847-854, **1984b**.

Pitts, J.N. Jr.; Wallington, T.J.; Biermann, H.W.; Winer, A.M., "Identification and Measurement of Nitrous Acid in an Indoor Environment", *Atmos. Environ.*, *19*, 763-767, **1985**.

Platt, U.; Hausmann, M., "Spectroscopic Measurement of the Free Radicals NO_3, BrO, IO, and OH in the Troposphere", *Res. Chem. Intermed.*, *20*, 557-578, **1994**.

Ponche, J.L., George, C., Mirabel, P. "Mass Transfer at the Air Water Interface - Mass Accomodation Coefficients of SO_2, HNO_3, NO_2 and NH_3", *J. Atmos. Chem.*, *16*, 1-21, **1993**.

Querry, M.R.; Tyler, I.L., "Reflectance and Complex Refractive Indices in the Infrared for Aqueous Solutions of Nitric Acid", *J. Chem. Phys.*, *72*, 2495-2499, **1980**.

Radüge, C.; Pflumio, V.; Shen, Y.R., "Surface Vibrational Spectroscopy of Sulfuric Acid-Water Mixtures at the Liquid-Vapor Interface", *Chem. Phys. Lett.*, *274*, 140-144, **1997**.

Raes, F.; VanDingenen, R.; Vignati, E.; Wilson, J.; Putaud, J.-P.; Seinfeld, J.H.; Adams, P., "Formation and Cycling of Aerosols in the Global Troposphere", *Atmos. Environ.*, *34*, 4215-4240, **2000**.

Rasmussen, T.R.; Brauer, M.; Kjærgaard, S., "Effects of Nitrous Acid Exposure On Human Mucous Membranes", *Amer. J. Respir. Crit. Care Med.*, *151*, 1504-1511, **1995**.

Ravishankara, A.R., Longfellow, C.A. "Reactions on Tropospheric Condensed Matter"**,** *Phys. Chem. Chem. Phys.*, *1*, 5433-5441, **1999**.

Redlich, O.; Bigeleisen, J. "The Ionization of Strong Electrolytes. I. General Remarks, Nitric Acid", *J. Am. Chem. Soc.*, *65*, 1883, **1943**.

Redlich, O. "The Dissociation of Strong Electrolytes", *Chem. Revs.*, *39*, 333, **1946**.

Ritzhaupt, G.; Devlin, J.P., "Ionic Vs. Molecular Nature of Monomeric Ammonium and Hydronium Nitrate. Infrared Spectra of $H_3O^+NO_3^+$, and $NH_4^+NO_3^-$ Solvated in Argon Matrices", *J. Phys. Chem.*, *81*, 521-525, **1977**.

Ritzhaupt, G.; Devlin, J.P., "Infrared Spectra of Nitric and Hydrochloric Acid Hydrate Thin Films", *J. Phys. Chem.*, *1991*, 90-95, **1991**.

Rogaski, C.A.; Golden, D.M.; Williams, L.R., "Reactive Uptake and Hydration Experiments on Amorphous Carbon Treated with NO_2, SO_2, O_3, HNO_3, and H_2SO_4", *Geophys. Res. Lett.*, *24*, 381-384, **1997**.

Sakamaki, F.; Hatakeyama, S.; Akimoto, H., "Formation of Nitrous Acid and Nitric Oxide in the Heterogeneous Dark Reaction of Nitrogen Dioxide and Water Vapor in a Smog Chamber", *Int. J. Chem. Kinet.*, *15*, 1013-1029, **1983**.

Saliba, N.A.; Mochida, M.; Finlayson-Pitts, B.J., "Laboratory studies of sources of HONO in polluted urban atmospheres", *Geophys. Res. Lett.*, *27*, 3229-3232, **2000**.

Sato, S.; Yamaguchi, D.; Senga, T.; Kawasaki, M., "Photodissociation cross sections of N_2O_3 adsorbed on An(III)", *J. Phys. Chem. B*, *104*, 4863-4866, **2000**.

Schnitzer, C.; Baldelli, S.; Campbell, D.J.; Shultz, M.J., "Sum Frequency Generation of O-H Vibrations on the Surface of H_2O/HNO_3 Solutions and Liquid HNO_3", *J. Phys. Chem. A*, *103*, 6383-6386, **1999**.

Schwartz, S.E.; White, W.E. In *Advances in Environmental Science and Engineering*; Pfafflin, J. R., Ziegler, E. N., Eds.; Gordon and Breach Science Publishers: New York, Vol. 4; pp 1-45, **1981**.

Sharma, H.D.; Jervis, R.E.; Wong, K.Y., "Isotopic Exchange Reactions in Nitrogen Oxides", *J. Phys. Chem.*, *74*, 923-933, **1979**.

Shultz, M.J.; Schnitzer, C.; Simonelli, D.; Baldelli, S., "Sum Frequency Generation Spectroscopy of the Aqueous Interface: Ionic and Soluble Molecular Solutions", *Int. Rev. Phys. Chem.*, *19*, 123-153, **2000**.

Simon, A.; Horakh, J.; Obermeyer, A.; Borrmann, H., "Crystalline Nitrogen Oxides - Crystal Structure of N_2O_3 and a Remark Concerning the Crystal Structure of N_2O_5", *Angew. Chem. Int. Ed. Engl.*, *31*, 301-303, **1992**.

Sjodin, A.; Ferm, M., "Measurement of Nitrous Acid in Urban Air", *Atmos. Environ.*, *19*, 985-992, **1985**.

Smith, J.H., "A Rate Study of the Oxidation of Nitric Oxide with Nitric Acid Vapor", *J. Am. Chem. Soc.*, *69*, 1741-1747, **1947**.

Smith, D.M., Welch, W.F., Graham, S.M., Chughtai, A.R., Wicke, B.G., Grady, K.A., "Reaction of Nitrogen Oxides with Black Carbon: An FTIR Study", *Appl. Spectrosc.*, *42*, 674-680, **1988**.

Smith, R.H.; Leu, M.-T.; Keyser, L.F., "Infrared Spectra of Solid Films Formed from Vapors Containing Water and Nitric Acid", *J. Phys. Chem.*, *95*, 5924-5930, **1991**.

Sneh, O.; Cameron, M.A.; George, S.M., "Adsorption and Desorption of Kinetics of H_2O on a Fully Hydroxylated SiO_2 Lattice", *Surf. Sci.*, *364*, 61-78, **1996**.

Snyder, R.G.; Hisatsune, I.C. "Infrared Spectrum of Dinitrogen Tetroxide", *J. Mol. Spectrosc.*, *2*, 139-150, **1957**.

Spengler, J.D.; Brauer, M.; Samet, J.M.; Lambert, W.E., "Nitrous Acid in Albequerque, New Mexico Homes", *J. Air Waste Manage. Assoc.*, *43*, 1479-1485, **1993**.

Spicer, C.W.; Kenny, D.V.; Ward, G.F.; Billick, I.H., "Transformations, Lifetimes, and Sources of NO_2, HONO, and HNO_3 in Indoor Environments", *J. Air Waste Manage. Assoc.*, *43*, 1479-1485, **1993**.

Streit, G.E.; Wells, J.S.; Fehsenfeld, F.C.; Howard, C.J., "A Tunable Diode Laser Study of the Reactions of Nitric and Nitrous acids: HNO_3 + NO and HNO_2 + O_3", *J. Chem. Phys.*, *70*, 3439-3443, **1979**.

Stutz, J.; Platt, U., "Numerical Analysis and Estimation of the Statistical Error of Differential Optical Absorption Spectroscopy Measurements With Least-Squares Methods", *Applied Optics*, *35*, 6041-6053, **1996**.

Stutz, J.; Kim, E.S.; Platt, U.; Bruno, P.; Perrino, C.; Febo, A., "UV-Visible Absorption Cross Sections of Nitrous Acid", *J. Geophys. Res.-Atmos.*, *105*, 14585-14592, **2000**.

Svensson, R.; Ljungström, E.; Lindqvist, O., "Kinetics of the Reaction Between Nitrogen Dioxide and Water Vapour", *Atmos. Environ.*, *21*, 1529-1539, **1987**.

Tabor, K.; Gutzwiller, L.; Rossi, M.J. "The heterogeneous interaction of NO_2 with amorphous carbon", *Geophys. Res. Lett.*, *20*, 1431-1434, **1993**.

Tabor, K.; Gutzwiller, L.; Rossi, M.J., "Heterogeneous Chemical Kinetics of NO_2 on Amorphous Carbon at Ambient Temperature", *J. Phys. Chem.*, *98*, 6172-6186, **1994**.

Taira, M.; Kanda, Y., "Continuous Generation System for Low-Concentration Gaseous Nitrous Acid", *Anal. Chem.*, *62*, 630-633, **1990**.

Tao, F.-M.; Higgins, K.; Klemperer, W.; Nelson, D.D., "Structure, Binding Energy, and Equilibrium Constant of the Nitric Acid-Water Complex", *Geophys. Res. Lett.*, *23*, 1797-1800, **1996**.

TenBrink, H.M.; Spoelstra, H., "The dark decay of HONO in environmental (SMOG) chambers", *Atmos. Environ.*, *32*, 247-251, **1998**.

Tolbert, M.A.; Middlebrook, A.M., "Fourier Transform Infrared Studies of Model Polar Stratospheric Cloud Surfaces: Growth and Evaporation of Ice and Nitric Acid/Ice", *J. Geophys. Res.*, *95*, 22,423-22431, **1990**.

Tyndall, G.S.; Orlando, J.J.; Calvert, J.G., "Upper Limit for the Rate Coefficient for the Reaction HO_2 + NO_2 --> HONO + O_2", *Environ. Sci. Tech.*, *29*, 202-206, **1995**.

Underwood, G.M.; Miller, T.M.; Grassian, V.H., "Transmission FT-IR and Knudsen Cell Study of the Heterogeneous Reactivity of Gaseous Nitrogen Dioxide on Mineral Oxide Particles", *J. Phys. Chem. A*, *103*, 6184-6190, **1999**.

Valyon, J.; Hall, W.K., "Studies of Surface Species Formed from NO on Copper Zeolites", *J. Phys. Chem.*, *97*, 1204-1212, **1993**.

Varetti, E.L.; Pimentel, G.C., "Isomeric Forms of Dinitrogen Trioxides in a Nitrogen Matrix", *J. Chem. Phys.*, *55*, 3813-3821, **1971**.

Vecera, Z.; Dasgupta, P.K., "Indoor NItrous Acid Levels: Production of Nitrous Acid from Open Flame Sources", *Intern. J. Environ. Anal. Chem.*, *56*, 311-316, **1994**.

Wagman, D. D.; Evans, W. H.; Parker, V. B.; Schumm, R. H.; Halow, I.; Bailey, S. M.; Churney, K. L.; Nuttall, R. L. The NBS tables of chemical thermodynamic properties. Supp. No 2, *J. Phys. Chem. Ref. Data*, *11*, 65, **1982**.

Wallington, T.J.; Japar, S.M., "Fourier Transform Infrared Kinetic Studies of the Reaction of Hono with HNO_3, NO_3 and N_2O_5 at 295-K", *J. Atmos. Chem.*, *9*, 399-409, **1989**.

Wang, X.; Zheng, Q.; Fan, K., "Ab Initio Study on the Structure and Vibrational Spectra of Dinitrogen Trioxide and its Isomers", *J. Mol. Structure*, *403*, 245-251, **1997**.

Wang, J.; Koel, B.E., "IRAS Studies of NO_2, N_2O_3, and N_2O_4 Adsorbed on Au(111) Surfaces and Reactions with Coadsorbed H_2O", *J. Phys. Chem. A*, *102*, 8573-8579, **1998a**.

Wang, J.; Voss, M.R.; Busse, H.; Koel, B.E., "Chemisorbed Oxygen on Au(111) Produced by a Novel Route: Reaction in Condensed Films of $NO_2 + H_2O$", *J. Phys. Chem. B*, *102*, 4693-4696, **1998b**.

Wayne, L.G.; Yost, D.M., "Kinetics of the Rapid Gas Phase Reaction Between NO, NO_2 and H_2O", *J. Chem. Phys.*, *19*, 41-47, **1951**.

White, J.U., "Long Optical Paths of Large Aperture", *Journal of the Optical Society of America*, *32*, 285-288, **1942**.

Wiesen, P.; Kleffmann, J.; Kurtenbach, R.; Becker, K.H., "Mechanistic Study of the Heterogeneous Conversion of NO_2 into HONO and N_2O on Acid Surfaces", *Faraday Discussions*, *100*, 121-127, **1995**.

Winer, A.M.; Biermann, H.W., "Long Pathlength Differential Optical Absorption Spectroscopy (DOAS) Measurements of Gaseous HONO, NO_2 and HCHO in the California South Coast Air Basin", *Res. Chem. Intermed.*, *20*, 423-445, **1994**.

Wingen, L.M.; Barney, W.S.; Lakin, M.J.; Brauers, T.; Finlayson-Pitts, B.J., "A Unique Method for Laboratory Quantification of Gaseous Nitrous Acid (HONO) Using the Reaction $HONO + Cl \rightarrow ClNO + H_2O$", *J. Phys. Chem. A.*, *104*, 329-335, **2000**.

Zhang, R.; Leu, M.; Keyser, L.F., "Heterogeneous Chemistry of HONO on Liquid Sulfuric Acid: A New Mechanism of Chlorine Activation on Stratospheric Sulfate Aerosols", *J. Phys. Chem.*, *100*, **1996**.

Zhuravlev, L.T., "Surface Characterization of Amorphous Silica - a Review of Work From the Former USSR", *Coll. Surf. A*, *74*, 71-90, **1993**.

LIST OF PUBLICATIONS

1. Barney, W.S., Finlayson-Pitts, B.J., "Enhancement of N_2O_4 on Porous Glass at Room Temperature: A Key Intermediate in the Heterogeneous Hydrolysis of NO_2", *J. Phys. Chem. A 104*, 171-175, **2000**; http://pubs.acs.org/CHECKCCIP-993920638/isubscribe/journals/jpcafh/104/i02/pdf/jp993169b.pdf

2. Wingen, L.M., Barney, W. S., Lakin, M.J., Brauers, T., Finlayson-Pitts, B.J., "A Unique Method for Laboratory Quantification of Gaseous Nitrous Acid (HONO) Using the Reaction HONO + HCl → ClNO + H_2O", *J. Phys. Chem. A 104*, 329-335, **2000**; http://pubs.acs.org/isubscribe/journals/jpcafh/104/i02/pdf/jp992890e.pdf

3. Barney, S.W., Wingen, L.M., Lakin, M.J., Brauers, T., Stutz, J., Finlayson-Pitts, B.J., "Infrared Absorption Cross-Section Measurements for Nitrous Acid (HONO) at Room Temperature", *J. Phys. Chem. A 104*, 1692-1699, **2000**; http://pubs.acs.org/isubscribe/journals/jpcafh/104/i08/pdf/jp9930503.pdf; *Erratum, J. Phys. Chem. A 105*, 4166, 2001; http://pubs.acs.org/isubscribe/journals/jpcafh/105/i16/pdf/jp010734d.pdf

4. Michihiro, M., Finlayson-Pitts, B.J., "FTIR Study of N_2O_3 on Porous Glass at Room Temperature", *J. Phys. Chem. A 104*, 8038-8044, **2000**; http://pubs.acs.org/isubscribe/journals/jpcafh/104/i34/pdf/jp0014840.pdf

5. Michihiro, M., Finlayson-Pitts, B.J., "FTIR Studies of Gaseous NO with HNO_3 on Porous Glass: Implications for Conversion of HNO_3 to Photochemically Active NO_x in the Atmosphere", *J. Phys. Chem. A 104*, 9705-9711, **2000**; http://pubs.acs.org/isubscribe/journals/jpcafh/104/i43/pdf/jp00147a.pdf

6. Saliba, N.A., Michihiro, M., Finlayson-Pitts, B.J., "Laboratory Studies of Sources of HONO in Polluted Urban Atmospheres", *Geophys. Res. Lett. 27*, 3229-3232, **2000**; http://www.agu.org/journals/gl/gl0019/2000GL011724/pdf/2000GL011724.pdf

7. Yang, H., Finlayson-Pitts, B.J., "Infrared Spectroscopic Studies of Binary Solutions of Nitric Acid and Water and Ternary Solutions of Nitric Acid, Sulfuric Acid, and Water at Room Temperature: Evidence for Molecular Nitric Acid at the Surface", *J. Phys. Chem. A 105,* 1890-1896, **2001**; http://pubs.acs.org/isubscribe/journals/jpcafh/105/i10/pdf/jp004224f.pdf

GLOSSARY OF TERMS, ABBREVIATIONS AND SYMBOLS

Chemical Molecular Formulas

AgBr:	Silver bromide
Al_2O_3:	Alumina
$CaCO_3$:	Calcium carbonate
CaF_2:	Calcium fluoride
CCl_4:	Carbon tetrachloride
Cl^-.HONO:	Chloride adduct of nitrous acid for detection by mass spectrometry
ClNO:	Nitrosyl chloride
Cl_2:	Chlorine
CO:	Carbon monoxide
CO_2:	Carbon dioxide
D_2SO_4:	Deuterated sulfuric acid
Fe_2O_3:	Iron oxide
HBr:	Hydrogen bromide
HCHO:	Formaldehyde
HCl:	Hydrochloric acid
He:	Helium
HF:	Hydrogen fluoride
HNO_3:	Nitric acid
$HNO_3.H_2O$:	Monohydrated nitric acid
HNO_3 $3H_2O$:	Trihydrated nitric acid
HONO:	Nitrous acid
HO_2:	Hydro peroxy radical
H_2O:	Water
H_2SO_4:	Sulfuric acid
H_3O^+:	Hydronium ion
NaCl:	Sodium chloride
$NaHSO_3$:	Sodium bisulfite
$NaNO_2$:	Sodium Nitrite
$NaNO_3$:	Sodium Nitrate
NaOH:	Sodium hydroxide
Na_2CO_3:	Sodium carbonate
Na_2SO_4:	Sodium sulfate
NH_3:	Ammonia
NH_4NO_3:	Ammonium nitrate
$(NH_4)_2SO_4$:	Ammonium sulfate
NO:	Nitrogen oxide
NO_2:	Nitrogen dioxide
NO_2^+:	Nitronium ion
NO_3:	Nitrate radical
NO_3^-:	Nitrate ion
NO_x:	$NO + NO_2$
NO_y:	Sum of nitrogen oxides, $NO + NO_2 + HNO_3 + PAN + 2N_2O_5 + \cdots$

N_2:	Nitrogen
N_2O:	Nitrous oxide
N_2O_2:	Dimer of NO
N_2O_3:	Dinitrogen trioxide
N_2O_4:	Dinitrogen tetraoxide
O_2:	Oxygen
$O(^3P)$:	Oxygen triplet "P" state (ground electronic state)
O_3:	Ozone
OH:	Hydroxyl radical
PAN:	Peroxy acetyl nitrate
RCH_2R':	Hydrocarbon
$RCHR'.$:	Hydrocarbon radical
$RCH(OO)R'.$:	Alkyl peroxy radical
$RCH(O)R'.$:	Alkoxy radical
Si:	Silicon
TiO_2:	Titanium dioxide
VOC:	Volatile Organic Compound
Xe:	Xenon

<u>Units</u>

ppb:	Parts per billion by volume
ppm:	Parts per million by volume
cm^{-1}:	Wavenumber
h:	hour
MΩ:	Megaohm
M:	Molarity
nm:	nanometer
S/V:	Ratio of available surface area to volume

<u>Acronyms</u>

ACS:	American Chemical Society
ACUCHEM:	Acronym for numerical integration package used for kinetics analysis
AMTIR:	Type of infrared transmitting material made of Ge-As-Se glass
API-MS:	Atmospheric Pressure Ionization Mass Spectrometry
ATR:	Attenuated Total Reflectance
BET:	Brunauer-Emmett-Teller
CIT:	California Institute of Technology
DOAS:	Differential Optical Absorption Spectroscopy
FTIR:	Fourier Transform Infra-Red
HgCdTe:	Mercury-Cadmium-Tellurium
IR:	Infra-Red
k:	Rate constant
KK:	Kramers-Kronig
M:	Any third molecule to remove excess energy
MCT:	Mercury-Cadmium-Tellurium

MFC:	Name of spectral analysis fitting software
MS-MS:	Tandem Mass Spectrometry
NAM:	Nitric Acid Monohydrate
NAT:	Nitric Acid Trihydrate
PM:	Particulate Matter
PM2.5:	Particulate Matter with diameter ≤ 2.5 μm
PM10:	Particulate Matter with diameter ≤ 10 μm
RH:	Relative Humidity
SCAQS:	South Coast Air Quality Study
SFG:	Sum Frequency Generation
SR:	Single Reflectance
TDLS:	Tunable Diode Laser Spectrometry
UV:	Ultra-Violet
UHP:	Ultra High Purity
ZnSe:	Zinc Selenide

<u>Symbols</u>

$h\nu$:	Energy of a light photon of frequency ν, where h = Plank's constant
ν:	Stretching mode
ΔH^0:	Enthalpy of the reaction at normal conditions
ℓ:	Path length
σ:	Standard deviation (error)
σ^{IR}:	Infrared absorption cross-section

APPENDIX

A. ANALYSIS OF SPECTROSCOPIC DATA

A.1. UV/Visible and FTIR Spectral Analysis.

Spectral analysis was accomplished using the program MFC (*Gomer et al.*, 1995). In a gas mixture with *m* absorbers, the intensity $I(\lambda)$ at the detector may be written as equation (Eq. A.1).

$$I(\lambda) = I_0(\lambda)\exp\left[-R(\lambda) - \ell\sum_{j=1}^{m}\sigma(\lambda)_j C_j\right] \qquad \text{(Eq. A.1)}$$

Here $I_0(\lambda)$ is the source intensity transmitted through an empty chamber, and ℓ is the path length. $R(\lambda)$ represents other changes in the background intensity not due to absorption, including scattering and time-variation of the detector sensitivity. C_j and σ_j are the concentration and absorption cross-section, respectively, of the *j*th absorber. We further make the simplifying assumption that $\sigma(\lambda)$ can be split into a structured part, $\sigma_S(\lambda)$, and $\sigma_B(\lambda)$ which represents the broad, structureless part of the absorption. Taking the logarithm of (Eq. A.1), and showing the contributions of the structured and broad absorptions separately, one obtains equation (Eq. A.2).

$$\ln\frac{I(\lambda)}{I_0(\lambda)} = -R(\lambda) - \ell\sum_{j=1}^{m}C_j\sigma_{B\,j}(\lambda) - \ell\sum_{j=1}^{m}C_j\sigma_{S\,j}(\lambda) \qquad \text{(Eq. A.2)}$$

The broad component of the absorption can be simplified to a single function of wavelength

$$B(\lambda) = \ell\sum_{j=1}^{m}C_j\sigma_{B\,j}(\lambda) \qquad \text{(Eq. A.3)}$$

giving

$$\ln\frac{I_0(\lambda)}{I(\lambda)} = R(\lambda) + B(\lambda) + \ell\sum_{j=1}^{m}C_j\sigma_{S\,j}(\lambda) \qquad \text{(Eq. A.4)}$$

$R(\lambda)$ and $B(\lambda)$ are both broad, and can be described by a low-order polynomial in λ. If the structured absorption $\sigma_{Sj}(\lambda)$ of the *j*th individual absorber can be fit by an independent reference spectrum $S_j(\lambda)$, then the concentration C_j can be determined by a linear least-squares using the model function $F(\lambda)$ to fit the observed spectrum:

$$F(\lambda) = P(\lambda) + \ell\sum_{j=1}^{m}a_j S_j(\lambda) \qquad \text{(Eq. A.5)}$$

Here a_j are the scaling parameters for the reference spectra $S_j(\lambda)$ which give the best fit to the observed spectrum. The a_j are proportional to the true concentrations C_j. $P(\lambda)$ is a polynomial of sufficiently high order that it will fit the broad absorption spectrum very well, but not so high as to reproduce structured absorptions. For the work described in this paper, polynomial of order 0-3 were typically used. The polynomial is not strictly independent of the concentrations C_j because $B(\lambda)$ in equation (EqA.3) depends on C_j, and the scattering tern

In the above discussion, we have neglected the effects of using a discrete diode array; however, these effects were included in our analysis for the UV spectra. In particular, we used a "shift and squeeze" method to compensate for the possibility that the grating position or dispersion might change slightly between experiments. For a complete discussion, see Stutz and Platt (1996) and Platt and Hausmann (1994).

A.2. Single Beam Spectra.

Single beam spectra are spectra which are not automatically ratioed to one background spectrum. This was particularly useful for porous glass cell experiments in which many different backgrounds were compared. Single beam spectra were recorded with the porous glass either in the path of the infrared beam or withdrawn from the beam, as well as with and without the reactants in the cell. The ratio of the single beam spectrum with the porous glass and reactant/product mixture in the beam (S_{pg}) to that without the reactants (S_{pg}^0) was used to obtain the absorbance due to gases plus surface-adsorbed species. This allowed the strong silica absorptions to be ratioed out. Similarly, the ratio of the analogous single beam spectra with (S_g) and without (S_g^0) the reactants/products and with the porous glass withdrawn from the infrared beam was used to obtain the absorbance of the gases alone. Subtracting the spectrum of the gas species from that of the combined gas plus surface species gave the spectrum due to surface-adsorbed species alone. Infrared spectra were typically recorded at a resolution of 1 cm^{-1}, or for the kinetic studies, at 4 cm^{-1}. The number of scans was varied between 1-1024, depending on the S/N ratio and time resolution required for experiments.

A.3. ATR Data Analysis.

ATR is an internal reflection technique in which light is directed into an infrared transmitting crystal, which in this case is immersed in the acid solution. It strikes the interface at an angle greater than the critical angle and hence undergoes total internal reflection (*Harrick*, 1967; *Marley et al.*, 1992). However, there is an evanescent wave that penetrates into the surrounding medium, with the depth of penetration depending on the angle of incidence and the indices of refraction of the crystal and the surrounding solution. As a result, if single beam spectra with and without the absorbing species are ratioed, an absorption spectrum of the species can be obtained.

ATR spectra of bulk solutions are known to be very similar to transmission spectra, with some differences (*Harrick*, 1967; *Marley et al.*, 1992). For one particular

angle of incidence and crystal-solution combination, the major factor is that the depth of penetration of the evanescent wave, and hence total absorption, varies directly with the wavelength (*i.e.* inversely with wavenumber). As a result, in bulk solutions the relative peak intensities using ATR decrease with increasing wavenumber in the infrared compared to those measured using a direct transmission cell. The position of peaks may also appear to have shifted slightly to shorter wavenumbers (up to ~10 cm^{-1}, depending on the angle of incidence), and for wide bands, broadening of the peak on the short wavenumber side is often seen (*Harrick*, 1967). The relative intensities for ATR spectra reported here have been corrected for the dependence on wavenumber by multiplying the measured absorbances by the wavenumber.

A.4. Single Reflectance-FTIR Data Analysis.

The single reflectance spectra were analyzed in the following manner to obtain the absorption spectra. First, a reflectance spectrum ($R_{\bar{v}}$) was obtained by taking the ratio between a single beam reflectance spectrum of the sample ($R_{\bar{v}}^{s}$) and that obtained by replacing the aqueous solution with a gold mirror ($R_{\bar{v}}^{gm}$), *i.e.,* $R_{\bar{v}} = \frac{R_{\bar{v}}^{s}}{R_{\bar{v}}^{gm}}$. In regions of strong light absorption, the refractive index (*N*) changes rapidly because of the contribution of the imaginary part, (*k*), due to absorption of light at that frequency:

$$N_{\bar{v}} = n_{\bar{v}} + ik_{\bar{v}} \qquad \text{(Eq. B.1)}$$

The reflectance spectrum contains information on the real part (*n*) of the refractive index of the liquid as a function of wavenumber ($\bar{v}$), as well as the imaginary part (*k*) when absorption of the light occurs. Absorption peaks in the reflectance mode typically appear as differential shaped peaks in the spectrum. The coefficient $k_{\bar{v}}$ of the imaginary part of the index of refraction is related to the absorption coefficient, $\sigma_{\bar{v}}$ at wavenumber $\bar{v}$ by equation (Eq. B.2),

$$k_{\bar{v}} = \frac{C\sigma_{\bar{v}}}{4\pi\bar{v}} \qquad \text{(Eq. B.2)}$$

where *C* is the concentration of the absorbing species in molecule cm^{-3} and $\sigma_{\bar{v}}$ is the absorption coefficient in cm^2 $molecule^{-1}$. The absorption coefficient $\sigma_{\bar{v}}$ is proportional to $k_{\bar{v}}(\bar{v}) = k_{\bar{v}}\left(\frac{1}{\lambda}\right)$. For direct comparison to the ATR/transmission spectra which are also proportional to $\sigma_{\bar{v}}$, the *k* spectrum has been multiplied by wavenumber and the spectra scaled appropriately. The *k* spectra are therefore reported not in terms of, $k_{\bar{v}}$, but in terms of relative intensities which are proportional to $\sigma_{\bar{v}}$.

The Kramers-Kronig (KK) transform (*Ohta and Ishida*, 1988; *Krcho*, 1998) was applied to the reflectance spectrum to obtain the absorption coefficient (k) spectrum as a function of wavenumber. The KK relationship relates the real and imaginary parts of the index of refraction using the measured reflectance spectrum, $R_{\bar{\nu}}$:

$$n_{\bar{\nu}} = \frac{1 - R_{\bar{\nu}}}{1 + R_{\bar{\nu}} - 2\cos\theta_{\bar{\nu}}\sqrt{R_{\bar{\nu}}}} \qquad k_{\bar{\nu}} = \frac{-2\sin\theta_{\bar{\nu}}\sqrt{R_{\bar{\nu}}}}{1 + R_{\bar{\nu}} - 2\cos\theta_{\bar{\nu}}\sqrt{R_{\bar{\nu}}}} \qquad \text{(Eq. B.3)}$$

In equations (Eq. B.3), $\theta_{\bar{\nu}}$ is the phase shift angle given by

$$\theta_{\bar{\nu}_m} = \frac{2\bar{\nu}_m}{\pi}\int_0^\infty \frac{\ln(\sqrt{R_{\bar{\nu}}})d\bar{\nu}}{\bar{\nu}^2 - \bar{\nu}_m^2} \qquad \text{(Eq. B.4)}$$

where $\bar{\nu}_m$ is the measured wavenumber. The integration is carried out in practice over a finite range of wavenumbers, $\bar{\nu}$, from 500 to 4000 cm^{-1}. KK transforms were performed using the IR/Raman application package provided by GRAMS/32 (Galactic Industries Corp., Salem, NH), which uses a double Fourier transform method to calculate the integrals.

Simulation of the SR-FTIR spectra at the air-water interface and calculation of the penetration depths as a function of wavenumber in water, the 40 mol% nitric acid solution and the H_2SO_4 – HNO_3 – H_2O solution containing 25 mol% each of HNO_3 and H_2SO_4 were performed using MATLAB (The MathWorks, Inc., Nartic, MA). The program was originally written in FORTRAN code by Professor Richard A. Dluhy at the University of Georgia; we converted to MATLAB functions for convenience of calculation. The real part (n) and imaginary part (k) of the refractive index for water and for the solutions were obtained from literature (*Bertie and Lan*, 1996). The optical constants of the 40 mol% HNO_3 solution and the ternary solution were obtained by taking the KK transform of the SR-FTIR spectra measured using the single reflectance cell. For air, n was taken as 1 and k as 0 at all wavenumbers. The calculated penetration depths in the region from 4000 to 500 cm^{-1} lie in the range from 0.7 - 90 μm, being smallest in the regions of water absorption, *i.e.* ~0.7 μm at 3414 cm^{-1} and 3 - 6 μm at 1638 cm^{-1}.

A.5. Comparison of Transmission/ATR and SR-FTIR Spectra.

Ideally, if the composition of the surface is the same as the bulk, the absorption spectra obtained using transmission/ATR and SR should be identical. However, in practice, this is not the case, with potential deviations in both cases. For transmission/ATR spectra, there is a dispersion in the refractive index in the vicinity of an absorption band; this change in the refractive index causes changes in reflectivity losses which can be manifested in deviations from the true absorption spectrum (*Harrick*, 1967). In the case of the SR spectrum, deviations from the k-spectrum arise mainly from approximations in applying the KK transform. As discussed above, the KK transform involves the calculation of an integral from 0 to ∞ wavenumbers, but in practice, only a

finite range of spectrum was measured (4000 to 500 cm^{-1} in our studies). The KK transform also assumes normal incidence, while in our experiment, the angle of incidence is 35°; however, as discussed earlier, calculations for water show that the shape and position of the peaks is insensitive to angles up to ~45°.

To probe for such deviations, transmission and SR spectra were measured for a saturated solution of $NaHSO_3$. Figure B.1a shows the SR spectrum as recorded, and Figure B.1b shows the same spectrum after application of the KK transform. Figure B.1c shows the transmission spectrum of the same solution held between CaF_2 windows and Figure B.1d the ATR spectrum. As expected, absorption peaks in the transmission and ATR spectra appear in the reflectance spectrum (Figure 2a) as differential peaks. Comparison of the transmission and ATR spectra to the SR spectrum after the KK transform shows that they agree well, except for a small change in the baseline from 3000 to 2350 cm^{-1}, and a weak band at 1236 cm^{-1} in the SR spectrum. (The latter band occurs in all of our SR spectra, including neat H_2O, and appears to be an artifact due to aging of the gold surface used for the background spectra). The excellent agreement between the ATR/transmission and SR spectra establish that there are no anomalies that need to be taken into account in comparing these spectra for the acid solutions.

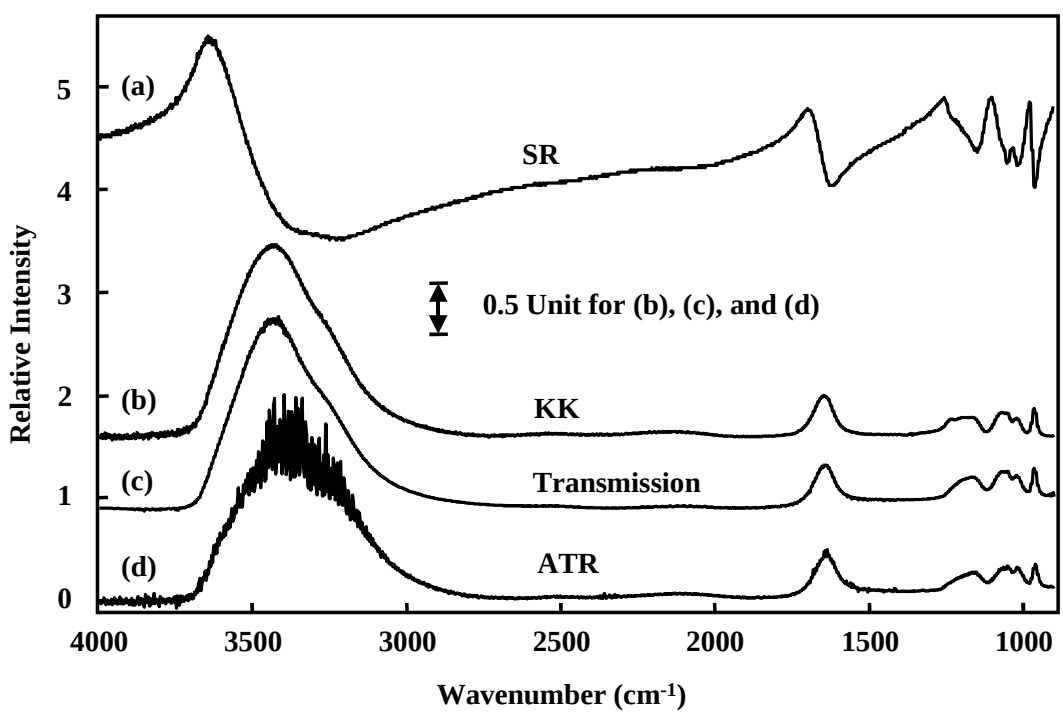

Figure A.1. Comparison of SR and transmission spectra for a saturated $NaHSO_3$ solution. (a) reflectance spectrum ($R_{\bar{\nu}}$) using a reflecting gold mirror for the background; (b) KK transform of the reflectance spectrum; (c) transmission spectrum with solution sandwiched between CaF_2 windows; (d) ATR spectrum.